

MOLECULAR MODELING OF BCL-X_L POST-TRANSLATIONAL MODIFICATIONS
AND OF KETENIMINIUM SALTS

by

Gamze Tanrıver

B.S., Chemistry, Ondokuz Mayıs University, 2007

M.S., Chemistry, Boğaziçi University, 2010

Submitted to the Institute for Graduate Studies in
Science and Engineering in partial fulfillment of
the requirements for the degree of
Doctor of Philosophy

Graduate Program in Chemistry

Boğaziçi University

2021

ACKNOWLEDGEMENTS

I wish to express my deepest gratitude to my thesis supervisors Assoc. Prof. Şaron Çatak (Boğaziçi University) and Prof. Gérald Monard (Université de Lorraine) for their precious scientific guidance, endless attention, never-failing support and understanding. I am really proud of being the first student of Şaron Çatak and the last student of Gérald Monard. They supported and motivated me to continue and reach my goals. I also wish to express my gratitude to Prof. Viktorya Aviyente for her support and encouragement to start my journey in computational chemistry.

I would also like to extend my appreciation to the members of the examining committee, Prof. F. Aylin Sungur (Istanbul Technical University), Assoc. Prof. Başak Kayıtmazer (Boğaziçi University), Prof. Florent Barbault, (Université de Paris), and Prof. Mounir Tarek (Université de Lorraine) for their constructive comments and helpful suggestions for further studies. I also wish to express my gratitude to my "comite de suivre" Prof. Dr. Marco Cecchini and Prof. Dr. Bernard Maigret for their supporting remarks and their time.

Z. Pinar Haşlak, my office mate, Nancy is a beautiful place with your companion and I enjoyed ever moment with you. I would like to also thank Deniz Akgül for her endless support. I also want to thank Melin and Erdem from ITU for their friendship.

I would like to thank the former and current members of Computational Chemistry and Biochemistry Group (CCBG) and CCBU in Bogaziçi University. I am grateful of all of my lab mates; Pelin, Basak, Busenur, Beyza, Zeynep, Volkan, Aslıhan, Öyküm, Oğuzhan, Taylan, Özlem and Esmâ for warm and friendly environment. I will miss our coffee time in Dunkin and our lunch time. I also want to thank all members of LPCT in Université de Lorraine for warm environment. I would like to thank Mrs Severine Bonenberger for spreading smiles and helping us. I would like to thank Alekos and Toni for their friendships. It is always a pleasure to work and have fun with you all.

I would like to thank the French Embassy in Ankara, Turkey for the ‘co-tutelle de thèse’ scholarship (Joint PhD scholarship) that enabled my residence in Nancy. This research was supported by TUBITAK 1001 (116Z513), Bogazici University Research Fund (BAP Grant numbers: 14260, 16863, and 15325), and TUBITAK 3001 (115Z738). GPU resources were allocated by the Mésocentre EXPLOR of the Université de Lorraine and the Centre de Calcul ROMEO of the Université de Reims Champagne-Ardenne as well as TUBITAK ULAKBIM High Performance and Grid Computing Center (TRUBA resources).

I would like to extend my gratitude to my friends, Seçil Soyutemiz, Gönül Mutlu, and Mehtap Karamanlı for their encouragement and invaluable support throughout these years. I would like to thank you my prep-class friends (INT-J) Gökçe and Emel. We laughed together, cried together and stayed strong. I am really lucky to have you as my close friends. Additionally, I do not want to forget to thank my friends Selda, Eda and Neşe. We grew up together in Samsun. We shared really unforgettable moments and always support each other. Time flies. I really missed those times.

Additionally, I thank all lecturers and my classmates in the chemistry department of Ondokuz Mayıs University, particularly Prof. Ömer Andaç and Prof. Zerrin Heren for encouraging me in the beginning of Boğaziçi University journey.

Finally, my deepest thanks go to my family for their continuous support, encouragement, and never-ending love. I dedicate my dissertation to my family, particularly my mother and father İlvan and Yılmaz Tanrıver. They dedicated their lives to support me and my sister to achieve our goals and to have a bright future. I would like to thank for Pelin and Erkan Sağlam for their support and assistance. We succeeded together. Lastly, Ece and Mete Han you make my life is happier than ever. I am really lucky to have you all.

See you on next journeys.

ABSTRACT

MOLECULAR MODELING OF BCL-X_L POST-TRANSLATIONAL MODIFICATIONS AND OF KETENIMINIUM SALTS

Computational chemistry plays an important role in deciphering the structural properties of systems by using different approaches, such as quantum mechanics (QM) and molecular mechanics (MM) and gives insight by mimicking their dynamic environments. This dissertation contains two main topics, namely investigation of Bcl-x_L deamidation via molecular dynamics (MD) simulations and investigation of keteniminium salts via QM methods.

Investigation of post-translational modifications (PTMs) is important to understand their role on the structure and function of proteins. Deamidation, one of the PTMs is a crucial switch used for regulating the biological function of anti-apoptotic Bcl-x_L. In the first part of the thesis, deamidation-induced conformational changes in Bcl-x_L were explored to gain insight into its loss of function by performing MD simulations. MD outcomes suggest that deamidation allosterically causes remarkable changes in conformation, interaction, and dynamics of Bcl-x_L and conceivably impair its function. This study will provide a unique perspective on the underlying mechanism of Bcl-x_L deamidation-induced cell death.

Keteniminium salts (KIs), nitrogen analogues of ketenes are widely used intermediates for the synthesis of various organic substances due to their higher electrophilicity, reactivity and regioselectivity. In the second part of the thesis, KIs were scrutinized, from their formation mechanisms to their involvement in organic reactions, by means of a DFT study. Experimentally observed reactivity differences in the [2 + 2] cycloaddition and electrocyclization reactions were rationalized via a range of different analysis techniques. The outcomes of this study are expected to contribute to the understanding of the formation mechanism as well as the reactivity differences of keteniminium salts and aid synthetic applications.

ÖZET

BCL-X_L POST-TRANSLASYONEL MODİFİKASYONLARININ VE KETENİMİNYUM TUZLARININ MOLEKÜLER MODELLENMESİ

Hesapsal kimya, kuantum mekanik (QM) ve moleküler mekanik (MM) gibi farklı yaklaşımları kullanarak sistemlerin yapısal özelliklerinin deşifre edilmesinde önemli bir rol oynamaktadır ve dinamik çevrelerini taklit ederek bilgiler vermektedir. Bu tez, moleküler dinamik (MD) simülasyonları yoluyla Bcl-x_L deamidasyonunun incelenmesi ve keteniminyum tuzlarının QM yöntemleriyle araştırılması olmak üzere iki ana konuyu içermektedir.

Post-translasyonel modifikasyonların (PTM'ler) araştırılması, proteinlerin yapıları ve işlevleri üzerindeki rollerinin anlaşılması için önemlidir. PTM'lerden biri olan deamidasyon, anti-apoptotik Bcl-x_L'in biyolojik fonksiyonunun düzenlenmesinde kullanılan çok önemli bir anahtardır. Tezin ilk bölümünde, MD simülasyonları ile Bcl-x_L'deki deamidasyon kaynaklı konformasyonel değişiklikler araştırılmıştır. MD sonuçları, deamidasyonun allosterik olarak Bcl-x_L'in konformasyon, etkileşim ve dinamiklerinde önemli değişikliklere neden olduğunu ve muhtemel olarak işlevini bozduğunu göstermektedir. Bu çalışmanın sonuçları, Bcl-x_L deamidasyonunun neden olduğu hücre ölümünün altında yatan mekanizma hakkında benzersiz bir bakış açısı sağlayacaktır.

Ketenlerin nitrojen analogu keteniminyum tuzları, yüksek elektrofilikliği, reaktivitesi ve bölgesel seçiciliği nedeniyle çeşitli organik yapıların sentezi için yaygın olarak kullanılan bir ara üründür. Tezin ikinci bölümünde, KI'ların oluşumu ve kullanıldığı tepkimeler DFT çalışması ile incelenmiştir. [2 + 2] siklokatalizasyon ve elektrohalkalaşma tepkimelerinde deneysel olarak gözlenen reaktivite farklılıkları, farklı analiz teknikleriyle rasyonelleştirilmiştir. Bu çalışmanın sonuçlarının keteniminyum tuzlarının oluşum mekanizmaları ve reaktivite farklılıklarının anlaşılmasına ve sentetik uygulamalara yardımcı olması beklenmektedir.

TABLE OF CONTENTS

ACKNOWLEDGEMENTS	iii
ABSTRACT	v
ÖZET	vi
LIST OF FIGURES	xii
LIST OF TABLES	xxii
LIST OF SYMBOLS	xxv
LIST OF ACRONYMS/ABBREVIATIONS	xxvii
1. INTRODUCTION	1
2. OBJECTIVE AND SCOPE	3
3. THEORETICAL BACKGROUND	4
3.1. Molecular Mechanics (MM)	4
3.1.1. Newton’s Equation of Motion	5
3.1.2. Integration of Newton’s Equations of Motion	5
3.1.3. Molecular Dynamics Simulations	6
3.1.4. Replica Exchange Molecular Dynamics (REMD)	9
3.1.5. Principal Components Analysis (PCA)	10
3.1.6. Clustering Analysis	10
3.2. Quantum Mechanics (QM)	10
3.2.1. The Schrödinger Equation	10
3.2.2. The Hartree-Fock (HF) Theory	13
3.2.3. Semi-Empirical Methods	15
3.2.4. Density Functional Theory	16
3.2.4.1. Basis Sets	20
3.2.4.2. Solvation Models	21
3.2.4.3. Population Analysis (Atomic Charge Models)	22
3.2.5. Non-covalent Interaction Analysis (NCIs)	23
3.2.6. Nucleus-Independent Chemical Shifts (NICS)	24
3.2.7. Anisotropy of the Induced Current Density Analysis (ACID)	24
3.2.8. Atoms in Molecules (AIM)	24

3.2.9.	Conceptual Density Functional Theory (CDFT)	25
3.2.9.1.	Global Reactivity Descriptors	25
3.2.9.2.	Local Reactivity Descriptors	26
4.	IMPACT OF DEAMIDATION ON THE STRUCTURE AND FUNCTION OF ANTI- APOPTOTIC BCL-X _L IN WATER	28
4.1.	Introduction	28
4.1.1.	Bcl-2 Family Protein	28
4.1.2.	B-cell Lymphoma-extra-large (Bcl-x _L)	29
4.1.3.	Post-Translational Modifications (PTMs)	30
4.1.4.	Deamidation of Bcl-x _L	31
4.2.	Methodology	35
4.3.	Results and Discussion	37
4.3.1.	Stability of the Wild type and Deamidated Bcl-x _L Systems	38
4.3.2.	Intrinsically Disordered Region (IDR)	38
4.3.3.	Cluster Analysis	45
4.3.4.	Principal Components Analysis (PCA)	51
4.4.	Conclusions	56
5.	IMPACT OF DEAMIDATION ON STRUCTURE AND FUNCTION OF BCL-X _L IN MEMBRANE	58
5.1.	Introduction	58
5.2.	Methodology	63
5.2.1.	Preparation of the C-tail and REMD Simulation Details	63
5.2.2.	Simulation Details in Water Systems	64
5.2.3.	Generation of Membrane-associated Bcl-x _L and Simulation Details	64
5.3.	Results and Discussion	65
5.3.1.	Evaluation of the C-terminal Tail	66
5.3.2.	Stability of Bcl-x _L Systems prior to and subsequent to Deamidation	67
5.3.3.	Bcl-x _L and Deamidated Bcl-x _L in Water	69
5.3.3.1.	Intrinsically Disordered Region (IDR, loop)	71
5.3.3.2.	Deamidation Impact on the Binding Groove (BG)	75
5.3.4.	Bcl-x _L and Deamidated Bcl-x _L in Membrane	76

5.3.4.1.	Structural Behavior and Interactions of the C-tail in Membrane	77
5.3.4.2.	Intrinsically Disordered Region (IDR)	79
5.3.4.3.	Deamidation Impact on the Binding Groove (BG)	81
5.3.5.	Principal Components Analysis (PCA)	85
5.4.	Conclusions	87
6.	INVESTIGATION of Bcl-x _L -BH3-only PEPTIDE COMPLEX	90
6.1.	Introduction	90
6.2.	Methodology	92
6.3.	Results and Discussion	92
6.3.1.	Stability of BH3-only Peptides in Water	93
6.3.2.	Analysis of Complex Systems	93
6.4.	Conclusions	95
7.	KETENIMINIUM CHEMISTRY	96
7.1.	Introduction	96
7.1.1.	Formation of Keteniminium Salts	96
7.1.1.1.	Methodology	98
7.1.1.2.	Results and Discussion	99
7.1.1.3.	Energetics Analysis of KI Formation	99
7.1.1.4.	Amide Reactivity	100
7.1.1.5.	KI Reactivity	103
7.1.2.	[2 + 2] Cycloaddition Reactions	103
7.1.2.1.	Methodology	109
7.1.2.2.	Results and Discussion	109
7.1.3.	Intramolecular Competition Reactions	113
7.1.3.1.	Methodology	116
7.1.3.2.	Results and Discussion	116
7.2.	General Conclusions	120
8.	KETENIMINIUM SALTS: REACTIVITY AND PROPENSITY TOWARD ELECTROCYCLIZATION REACTIONS	122
8.1.	Introduction	122

8.2. Methodology	124
8.3. Results and Discussion	125
8.3.1. Structure, Energetics and Reactivity of Keteniminium Ions in Elec- trocyclization Reactions	126
8.3.1.1. Structural Features of Keteniminium Ions	126
8.3.1.2. Effect of Nx-substituents on Enamine and Aniline Bearing Keteniminium Ions	127
8.3.2. Energetic Analysis of Electrocyclization Reactions Involving Keten- iminium Ions	130
8.3.3. Population Analysis and Local Reactivity Descriptors	133
8.3.3.1. Population Analysis	133
8.3.3.2. Local Reactivity Descriptors	135
8.3.4. Nature of the Electrocyclization Reaction of Keteniminium Ions . . .	135
8.3.4.1. Atoms in molecules (AIM) Analysis	136
8.3.4.2. Nucleus-Independent Chemical Shifts (NICS) Analysis . .	137
8.3.4.3. Anisotropy of the Induced Current Density Analysis . . .	137
8.3.5. Understanding Effect of Substituents on Keteniminium Reactivity .	140
8.3.5.1. Role of the Substituents in Group I	143
8.3.5.2. Role of the Substituents in Group II	144
8.4. Conclusions	145
9. CONCLUDING REMARKS	146
REFERENCES	148
APPENDIX A: SUPPORTING INFORMATION	181
A.1. Supporting Information for Chapter 4.	181
A.1.1. Force Field Parameterization of Non-standard Iso-Aspartate	181
A.1.2. Secondary Structure Analysis	183
A.1.3. B-factor Coloring	185
A.1.4. Distance Analyses for the Combined Trajectories	186
A.1.5. Protein (Δ C terminal)-C terminal Interactions (residues 196-209) for the Combined Trajectories	188
A.2. Supporting Information for Chapter 5.	190

A.2.1. Area Per Lipid (APL)	190
A.3. Supporting Information for Chapter 8	191
A.3.1. DFT Survey	191
A.3.2. Frontier Molecular Orbitals (FMO) Analysis	198
APPENDIX B: ARTICLES	199
B.1. Impact of Deamidation on the Structure and Function of Anti-apoptotic Bcl- x_L (Article 1)	199
B.2. Keteniminium Salts: Reactivity and Propensity Toward Electrocyclization Reactions (Article 2)	200
B.3. Keteniminium Salts as Key Intermediates for the Efficient Synthesis of 3- Amino-Indoles and -Benzofurans (Article 3)	201
B.4. Straightforward Synthesis of 3-Aminothiophenes Using Activated Amides (Article 4)	202
B.5. Access to 3-Aminobenzothiophenes and 3-Aminothiophenes Fused to 5- membered Heteroaromatic Rings through 6π -electrocyclization Reaction of Keteniminium Salts (Article 5)	203
B.6. Synthesis of 4-membered Ring Alkaloid Analogues via Intramolecular [2+2] Cycloaddition Involving Keteniminium Salt Intermediates (Article 6)	204
B.7. Synthesis of Amino-cyclobutanes via [2+2] Cycloadditions Involving Keten- iminium Intermediates (Article 7)	205
APPENDIX C: COPY-RIGHT LIST	206
C.1. The License for Article 1 in Chapter 4	206
C.2. The License for Article 2 in Chapter 8	207
C.3. The License for Article 3 in Chapter 7	208
C.4. The License for Article 4 in Chapter 7	213
C.5. The Licenses for Articles 5-7 in Chapter 7	218

LIST OF FIGURES

Figure 3.1.	Representative MD simulation flow.	8
Figure 3.2.	Schematic representation of REMD.	9
Figure 4.1.	General presentation of Bcl-2 family.	28
Figure 4.2.	Front and side views of Bcl-x _L (PDB code: 1LXL).	30
Figure 4.3.	Representation of Bcl-x _L (PDB ID:1LXL) with known PTM residues on the IDR region.	31
Figure 4.4.	General mechanism of Asn and Gln deamidations.	32
Figure 4.5.	RMSD histogram for the core, the BG, and the IDR of WT, DM1 and DM2 simulations with respect to initial/starting structures before MD simulations.	39
Figure 4.6.	Backbone per-residue RMSD plots for a) core helices and b) the binding groove of all WT, DM1, and DM2 simulations with respect to initial/built structure.	40
Figure 4.7.	H-bond interactions plots for α 1 residues of the protein-IDR residues of WT, DM1, and DM2. The color bar shows overall contact percentage during the simulations.	40
Figure 4.8.	H-bond interactions plots for the protein (α 2-C-terminal residues)-IDR residues of WT, DM1, and DM2 simulations. The color bar shows overall contact percentage during the simulations.	41

Figure 4.9.	H-bond interactions between residue 52, residue 66, and protein core in representative a) WT, b) DM1, and c) DM2. Blue color denotes IDR region.	42
Figure 4.10.	H-bond interactions plots (expressed in overall contact percentage) for the IDR-IDR residues of WT, DM1, and DM2 simulations. The color bars show the contact percentage during the simulations.	44
Figure 4.11.	Representative positions of the IDR for a) DM2-SIM4 and b) DM2-SIM5. (Blue color denotes the IDR.)	44
Figure 4.12.	a-c) Radial distribution function, $g(r)$, vs the distance between side chain oxygen atoms of residues 52 and 66 and H atoms of the guanidinium moieties in Arg cluster.	46
Figure 4.13.	Distance plot between a) N66@OD1 and guanidinium H atoms of R100. b) D52@CG and R100,102,103@CZ.	46
Figure 4.14.	Front and side superimposition of the representative structures for clusters 0 and 3. Blue and tan color refer to C0 and C3 representative structures, respectively.	48
Figure 4.15.	Radius of gyration (R_g) of the backbone atoms of Y101-A104 in J23 and L130-D133 in J45 of the most populated clusters (C0-C4).	48
Figure 4.16.	Backbone RMSD histogram for the helices of clusters 1-4 with respect to NMR structure.	49
Figure 4.17.	Representation of key H-bond interactions between the BG residues in DM1 (C3).	49

Figure 4.18.	Distance histograms for the key interactions in the binding groove of the representative clusters (WT:C1, C2, DM1:C3, DM2:C4).	50
Figure 4.19.	Distance histograms for the selected H-bonded residues between the C-terminal and $\alpha 8$ of the representative clusters (WT:C1, C2, DM1:C3, DM2:C4).	50
Figure 4.20.	a) Proportion of variance b) Cumulative sum of total variance captured by the first 10 PCs for the combined clusters (From C1 to C9 for WT, DM1, and DM2).	52
Figure 4.21.	Top four PC projections (modes) for each system (WT, DM1, and DM2).	53
Figure 4.22.	Projection of top three PC modes onto the combined MD runs shown in heatmaps.	54
Figure 4.23.	The first three PC modes for a) the BG of WT b) DM1 (front and side views) and c) DM2 simulations.	55
Figure 5.1.	Schematic representation of membrane-anchored Bcl-x _L	58
Figure 5.2.	Schematic representation of this study: Bcl-x _L and deamidated Bcl-x _L <i>i.</i>) in water, and <i>ii.</i> in membrane.	62
Figure 5.3.	Backbone RMSD plots for core helices of FL, DM1 and DM2-Bcl-x _L simulations with respect to initial/built structures.	68
Figure 5.4.	Backbone RMSD plots for the C-tails of FL, DM1 and DM2-Bcl-x _L simulations with respect to initial/built structures.	69

Figure 5.5.	Representative positions of the C-tails among Bcl-x _L and deamidated Bcl-x _L in water.	70
Figure 5.6.	Representative orientations of the BG and the C-tail residues in water.	71
Figure 5.7.	H-bond interactions plots for α 1 residues of the protein-IDR residues of FL, DM1, and DM2. The color bar shows overall contact percentage during the simulations.	73
Figure 5.8.	H-bond interactions plots for the protein (α 2-C-terminal residues)-IDR residues of FL, DM1, and DM2 simulations. The color bar shows overall contact percentage during the simulations.	74
Figure 5.9.	Radial distribution function, $g(r)$, vs the distance between side chain oxygen atoms of residues 52 and 66 and H atoms of the guanidinium moieties in Arg cluster in DM1-wat simulations.	75
Figure 5.10.	Distance plot between Asn52@CG and CZ atoms of guanidinium moieties of R102 in the simulation of DM1-C3) in water.	75
Figure 5.11.	Distance evolution plots for key H-bonded residues in the BG of FL-wat, DM1-wat and DM2-wat in water.	76
Figure 5.12.	The representative snapshots of membrane-embedded C-tails and its water interactions.	78
Figure 5.13.	The tilt angle evolution plots for the C-tails of FL, DM1, and DM2 simulations with respect to the membrane plane simulations in membrane during simulations.	78

Figure 5.14.	H-bond interactions plots for $\alpha 1$ residues of the protein-IDR residues of FL, DM1, and DM2 in membrane. The color bar shows overall contact percentage during the simulations.	79
Figure 5.15.	H-bond interactions plots for the protein ($\alpha 2$ -C-terminal residues)-IDR residues of FL, DM1, and DM2 simulations. The color bar shows overall contact percentage during the simulations in membrane.	80
Figure 5.16.	Initial structures of FL models in membrane.	82
Figure 5.17.	Representative orientation of the BG of FL-C3 toward the membrane.	82
Figure 5.18.	Representative protein head-membrane interactions in the simulations.	83
Figure 5.19.	Distance evolution plots for key H-bonded residues in the BG of FL-memb, DM1-memb and DM2-memb in membrane.	84
Figure 5.20.	Rg as a function of time for the backbone atoms of J23 and J45 of FL, DM1 and DM2 simulations in membrane.	85
Figure 5.21.	a) Proportion of variance b) Cumulative sum of total variance captured by the first 10 PCs for the combined clusters (FL, DM1, and DM2).	86
Figure 5.22.	PC scatter plots for top three PC modes of all MD runs onto all MD runs.	87
Figure 5.23.	PC scatter plots for top three PC modes of water (left) and membrane systems (right) onto all MD runs.	88
Figure 6.1.	The BOP family.	90

Figure 6.2.	Backbone RMSD plot for BH3-only peptides with respect to X-Ray structures.	93
Figure 6.3.	Secondary structure plots of a) BIM b) BID peptides.	93
Figure 6.4.	Representative structure of a) Bcl-x _L -BIM complex b) Bcl-x _L -BID complex.	94
Figure 6.5.	Backbone RMSD plots of a) Bcl-x _L -BIM complex b) Bcl-x _L -BID complex with respect to the built structures.	94
Figure 6.6.	Secondary structure plots of a) Bcl-x _L -BIM complex b) Bcl-x _L -BID complex.	95
Figure 7.1.	General structures of KIs.	96
Figure 7.2.	Summary of the reactions involving KIs.	97
Figure 7.3.	Various formation reactions of KI.	98
Figure 7.4.	Ghosez's KI formation reaction from amides with triflic anhydride. . .	99
Figure 7.5.	HOMO orbitals of C ₃ -substituted amides.	105
Figure 7.6.	HOMO orbitals of N-substituted amides.	106
Figure 7.7.	Competition reaction between allylammonium 3 and corresponding alkene 2 in a [2 + 2] cycloaddition with KI 1.	108
Figure 7.8.	Competition reaction experiment between 10, 11, and 12 in a [2 + 2] cycloaddition with KI 1.	108

Figure 7.9.	Possible reaction mechanisms for the [2 + 2] cycloaddition of keteniminium 1 with olefins 2 and 3.	110
Figure 7.10.	Free energy profile for the [2 + 2] cycloaddition reaction of KI 1 with alkenes 2 and 3. Optimized TS1s and intermediates. Free energies in kcal/mol; M06-2X/6-31+G(d,p) with IEF-PCM in CHCl ₃	111
Figure 7.11.	HOMO-LUMO gaps between KI 1 and alkenes 2 and 3. M06-2X/6-31+G(d,p); iso-surface value = 0.02 au.	112
Figure 7.12.	Intramolecular competition reactions between formation of thiophene, benzothiophene, and [2 + 2]-cycloadduct.	115
Figure 7.13.	Intramolecular competition reaction to access five vs six membered rings.	115
Figure 7.14.	Free energy profiles for the competition reactions.	117
Figure 7.15.	Optimized TSs for the intramolecular [2 + 2] cycloaddition and 6 π electrocyclization of En=3 and En=5.	119
Figure 7.16.	Optimized TS structures for the intramolecular cycloaddition of 16.	120
Figure 8.1.	Access to (hetero)cyclic compounds using KI intermediates.	122
Figure 8.2.	Illustration of bioactive heterocyclic compounds.	123
Figure 8.3.	Optimized structures of KIs.	127
Figure 8.4.	Optimized structures for KIs of N _x -substituted enamine derivatives in Group I. M06-2X/6-31+G(d,p) in CHCl ₃ , extra basis set for S atom.	128

Figure 8.5.	Optimized structures for KIs of N _x -substituted aniline derivatives in Group II. M06-2X/6-31+G(d,p) in CHCl ₃ , extra basis set for S atom.	129
Figure 8.6.	Optimized transition state structures. M06-2X/6-31+G(d,p) in CHCl ₃ , extra basis set for sulfur atom.	132
Figure 8.7.	AIM analysis of the TS structures for Groups I and II. (Values in a.u., M06-2X/ATZ2P//M06-2X/6-31+G(d,p) in CHCl ₃ .)	136
Figure 8.8.	One of the representative image of points (Bq ghost atoms) for NICS calculations.	137
Figure 8.9.	Variation of NICS along the reaction coordinates 1 Å below the RCPs for Groups I and II.	138
Figure 8.10.	ACID plots for the transition states of Groups I and II.	139
Figure 8.11.	R group positions for Groups I and II.	140
Figure 8.12.	Optimized TS structures for the E and Z isomers (entries 6 and 7 in Table 8.5) of enamine systems (Group I).	143
Figure A.1.	The optimized structure of ACE-iso-ASP-NME (HF/6-31G(d)).	182
Figure A.2.	Secondary structure plots for WT simulations.	183
Figure A.3.	Secondary structure plots for DM1 simulations.	184
Figure A.4.	Secondary structure plots for DM2 simulations.	185

Figure A.5.	B-factor coloring based on average LIE calculations between the IDR and protein (Δ IDR) for a) WT, b) DM1, and c) DM2.	186
Figure A.6.	Representative structures of clusters 0 – 4.	187
Figure A.7.	Front and side views of representative snapshots of each system.	187
Figure A.8.	Distance histogram for the key interactions in the binding groove of WT, DM1, and DM2 simulations.	188
Figure A.9.	H-bond interaction plots for protein (Δ C terminal)-C terminal residues of WT, DM1, and DM2 simulations.	189
Figure A.10.	Distance histogram for the key interactions in the selected H-bonded residues between the C-terminal and α 8 of WT, DM1, and DM2 simulations.	190
Figure A.11.	APL plots for the POPC membranes in equilibrium runs.	190
Figure A.12.	Backbone RMSD plots for the IDR of FL, DM1 and DM2-Bcl-x _L simulations with respect to initial/built structures.	191
Figure A.13.	Secondary structure evolution for the selected FL, DM1 and DM2 simulations in water (wat) and membrane (memb).	192
Figure A.14.	FL models in water.	193
Figure A.15.	The non-covalent interaction (NCI) plots of the optimized KI structures. NCI isosurface values= 0.5 and 0.7 au using SCF densities. NCI color scale is $-0.04 < \rho < 0.04$ au.	194

Figure A.16. Optimized TS structures. All energies for the formation of pyrrole and indole derivatives are relative to the pre-reactive conformer (PRC).	196
Figure A.17. Optimized INT structures.	197
Figure A.18. Optimized end product structures.	197
Figure A.19. HOMO of keteniminium ions.	198

LIST OF TABLES

Table 4.1.	Summary of the initial set up.	37
Table 4.2.	Combined clustering summary for WT, DM1, and DM2.	47
Table 5.1.	Summary of the initial system setup.	66
Table 5.2.	Representative C-tail candidates used in the study.	67
Table 6.1.	Initial structure set up.	92
Table 7.1.	Gibbs free energies of activation (ΔG^\ddagger) and reaction (ΔG_{rxn}) for the RDS of Ghosez's reaction with C3 and N substituted amides.	101
Table 7.2.	Calculated HOMO energy, nucleophilicity index, and local nucleophilicity indices for the substituted amides for the substituted amides.	102
Table 7.3.	Calculated condensed fukui (f-) and condensed dual descriptors (CDD) for the heteroatom substituted amides.	104
Table 7.4.	Calculated activation barrier differences between main reaction leading to KI major product and side reaction leading N-sulfonylated minor product.	106
Table 7.5.	Calculated LUMO energy and electrophilicity index for the substituted KIs.	107
Table 7.6.	Natural Population Analysis (NPA) of alkenes 2, 3, and <i>N,N</i> -diallyl keteniminium. M06-2X/6-31+G(d,p).	112

Table 7.7.	Free energies of activation (ΔG^\ddagger) and reaction (ΔG_{rxn}) (kcal/mol) for the [2 + 2] cycloaddition reaction of KI 1 with alkyne 10, alkenes 11 and 12. M06-2X/6-31+G(d,p) with IEF-PCM in CHCl_3	113
Table 7.8.	Intramolecular competition reaction between a 6π electrocyclization and [2 + 2] cycloaddition.	114
Table 7.9.	Gibbs free energies of activation (ΔG^\ddagger) and reaction (ΔG_{rxn}) (kcal/mol) for the competition reaction.	118
Table 7.10.	Gibbs free energies of activation (ΔG^\ddagger) and reaction (ΔG_{rxn}) for the competition reactions.	119
Table 8.1.	Electrocyclization reactions of KI leading to (hetero)cyclic systems. . .	124
Table 8.2.	Free energy barriers (ΔG^\ddagger), and reaction free energies (ΔG_{rxn}) for electrocyclization reactions of KIs. Free energies in kcal/mol.	131
Table 8.3.	Evolution of NPA atomic charges throughout the electrocyclization reaction. M062X/6-31+G(d,p)//M062X/6-31+G(d,p) in CHCl_3	134
Table 8.4.	Calculated P_k^+ and f_k^+ for the C2 and C5 carbon atoms of Groups I and II KIs.	135
Table 8.5.	Effect of substituents on free energy barriers (ΔG^\ddagger), and reaction free energies (ΔG_{rxn}) of 6π -electrocyclizations of KI–Group I.	141
Table 8.6.	Effect of substituents on free energy barriers (ΔG^\ddagger) and reaction free energies (ΔG_{rxn}) of 10π -electrocyclizations of KI–Group II.	142
Table A.1.	Experimentally available structures.	181

Table A.2.	Preparation file for iso-Asp residue.	182
Table A.3.	Free energy barriers (ΔG^\ddagger), and reaction free energies (ΔG_{rxn}) for 6π - electrocyclization reactions of KIs.	193
Table A.4.	Evolution of distances through the electrocyclization reaction (distances in Å).	195

LIST OF SYMBOLS

Br	Bromine atom
C	Carbon atom
Cl	Chlorine atom
e	Electron charge
E or E_{el}	Electronic energy
eV	Electron volt
E_{XC}	Exchange-correlation energy
$E_c[\rho]$	Correlation energy
$E_x[\rho]$	Exchange energy
$f(r)$	Fukui function
GB^{HCT}	Solvation model igb=1
GB^{OBC}	Solvation model igb=2
GB^{OBC2}	Solvation model igb=5
GB^{neck}	Solvation model igb=7
GB^{neck2}	Solvation model igb=8
H	Hamiltonian operator
h_{KS}	Kohn-Sham Hamiltonian Operator
H	Hydrogen atom
K_i	Binding affinity
N	Nitrogen atom
O	Oxygen atom
q_A	Atomic charge
$P(r)$	Parr function
S	Sulfur atom
$V_{ext}(r)$	External potential
$V_{ee}[\rho(r)]$	Electron-electron interactions
Z	Atomic number

$^{\circ}$	Degree
\AA	Angstrom
\approx	Approximately equal to
ΔG^{\ddagger}	Gibbs free energy of activation
ΔG_{rxn}	Gibbs free energy of reaction
ΔG_{solv}	Solvation free energy
ϵ	Dielectric constant
m_i	Mass of a particle
η	Chemical hardness
$\rho(\mathbf{r})$	Electron Density at \mathbf{r}
ψ	Wave function

LIST OF ACRONYMS/ABBREVIATIONS

3D	Three Dimensional
ACID	Anisotropy of the Induced Current Density Analysis
ADF	Amsterdam Density Functional
AIM	Atoms in Molecules
AMBER	Assisted Model Building with Energy Refinement
approx.	approximately
Arg	Arginine
ASD	Atomic Spin Density
Asp	Aspartate
a.u.	Atomic Unit
B3LYP	Becke-3-parameter Lee-Yang-Parr functional
BG	Binding Groove
BLYP	Becke-Lee-Yang-Parr
BMK	Boese-Martin for Kinetics
CDFT	Conceptual Density Functional Theory
CPCM	Conductor-like Polarizable Continuum Model
DFT	Density Functional Theory
DM1	Aspartate deamidated Bcl-x _L
DM2	iso-Aspartate deamidated Bcl-x _L
DSSP	Definition of Secondary Structure Prediction
DZ	Double Zeta (basis set)
DZP	Double Zeta Polarized (basis set)
EDG	Electron-Donating Group
EWG	Electron-Withdrawing Group
Exp.	Experimental
FMO	Frontier Molecular Orbital
GAFF	General AMBER Force Field
GGA	Generalized Gradient Approximation

GIAO	Gauge Independent Atomic Orbital
Glu	Glutamate
GTO	Gaussian Type Orbital
H-bond	Hydrogen Bond
HF	Hartree-Fock theory
HMR	Hydrogen Mass Partitioning
HOMO	Highest Occupied Molecular Orbital
IDR	Intrinsically Disordered Region
IEFPCM	Integral Equation Formalism Polarizable Continuum Model
IRC	Intrinsic Reaction Coordinate
iso-Asp	iso-Aspartate
ITC	Isothermal Titration Calorimetry
KDE	Kernel Density Estimator
KI	Keteniminium Salt
KS	Kohn-Sham
LCAO	Linear Combination of Atomic Orbitals
LDA	Local Density Approximation
LIE	Linear Interaction Energy
LUMO	Lowest Unoccupied Molecular Orbital
Lys	Lysine
M06-2X	Hybrid Meta Exchange-Correlation Functional
MD	Molecular Dynamics
MM	Molecular Mechanics
MO	Molecular Orbitals
MOMP	Mitochondrial Outer Membrane Permeabilization
MM-GB/SA	Molecular Mechanics-Generalized Born/Surface Area
MM-PB/SA	Molecular Mechanics Poisson Boltzman Surface Area
MPW1K	Modified Perdew-Wang 1-parameter model (kinetic functional)
NBO	Natural Bond Orbital
NCI	Non-Covalent Interactions
NICS	Nucleus-Independent Chemical Shifts

NMR	Nuclear Magnetic Resonance
NPA	Natural Population Analysis
PC	Principal Components
PCA	Principal Component Analysis
PBC	Periodic Boundary Conditions
PCM	Polarizable Continuum Method
PDB	Protein Data Bank
PES	Potential Energy Surface
PM3	Parameterization Method 3
PM6	Parameterization Method 6
PME	Particle-Mesh Ewald
POPC	1-Palmitoyl-2-oleoylphosphatidylcholine
PRC	Pre-reactive Complex or Conformer
PTM	Post-Translational Modification
RT	Room Temperature
QM	Quantum Mechanics
QTAIM	Quantum Theory of Atoms in Molecules
RDF	Radial Distribution Functions
R _g	Radius of Gyration
RMSD	Root Mean Square Deviation
SS	Secondary Structure
SCF	Self Consistent Field
SCRf	Self Consistent Reaction Field
SE	Semi-Empirical
SMD	Solvation Model Based on Density
STO	Slater Type Orbital
TS	Transition State
TZ	Triple Zeta (basis set)
TZP	Triple Zeta Polarized (basis set)
WT	Wild Type

1. INTRODUCTION

Bcl-x_L is the main focus in the first part of the thesis. Bcl-x_L is a mitochondrial transmembrane protein that regulates apoptosis in response to various apoptotic stimuli. Bcl-x_L was characterized as an anti-apoptotic protein in 1993 [1]. In 1996, experimental structure of human Bcl-x_L was resolved by X-ray crystallography and nuclear magnetic resonance (NMR) [2]. In recent years (over 8400 research articles) Bcl-x_L has been subject to many experimental and computational articles, owing to its biological significance in cell survival and its potential for cancer therapy. Notably, Bcl-x_L undergoes post-translational modifications (PTMs) on its loop region (intrinsically disordered region-IDR), which is also the essential site for deamidation –a non-enzymatic reaction and regulatory mechanism in many biological processes. Deamidation on the IDR of Bcl-x_L induces loss of anti-apoptotic function. Hence, deamidation of Bcl-x_L is a pivotal switch that regulates its biological function. In recent studies, the importance of the IDR as well as hotspots on the IDR have been reported; nearly 20 experimental articles, reviews, and conference papers have been published with various aspects of deamidation in Bcl-x_L, but deamidation-induced structural changes and their effects on the anti-apoptotic function of Bcl-x_L are not yet completely understood. Understanding the dynamics of the IDR and the structural changes upon its deamidation plays a crucial role in elucidating potential impacts of deamidation on the structure and function of Bcl-x_L. This study aims to computationally unravel the structural consequences of deamidation that leads to loss of Bcl-x_L anti-apoptotic function at the atomic level. The outcomes of this project are expected to pave the way for future experimental and computational studies.

Keteniminium salts are the main interest in the second part of the thesis combining computational and experimental studies. In recent years keteniminium salts (KIs) have gained considerable attention and have been subject to over 120 research articles and reviews. KIs are an improved alternative to their ketene analogues, due to their higher reactivity and high electrophilicity. Keteniminium salts are versatile and reactive cationic intermediates in organic chemistry and are used in a wide range of reactions such as cycloadditions, $6\pi/10\pi$ electrocyclizations, Pictet–Spengler cyclizations, and so on. Historically, the pioneers of the use and synthesis of KI are Viehe and Ghosez [3, 4]. Various KI formation

reactions, allowing a broader use of these intermediates, have been disclosed, namely reactions of α -haloenamines with Lewis acids, [4–6] triflation of amides, [7] methylation of ketenimines, [8] and protonation of ynamines [9, 10] and ynamides [11–13]. In this thesis, keteniminium salts were investigated starting from their formation reactions to their role in several organic reactions. KI chemistry was divided into two chapters (Chapters 7 and 8). Chapter 7 was divided into three topics, namely formation of KI, [2 + 2] cycloaddition reaction and intra-molecular competition reactions. Intramolecular and intermolecular [2 + 2] cycloaddition reactions of KIs with alkenes or alkynes are widely used methods to obtain cyclobutanone/cyclobutenone derivatives. Briefly, structural and energetic analysis and the reactivity differences in starting amides and keteniminium derivatives bearing different substituents were scrutinized by structural and energetic analysis using density functional theory (DFT). Electrocyclization is a powerful method to build complex structural motifs. Chapter 8 covers reactivity and propensity of KIs toward electrocyclization reactions. In addition, the true nature of the cyclization mechanism of keteniminium salts is disclosed via a range of different analysis techniques. Computational findings were in line with experiments.

2. OBJECTIVE AND SCOPE

Brief information about the research topics was presented in Chapter 1. Chapter 3 includes basic principles of Molecular Mechanical (MM) and Quantum Mechanical (QM) methods.

The first topic of interest in this thesis is the investigation of deamidation's impact on the structure and function of anti-apoptotic Bcl-x_L to gain insight into its loss of function by performing microsecond-long molecular dynamics (MD) simulations. In Chapter 4 structural consequences of deamidation on Bcl-x_L in water is highlighted at the atomic level. In Chapter 5, the potential impacts of deamidation in the IDR and membrane association induced conformational changes is investigated by employing molecular dynamics simulations. Chapters 6 covers the investigation of the structural behavior of BH3-only peptide to understand complex systems between anti-apoptotic protein and BH3-only peptide.

In the second part of the thesis, keteniminium salts (KIs) are investigated from their formation to their reactions (Chapters 7 and 8). Thus, understanding the mechanistic aspect of the KI formation reactions eases the design and development processes of these intermediates to access complex structures. Chapter 7 includes three topics. Firstly, an extensive range of substituents and their effects on the reactivity of the starting amide is scrutinized to give insight on their contributions to the KI formation mechanism by activation of an amide. Then, [2+2] cycloaddition reactions of KIs with alkene/alkyne computationally is investigated and the outcomes are discussed. Competition reactions between intramolecular [2+2] cycloaddition and 6 π -electrocyclization of KI are examined and experimental findings are elucidated by means of DFT study. Lastly, in Chapter 8 keteniminium derivatives bearing different substituents leading to six different heterocyclic systems are explored via DFT and a range of different analysis techniques. This study aims to give insight on reactivity of KI derivatives bearing different substituents and heteroatoms towards electrocyclization reactions.

3. THEORETICAL BACKGROUND

This chapter summarizes Molecular Mechanics (MM), particularly Molecular Dynamics (MD) and Quantum Mechanics (QM) in order to provide the basic principles of the theoretical approaches used in the thesis.

3.1. Molecular Mechanics (MM)

Molecular Mechanics is a powerful method in order to calculate and predict properties of molecules and mostly used in molecular modeling. Molecular mechanics defines the total energy through a Force field (FF) which is a combination of a parameterized equation and its parameter value set. A typical force field consists of bonded and non-bonded terms as follows

$$V = \sum_{bonds} V_{bond} + \sum_{angles} V_{bend} + \sum_{dihedrals} V_{tors} + \sum_{pairs} V_{vdW} + \sum_{pairs} V_{elec} \quad (3.1)$$

$$V = \sum_{bonds} K_{bond}(r - r_0)^2 + \sum_{angles} K_{bend}(\theta - \theta_0)^2 + \sum_{dihedrals} \frac{V_n}{2} [1 + \cos(n\phi - \gamma)] \quad (3.2)$$

$$+ \sum_{pairs} \frac{A_{ij}}{r_{ij}^{12}} - \frac{B_{ij}}{r_{ij}^6} + \sum_{pairs} \frac{q_i q_j}{\epsilon r_{ij}}$$

where K_{bond} is specific bond force constant, r is bond length and r_0 is equilibrium bond distance, K_{bend} is the angle bending force constant, θ is the bond angle, θ_0 is equilibrium bond angle, V_n is the amplitude, n is the number of minima on the potential energy surface (PES), ϕ is the torsion angle/dihedral angle and γ is the phase factor. For non-bonded terms: where van der Waals interaction between two atoms i and j separated by distance r_{ij} is described by the 12-6 Lennard Jones potential (LJ) with parameters A_{ij} and B_{ij} . LJ describes the repulsive and attractive forces between two particles as successively shown in the equation. Coulomb potential is described by electrostatic interaction between a pair of atoms i and j using the point charge q_i and q_j on atom, ϵ as the dielectric constant of medium and r as distance between charges.

Selection of force field (FF) depends on the system (the number of atoms, the research problem, details, and so on). Coarse grain (CG), united atoms (UA) and all atoms (AA) FFs are commonly used force fields. In this dissertation, we used an all atom model using Amber force fields.

3.1.1. Newton's Equation of Motion

MM is often used in conjunction with molecular dynamics (MD) using Newton's equations of motion given as

$$F_i = m_i \mathbf{a}_i. \quad (3.3)$$

The force is derived from the potential energy function with respect to the internal coordinates

$$F_i = -\frac{\partial U(r)}{\partial r_i}. \quad (3.4)$$

Equation (3.3) and Equation (3.4) define Newton's second law of motion

$$m_i \mathbf{a}_i = \mathbf{F}_i - \frac{\partial U(r)}{\partial r_i} \quad (3.5)$$

where F_i is force on an atom, m_i is mass of the atom along the coordinate r_i , \mathbf{a}_i is acceleration of the atom.

3.1.2. Integration of Newton's Equations of Motion

The equations of motion are integrated by using finite difference methods, such as leapfrog, Verlet algorithm, or velocity Verlet algorithm, which give approximate position and dynamic properties. The velocity Verlet algorithm calculates positions, accelerations, and velocity at the same time shown as

$$v(t + \frac{1}{2}\Delta t) = v(t) + \frac{1}{2}a(t)\Delta t \quad (3.6)$$

$$x(t + \Delta t) = x(t) + v(t + \frac{1}{2}\Delta t)\Delta t \quad (3.7)$$

$$a(t + \Delta t) = f(x(t + \Delta t)) \quad (3.8)$$

$$v(t + \Delta t) = v(t + \frac{1}{2}\Delta t) + \frac{1}{2}a(t + \Delta t)\Delta t. \quad (3.9)$$

Iterating those equations over time using molecular mechanics as a definition of the energy of a molecular system defines a molecular dynamics (MD) simulation.

3.1.3. Molecular Dynamics Simulations

MD simulation provides time-dependent behavior of a biomolecular system and change in conformational properties by mimicking the biological environment conditions. Historically, the first MD simulations were performed for a liquid hard sphere model by Alder and Wainwright in the late 1950's [14, 15]. In 1974, Rahman and Stillinger performed the first simulation in realistic environment, that is, in liquid water [16]. Then, the first MD simulation of proteins were studied by McCammon et al in 1977 [17]. They studied the dynamics of a folded globular protein (bovine pancreatic trypsin inhibitor).

Periodic boundary conditions (PBC) are used to mimic the bulk effect and avoid boundary effects caused by finite size. PBC is the repetition of the simulation box (the unit cell) in all directions throughout space- so called images of the system in order to form an infinite lattice. When a molecule/particle moves and leaves the simulation box, one of its periodic images will enter from the opposite side with exactly the same way (direction). Thus, the number of molecules in the simulation box will be conserved and the system perceives no surface. Various periodic cell shapes, such as cubic, truncated octahedron, and rhombic dodecahedron (RHDO) are possible and the periodic cell is chosen according to the system size/shape and simulation program functionality.

There are two approaches in solvation models, namely implicit and explicit models. In PBC, the explicit solvent model is used. In explicit solvation, three types of water models are possible which are rigid point charges (i.e., fix atom positions), flexible point charges

(i.e., atoms on spring) and polarizable (i.e., accounting for explicit polarization) models. The most commonly used solvation model is the rigid TIP3P water model.

In PBC, direct summation, Ewald summation, and Particle-mesh Ewald (PME) are the most common approaches to calculate long-range interactions. Ewald summation method is computationally expensive. Particle Mesh Ewald (PME) is the most used method in MD to consider long-range electrostatic interactions [18, 19]. Compared to Ewald summation ($O(N^2)$), PME uses Fast-Fourier transform (FFT) to accelerate reciprocal space computations and scales as $O(N\log(N))$. Thus, it is a faster algorithm and reduces time for calculations.

Potential energy surface (PES) covers all possible conformations of a molecule/system. The ergodic hypothesis states that the ensemble averages utilized to compute expectation values can be substituted by time averages over the simulation. In other words, an average ensemble observable equals a time-averaged observable as follows

$$\langle A \rangle_{ensemble} = \langle A \rangle_{time} \quad (3.10)$$

In addition, MD simulations allow the observation of macroscopic properties of a system through microscopic simulations. A macroscopic state's properties are calculated by using thermodynamic ensembles, which are a collection of microscopic states. The most common ensembles are:

- Microcanonical ensemble (NVE) ensemble; constant N, V, and E,
- Canonical ensemble (NVT); constant N, V, and T,
- Isothermal-isobaric ensemble (NTP); constant N, T, and P,
- Grand canonical ensemble (μVT); constant μ , V, and T.

where number of particles (N), volume (V), energy (E), temperature (T), pressure (P), and chemical potential (μ). The most commonly used ensemble is NVT due to its computational efficiency. In this dissertation, NVT ensemble was used in all sampling simulations.

Various temperature algorithms are available in order to maintain a constant temperature during the simulations and to adjust the temperature to the desired value. Berendsen thermostat modifies/updates the velocity at an assigned time scale by using a weak-coupling algorithm [20]. The drawback of the Berendsen thermostat is its weak velocity rescaling to ensure temperature distribution. In 1980, Andersen developed a stochastic collision model by having random (imaginary) collisions of molecules with an imaginary heat bath at the desired temperature. [21]. Langevin thermostat introduces the (random) collision frequency " γ " by imposing a frictional drag force on the motion of the solute in the solvent. This thermostat is the most widely used thermostat in production simulations. Nosé-Hoover, another frequently used thermostat, includes the heat bath explicitly as an additional degree of freedom. In order to maintain constant pressure Berendsen, Andersen, and Parrinello-Rahman barostats can be used in MD simulations.

The discrete time step, Δt is a limitation of MD. Longer time length can yield less efficient sampling. In order to increase the time steps and reach longer time length, constraints can be employed. H-bond vibration being the fastest motions in a simulation, the SHAKE algorithm can be carried out in order to constrain bonds involving all hydrogen bonds (i.e., by eliminating the fastest H bond vibrations) [22]. The SHAKE algorithm allows an increase of the time step, usually 2 fs. Hydrogen Mass Repartitioning(HMR) can help increase the time step to 4 fs by transferring a fraction of the mass of heavy elements (e.g., C, N, O, etc.) to their neighbouring hydrogen atoms, and in turn, slowing down the bond vibrations [23].

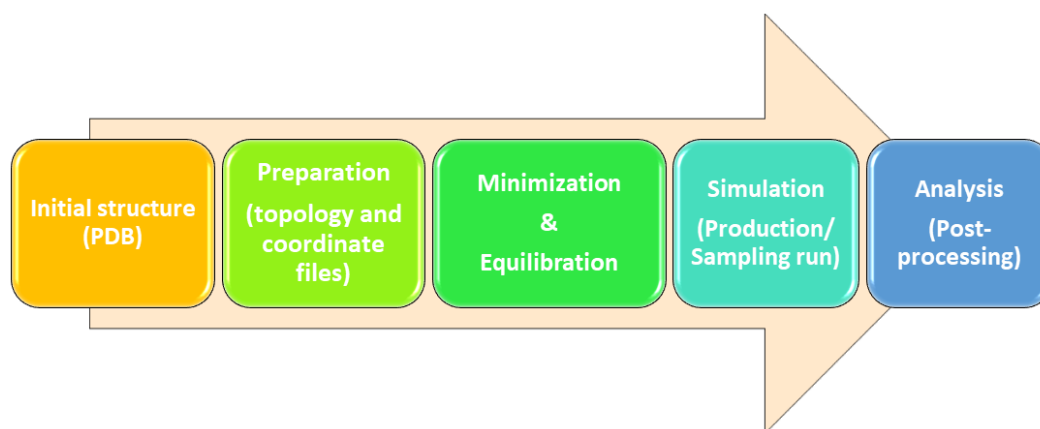


Figure 3.1. Representative MD simulation flow.

Taken together, MD simulations are a useful method to scrutinize protein, complex, and dynamic processes that occur in biological systems. MD parameters (temperature, length of run, and step size, etc.) and starting structure play crucial roles in MD simulation in order to sample representative conformations. In the end, a typical MD flow is depicted in Figure 3.1.

3.1.4. Replica Exchange Molecular Dynamics (REMD)

In classical/conventional MD, it is hard to scan/discover large areas of the energy landscape due to energy barriers between different local energy minima. To overcome the sampling problem in classical MD one of the mostly used methods is replica exchange molecular dynamics (REMD), also known as parallel tempering. REMD is a useful technique, which enhances the conformational sampling of proteins [24, 25]. Basically, REMD includes parallel multiple independent simulations at different temperatures, which periodically attempt an exchange in temperature (Figure 3.2). Therefore, low temperature replicas can exchange temperature with higher temperatures and rapidly pass potential barriers by allowing enhanced sampling of conformations. Besides temperature exchanges between replicas (T-REMD), Hamiltonian REMD (H-REMD), pH-REMD, Reservoir REMD, constant Redox Potential REMD (E-REMD) are other types of exchange attempts.

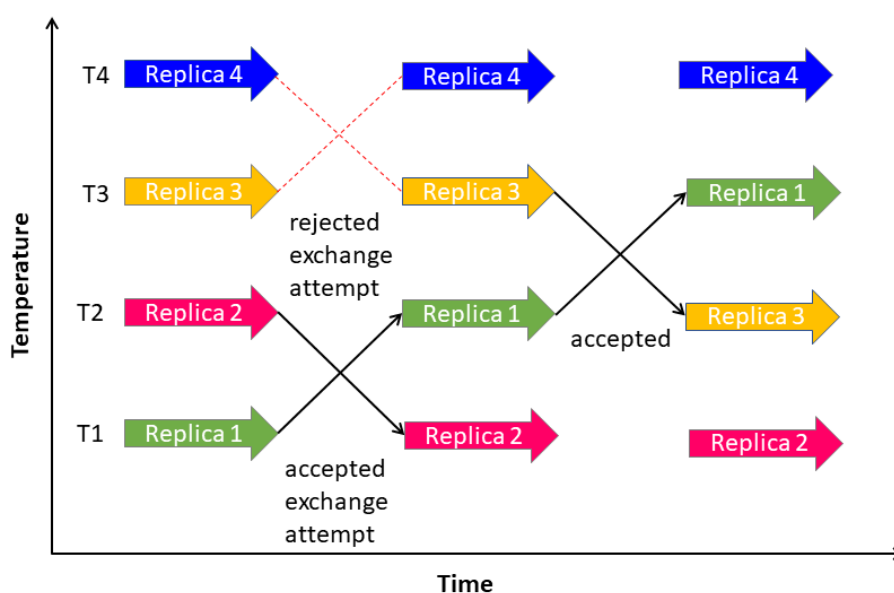


Figure 3.2. Schematic representation of REMD.

3.1.5. Principal Components Analysis (PCA)

Principal Components Analysis (PCA) provides insight into the dominant motions and the essential dynamics of the system [26]. Briefly, principal components analysis translates Cartesian coordinates (trajectories) into the dominant motions. Through PCA, the conformational differences between simulations are explored by investigating the distribution overlap. Visual inspections of principle component (PC) provide information on the similarity of the motions. PCs (Normal modes) can be visualized with Normal Mode Wizard (NMWiz) [27] in VMD (1.9.3) [28].

3.1.6. Clustering Analysis

Clustering is one of the popular techniques in order to group similar conformations into subsets (i.e., clusters) [29, 30]. Various clustering algorithms are available, such as db-scan, hierarchical, k-means. Clustering algorithms detect and distinguish different clusters and group them based on conformational (dis)similarities. Clustering analysis gives insight into conformational changes/states during the simulations and help to understand structural and function relationships for a given system. In the thesis, HierAgglo algorithm (hierarchical agglomerative) with linkage and sieve was used by performing the combined clustering analysis.

3.2. Quantum Mechanics (QM)

3.2.1. The Schrödinger Equation

QM provides mathematical tools in order to describe the properties of microscopic systems. The behavior of electrons in molecules under the influence of the electromagnetic field exerted by nuclear charges can be described by the time-independent Schrödinger equation

$$\hat{H}\psi = E\psi \quad (3.11)$$

where \hat{H} is the Hamiltonian operator and energy of the system E is the eigenvalue. ψ is the wave function, which is the mathematical function that describes the spatial distribution of electrons and nuclei in the system. The Hamiltonian operator is the sum of kinetic energy operator and potential energy operator

$$\hat{H} = \hat{T} + \hat{V}. \quad (3.12)$$

For " m " is mass of a particle, the kinetic energy operator (\hat{T}) can be expressed in three dimensions as

$$\hat{T} = -\frac{\hbar^2}{2m} \nabla^2 \quad (3.13)$$

where

$$\nabla^2 = \left[\frac{\partial^2}{\partial x^2} + \frac{\partial^2}{\partial y^2} + \frac{\partial^2}{\partial z^2} \right] \quad (3.14)$$

and

$$\hbar = \frac{h}{2\pi} \quad (3.15)$$

where \hbar is Planck's constant divided by 2π . For a n particle system, the kinetic energy operator is represented as

$$\hat{T} = -\frac{\hbar^2}{2m_i} \sum_{i=1}^n \nabla^2. \quad (3.16)$$

The potential energy operator for a system of charged nuclei i and j is as follows

$$\hat{V}(\mathbf{r}) = \sum_{i>j} \frac{Z_i Z_j e^2}{4\pi\epsilon_0} \frac{1}{|\mathbf{r}_i - \mathbf{r}_j|} \quad (3.17)$$

where the atomic number of particle is represented as Z , the unit charge is e , ϵ_0 is the permittivity constant (value) and the distance between particles is r .

For a molecular system composed of electrons and nuclei, the potential energy operator in Equation (3.17) becomes

$$\hat{V}(\mathbf{r}) = -\sum_{A,i} \frac{Z_A e^2}{4\pi\epsilon_0} \frac{1}{|\mathbf{r}_A - \mathbf{r}_i|} + \sum_{A>B} \frac{Z_A Z_B e^2}{4\pi\epsilon_0} \frac{1}{|\mathbf{r}_A - \mathbf{r}_B|} + \sum_{i>j} \frac{e^2}{4\pi\epsilon_0} \frac{1}{|\mathbf{r}_i - \mathbf{r}_j|}. \quad (3.18)$$

In Equation (3.18), the electron-nuclei attraction is defined with the first term, nuclei-nuclei repulsion is accounted in the second term and the last term also presents electron-electron repulsion. Hence, Equation (3.12) can be written as

$$\hat{H} = T_n + T_e + V_{e-n} + V_{n-n} + V_{e-e}. \quad (3.19)$$

Two-particle systems can be solved accurately by the Schrödinger equation. However, the Schrödinger equation for multi-electron (many particle systems) is hard to solve and need some approximations. Hence, some approximations were proposed in order to solve the equation/problem, such as the Born-Oppenheimer Approximation, the Hartree-Fock (HF) theory, and the Density Functional Theory (DFT). The nuclei are much heavier than electrons therefore their motions are much slower than electron motions and the electronic wave function depends upon the nuclear positions but not upon their velocities. Born-Oppenheimer Approximation assumes that the positions of the nuclei can be considered to be fixed. This allows the separation of the Hamiltonian into nuclear $\hat{\mathcal{H}}_n$ and electronic $\hat{\mathcal{H}}_{el}$ parts. Equation (3.19) can be expressed as

$$\hat{H} = T_n + V_{n-n} + \hat{\mathcal{H}}_{el}. \quad (3.20)$$

The nuclear kinetic energy term in Equation (3.19) is therefore neglected, and nuclear-nuclear potential energy term is considered as a constant. Thus, the electronic structure of a molecule can be solved by the electronic Schrödinger equation

$$\hat{\mathcal{H}}_{el} \Psi_{el} = E_{el} \Psi_{el}. \quad (3.21)$$

And the total energy of the system is defined as

$$E_{total} = E_{el} + V_{n-n}. \quad (3.22)$$

One of the main approximation methods used in quantum mechanics in order to solve Equation (3.21) is the variational method which allows us to estimate the energy of the ground state of a many particle system. Variational principle states that the expectation value of the Hamiltonian which is computed with any trial wave function (Φ) is always higher than or equal to the energy of the ground state (ϵ_0) given as

$$\frac{\int \Phi^* \hat{H} \Phi}{\int \Phi^* \Phi} \geq \epsilon_0. \quad (3.23)$$

An approximation to the ground state can be found by varying Φ inside a given set of functions and looking for the function that minimizes the expectation value of the Hamiltonian. Hartree-Fock Theory and Density Functional Theory are based on this variational principle.

3.2.2. The Hartree-Fock (HF) Theory

The Hartree-Fock (HF) theory is one of the approximate theories in order to solve the many-body Hamiltonian. In the Hartree-Fock method, the electrons are considered as occupying single-particle orbitals making up the many-electron wave function. By an effective potential each electron experiences the presence of electrons in other orbitals. The overall electronic wave function of a system composed of N number of electrons is defined as a Slater determinant which is constructed by antisymmetrized product of one-electron wave functions, satisfying the Pauli Exclusion Principle

$$\Psi^{SD}(\vec{x}_1, \vec{x}_2, \dots, \vec{x}_N) = \frac{1}{\sqrt{N!}} \begin{vmatrix} \chi_1(\vec{x}_1) & \chi_2(\vec{x}_1) & \dots & \chi_N(\vec{x}_1) \\ \chi_1(\vec{x}_2) & \chi_2(\vec{x}_2) & \dots & \chi_N(\vec{x}_2) \\ \vdots & \vdots & & \vdots \\ \chi_1(\vec{x}_N) & \chi_2(\vec{x}_N) & \dots & \chi_N(\vec{x}_N) \end{vmatrix}. \quad (3.24)$$

A spin orbital (χ) is simply the product of a spatial orbital (φ) and the spin function (g) in a given coordinate r represented as

$$\chi_i(r) = \varphi(r)g(m_s) \quad (3.25)$$

where the value of $g(m_s)$ can be either α or β depending on the value of the quantum number m_s .

Molecular orbital coefficients are varied according to the variational principle and the overall wave function is optimized in an iterative manner until no further changes occur. This procedure is called the Self-Consistent Field (SCF). Hartree-Fock equation is used for the minimum energy calculations of the corresponding orbital of energy ε_i

$$\hat{F} = \varepsilon_i \chi_i. \quad (3.26)$$

The Fock operator for each electron i (\hat{F}_i) is expressed by

$$\hat{F}_i = -\frac{1}{2}\nabla_i^2 \sum_k^{nuclei} \frac{Z_k}{r_{ik}} + V_{HF(i)} \quad (3.27)$$

where $V_{HF(i)}$ is the Hartree-Fock potential which accounts for the average repulsive potential experienced by each electron due to the other electrons.

The SCF strategy uses some guess wave functions to construct the Fock operator, and then solve the Schrödinger equation. The procedure is then iterated by using the output functions as new input functions or with more sophisticated methods until the input and output functions are the same. If the convergence fails, the trial functions are varied and the process is iterated upon till self-consistency is attained to yield numerical solutions to the Hartree-Fock potential.

Electrons as charged particles expose Coulomb repulsion and the motion of one electron has an impact on the motion of the others. Hartree-Fock theory stems from the descrip-

tion of the dynamic electron correlation as induced by their instantaneous mutual repulsion. The methods, which are based on the wave function calculation, such as Configuration Interaction (CI), Møller-Plesset Perturbation Theory and Coupled Cluster are computationally very expensive. Density functional methods potentially offer as accurate results but with a lower computational cost.

3.2.3. Semi-Empirical Methods

Semi-empirical (SE) methods use of parameters derived from experimental (empirical) data and theoretical approximations in order to simplify the Hartree–Fock (HF) method. Semi-empirical methods proposed distinct approximations to the Hamiltonian by neglecting many integrals (particularly two electron integrals) in order to speed up/simplify the calculations and reduce the computational cost. Additionally, SE methods consider only the valence shell electrons and a minimal basis set is used. Several semi-empirical methods have been developed and parameterized with different approximations. SE are commonly based on the Zero Differential Overlap approximation (ZDO) which neglects the overlap between different basis functions centered on different atoms

$$\phi_{\mu}^A(i)\phi_{\mu}^B(i) = 0 \quad \text{if } A \neq B. \quad (3.28)$$

The various ZDO models can be grouped according to their approximations for the one and two electron integrals. When complete neglect of differential overlap (CNDO) [31] uses zero-differential overlap (ZDO) for the two-electron integrals, intermediate neglect of differential overlap model (INDO) [32] covers the integrals that are over orbitals centred on the same atom (one-center two electron integrals).

Mostly used modern semi-empirical methods are neglect of diatomic differential overlap model (NDDO) based, [33] such as MNDO, AM1, PM3, PM6, and PM7. In the MNDO method (modified neglect of diatomic overlap) introduced by Dewar and Thiel [34], the repulsions between atoms which are separated by their van der Waals distances are overestimated. AM1 (Austin Model 1) [35] treats the hydrogen bondings better than MNDO but the misrepresentation of the hydrogen bonds is still a problem. PM3 (parametrized model

number 3) [36] method uses the same equations and formalism as the AM1 method but the number of parameters for each element is different. PM6 (Parameterized Model 6) includes improved parameters (esp. transition metal systems) and core-core interaction [37]. PM7 (Parameterized Model 7) is an improved version of PM6 which adds explicit terms to describe non-covalent interactions (NCIs).

3.2.4. Density Functional Theory

Density Functional Theory (DFT) is one of the most extensively used method for quantum mechanical calculations of many-body systems [38,39]. Contrary to Hartree-Fock Theory which deals directly with the wave function, DFT is based on the electron density. In 1964, DFT was introduced with the Hohenburg-Kohn that proposed that the density of a system determines all its ground-state properties. Calculation of the kinetic energy of the system is the main difficulty in the Hohenburg-Kohn approach. The Kohn-Sham (KS) density functional theory provides a workaround by dividing the kinetic energy (KE) functional of a system into two parts: a) one that considers electrons as non-interacting particles and b) a small correction term accounting for electron-electron interaction as follows

$$E[\rho(r)] = E_{KE}[\rho(r)] + E_H[\rho(r)] + E_{XC}[\rho(r)] \quad (3.29)$$

where $\rho(r)$ refers to the total electron density at a particular point "r". $E_{KE}[\rho(r)]$ is the kinetic energy of the non-interacting electrons

$$E_{KE}[\rho(r)] = \sum_i^N \int \psi_i(r) - \frac{\nabla^2}{2} \psi_i(r) dr \quad (3.30)$$

where $\psi_i(r)$ is the Kohn-Sham molecular orbitals.

$E_H[\rho(r)]$ is the electron-electron Coulombic energy which does not consider the correlation between motions of electrons expressed as

$$E_H[\rho(r)] = \frac{1}{2} \int \int \frac{\rho(r_1)\rho(r_2)}{|r_1 - r_2|} dr_1 dr_2. \quad (3.31)$$

The last term, the exchange-correlation (XC) energy ($E_{XC}[\rho(r)]$) corresponds to the correction to the kinetic energy appearing from the interacting nature of electrons of opposite spin (correlation term) and non-classical corrections to the electron-electron repulsion energy between electrons of the same spin (exchange term) given by

$$E_{XC}[\rho(r)] = \int \rho(r)\epsilon_X[\rho(r)]dr + \int \rho(r)\epsilon_C[\rho(r)]dr. \quad (3.32)$$

The wave function of this system with N number of electrons can be shown as a Slater determinant of one-electron functions χ_i . Hence, the electron density can be written as

$$\rho(r) = \sum_i^N \langle \chi_i | \chi_i \rangle. \quad (3.33)$$

Therefore, the hamiltonian h_i^{KS} of the Kohn-Sham equations

$$h_i^{KS} \chi_i = \epsilon_i \chi_i \quad (3.34)$$

where h_i^{KS} is the Kohn-Sham Hamiltonian and ϵ_i is the KS orbital energy. The KS Hamiltonian can be expressed as

$$h_i^{KS} = -\frac{\nabla^2}{2} - \sum_k^{nucleus} \frac{Z_k^2}{|r_i - r_k|} + \int \frac{\rho(r)}{|r_i - r_j|} dr + V_{XC}. \quad (3.35)$$

The exchange correlation potential V_{XC} is the functional derivative of the XC in Equation (3.32) shown as

$$V_{XC}[\rho(r)] = \epsilon_X[\rho(r)] + \epsilon_C[\rho(r)] + \frac{\partial \epsilon_X(r)}{\partial \rho} + \frac{\partial \epsilon_C(r)}{\partial \rho}. \quad (3.36)$$

The exchange-correlation energy (EXC) is separated into two terms, namely an exchange term "E_X", which is related to the interactions between electrons of the same spin and a correlation term "E_C", which is associated with the interactions between electrons of opposite spin represented as

$$E_{XC}[\rho(r)] = E_X[\rho(r)] + E_C[\rho(r)]. \quad (3.37)$$

These terms also denote the electron density functionals.

Most common DFT functionals were summarized herein. The local density approximation (LDA) includes the exchange-correlation functional together and assumes that the electron density is uniform everywhere given by

$$E_{XC}^{LDA}[\rho(r)] = E_X^{LDA}[\rho(r)] + E_C^{LDA}[\rho(r)] = \int \rho(r) \varepsilon_X^{LDA} \rho(r) dr + \int \rho(r) \varepsilon_C^{LDA} \rho(r) dr \quad (3.38)$$

where Thomas- Fermi-Dirac method (approx. to the exchange energy)

$$E_X^{LDA}[\rho(r)] = C_X \int \rho(r)^{4/3} dr \quad (3.39)$$

and ε_X^{LDA} referring the exchange energy per electron

$$\varepsilon_X^{LDA} = C_X \rho^{1/3} \quad (3.40)$$

with C_X a constant, which is equal to 0.7386. The correlation energy $E_C[\rho(r)]$ is based on Monte Carlo (MC) calculations for a homogeneous electron gas of different densities [40–42].

Local Spin Density Approximation (LSDA) accounts for spin dependence into the functionals and allows different orbitals for electrons with different spins for the spin polarized systems. $E_{XC}^{LSDA}[\rho(r)]$ is expressed as

$$E_{XC}^{LSDA}[\rho(r)] = E_{XC}^{LSDA}[\rho_\alpha(r), \rho_\beta(r)] = E_X^{LSDA}[\rho_\alpha(r), \rho_\beta(r)] + E_C^{LSDA}[\rho_\alpha(r), \rho_\beta(r)] \quad (3.41)$$

where α and β refers to spin up and down densities, respectively. $E_X^{LSDA}[\rho_\alpha(r), \rho_\beta(r)]$ is

$$E_X^{LSDA}[\rho_\alpha(r), \rho_\beta(r)] = -2^{1/3} C_X \int [\rho_\alpha^{4/3}(r) + \rho_\beta^{4/3}(r)] dr \quad (3.42)$$

and exchange energy per electron ϵ_X^{LSDA} is described as

$$\epsilon_X^{LSDA} = -2^{1/3} C_X [\rho_\alpha^{1/3} + \rho_\beta^{1/3}]. \quad (3.43)$$

Generalized gradient approximation (GGA) is the second generation of density functionals. In contrast to LDA methods, GGA method assumes that the electron density is inhomogeneous and includes both the density and gradients ($\Delta\rho(r)$) for the variation of ρ with position

$$E_{XC}^{GGA}[\rho_\alpha(r), \rho_\beta(r)] = \int f(\rho_\alpha(r), \rho_\beta(r), \Delta\rho_\alpha, \Delta\rho_\beta) \quad (3.44)$$

where f is a function of ρ_α and ρ_β , and their gradients. E_{XC}^{GGA} is divided into exchange and correlation parts and each part is modelled independently. The commonly used E_X functionals are B88, PW86, PW91, PBE [43]. The frequently used the E_C functionals are LYP, PW91, PBE, P86 [44] and any exchange functional can be used with any correlation functional; BLYP functional [45, 46] is also an combination of B88 exchange functional and Lee-Yang-Parr correlation functional [45, 47].

Meta-GGA (M-GGA) depend on the kinetic energy density or higher order density gradients. Hybrid density functional (H-GGA) methods join non-local Hartree-Fock exchange (HFX) with local/semi-local conventional GGA exchange in the E_{XC} term obtained from KS orbitals

$$E_{XC}[\rho(r)] = a_0 E_X^{HFX}[\{\psi_i\}] + (1 - a_0) E_X^{DFT}[\rho(r)] + E_C^{DFT}[\rho(r)] \quad (3.45)$$

where a_0 coefficient refers to the fraction of HFX [48]. B3LYP, MPW1K, and O3LYP are some of the popular examples of HGGA functionals.

Hybrid-meta GGA (HM-GGA) functionals depend on the HF exchange, the electron density and its gradient, and the kinetic energy density. Examples of HM-GGA are BMK, MPWB1K, M06-2X and so on. Range-separated (RS) functionals (CAM-B3LYP, ω B97X, M11 and so on.) account for long-range and short-range interactions. Double-hybrid DFT

(DH-DFT) functionals (B2-PLYP, DSD-BLYP, DSD-PBEP86, etc.) includes Møller–Plesset perturbation theory methods and show considerably better performance. However, computational cost is high compared to the methods mentioned above.

Lastly, the functionals used in this thesis are B3LYP, [45,49], M06-2X, [39,50], hybrid-GGA MPW1K, [51] range-separated ω B97XD and double hybrid B2PLYP functionals [52] to establish hierarchy in the “Jacob’s Ladder”.

3.2.4.1. Basis Sets. Basis set is the mathematical expression to define the orbitals within a system and is based on linear combination of atomic orbitals (LCAO-MO) approximation, expressed as

$$\psi_i = \sum_{\mu=1}^n \phi_{\mu} c_{\mu i} \quad (3.46)$$

where ψ is the i^{th} molecular orbital, ϕ_{μ} denotes the μ^{th} atomic orbital, $c_{\mu i}$ molecular orbital coefficients, and n is the number of atomic orbitals.

There are three types of basis sets, namely Slater-Type Orbitals (STO’s), Gaussian-Type Orbitals (GTO’s), and Contracted Gaussian-Type Orbitals (CGTO’s). The STO’s are useful for hydrogen-like species and have higher accuracy but they fail to describe non-spherical orbitals and computational cost is high. Therefore, GTO’s were proposed to overcome these pitfalls. They are much easier to compute and are widely used in DFT calculations. There are several different types of basis sets, such as minimal, double zeta (DZ), triple zeta (TZ), quadruple-zeta (QZ), and so on.

Various basis sets have been developed over the years. Split-valence basis was introduced by Pople *et al.* to split and treat valence and core orbitals separately. It uses only one basis function for each core atomic orbital (AO), and a larger basis for the valence AO’s, thus decrease the computational cost. The mostly used Pople basis sets are 3-21G, 6-21G, 6-31G*, 6-311G** and 6-31++G**. The former notation at left hand-side of the dash denotes the number of primitive Gaussian functions used to calculate core atomic orbitals and right

hand-side of the dash presents the valence shell orbitals, which are composed of a linear combination of many Gaussian functions.

Polarization and diffuse functions are used to improve the basis sets to get more reliable/accurate results for electronic energy. In Pople basis sets, one asterisk (*) or (d) implies that polarization functions added to heavy atoms. Two asterisks (**) or (d,p) is used to consider both heavy atoms and hydrogens. In diffuse function, when a plus sign (+) refers to addition of diffuse functions to heavy atoms, two plus signs (++) show the diffuse function addition to light atoms.

3.2.4.2. Solvation Models. Solvation models account for solvent environments of molecular systems and mimic biological environment/experimental environment to obtain more accurate and realistic outcomes. The solvent models are divided into two groups, namely explicit and implicit solvent models. In the explicit solvent models, all solvent molecules are included and free energy of solvation is calculated by considering solvent-solute interactions. Explicit models enable more realistic approach, yet are computationally expensive. Implicit solvent model, also known as continuum solvation model presents the solvent as a continuous medium and provides uniform polarizability by employing static dielectric constant (ϵ). The solute molecule is placed inside a cavity embedded in an uniform polarizable medium. The main advantages of implicit solvent models is to reduce computational cost. In general, total free energy of solvation is given by

$$\Delta G_{solvation} = \Delta G_{cavity} + \Delta G_{dispersion} + \Delta G_{electrostatic} + \Delta G_{repulsion} \quad (3.47)$$

where ΔG_{cavity} denotes the free energy required to form the solute cavity. Dispersion interactions between solute and solvent is represented as $\Delta G_{dispersion}$. The third term, $\Delta G_{electrostatic}$, is the electrostatic energy and $\Delta G_{repulsion}$ is the energy caused by the exchange solute-solvent interactions, which is not included in the cavitation energy term.

Various implicit solvation models are available, namely conductor-like polarizable continuum model (CPCM), [53] integral equation formalism polarizable continuum model

(IEF-PCM), [54] solute model based on density (SMD), [55] and COSMO, [56] etc. Polarizable Continuum Model (PCM) is one of the widely used implicit solvent models introduced by Tomassi and coworkers [57, 58]. This model defines the cavity surface through spheres defined by Van der Waals (vdW) radii centered at each atom. Conductor-like PCM (CPCM) treats the conductor-like screening solvation boundary condition. Another widely used continuum solvation model is IEFPCM, formulated by Cancés and Menucci [54, 59]. It uses connected spheres (a set of overlapping spheres) to model the solute, with radii of the spheres similar to solute atoms. Integral Equation Formalism of PCM was conducted for DFT solvent calculations in this thesis. SMD is based on the QM charge density of a solute molecule interacting with a continuum description of the solvent [55].

3.2.4.3. Population Analysis (Atomic Charge Models). Since partial atomic charges are not physical observables, several charge models have been developed. Atomic charges are mainly calculated by using the Mulliken population analysis, the natural population analysis (NPA), or the Hirshfeld population analysis. The atomic charges basically gives insight into the charge distribution in a structure/molecule, which, in turn, can help picturing structural and reactivity differences. While Mulliken, Löwdvin, and NPA charge schemes are based on wave functions, Hirsfeld analysis is based on electron density. If the electron density of each atom is known, the atomic partial charge can be determined by using Equation 3.48 [60]. The partial charge of an atom A is equal to nuclear charge Z_A minus to electron density in r as follows

$$q_A = Z_A - \int \rho_A(r) dr. \quad (3.48)$$

In QM calculations, the total number of electrons (N) can be defined as

$$N = \sum_{\mu}^{AO} (PS)_{\mu\mu} \quad (3.49)$$

where \mathbf{P} is the electron density and \mathbf{S} is the overlap population summed over all atomic orbitals.

The Mulliken population is one of the well known methods for atomic charge analysis and is expressed as

$$q_A = Z_A - \sum_{\mu \in A}^{AO} (PS)_{\mu\mu} \quad (3.50)$$

in which for the atom A, the atomic charge and the atomic number is denoted by q_A and Z_A , respectively. Sum of $\mu \in A$ indicates consideration of atomic orbitals, which is centered on the A_{th} atom. Of note, even if Mulliken population analysis is a simple and computationally attractive method, it is highly sensitive to basis set choice and fails to give realistic results in ionic species.

Natural population analysis (NPA) based on Natural Bond Orbitals (NBO) is a frequently used method developed by Weinhold and co-workers [61]. Natural bond orbitals are an orthonormal set of localized orbitals that describe possible Lewis structures of bonding electrons and lone pairs. Advantages of this method over Mulliken population are that NPA displays less basis set sensitivity/dependence and more rational electron distribution in ionic compounds.

Charges from electrostatic potentials (CHELP), charges from electrostatic potentials using a grid (CHELPG), and the Merz-Kollman-Singh (MKS) are also broadly used charge models and depend on the reproduction of the molecular electrostatic potential, that is, electrostatic potential fitting. Atoms in molecules (AIM) and Hirshfeld are density related charge schemes, that are, based on the electron density.

3.2.5. Non-covalent Interaction Analysis (NCIs)

Non-covalent Interactions (i.e., H-bond, cation- π , π - π interactions, electrostatic interactions and van der Waals interactions, and so on) are known to contribute to the stability of molecules, such as proteins. Non-covalent interactions can be determined *via* NCI index

based on the electron density ($\rho(r)$) and the reduced density gradient(s) [62] as follows

$$s = \frac{1}{2(3\pi^2)^{1/3}} \frac{|\nabla\rho(r)|}{\rho(r)^{4/3}} \quad (3.51)$$

in which, s is the reduced density gradient and ρ is the electron density. "s" dramatically changes in the presence of a weak interaction producing density critical points on 2D plot of s and ρ . Additionally, NCIs are visualized by using NCIPLOT program [62].

3.2.6. Nucleus-Independent Chemical Shifts (NICS)

Nucleus-Independent Chemical Shifts was introduced by Schleyer et al [63, 64] and is a magnetic measure of aromaticity, particularly for the evaluation of transition state aromaticity. While negative NICS values indicate aromaticity, positive NICS values indicate anti-aromaticity. NICS analysis was performed in Chapter 8.

3.2.7. Anisotropy of the Induced Current Density Analysis (ACID)

Herges and Geuenich developed the anisotropy of the induced current density method to quantify and visualize electronic delocalization and conjugation [65, 66]. Additionally, ACID method is used for the measurement of aromaticity in order to differentiate the type of reactions, such as pericyclic and pseudopericyclic reactions [65–68]. In Chapter 8 ACID analysis was performed for TS structures.

3.2.8. Atoms in Molecules (AIM)

Quantum theory of atoms in molecules was developed by Bader and is a useful method to analyze electron density distribution and to distinguish the nature of a reaction for transition state structures [69]. Presence or absence of critical points, namely ring critical (RCP) points and bond (BCP) points are important indicators to understand the nature of the reaction [70, 71]. AIM analysis can be performed using the ADF program package, Multiwfn and Xaim programs.

3.2.9. Conceptual Density Functional Theory (CDFT)

Conceptual DFT (CDFT) involving global and local reactivity descriptors is a powerful tool to understand chemical reactivity and regioselectivities [72–74]. Parr and coworkers are the pioneers of Conceptual DFT [72]. In CDFT, the electron density plays a crucial role on the description of atomic and molecular ground states in quantum mechanics. CDFT is based on the Hohenberg-Kohn theorem, where the ground state energy of a system with N electrons and external potential $V(r)$ are defined as a function of electron density depicted as

$$E[\rho(r)] = E[N; v(r)]. \quad (3.52)$$

3.2.9.1. Global Reactivity Descriptors. Global reactivity descriptors -chemical potential " μ ", hardness " η ", electronegativity " χ ", softness " S ", electrophilicity index " ω ", nucleophilicity index " N " and so on- were introduced to calculate and predict chemical concepts, such as reactivity, chemoselectivity, and regioselectivity. Chemical potential " μ " is introduced by Parr et al. [75]

$$\mu = \left(\frac{\partial E}{\partial N} \right)_{v(r)} \quad (3.53)$$

where E is total energy, N is the number of electrons, and $v(r)$ is the external potential of the system. Hardness " η " is the second derivative of energy " E " and based on the HSAB principles defined by Domingo et al. [76]

$$\eta = \left(\frac{\partial^2 E}{\partial N^2} \right)_{v(r)}. \quad (3.54)$$

Softness S is expressed as the inverse of hardness " η ". Hardness " η " is the second derivative of energy " E " defined by Domingo et al. [77]

$$S = \frac{1}{\eta}. \quad (3.55)$$

The electrophilicity index " ω ", combines electronic chemical potential " μ " and absolute chemical hardness " η " to measure the reactivity of an electrophilic reagent. The electrophilicity index ω was defined by Parr et al. [78] as follows

$$\omega = \frac{\mu^2}{2\eta}. \quad (3.56)$$

Nucleophilicity index " N_u " was developed by Domingo and co-worker. The relative nucleophilicity index N is the HOMO energies with respect to HOMO energy of tetracyanoethylene (TCE). Tetracyanoethylene (TCE) is taken as a reference since it has the lowest HOMO energy and provides nucleophilicity scale of positive values shown as

$$N_u = E_{HOMO(Nu)} - E_{HOMO(TCE)}. \quad (3.57)$$

3.2.9.2. Local Reactivity Descriptors. Local reactivity descriptors provide several ways to predict and give insight into the activity of a specific atomic site (r) within a molecule. Electron density play a crucial role on the fundamental local reactivity descriptors. The Fukui function $f(r)$ was proposed by Parr and Yang [78] based on Fukui's frontier orbital theory, assuming a reagent approaches others from the reactive side which has the highest value of $f(r)$, defined as

$$f(r) = \left(\frac{\partial \rho(r)}{\partial N} \right)_{v(r)}. \quad (3.58)$$

They assumed a frozen core [79], in which

$$\partial \rho = \partial \rho_{valence} \quad (3.59)$$

and defined $f^-(r)$ for electrophilic and $f^+(r)$ for nucleophilic attacks as

$$f^-(r) \approx \rho_{HOMO}(r) \quad (3.60)$$

$$f^+(r) \approx \rho_{LUMO}(r). \quad (3.61)$$

The condensed Fukui functions based on Mulliken charges proposed by Yang and Mortier [80] and Fukui functions are used to determine the most favored electrophilic, nucleophilic, and radical attack sites as follow

$$f^- = q_k(N) - q_k(N-1) \quad (3.62)$$

$$f^+ = q_k(N+1) - q_k(N) \quad (3.63)$$

$$f^0 = 1/2[q_k(N+1) - q_k(N-1)] \quad (3.64)$$

where, N is the number of total electrons and $q_k(N)$, $q_k(N+1)$, $q_k(N-1)$ are the atomic charges in the original, anionic radical and cationic radical species, respectively corresponding to the site k.

Domingo and coworkers [79] introduced Parr functions $P(r)$ based on atomic spin density (ASD) for the radical of the original reagent. Local electrophilic P_k^+ and nucleophilic P_k^- Parr functions are used to predict nucleophilic and electrophilic attacks, respectively. The Parr functions $P(r)$ (Equation 3.65 and Equation 3.66) are given by

$$P^-(r) = \rho_s^{rc}(r) \quad (3.65)$$

$$P^+(r) = \rho_s^{ra}(r) \quad (3.66)$$

where $\rho_s^{rc}(r)$ and $\rho_s^{ra}(r)$ are the ASD of the radical cation and anion, respectively.

Furthermore, the local electrophilicity ω_k and nucleophilicity N_k indices of a site k also permit to detect to predict the most favored nucleophilic-electrophilic attack sites. They are calculated using the Fukui functions and the Parr functions defined as

$$\omega_k = \omega f_k^+ \quad (3.67)$$

$$N_k = N f_k^- \quad (3.68)$$

$$\omega_k = \omega P_k^+ \quad (3.69)$$

$$N_k = N P_k^- \quad (3.70)$$

4. IMPACT OF DEAMIDATION ON THE STRUCTURE AND FUNCTION OF ANTI-APOPTOTIC BCL-X_L IN WATER

4.1. Introduction

Apoptosis, known as programmed cell death, is a complex process and is initiated by three pathways, namely intrinsic, also known as mitochondrial pathway via diverse intracellular stresses, extrinsic (death receptor-mediated pathway) via death receptors, and perforin/granzyme pathways [81–84]. Each pathway is regulated by different apoptotic stimuli [84]. The Bcl-2 family proteins mainly play an important role on the mitochondrial pathway of apoptosis by regulating mitochondrial outer membrane permeabilization and subsequent apoptosis [85–88].

4.1.1. Bcl-2 Family Protein

The Bcl-2 family was classified into three sub-classes, namely anti-apoptotic proteins, pro-apoptotic proteins, and BH3-only proteins (BOPs; activator and sensitizer BOPs) (Figure 4.1) and mediates the mitochondrial (intrinsic) apoptotic pathway in response to various apoptotic stimuli (cellular stress or damage signals) [89, 90]. Bcl-2 family proteins maintain/preserve balance in healthy cells. When this balance is disrupted, elevated numbers of anti-apoptotic proteins are observed in various cancer cells, such as chronic myelogenous leukemia (CML), pancreatic cancer, ovarian and small-cell lung cancer [50, 91, 92].

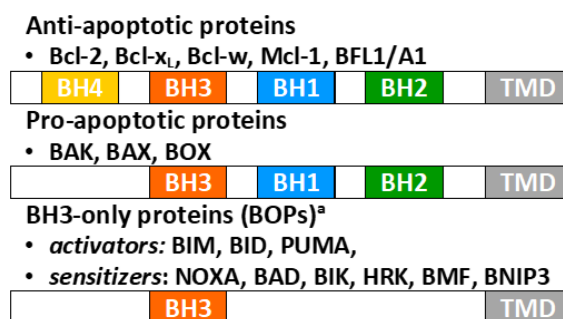


Figure 4.1. General presentation of Bcl-2 family.^a Only BIK and HRX comprise the TMD.

4.1.2. B-cell Lymphoma-extra-large (Bcl-x_L)

Structurally, Bcl-x_L consists of two hydrophobic, six amphiphilic helices (Figure 4.2) and a C-tail composed of an α -helix (α 9), known as the transmembrane domain (TMD) [2, 93–95]. Note that to date, the C-tail (α 9 helix) had not been resolved in any of the available PDB structures of Bcl-x_L, but more recently the C-tail alone was experimentally resolved in phospholipid nanodiscs (PDB ID: 6F46_{NMR} [96] and PDB ID: 6X7I_{NMR}). Bcl-x_L also comprises four Bcl-2 homology domains (BH1-4) and a hydrophobic “binding groove” between α 2- α 5 helices capped by a short C-terminal (α 8 helix). The binding groove (BG) of Bcl-x_L accommodates the BH3 domain of the BOP and pro-apoptotic proteins. Furthermore, Bcl-x_L has an intrinsically disordered region (IDR) (residues 21-84), the so-called “loop region” between α 1- α 2. Specific residues within the IDR of Bcl-x_L are post-translationally modified in response to diverse stimuli. Most of the previous studies lacked/omitted the IDR, [97–100] however, the deletion of IDR increases the anti-apoptotic activity of Bcl-x_L (hyper-function), [101] hence, Bcl-x_L without IDR fails to give full insight into the structure and function of the protein. Analysis of the intrinsically disordered region is essential since the IDR is the main site for post-translational modifications (PTMs) [102–105]. The importance of the IDR as well as hotspots on the IDR have been reported in recent studies [106–110]. Two asparagine residues (Asn52 and Asn66) [107] on the IDR are well documented to deamidate and this, in turn, is known to play a pivotal role on reduction/loss of anti-apoptotic activity of Bcl-x_L [106–108]. The impact of PTMs on Bcl-x_L are not yet completely understood, however, apoptotic stimuli (DNA damage, UV, nutrient deprivation, chemotherapy, etc.) is known to induce PTMs in Bcl-x_L that lead to a) the release of BOP and the subsequent activation of pro-apoptotic proteins, and b) the inhibition of its binding to pro-apoptotic and BH3-only proteins, leading to apoptotic cell death [84, 111]. One of the goals of this study is to elucidate the impact of PTMs that take place on the IDR, specifically deamidation, on the general structure of Bcl-x_L, which may eventually lead to the release of BOPs or an inefficiency of sequestering BOPs.

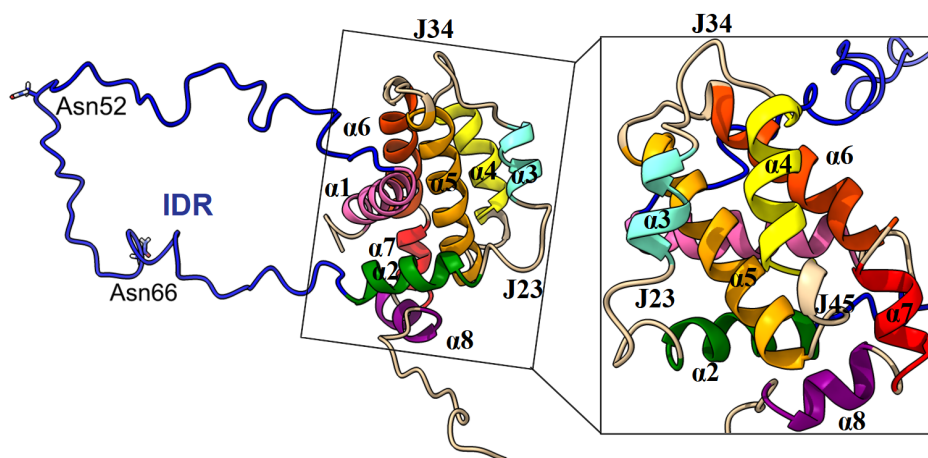


Figure 4.2. Front and side views of Bcl-x_L (PDB code: 1LXL). (The black rectangle indicates the front view of the binding groove. Blue color represents the IDR region (IDR), α 1 in pink, α 2 in green, α 3 in cyan, α 4 in yellow, α 5 in light orange, α 6 in orange, α 7 in red, and α 8 in purple. “J” refers to the junction between two helices. J23 connects α 2 and α 3, J34 is the junction of α 3 and α 4 and J45 connects α 4 and α 5.)

4.1.3. Post-Translational Modifications (PTMs)

Post-translational modification (PTM) is a regulatory mechanism in many biological processes. Most common modifications are acetylation, acylation, amidation, deamidation, phosphorylation, glycosylation, ubiquitination, nitrosylation and SUMOylation [112–114]. Influence of post-translational modifications within the IDR are important to understand regulation and downregulation of Bcl-x_L [106–108, 115]. Specific residues within the IDR of Bcl-x_L are post-translationally modified in response to diverse stimuli. However, the effects of PTM on Bcl-x_L are not completely understood. Figure 4.3 presents known PTM sites on the IDR region, [107, 108] namely deamidation (Asn52 and Asn 66) [93, 116–118], phosphorylation (Thr47, Ser49, Ser62, and Ser 73) [102, 119], and cleavage (Asp61 and Asp76) [104, 105, 120]. Notably, the modifications increase negatively charged residues on the IDR and these can change the interactions between IDR and core of Bcl-x_L and hence structural behaviour. Among PTMs, deamidation is of particular interest to this study.

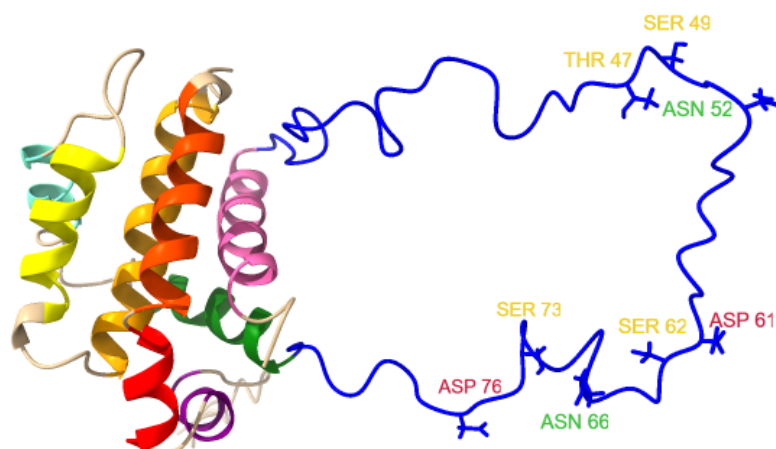


Figure 4.3. Representation of Bcl-x_L (PDB ID:1LXL) with known PTM residues on the IDR region. (Blue color denotes the IDR regions, α 1 in pink, α 2 in green, α 3 in cyan, α 4 in yellow, α 5 in light orange, α 6 in orange, α 7 in red, and α 8 in purple.)

4.1.4. Deamidation of Bcl-x_L

Deamidation is a non-enzymatic reaction and one of the pivotal post-translational modifications, which is a regulatory mechanism in many biological processes. ‘Molecular clocks’ hypothesis by Robinson et al. emphasizes the importance of asparagine and glutamine deamidation and suggests that deamidation is a biological molecular timing mechanism that serves a programmable genetic control to any desired time interval and control of biological processes [121]. Deamidation rate is determined by protein structure and environment; deamidation half times of proteins are shown to vary from a few hours to more than 100 years [122]. Asparagine (Asn) and glutamine (Gln), two of the 20 naturally occurring amino acids, are inherently unstable under physiological conditions [123]. Gln and Asn are known to spontaneously yet non-enzymatically deamidate into a mixture of glutamyl (Glu) and iso-glutamyl (iso-Glu) and a mixture of aspartyl (Asp) and iso-aspartyl (iso-Asp) residues, respectively (Figure 4.4) [121, 124, 125]. This, in turn, replaces a neutral residue with a negatively charged one and has the potential to cause severe electrostatic clashes leading to structural deformations, which may eventually have dramatic biological consequences. Gln deamidation is usually substantially slower than Asn deamidation, hence asparagine deamidation has more biologically relevant consequences. PIMT/PCMT repair mechanism converted iso-Asp to the mixture of Asp and iso-Asp over succinimide intermediate and

does not fully go back to Asn [107, 117, 121–123]. It is important to mention that contrary to reversible PTMs, such as phosphorylation which is a fast process, [107] deamidation is a slower reaction and an irreversible PTM. The only way, which can mitigate its effects is the neosynthesis of natural protein, in this case, Bcl-x_L. Hence, deamidation is different from other PTMs and drew our attention to understand its impacts on proteins with time.

A notable example is the mitochondrial trans-membrane protein, Bcl-x_L, [2, 93] which functions as an anti-apoptotic protein. Bcl-x_L belongs to the Bcl-2 family, [126] which regulates the mitochondrial pathway of apoptosis in response to various apoptotic stimuli [1]. Bcl-x_L indirectly binds to BH3-only proteins and prevents them from activating pro-apoptotic proteins or directly binds to pro-apoptotic proteins and inhibits their pro-apoptotic activities, which lead to cell death [111, 127, 128]. Additionally, Bcl-x_L also indirectly plays a major role in autophagy [95, 129] and senescence [130, 131] pathways. Since Bcl-x_L is known to play a pivotal role in the survival of tumor cells, understanding the inter-relations among apoptosis, autophagy and senescence is pertinent in determining how Bcl-x_L regulates cell survival or cell death [132].

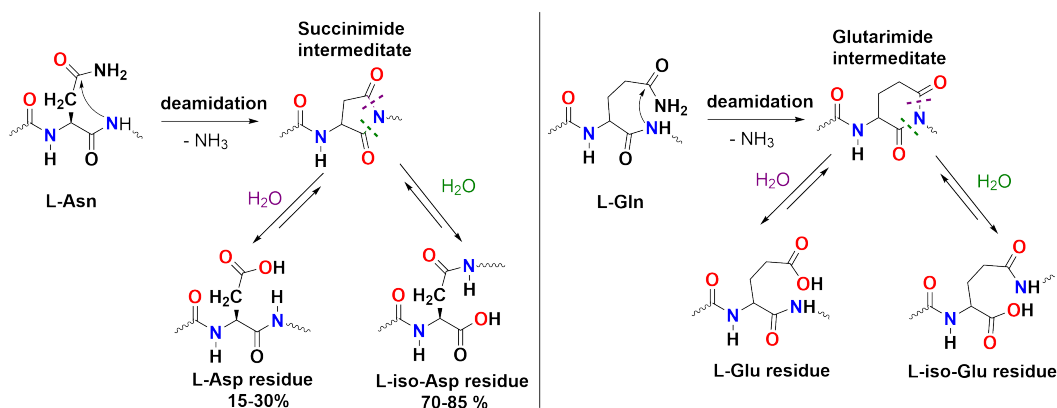


Figure 4.4. General mechanism of Asn and Gln deamidations.

Only three asparagine residues (Asn52, Asn66 and Asn185) with an (n+1) glycine residue (Asn-Gly) exist in structure of Bcl-x_L. However, Asn185, being embedded in the core region, is not prone to deamidation due to less water-exposure; as a result, it has a much longer deamidation half-life when compared to Asn52 and Asn66. Both asparagine residues, Asn52 and Asn66, are located in the IDR and undergo deamidation leading to a

complete loss of protein function [50, 91, 93, 116, 118]. While Bcl-x_L deamidation leads to apoptosis in normal cells, tumor cells are known to have acquired resistance to apoptosis and a clear survival advantage by suppressing Bcl-x_L deamidation and its biological consequences [91]. In 1997, Aritomi et al. published the first report on Bcl-x_L's susceptibility to deamidation, when defining the crystal structure of rat Bcl-x_L (PDB ID: 1AF3_{X-Ray}) [93]. They defined the deamidation sites of rat Bcl-x_L by high performance liquid chromatography (HPLC) and iso-Asp was only detected in Asn52 and Asn66 showing the susceptibility of both residues. Similarly, Takehara and Takahashi reported that Asn52 and Asn66 residues of human Bcl-x_L are prone to deamidation [91]. In general, Bcl-x_L deamidation is accelerated by DNA-damage inducing agents used in cancer treatment [50, 118, 133]. Notably, unlike the rest of the Bcl-2 family, asparagine-glycine (Asn-Gly) sequences in the IDR of Bcl-x_L are evolutionarily conserved, showing their biological significance.

Previously, Deverman et al. (Weintraub lab) reported that the deamidation of Bcl-x_L downregulates the anti-apoptotic activity of Bcl-x_L [116]. However, in 2003 they published an erratum indicating that an undetected mutation was observed and Bcl-x_L-BIM binding was recovered, that is, Bcl-x_L does not lose its ability to bind to the BH3-only proteins upon deamidation [134]. However, they had failed to consider the possibility of iso-Asp conversion in their study. Later, Alexander and coworkers confirmed the initial results of Deverman et al. by showing the loss of Bcl-x_L's anti-apoptotic function when deamidated, and reported that iso-Asp52/iso-Asp66 residues in the IDR region prevent the sequestering of BH3-only proteins [118]. Therefore, it is imperative to further investigate the structural changes in Bcl-x_L upon deamidation of Asn52 and Asn66 in order to clarify these seemingly controversial experimental results. The current study is the first step towards this goal, where we computationally explore the structural and biological consequences of Bcl-x_L deamidation at the atomic level. More recently, in 2018, Follis et al. reported a new NMR structure of a Bcl-x_L phosphomimetic mutant (S62E-Bcl-x_L, PDB ID: 6BF2_{NMR}, 20 conformers) and experimentally investigated the effect of PTMs in the intrinsically disordered region (phosphorylation and deamidation in IDR) on the regulation of apoptosis [106]. They proposed that phosphorylation (S62E) and deamidation (N52D and N66D) in the IDR induce allosteric interactions in the BG leading to the release of pro-apoptotic proteins, which in turn trigger apoptosis.

Previous experimental studies, mentioned earlier, indicated the significant impact of deamidations in the IDR on the function of Bcl-x_L [106–108, 135–137]. On the other hand, there is only a limited number of computational studies performed on Bcl-x_L that includes the IDR. In 2013, Maity et al. reported significant differences between the conformational dynamics of Bcl-x_L in water and in membrane (total 1.6 μ s, implicit models) [99]. In water, the C-tail covered the binding groove and acted as a lid. In water and membrane environments, principal components of the motions were significantly different implying conformational transitions of Bcl-x_L in the membrane. However, the model used by Maity et al. was truncated by removing the Bak peptide from its complex with Bcl-x_L (PDB ID: 1BXL_{NMR}), moreover, the IDR was not present. In 2017 Priya et al. [138] investigated the influence of the IDR on the function of Bcl-x_L by comparing Bcl-x_L with and without the IDR (total 800 ns, NPT simulations). They showed that the IDR allosterically modulates the structural dynamics of Bcl-x_L and they validated this finding through testing the effect of phosphorylation of S49 and S62 in the IDR. Phosphorylation in the IDR induced changes in electrostatic interactions in the BG, showing allosteric regulation. In Priya's study, deamidation in the IDR was not explored and the complete experimental (NMR) structure (PDB ID: 1LXL (residues 2–196)) of Bcl-x_L was not utilized. More recently, in 2020, Marassi and coworkers described and investigated the conformation of full-length Bcl-x_L in both its soluble and membrane-anchored states using NMR spectroscopy, isothermal titration calorimetry (ITC) and molecular dynamics (1 μ s \times 5 MD simulations) [139]. The study mostly focused on the tail-groove interaction in solution. Their model was modified Bcl-x_L/Bak-BH3 complex (PDB: 1BXL_{NMR}) by adding a loopIDR section from 1LXL_{NMR} and by replacing the C-terminal His-tag with the C-tail (residues 210–233) from 6X7I_{NMR}. The Bak-BH3 peptide was removed, and the C-tail was docked into the binding groove. The MD simulations in their study was somewhat limited and did not offer any insight on deamidation in the IDR. Taken together, the computational studies, in general, had short simulation times (maximum 1 μ s) causing limited sampling; moreover, these studies used truncated or modified models of Bcl-x_L, where the IDR was subsequently added. To date, the mechanism by which Bcl-x_L deamidation induces apoptosis remains unclear. In the current study, we used a non-modified, non-truncated experimentally available form of Bcl-x_L, unlike previous studies. This study is the first attempt to investigate the structural and biological consequences of

Bcl-x_L deamidation at atomic resolution through microsecond long MD simulations [140]. In this context, clustering, principal component analysis (essential dynamics) and H-bond interactions were particularly scrutinized.

4.2. Methodology

Experimentally available structures were examined (Table A.1) and 1LXL having the IDR was selected as an candidate for this study. Initial structure “1LXL” was retrieved from the Protein Data Bank (Homo sapiens); cloning artifacts and histidine tags were removed. Deamidated structures (DM1 and DM2) were built by replacing Asn to Asp and iso-Asp, respectively. MD simulations were performed by using the Amber18 program package [141]. All MD simulations were performed using the Amberff14SB [142] force field implemented in the Amber18 program package [141] and solvation was carried out using the TIP3P [143] explicit water model forming cubic boxes. Counter ions (sodium or chloride) were added into each system to neutralize charges. Amber force field for L-iso-Asp, which is a non-standard amino acid, was parameterized with the antechamber and tleap modules as implemented in the Amber simulation package (see details in Appendix A: Figure A.1 and Table S1). After the preparation step, all systems (WT, DM1 and DM2) were minimized using the steepest descent method with harmonic restraints on all heavy atoms. In the minimization step, NVT ensemble with Andersen temperature coupling [21] was employed and the velocities were randomly updated every 10 steps. Long range interactions were calculated using the particle mesh Ewald (PME) [19] method with the default 8 Å cutoff distance. SHAKE algorithm was carried out in order to constrain bonds involving hydrogen atoms [22]. Equilibration runs were performed using the NPT ensemble with a Monte Carlo barostat. Time step for the equilibration runs was set to 2 fs. A five-step equilibration protocol was conducted as follows: 1) all heavy atoms were restrained with a harmonic potential of 50 kcal mol⁻¹ Å⁻² for 0.1 ns at 10 K, to provide a proper geometry for the H atoms. 2) restraints on the oxygen atoms of water molecules were removed to optimize the positions of water molecules with respect to the protein environment using the same restraining potential for 0.1 ns at 10 K. 3) the harmonic potential was decreased to 5 kcal mol⁻¹ Å⁻² by repeating the 2nd step. 4) the entire system was equilibrated without restraints for 0.1 ns at 10 K. Under the Andersen

thermostat [21] the velocities were randomly updated every 10 steps throughout equilibration steps 1-4. 5) The systems were gradually heated to 300 K for 2 ns using the Berendsen thermostat [20] with a coupling time of 1.0 ps. Production runs were performed at 300 K and an NVT ensemble utilizing Langevin temperature coupling [144] with a gamma of 1.0 ps⁻¹. The time step for production runs was set to 4 fs, using hydrogen mass repartitioning (HMR), [23] to accelerate MD simulations.

All analyses were performed with the cpptraj [145] module of Amber18. The backbone root mean-square deviation (RMSD) analysis was performed using the backbone atoms of Bcl-x_L's core region defined by residues 85-96, 120-131, 137-156, 162-176 in line with the core region definition (residues 85-98, 123-127, 140-156, and 162-175) of Liu et al [97,98]. Reference structure for wild-type (WT) simulations are NMR structure of Bcl-x_L (PDB ID: 1LXL). In deamidated systems initial/built structure was used as a reference. Secondary structure contents were calculated using the Definition of Secondary Structure Prediction (DSSP) algorithm [146]. For hydrogen bond (H-bond) calculations, the distance criteria was defined as $\geq 3.2 \text{ \AA}$ based on heavy atom distances (acceptor to donor heavy atom) and angle cutoff is 135°. Contact percentage (%) in H-bond analysis is defined as the percentage of total contacts during simulations. Linear Interaction Energy (LIE) analysis was performed to evaluate non-bonded long-range interactions. The results were visualized by B-factor coloring to effortlessly pinpoint the hotspots between IDR and protein (excluding IDR, Δ IDR). Combined clustering analysis was performed by using HierAgglo algorithm (10 clusters, linkage, based on the RMSD of C α of protein residues (Δ IDR) (1-20,85-209@CA)) to explore the major conformational changes among wild-type and deamidated systems (Table 4.2). Each system includes equal number of frames (625000 frames/each). The last 5 μ s were used in the calculations of longer simulations to keep the same number of frames for each system. Sieve (100, random) was also employed [29]. Clustering findings were also combined with Principal component analysis (PCA). The clusters from 1 to 9 of each system were also used in the calculation of principal component analysis. Principal component analysis (PCA) was performed with the cpptraj module and principal components (PCs) were visualized with the Normal Mode Wizard (NMWiz) [27] in VMD (1.9.3). Firstly, the combined trajectories were RMS-fitted to an overall averaged structure using the backbone atoms of the binding groove (residues 85-156) to remove global translational and rotational motions. The coordi-

nate covariance matrices (288 atoms total, 864 coordinates) were calculated using the same mask, namely the binding groove (residues 85-156). Then, the coordinate covariance matrices were diagonalized to obtain the first 10 PCs (i.e., eigenvectors) and their eigenvalues. All histograms in PCA were calculated using a Gaussian kernel density estimator (KDE). Graphics were plotted by Gnuplot (version 4.6) (<http://www.gnuplot.info/>) and Xmgrace (version 4.0). Chimera [147] (version 1.14), ChimeraX, [148] and VMD (version 1.9.3) [28] were used for the visualization and illustration of the studied models.

4.3. Results and Discussion

From a computational viewpoint, the identification of conformational differences plays a pivotal role in understanding the impact of deamidation in IDR. Up to now, there is no clear structural connection/explanation on how deamidation induces the loss of Bcl-x_L activity. In order to scrutinize conformational behaviors/differences of wild-type (WT) and deamidated Bcl-x_L systems, microsecond-long MD simulations were performed using different starting velocities. The stability of the systems and H-bond interactions were explored. Clustering analysis, H-bond interactions, and PCA analysis were combined to investigate the conformational changes upon deamidation. Using PCA, we specifically focused on the conformational changes in the binding groove (BG) upon deamidation of IDR residues Asn52 and Asn66, by considering both Asp and iso-Asp mutations. The terms “DM1” and “DM2” refer to Asp and iso-Asp deamidated Bcl-x_L, respectively. An overview of all the systems studied is shown in Table 4.1. Overall, the total amount of MD simulation time is 90 μ s.

Table 4.1. Summary of the initial set up.

Initial Structure	Water	Na ⁺	Total atoms	Simulation time
1LXL _{NMR} (Bcl-x _L , WT)	44408	14	136431	5 μ s \times , 9 μ s \times 1
DM1-1LXL (DM1)	44406	16	136423	5 μ s \times 4, 10 μ s \times 1
DM2-1LXL (DM2)	44406	16	136423	5 μ s \times 3, 8 μ s \times 2
			Total	90 μ s
Initial simulation box size = 111.757 \times 111.757 \times 111.757 \AA^3				

4.3.1. Stability of the Wild type and Deamidated Bcl-x_L Systems

A backbone root mean-square deviation (RMSD) analysis was performed for wild type and deamidated Bcl-x_L's core region and their binding grooves (residues 85-156) as well as the IDRs (residues 21-84) to evaluate the stabilities of the systems during the simulations. RMSD plots in Figure 4.5 illustrate that the core regions of WT, DM1, and DM2-Bcl-x_L are stable ($< 3.0 \text{ \AA}$) during the simulations. Figure 4.5 shows that the IDR is highly flexible with very large range of RMSD for each system during the simulations. The RMSD fluctuations are, on average, the same for each system in the range of 10 to 15 \AA , indicating that the large and similar mobility of the IDR in comparison to initial structure. Per-residue RMSD analysis was also performed to see which helices in the core and the BG are responsible for the increase in RMSD (Figures 4.6). Average per-residue RMSD analysis illustrates that $\alpha 2$ shows higher fluctuations in DM1. Additionally, regarding all simulations (WT, DM1, and DM2), the J23 junction connecting $\alpha 2$ and $\alpha 3$ displays larger deviation with higher per residue RMSD (Figure 4.6). We also evaluated the stability of the helices during the MD simulations through secondary structure analysis (Figures A.2-A.4). We saw that $\alpha 1$ - $\alpha 8$ helices were generally preserved in all simulations. Interestingly, persistent (long-lived) and/or 'transient but re-occurring' helical formations in the IDR were observed.

4.3.2. Intrinsically Disordered Region (IDR)

Literature studies have shown that understanding the influence of post-translational modifications, i.e., deamidation on the IDR will lead to better insight into regulation and downregulation of Bcl-x_L [106–108, 115]. Structurally, the initial extended form of the IDR was not preserved throughout the simulations. Instead, simulations show that the interactions between the IDR and the protein core region are transient (short-lived) and consistently re-occurring, and the IDR approaches the core region in various ways. Particularly to verify this observation we performed several simulations, and in each case the IDR did not stay extended and approached the protein core even though the simulation boxes were large enough to accommodate extended forms. Hence, it is safe to say that the 1LXL PDB structure does not constitute a representative structure of the IDR. The IDR generally approaches/moves towards the core regions and mostly interacts with $\alpha 1$, $\alpha 2$ and $\alpha 6$ throughout the simulations.

Despite the large flexibility of the IDR, transient (short-lived) but consistently re-occurring interactions, exist between the IDR and protein core.

Non-covalent interactions (NCI), such as salt-bridges, H-bonds, and cation- π interactions are known to contribute to the stability of proteins. Among the NCI, H-bond interactions in particular were explored. H-bond interactions between protein (Δ IDR)-IDR in Figures 4.7 and 4.8 depicted transient interactions and the changes in interaction pattern upon deamidation. While the IDR in WT transiently interact with $\alpha 1$, $\alpha 2$ and C-terminal part, deamidated Bcl-x_L, particularly DM2 transiently interacts with the residues between $\alpha 6$ and the C-terminal part. These outcomes imply that increase in negative charge and backbone changes can affect interaction pattern and movements of the IDR.

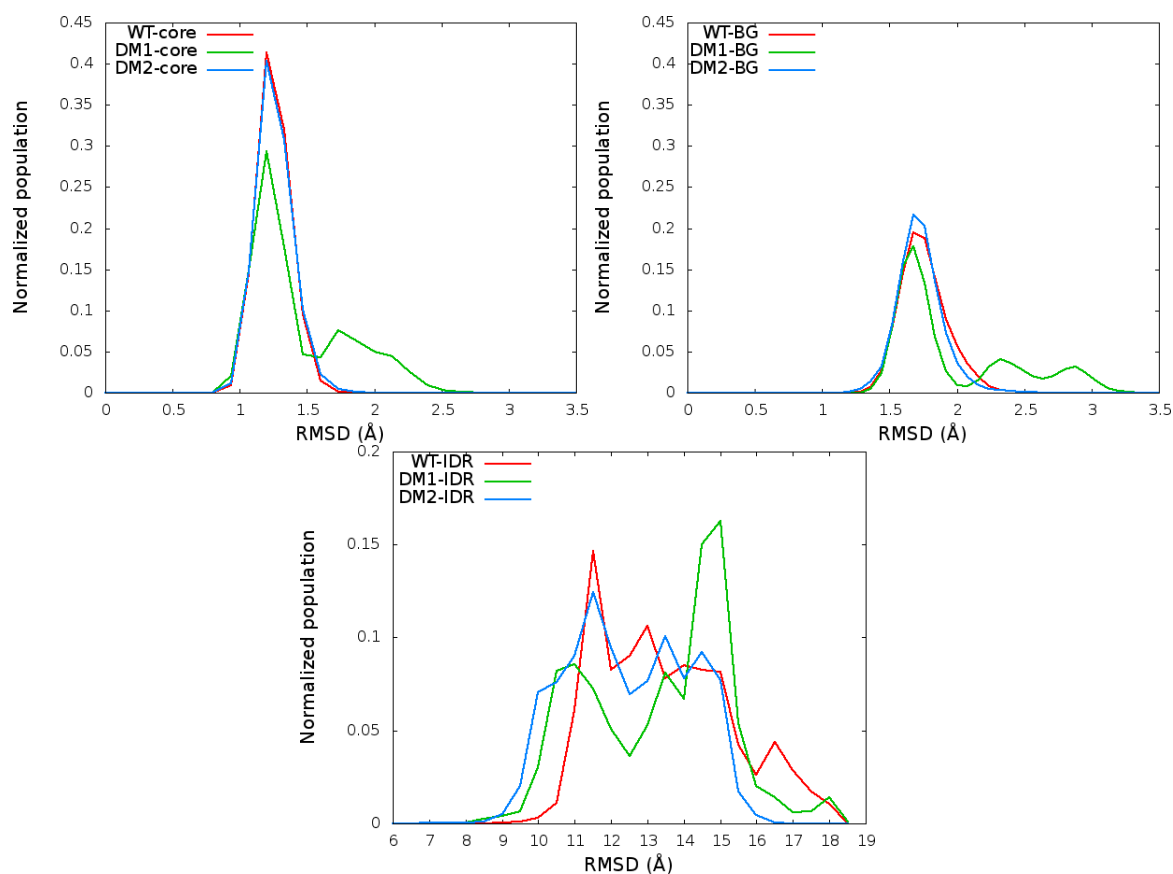


Figure 4.5. RMSD histogram for the core, the BG, and the IDR of WT, DM1 and DM2 simulations with respect to initial/starting structures before MD simulations.

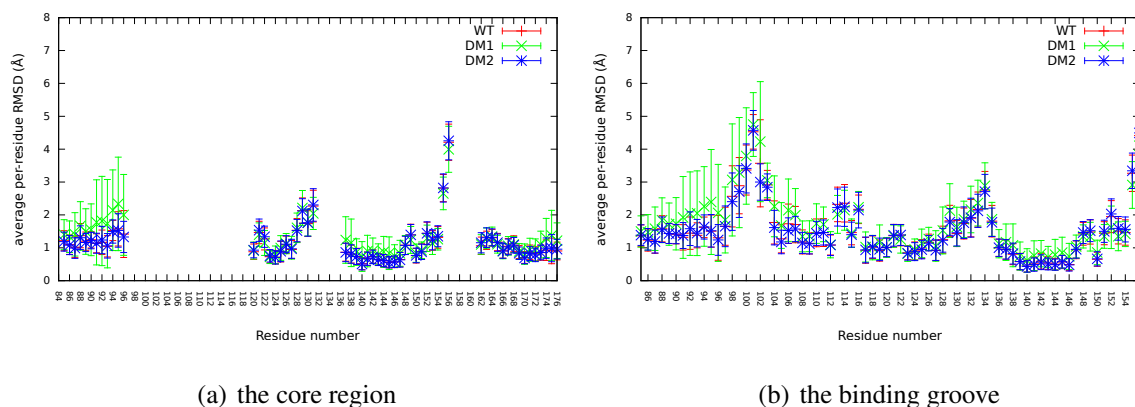


Figure 4.6. Backbone per-residue RMSD plots for a) core helices and b) the binding groove of all WT, DM1, and DM2 simulations with respect to initial/built structure.

H-bond interactions of IDR residues 52 (N52, D52, iso-D52) and 66 (N66, D66, iso-D66) with the protein core (excluding the IDR) were also examined before and after deamidation to check for disruption of pre-existing or formation of new interactions. Representative snapshots of WT, DM1, and DM2-Bcl-x_L involving H-bond interactions between residue 52, residue 66 in the IDR and core are shown in Figure 4.9. In wild type simulations, N52 transiently interacts with the core residues of the protein such as N52-R91, N52-R6, N52-S164, N52-E202, N52-R204 (Figures 4.7, 4.8, and 4.9a).

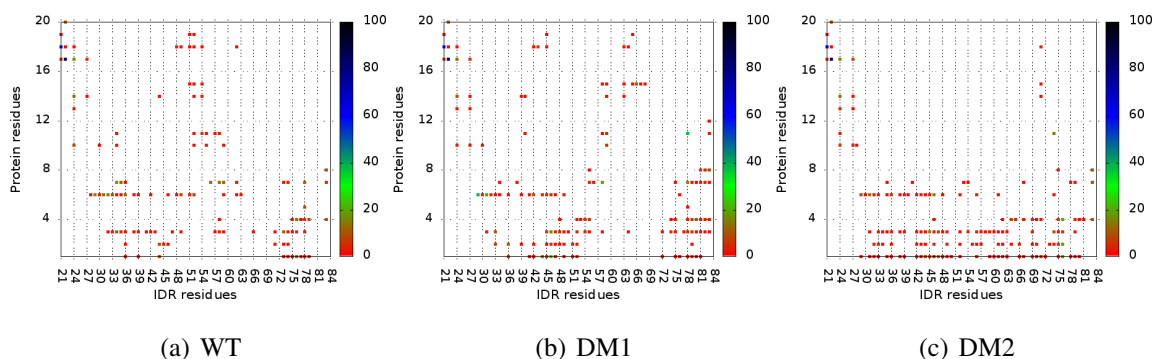


Figure 4.7. H-bond interactions plots for $\alpha 1$ residues of the protein-IDR residues of WT, DM1, and DM2. The color bar shows overall contact percentage during the simulations.

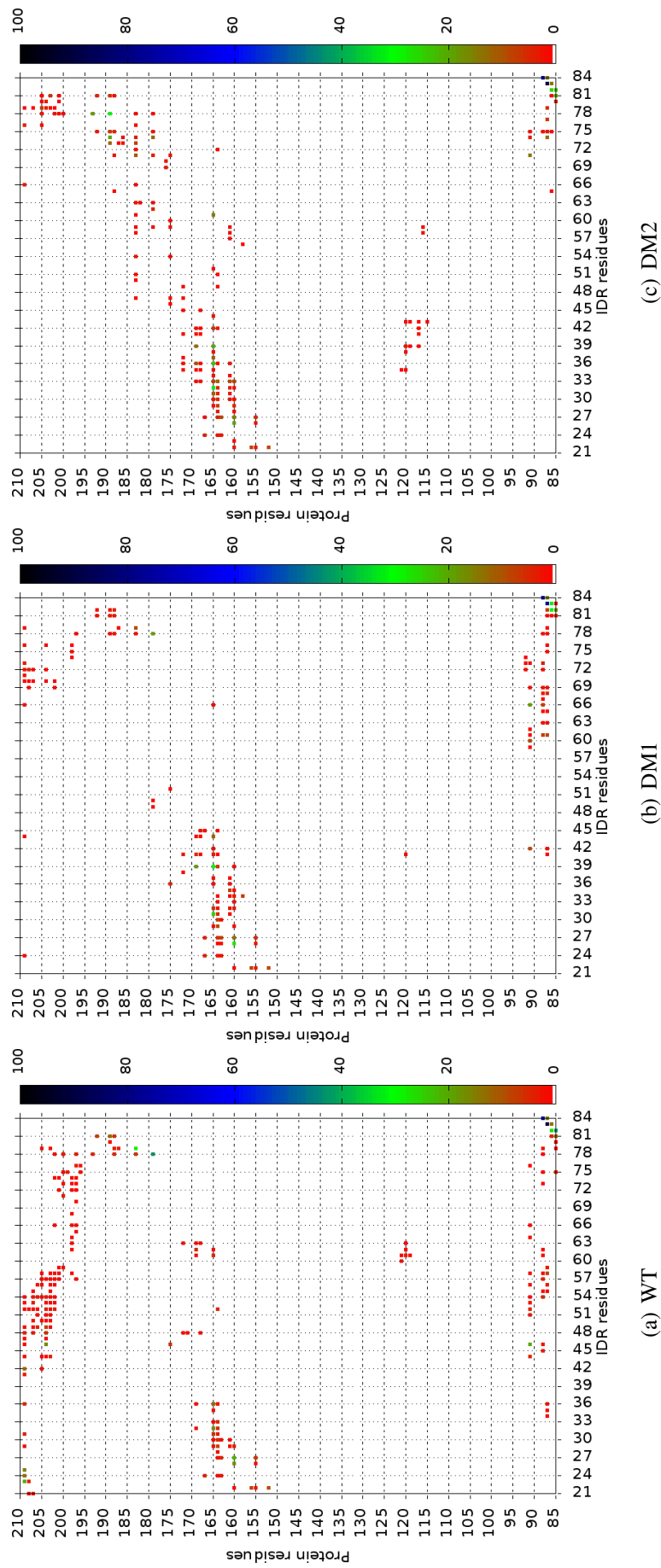


Figure 4.8. H-bond interactions plots for the protein (α 2-C-terminal residues)-IDR residues of WT, DMI, and DM2 simulations. The color bar shows overall contact percentage during the simulations.

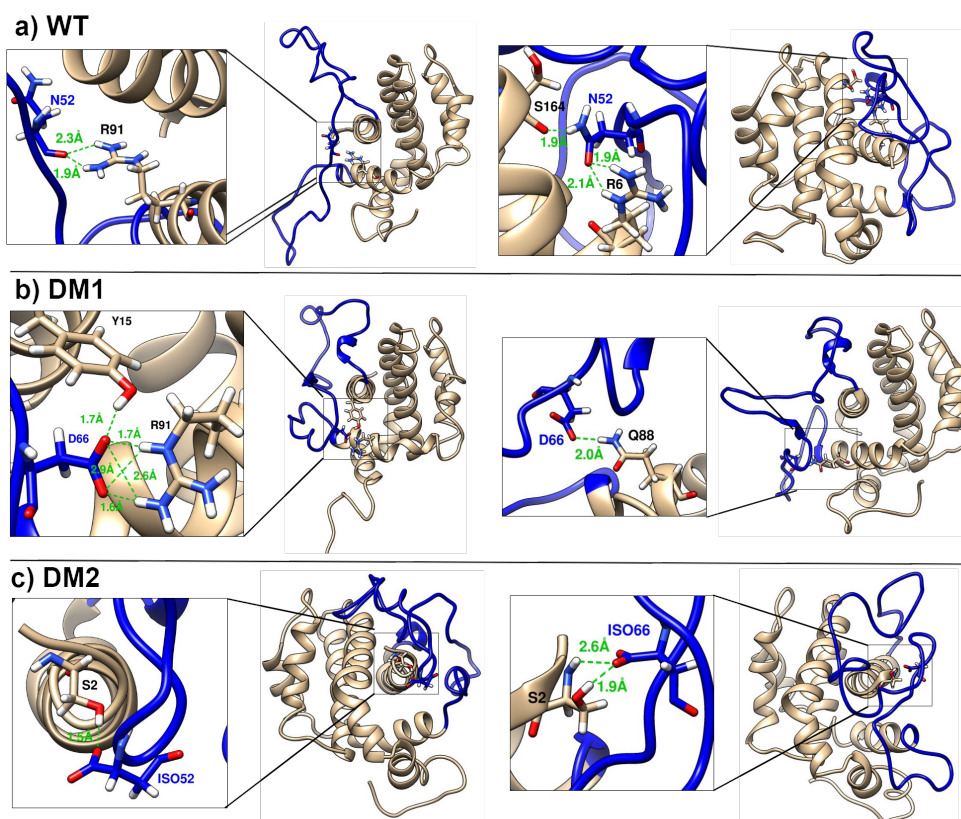


Figure 4.9. H-bond interactions between residue 52, residue 66, and protein core in representative a) WT, b) DM1, and c) DM2. Blue color denotes IDR region. ISO52 and ISO66 refer to iso-Asp52 and iso-Asp66, respectively.

More interestingly, once deamidated (simulation DM1), mostly D66 instead of D52, interacts with the core residues. D66 transiently interacts with R91, Y15, Q88 and R209 in DM1, while N66 in wild type did not interact with neither Tyr15, Gln88 nor R209 (Figures 4.7, 4.8 and 4.9a). D52 also transiently interacts with the first three residues (M1, S2, and Q3) in DM1. Compared to wild type and DM1, in DM2 (iso-Asp) simulations, S2 in $\alpha 1$ has transient interactions with iso-D52 and iso-D66 (Figure 4.7). As a result of the structural changes that iso-Asp deamidation introduces in the IDR backbone, the number of interactions between residues iso-D52 and iso-D66 and the protein core were considerably less. Linear Interaction Energy (LIE) analysis was also performed to evaluate long-range interactions between the protein core and the IDR. Bfactor coloring based on Average LIE analysis results (Figure A.5) illustrated that only N52 in WT, both D52 and D66 in DM1, and only iso-D66 in DM2 display stabilizing interactions with the protein core. Additionally, Figure A.5c demonstrated stabilizing interactions between $\alpha 8$ and the IDR in DM2.

Interestingly, R78 in the IDR interactions remarkably altered upon deamidation. While R78-E179 interaction (42.8 %) stands out in WT, this interaction dramatically decreases in DM1 (19.3%) or nearly non-exists in DM2 (1.1%) (Figure 4.8). Instead, R78-D11 (37.1 %) in DM1 and R78-D189 (31.8%) in DM2 interactions were observed and these interactions are nearly non-existent in WT. Although non-existent in WT simulations, transient but consistently recurring H-bond interactions between IDR residue S74 and a multitude of residues (D189, D11, K87, E179) in the protein core were observed in DM2. Moreover, the H-bond interaction profile of core residue R91 changed significantly. R91-N52 and R91-E46 interactions were originally observed in WT. However, consequent to deamidation, transient R91-D66, R91-E42, and R91-A60 in DM1 and R91-H71 in DM2 were detected. These findings indicate that the IDR behavior has changed significantly upon deamidation; this will be further analyzed in the following sections.

Additionally, the IDR transiently interacts with itself (intra-IDR regions) and hinge formations were observed. Different interaction patterns were clearly observed in each system (Figure 4.10). This outcome supports the flexibility of the IDR. Taken together, these results highlight the diversity of the IDR-protein core interactions. The extra negative charge introduced via deamidation understandably induces changes in the H-bond interaction patterns between the IDR and the protein core. These interactions could allosterically affect the dynamics of Bcl-x_L. Accordingly, clustering analysis and essential dynamics of WT and deamidated systems will be comparatively explored in the following section. Priya et al. [138] in their computational study (100 ns × 2 in total for Bcl-x_L with IDR) had reported transient interactions between the IDR and the core region of the Bcl-x_L. In line with the findings of Priya et al., most of our simulations for WT show that the IDR residues E31, E32, E39 and R78 temporarily interact with core residues R165, R6, R91, and E7, respectively. All interactions mentioned above are also observed in DM1 and DM2 simulations, except for the E39-R91 interaction. On the other hand, the increased/improved interactions between E31-R165 in DM1 and DM2 and between R78-E7 in DM1 are observed. Additionally, compared to WT, improved or new R165 interactions in deamidated systems, particularly in DM2 stand out. Our simulations verified the transient but re-occurring nature of these interactions. This, once again, is an indication that the contact patterns in the reported NMR structure are different than the simulated ones.

tional behavior of the IDR, as seen by the IDR's approach to the BG; this may prevent/affect binding ability of BOP or pro-apoptotic proteins to the binding groove of Bcl-x_L.

Furthermore, in the experimental work of Follis et al. in 2018, negatively charged D61, E62, D52, and D66 in the IDR region were positioned near and electrostatically interacted with the positively charged arginines (R100, R102, R103; known as the 'Arginine cluster') on the J23 of the BG. However, in the experimental NMR model reported by Muchmore et al. [2] (PDB ID: 1LXL), neither S62 and D61 nor N52 and N66 interacted with the Arginine cluster in J23. In the current study, we monitored interactions between deamidation residues 52 (N52, D52, and iso-D52) and 66 (N66, D66, and iso-D66) and the Arginine cluster in all systems (WT, DM1, and DM2). Radial distribution functions (RDF) between the Arginine cluster's guanidinium hydrogens and the side chain oxygen atoms of residues 52 and 66 were calculated to monitor these interactions. The RDF plots show no interaction in the range of 0-10 Å in 13 out of 15 simulations (Figure 4.12). However, in two simulations (WT-SIM4 and D1-SIM4), RDF showed interactions in the range of 3.0-6.0 Å. To check the viability of these interactions, distance analysis was performed on simulations WT-SIM4 and D1-SIM4. Distance plots depict that these interactions are not persistent during the simulations (Figures 4.13a and 4.13b). More importantly, Follis et al. claimed that PTMs (phosphorylation and deamidation) that lead to these interactions induce a structural rearrangement at the distal binding groove (BG), which could lower Bcl-x_L's affinity for BOP. Therefore, we focused on possible structural rearrangements in the binding groove, which stem from deamidation, and affect the dynamics of the distal BG. To do so we have performed thorough clustering analysis and Principal Component Analysis as shown in following sections.

4.3.3. Cluster Analysis

Clustering analysis was performed to group (dis)similar conformations into subsets and gives insight into conformational changes/states upon deamidation. The representative clusters of each system (WT, DM1, and DM2) were chosen/selected with respect to their contributions (Table 4.2) to each cluster for further analysis. "C" refers to cluster.

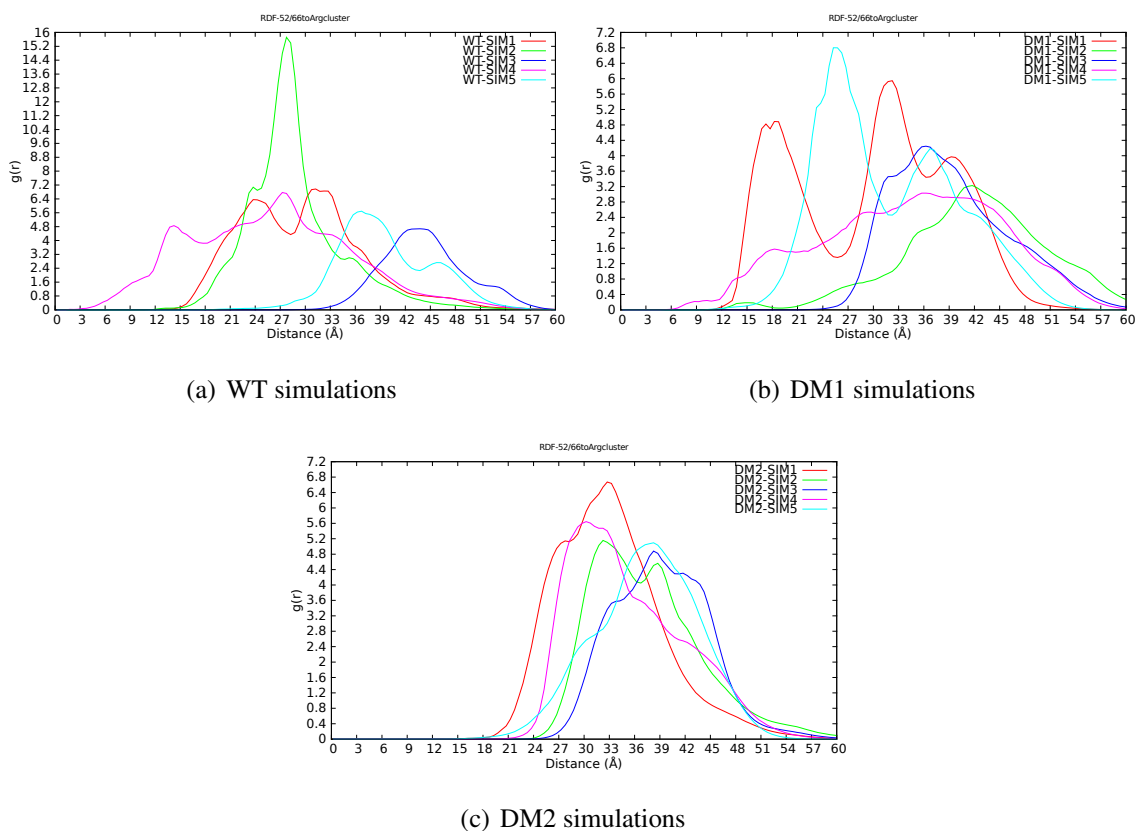


Figure 4.12. a-c) Radial distribution function, $g(r)$, vs the distance between side chain oxygen atoms of residues 52 and 66 and H atoms of the guanidinium moieties in Arg cluster.

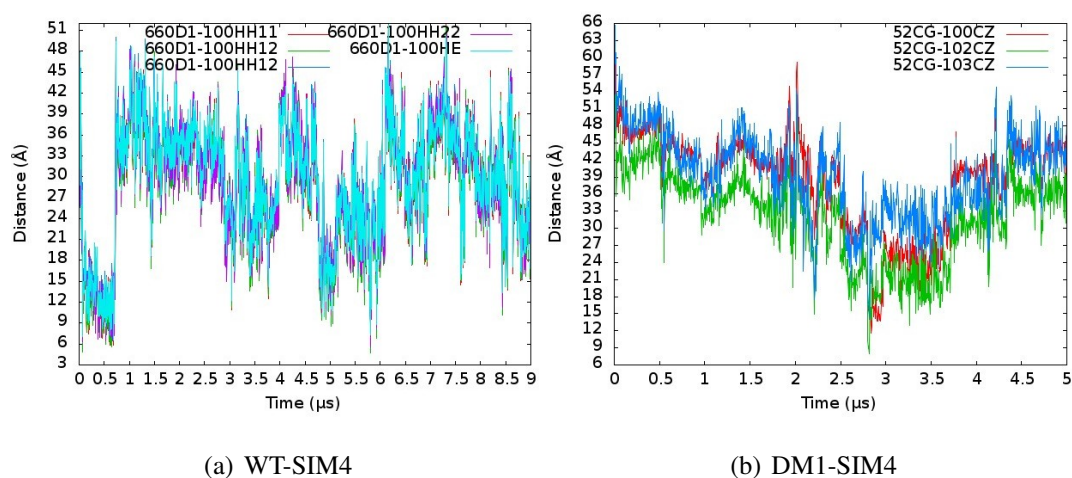


Figure 4.13. Distance plot between a) N66@OD1 and guanidinium H atoms of R100. b) D52@CG and R100,102,103@CZ.

10 clusters were investigated, and the first five clusters were detected as mostly populated clusters, accounting for more than 92% of the conformations (Table 4.2). The cluster zero (C0) is the largest cluster comprising more than 70 % for each system and includes the main conformation of the protein, that is common for three systems. Then, the next four clusters were explored, and representative clusters were identified for each system with respect to their contributions to the clusters. Notably, the clusters are well separated in each system (WT, DM1, and DM2). WT is mostly populated in the first (C1) and second clusters (C2). The third cluster is a representative cluster for DM1 and the fourth cluster, even the fifth cluster is mostly populated with DM2. We further investigated the first five clusters in order to understand the differences among them. Firstly, the structures of the representative clusters (C0-C4) were examined. Structural representatives of these five clusters (C0-C4) were depicted in Figure A.6. Remarkably, main differences in cluster 3 (C3), which is the representative cluster for DM1 are shifts in helices $\alpha 1$ - $\alpha 3$ and $\alpha 8$ (Figure 4.14) and the narrowing of the J23 towards J45 (Figure 4.15). Radius of gyration (Rg) of the back-bone atoms of Y101-A104 in J23 and L130-D133 in J45 were analyzed to follow the narrowing of the bottom side of the BG (Figure 4.15). Rg in C3, which is a representative cluster of DM1, is lower than the others indicating the narrowing bottom side of the BG. Figure 4.16 displayed that the RMSD of cluster 3 (C3) is higher than the rest. These outcomes suggest that DM1 induces considerable conformational changes in the BG.

Table 4.2. Combined clustering summary for WT, DM1, and DM2.

#Cluster	Total	Frac	# of WT frames	# of DM1 frames	# of DM2 frames	%Frac1	%Frac2	%Frac3	WT%	DM1%	DM2%
0	1371061	0.7312	442023	479201	449837	70.72	76.67	71.97	32.2	35.0	32.8
1	125061	0.0667	84785	17478	22798	13.57	2.80	3.65	67.8	14.0	18.2
2	113336	0.0604	91033	9597	12706	14.57	1.54	2.03	80.3	8.5	11.2
3	105247	0.0561	218	85876	19153	0.03	13.74	3.06	0.2	81.6	18.2
4	83539	0.0446	1526	7239	74774	0.24	1.16	11.96	1.8	8.7	89.5
5	26706	0.0142	627	4191	21888	0.10	0.67	3.50	2.3	15.7	82.0
6	19804	0.0106	822	1233	17749	0.13	0.20	2.84	4.2	6.2	89.6
7	14211	0.0076	1699	11400	1112	0.27	1.82	0.18	12.0	80.2	7.8
8	10451	0.0056	2038	4946	3467	0.33	0.79	0.55	19.5	47.3	33.2
9	5584	0.003	229	3839	1516	0.04	0.61	0.24	4.1	68.8	27.1

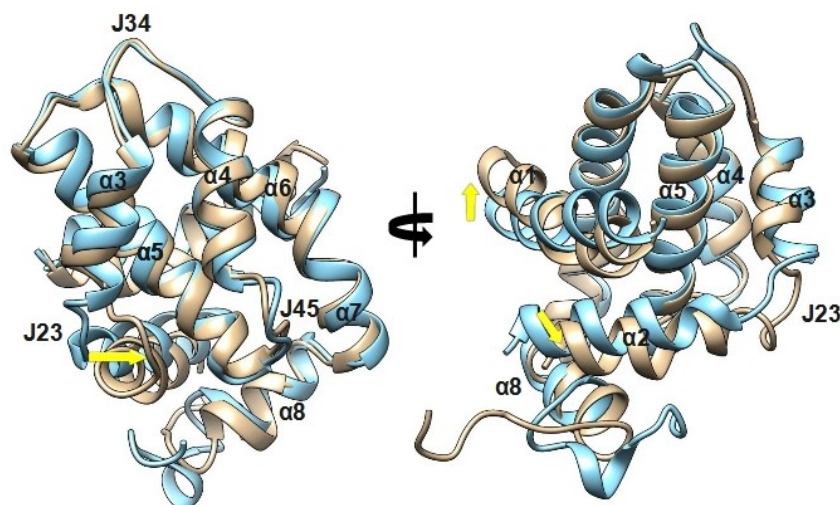


Figure 4.14. Front and side superimposition of the representative structures for clusters 0 and 3. Blue and tan color refer to C0 and C3 representative structures, respectively.

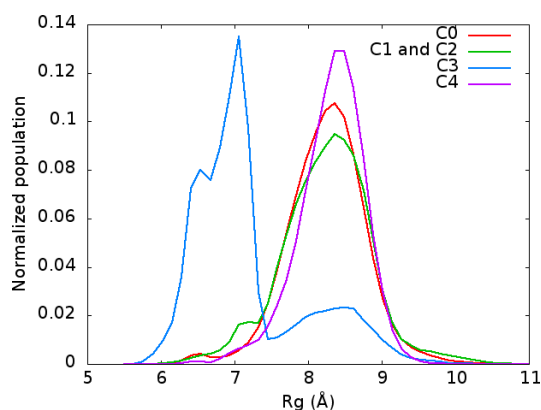


Figure 4.15. Radius of gyration (Rg) of the backbone atoms of Y101-A104 in J23 and L130-D133 in J45 of the most populated clusters (C0-C4).

Secondly, significant differences in the clusters encouraged us to further explore the impact of deamidation on the binding groove (BG) by studying more closely the interaction patterns, specifically H-bonding. In order to pinpoint the residues that contribute to the narrowing of the binding groove (Figures 4.14 and 4.15), hydrogen bonds (H-bond) between residues lying on either side of the BG were explored. Most prominently, in cluster 3, which is the representative cluster for DM1, R102 interactions are primarily responsible for the narrowing of the binding groove (Figures 4.17 and 4.18). Indeed, R102 on J23 interacts with D133 (J45) and E129 ($\alpha 4$) indicating the importance of the R102 residue. However, these interactions are nearly absent in other clusters. Instead, R102 mostly interacts with E98

in other clusters (C1, C2 and C4) and this interaction moves R102 away from the groove and causes the bottom side (J23 and J45) of the BG to stay open (Figure 4.18). Another important residue involved in the narrowing of the bottom side of the groove (J23-J45) is E129 ($\alpha 4$), which interacts with Y101 (J23) and R103 (J23) (Figure 4.18). Besides H-bond interaction, CH- π interaction between Y101-R102 and Y101-L130 was detected in cluster 3 by facilitating/supporting R102-D133 interaction, in turn narrowing of the BG (Figure 4.17). In DM1 H-bond interactions between R103 (J23) and Q111 ($\alpha 3$), and between E98 (J23), and F105 ($\alpha 3$) were observed, which result in the covering of the top of the groove (Figures 4.18 and A.9b). The distance plots for the combined trajectories are given in Figure A.8.

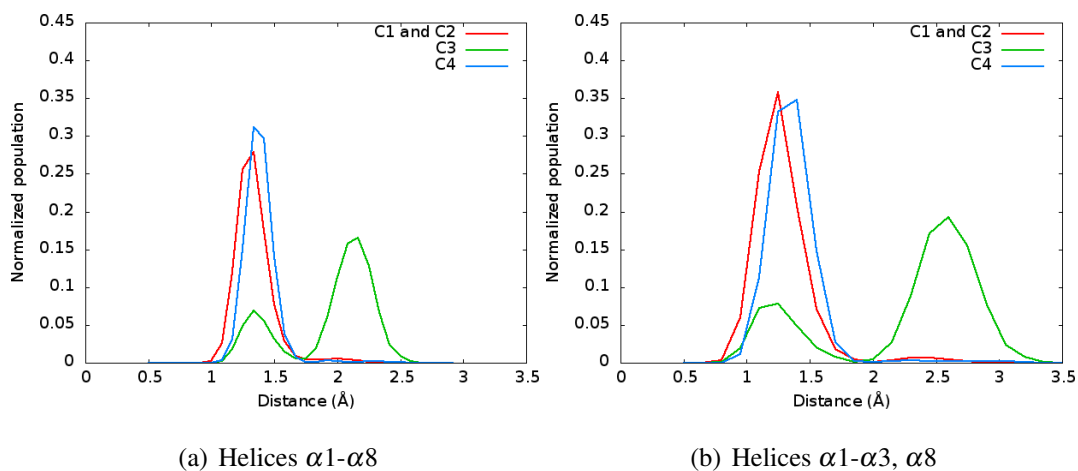


Figure 4.16. Backbone RMSD histogram for the helices of clusters 1-4 with respect to NMR structure.

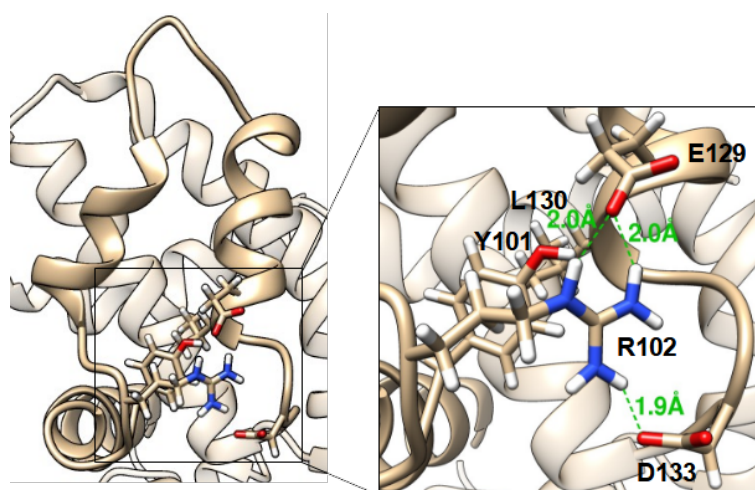


Figure 4.17. Representation of key H-bond interactions between the BG residues in DM1 (C3).

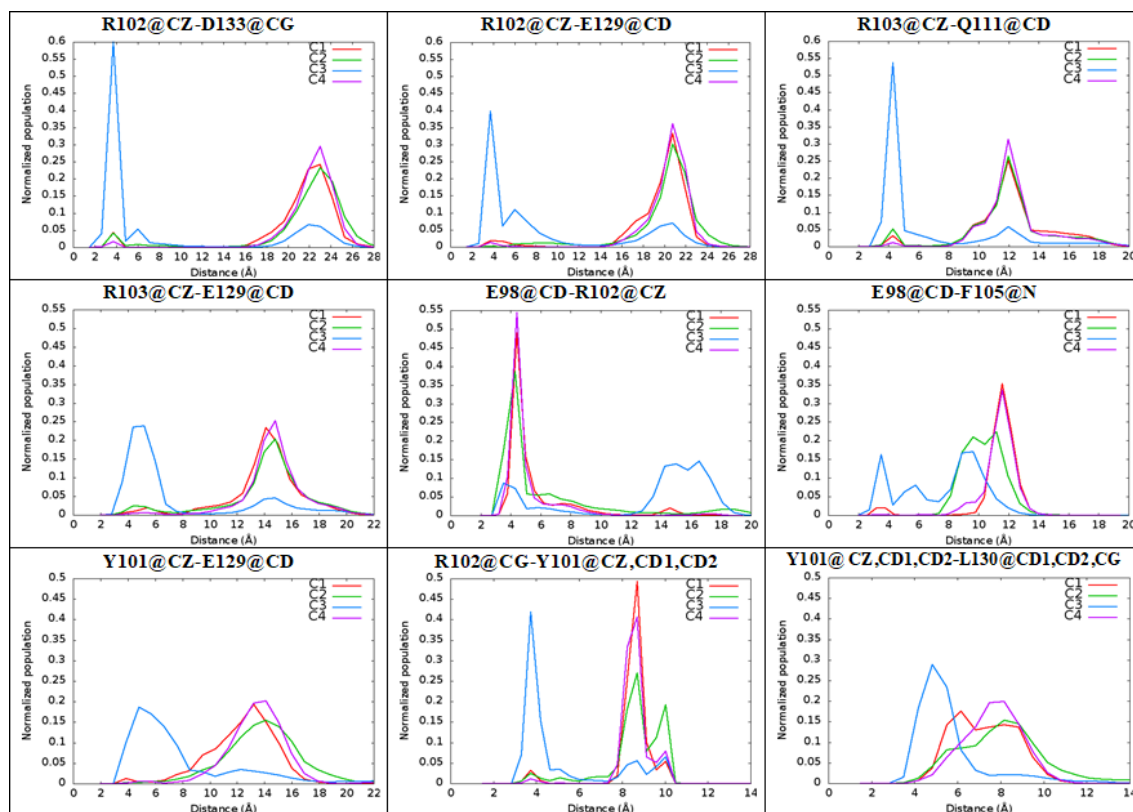


Figure 4.18. Distance histograms for the key interactions in the binding groove of the representative clusters (WT:C1, C2, DM1:C3, DM2:C4).

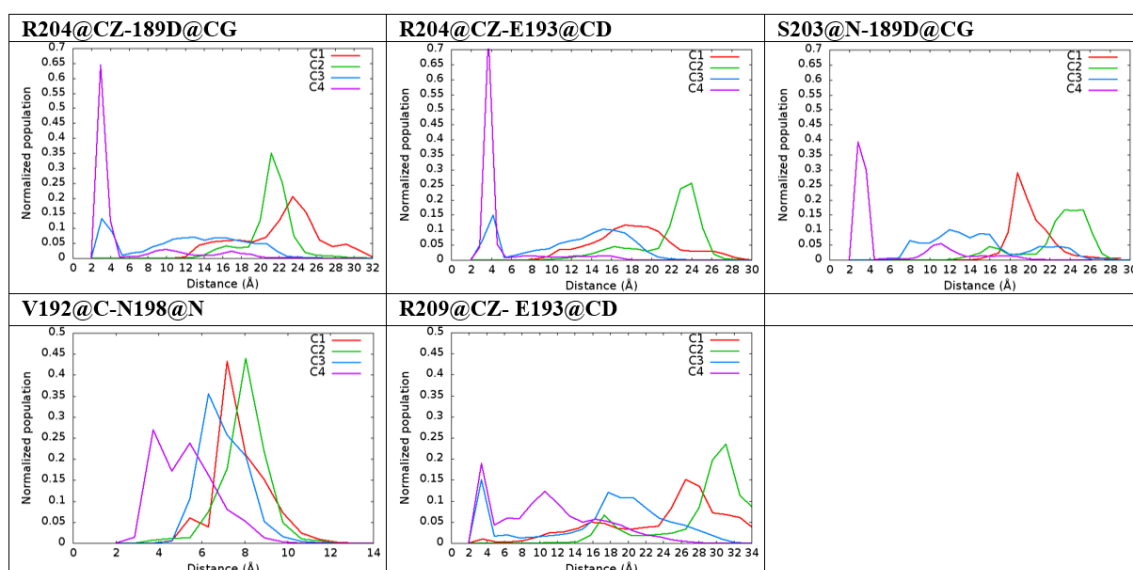


Figure 4.19. Distance histograms for the selected H-bonded residues between the C-terminal and $\alpha 8$ of the representative clusters (WT:C1, C2, DM1:C3, DM2:C4).

Additionally, the C-terminal part (residues 196-209) movements and interactions are generally different among the clusters. In DM2, the differences arise from the C-terminal part- $\alpha 8$ interactions, which are nearly non-existent in C1 and C2 (WT). Distance plots in Figure 4.19 display key interactions in the C-terminal. The distance plots for the combined trajectories are given in Figure A.10. Moreover, the IDR in C4 (DM2) is mostly oriented to $\alpha 6$ - $\alpha 8$ side and approach $\alpha 4$ in BG (Figure A.7). This could prevent access of the pro-apoptotics and BOPs to the BG and may impair its function.

Priya et al. also reported that R103 (J23) and R139 ($\alpha 5$) of wild-type Bcl-x_L behave like a gate by covering the bottom side of the binding groove compared to that of Bcl-x_L without IDR [138]. We observed this type of behavior in DM1, alas, between different residues (R102, D133, E129). Lastly, in 2019, Lee and Fairlie pointed out notable differences in the orientation of Phe105 ($\alpha 3$) and Tyr101 (J23) among Bcl-x_L complex structures depending on the identity of the BOP [149] and pro-apoptotic peptides it engaged [150]. It should be noted that these two residues play a pivotal role in binding to BOPs and pro-apoptotics [149, 151]. Remarkably, we observed that the Tyr101-Phe105 interaction decreases in DM1 simulations, indicating that deamidation has led to the disruption of a significant interaction enabling Bcl-x_L's binding to pro-apoptotic peptides. This in turn leads to its loss of anti-apoptotic function. Taken together, asparagine deamidation to aspartate in the IDR seems to allosterically induce the binding groove from an "open" to a "narrow" state. More specifically, the rotations and interactions of J23 and $\alpha 3$ residues, particularly R102 and R103 have a significant effect on the rearrangement of the binding groove (Figures 4.17 and 4.18).

4.3.4. Principal Components Analysis (PCA)

PCA provides insight into the dominant motions and the essential dynamics of the system [26]. Briefly, PCA translates Cartesian coordinates (trajectories) into the dominant motions. Through PCA, the conformational differences between simulations are explored by investigating the distribution overlap; visual inspection provides information on the similarity of the motions. Since the binding groove which accommodates the BOPs and pro-apoptotic proteins is the main/crucial site for the execution of the anti-apoptotic function of Bcl-x_L, we focused on the evaluation of the BG dynamics. The structural differences

induced by deamidation were further investigated by comparing the essential dynamics of the systems studied. PCA computations were performed in two steps: a) combining the trajectories, which were obtained from the cluster analysis (from C1 to C9) for each system and projected separately onto each system (WT, DM1, and DM2) and then identifying the differences among them b) visually comparing the PC modes of each system.

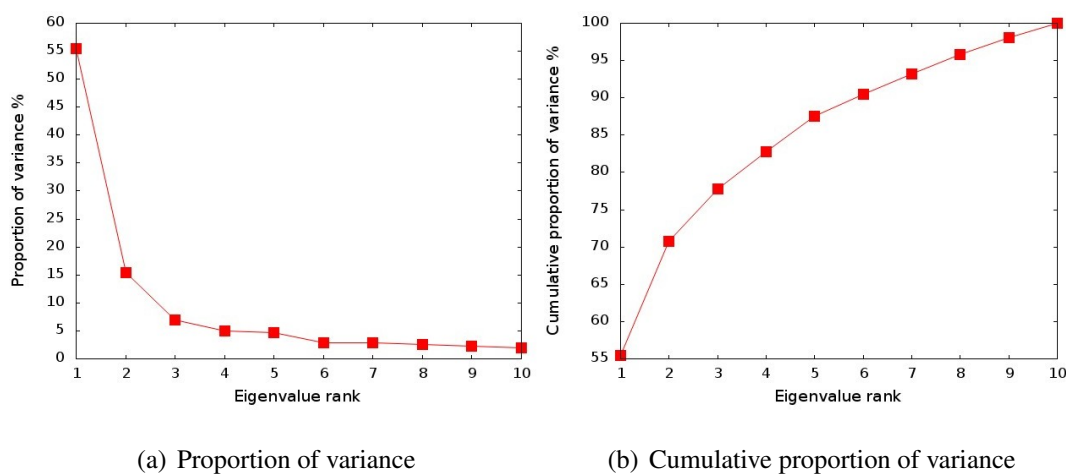


Figure 4.20. a) Proportion of variance b) Cumulative sum of total variance captured by the first 10 PCs for the combined clusters (From C1 to C9 for WT, DM1, and DM2).

Since we are interested in the differences between these systems, we have chosen to exclude the C0, which is common for three of them. First, all trajectories from C1 to C9 were combined and each system (WT, DM1 and DM2) was separately projected. We limited our analysis to the first four PCs, since approximately 80 % of the cumulative variance was covered by them (Figure 4.20b). PC projection histograms in Figure 4.21 illustrate that PC1 and PC2 show significant differences among the systems (WT, DM1 and DM2), particularly for DM1 indicating considerable conformational changes. These results also imply the difference in overall motions among the systems. PC projections shown in heatmap plots (Figure 4.22) show distribution of conformations along the first three PCs. PCs of deamidated Bcl-x_L illustrate notable differences compared to WT. Remarkably, DM1 scans a different and larger conformational spaces as depicted in Figure 4.22. Large conformational sampling in DM1 refers to notable conformational changes. Pertaining to DM2, the PCs in Figure 4.22 also depict considerable difference with respect to WT indicating that different types of motions and conformations were sampled.

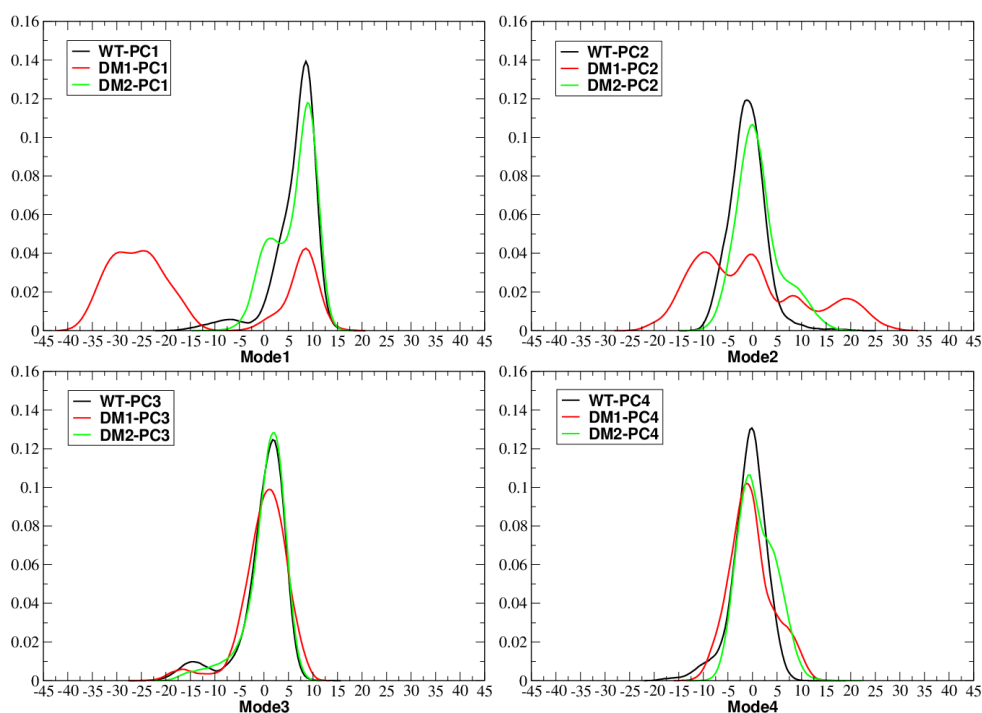


Figure 4.21. Top four PC projections (modes) for each system (WT, DM1, and DM2).
(Zero (0) indicates the average structure.)

Secondly, the three normal modes of deamidated systems were compared visually against WT system. Since the first three PCs generally cover the overall motion as verified earlier with PC plots, the first three PC motions (modes) were compared by using NMWiz [27] in VMD (1.9.3) [28] (Figure 4.23). The most prominent motion in the PCs of DM1 is the mobility of the $\alpha 2$ helix (Figure 4.23b). These results are also in line with the fluctuations of $\alpha 2$ in the per residue RMSD analysis of DM1 (Figure 4.6). Additionally, the proximal side of the junction 23 (J23) connecting $\alpha 2$ and $\alpha 3$ is highly mobile in DM1. In DM2 simulations, movement of J45 connecting $\alpha 4$ and $\alpha 5$ (junction of $\alpha 4$ - $\alpha 5$) was observed (Figure 4.23, Mode 3).

In general, DM1 displays remarkably higher fluctuations and scans different conformational spaces. DM2 simulations also behave different from the wild-type, implying change in structure and essential dynamics of the binding groove upon deamidation. In the deamidated systems, particularly DM1, the binding groove motions are significantly different from the rest, suggesting prominent impact of IDR deamidation on the distal BG. It should be noted that some motions in the binding groove (helices or junctions) seem partly similar for all

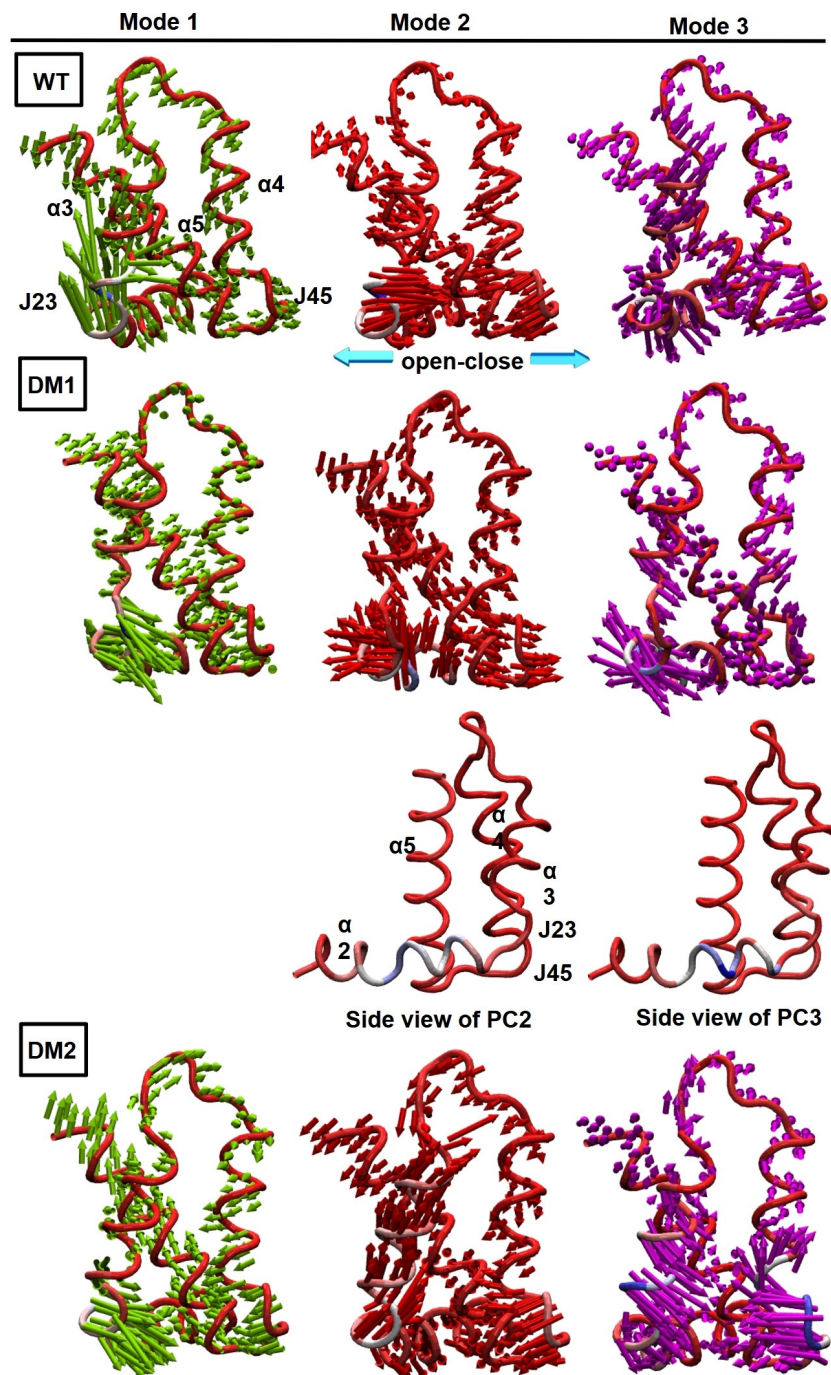


Figure 4.23. The first three PC modes for a) the BG of WT b) DM1 (front and side views) and c) DM2 simulations. (Blue color indicates higher residue mobility. Arrows display the direction and magnitude of the motion.)

Taken together, PCA findings revealed that PC motions of DM1 and DM2 considerably differ from WT and suggest that deamidation impacts the structure and motion of Bcl-x_L, in particular, the dynamics surrounding the BG. This, in turn, may lead to loss of ability to

bind BOP/pro-apoptotics, rendering Bcl-x_L unfit for its anti-apoptotic function. Particularly, DM1 deamidation in the IDR causes remarkable changes in the essential motions of the Bcl-x_L binding groove. Based on these outcomes, it could be concluded that deamidation of IDR allosterically influences the binding groove by changing the dynamics of the protein. This finding conforms with Follis's [106] suggestion that PTMs on the IDR may allosterically remodel the binding groove to trigger apoptosis. Furthermore, MD results also show the pivotal role of performing multiple simulation to understand the impact of deamidations and to explore the behavior of the studied systems more efficiently.

4.4. Conclusions

This study entails a significant contribution to the knowledge on structural consequences of deamidation on Bcl-x_L. The increase in negatively charged residues on the IDR, as a result of deamidation, was shown to change the essential dynamics of the binding groove of Bcl-x_L and hence, to alter its structural behavior and conceivably impair its function. One of the most important findings of this study is that the change in IDR motions upon deamidation may significantly affect accessibility of the binding groove. Indeed, the IDR allosterically influences the BG of the protein and induces conformational modifications that lead to changes in the interaction network. Our findings suggest that deamidation in the IDR changes both the number (%) and type of non-bonded interactions between the IDR and Bcl-x_L's core. The clustering analysis points out that the change in BG interactions occur mainly in subunits J23, α 3, α 4, and J45, and include five specific, previously non-existent or nearly non-existent, interactions, namely, R102-D133 and R102-E129, E129-Y101 and E129-R103, and R103-Q111. These allosterically induced interactions are shown to be responsible for the narrowing and covering of the groove upon deamidation. Moreover, PCA analysis along the first three principal components show remarkable differences in essential motions of the binding groove's of wild type and deamidated Bcl-x_L. The combination of clustering, H-bond and PCA analysis outcomes suggest that deamidation on the IDR not only impacts the structure by causing remarkable changes in the essential motions of the binding groove but alters its structural behavior, interaction patterns, and expectedly impairs its function. These findings will bring a unique perspective to the underlying mechanism of

Bcl-x_L deamidation-induced cell death by bringing forward the structural knowledge necessary to develop anti-cancer therapeutics. Additionally, a concerted effort is required to fully explore the structural changes that full-length Bcl-x_L (including both IDR and C-tail) undergoes upon PTMs and the consequences on its complex biological environment, including the dynamics of the mitochondrial outer membrane and its specific protein-protein interactions. This chapter describes a first step in understanding the effect of deamidation on the structure and function of Bcl-x_L by using a non-truncated and unmodified model, also highlighting the importance of longer and multiple simulations.

5. IMPACT OF DEAMIDATION ON STRUCTURE AND FUNCTION OF BCL-X_L IN MEMBRANE

5.1. Introduction

The Bcl-2 family proteins mainly play an important role on the mitochondrial pathway of apoptosis by regulating mitochondrial outer membrane permeabilization (MOMP) and subsequent apoptosis as discussed in the previous chapter [85–88]. MOMP as usually considered as the ‘point of no return’ causes the release of pro-apoptogenic factors (cytochrome c and apoptosis inducing factors (AIF) etc.) from intermembrane space (IMS) into the cytosol to promote caspase activation and apoptosis [87,88,109,152]. The exact mechanism of action of Bcl-2 family is still not well-defined/understood. However, direct activation, [153] displacement, [64] embedded together, [154] and unified [155] models [156–158] are the mainly proposed models to give insight into this process.

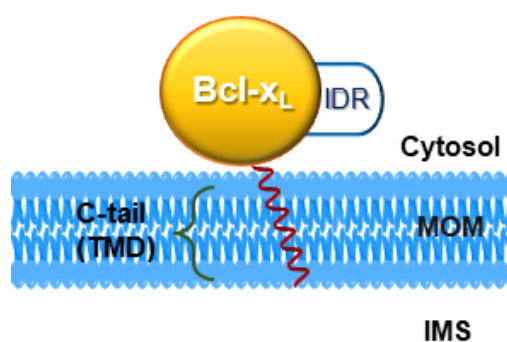


Figure 5.1. Schematic representation of membrane-anchored Bcl-x_L.

Briefly, BH3-only proteins (BOPs) are divided into two groups, namely activator and sensitizer in the direct activation model. Anti-apoptotic proteins (Bcl-x_L, Bcl-2, etc.) inhibit the activator BOPs, such as BIM and BID but not pro-apoptotic proteins (Bax and Bak) to suppress apoptosis. Sensitizer BH3-only proteins (BAD, NOXA, etc.) replace the activator BOPs from the anti-apoptotic proteins to promote apoptosis. Note that Bax and Bak are activated by activator BOPs. The displacement model, also known as the de-repression model, proposes that pro-apoptotic Bax and Bak are active in cells and must be sequestered by anti-apoptotic proteins for cell survival. BOPs only play the sensitizer role and inhibit their

respective anti-apoptotic proteins to promote apoptosis. Note that direct activation and the displacement models do not account for a role for the membrane. Embedded together model proposes an active role for the membrane and joins the key aspects of the direct activation and the displacement models. Bcl-2 family proteins are inserted into membrane and change their conformations that in turn dictate their function. Cytoplasmic anti-apoptotic proteins are recruited to membranes upon apoptotic stimuli. At the membrane, anti-apoptotic proteins inhibit the activator BOPs and pro-apoptotic proteins to prevent MOMP. Sensitizer BOPs displace the activator BOPs and pro-apoptotics from anti-apoptotic proteins to stimulate/initiate apoptosis. Activator BOPs recruit Bax to the membrane to induce MOMP and apoptosis. These interactions are reversible and are governed by equilibrium constants that are altered by the concentrations and interactions of the proteins with each other and with membranes. Lastly, unified model develops the embedded together model by offering that the anti-apoptotic proteins sequester the activator BOPs (mode 1) and sequester pro-apoptotic Bax and Bak (mode 2). However, the unified model postulates that inhibition of apoptosis through mode 1 is less efficient and therefore easier to overcome by sensitizer BOPs. In addition, the unified model extends the role of Bcl-2 family and the regulation of MOMP to mitochondria dynamics. In this chapter, we account for the role of the membrane.

As previously mentioned, Bcl-x_L, consisting of 233 amino acids, is an α -helical trans-membrane protein and possesses four Bcl-2 homology (BH1-4) regions and eight helices with a C-tail (residues 210–233) composed of an α helix (α 9). The C-tail, known as a trans-membrane domain (TMD) provides anchoring of Bcl-x_L to the mitochondrial outer membrane (MOM) (Figure 5.1) [2, 93–95]. It is important to stress that Bcl-x_L with the C-tail (i.e., full-length Bcl-x_L) is not experimentally resolved due to the experimental limitations (solubilization, low yields, production of the protein in a natively folded form etc.) [95, 96]. Recently, the C-tail alone was experimentally resolved inside phospholipid nanodiscs (PDB ID: 6F46_{NMR} [96] and 6X7I_{NMR}). Additionally, Bcl-x_L includes a long intrinsically disordered region (IDR), the so-called flexible loop between α 1- α 2. The IDR was omitted in most of the previous studies, yet recent studies exhibited the importance of the IDR since post-translational modifications (PTMs), which can affect function, stability and localization of the proteins in response to various apoptotic stimuli [102–105, 107, 109].

Bcl-x_L is mostly found on the mitochondrial outer membrane (MOM) and is in a dynamic equilibrium between cytosol and membrane in healthy cells [159–163]. Upon apoptotic induction, such as DNA damage and oxidative stress, Bcl-x_L translocated to the MOM and localized/anchored to the MOM by its C-tail (Figure 5.1) [160, 164]. In the previous studies the use of truncated Bcl-x_L or Bcl-x_L in the presence of detergents provided initial but limited insights on the structure and consequent impact on the function of the protein. In 2013, Todt et al experimentally reported that Bcl-x_L retro-translocated BAX from the MOM to cytoplasm and substitution or removal of the C-tail of Bcl-x_L decreases BAX retro-translocation, by increasing mitochondrial BAX level and cell death [160]. In 2013, Maity et al. investigated dynamics of Bcl-x_L (Δ 45-84 in the IDR) and Bcl-x_L-BH3 complex (PDB ID: 1BXL_{NMR}, Δ 45-84) in water and membrane by means of MD simulations (1.6 μ s in total) [99]. Simulation results showed that the conformational dynamics between water and membrane are considerably different, indicating the conformational transitions in membrane environment. Noted that they fully inserted Bcl-x_L inside the membrane instead of anchoring from the C-tail and the loop is missing. In water the C-tail (residues 197-217) was docked to the BG before MD as well. In 2015, Yao et al. reported structural information for Bcl-x_L (Δ 45-84) in water and membrane including a complete C-tail using NMR and ITC [110]. They observed that the C-tail behaved as a pseudo-inhibitor in water system and provided integration on membrane/lipid nanodiscs. The C-tail formed a transmembrane α -helix inside the membrane by adopting an approximately 25° tilt. They also developed methods to isolate and characterize the membrane-embedded C tail to prepare protein suitable for structural and biochemical studies [94]. In 2016, Maity et al. comparatively modelled the C-tail of Bcl-x_L with respect to the known C tail of Bax (PDB ID: 1F16 [165]) using Modeller [166]. They presented the insertion modes (from association to insertion) of the C-tail into the DOPC bilayer (80 lipid per layer) using PMF calculations [167]. Calculations showed that electrostatic interactions, especially R232 and K233 drive the membrane insertion and the C-tail adopts a tilt angle of approximately 30°. More recently, the same group showed the significance of the charged and polar residues at the terminal ends of C-tail by performing Adaptive Biasing Force based MD simulations (for a total of 2.67 μ s) [168]. While double mutated C-terminal residues (R232A and K233A) destabilized the membrane-associated states and the membrane-embedded states, N terminal (N211A and R212A) only reduced the stability of

the fully inserted state. In 2018, Follis et al. experimentally demonstrated that PTMs in the IDR (phosphorylation on S62 or deamidation of N52 and N66) cause a structural rearrangement in the distal BG that reduce the anti-apoptotic activity of Bcl-x_L [106]. Additionally they experimentally demonstrated that in membrane environment the IDR did not change the global conformation of the core region and the C-tail anchoring behavior. In 2018 Raltchev et al. described an experimental method to generate natively folded membrane-anchored proteins using SortaseA-based ligation approach and resolved the C-tail structure of Bcl-x_L using NMR (PDB ID: 6F46) [96]. They suggested that the BG of Bcl-x_L loosely interacted with the membrane. Intriguingly, Vasquez-Montes et al. hypothesized a membrane-inserted non-canonical mode of Bcl-x_L, and experimentally characterized membrane-inserted conformations of Bcl-x_L by modulating lipid composition [169, 170]. They reported that the $\alpha 6$ helix was inserted into the membrane leading to the disruption of Bcl-x_L packing and the release of BH4 domain ($\alpha 1$), and that the presence of the C-tail is not required. They showed conformational switching between the anchored (canonical) and the inserted conformations of Bcl-x_L (non-canonical). Recently, Ryzhov et al presented the preparation and conformations of Bcl-x_L both in water and membrane with combination of experimental and computational studies (1 μ s \times 5 NPT MD simulations per environment) [171]. In water system, they used modified Bcl-x_L by removing Bax peptide from the complex (PDB ID: 1BXL_{NMR}) and adding a loop from 1LXL_{NMR} and the C-tail from 6X7I_{NMR}. Their membrane systems include 156 DMPC, 39 DMPG and Bcl-x_L was formed using 1LXL_{NMR} and 6X7I_{NMR}. They investigated full-length Bcl-x_L both in water and membrane, yet they did not offer any insight into deamidation-induced conformational changes in Bcl-x_L. For these reasons, the contribution and impact of deamidation on Bcl-x_L function in membrane is still open for further investigation. In the current study, we will explore the impact of membrane (protein-membrane interactions (PMI)) to give deeper insight into the loss of Bcl-x_L function upon deamidation. From a structural point of view, since most of the previous studies lack the membrane environment and the IDR or use Bcl-x_L in the presence of detergents, the conformational changes between water and the membrane inserted state are poorly understood. However, while the detergents solubilize the C-tail, they also usually destabilize the soluble domain and change the interaction pattern. It may even lead to the distortion of the protein structure and function [158]. Thus, the C-tail was eliminated in the previous

studies. Moreover, structural information about Bcl-x_L prior and subsequent to deamidation are limited. Recent studies give insight into the structure of the membrane-inserted conformation of Bcl-x_L but little is still known about the molecular details or any deamidation impacts [106, 110, 169, 170]. Therefore, these findings provide only a glimpse to understand the structural reasons of the loss of Bcl-x_L function and interaction with membrane. In this context, the role of the membrane is crucial to provide a broader perspective on conformational changes of full-length Bcl-x_L in the membrane environment and to elaborate on the localization of the protein in the membrane.

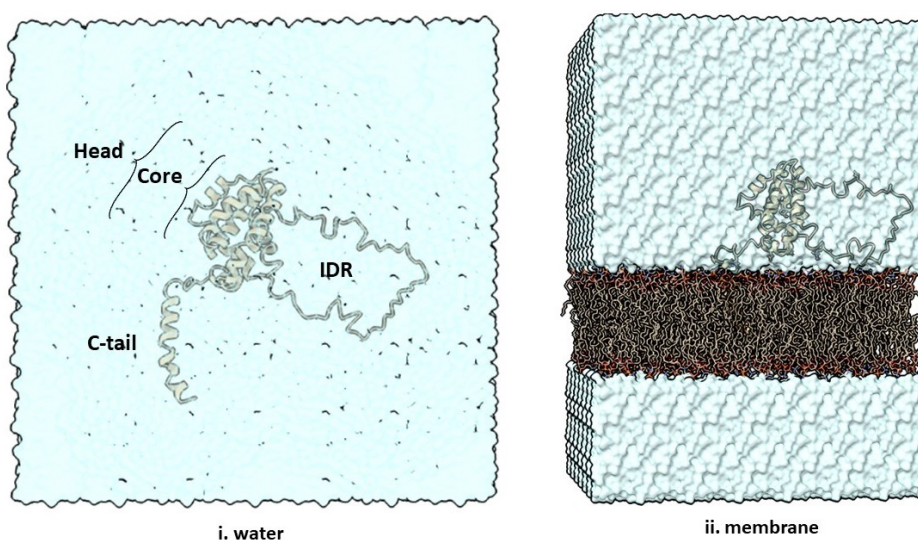


Figure 5.2. Schematic representation of this study: Bcl-x_L and deamidated Bcl-x_L *i.*) in water, and *ii.* in membrane. (Protein head refers to the core and the IDR excluding the C-tail. The water surface is generated using the ChimeraX surface presentation.)

More importantly, deamidated Bcl-x_L (Asp and iso-Asp deamidated versions) has not been elucidated both in water and membrane environments. Membrane insertion could also contribute to an allosteric change in the BG of the protein by promoting conformational and functional changes in combination with deamidation. Hence, a concerted effort is required to explore the structural changes in full-length Bcl-x_L upon deamidation and its consequences on the complex biological environment, focusing on the dynamics and possible collective effects of the protein head, the C-tail and protein-membrane interactions (PMIs). Therefore, the ultimate goal of this study is to fully understand deamidation-induced conformational

changes both in water and in membrane in order to scrutinize conceivable reasons of loss of its function (Figure 5.2). The impact of Bcl-x_L deamidation in water and in membrane is explored by monitoring the structural changes, particularly the BG during microsecond long MD studies. This study attempts to elucidate, for the first time, deamidation of Bcl-x_L in membrane environment to evaluate potential changes in the protein structure and dynamics and consequently understand its loss of function.

5.2. Methodology

5.2.1. Preparation of the C-tail and REMD Simulation Details

The initial structure of the C-tail (24 residues, F210-K233 residues) including acetyl (ACE) group cap was modelled by tleap implemented in the Amber18 program package [141]. Generalized Born model (GB-Neck2) was performed in combination with mbondi3 intrinsic radii, and ff14SBonlysc. An alpha helix shape was given by cpptraj [145] using the `make structure` command afterwards. The C-tail system was minimized and equilibrated without restraints in three steps as follows: 1) the system was gradually heated from 10K to 300K using Andersen thermostat [21] with random velocity update every 10 steps for 12 ns. 2) The microcanonical (NVE) ensemble was applied at 300 K for 0.1 ns. 3) Langevin temperature coupling [144] with a gamma of 1.0 ps⁻¹ was applied at 300 K for 1 μs. The SHAKE algorithm was carried out in order to constrain bonds involving hydrogen bonds. Time step for the third step of the equilibration and Replica-Exchange Molecular Dynamics (REMD) were carried out for 4 fs, using hydrogen mass repartitioning (HMR), [23] to accelerate REMD simulations. REMD [24] technique, which enhances the conformational sampling of proteins was used to sample representative C-tails. Eight replicas with temperature range between 270-468.7 K were used for REMD simulations with an acceptance ratio of ≈ 0.2 [172]. 20 μs long REMD simulations were performed for each replica. The Langevin thermostat [144] with a gamma of 1.0 ps⁻¹ was employed, and exchange attempts were tried every 5 fs.

5.2.2. Simulation Details in Water Systems

The initial structure of Bcl-x_L (ΔC) “1LXL_{NMR}” was extracted from the Protein Data Bank (Homo sapiens); extra residues were removed from the PDB file. Bcl-x_L and the C-tail candidates were joined using Chimera (version 1.14) to obtain full-length Bcl-x_L [147]. Deamidated structures (DM1 and DM2) were built by replacing Asn to Asp and iso-Asp, respectively. MD simulations were performed using the Amberff14SB82 force field implemented in the Amber18 program package [141]. Cubic boxes were built using the TIP3P [143] explicit water model and the boxes were designed large enough to accommodate extended forms for all systems. Counter sodium or chloride ions were added to neutralize each system. The Particle Mesh Ewald (PME) method with a default 8 Å cutoff distance was employed to account for long-range electrostatic interactions [18, 19]. All systems (FL, DM1 and DM2) in Table 5.1 were minimized using the NVT ensemble with the Andersen temperature coupling [21] with randomly updated velocities every 10 steps after a short steepest descent minimization using harmonic restraints on all heavy atoms. A five-step equilibration protocol was performed using the NPT ensemble with a Monte Carlo barostat as follows: 1) all heavy atoms are restrained with a harmonic potential of 50 kcal mol⁻¹ Å⁻² for 0.1 ns at 10 K. 2) only the oxygen atoms of the water molecules are restrained using the same restraining potential for 0.1 ns at 10 K. 3) the harmonic potential is decreased to 5 kcal mol⁻¹ Å⁻² while repeating the 2nd step. 4) the entire system is equilibrated without restraints for 0.1 ns at 10 K. 5) the system is gradually heated to 300 K for 2 ns using the Berendsen thermostat [20] with a coupling time of 1.0 ps. For the equilibration steps 1 to 4, velocities were randomly updated every 10 steps under the Andersen thermostat. Sampling simulations were performed at 300K and NVT ensemble with Langevin temperature coupling [144] with a gamma of 1.0 ps⁻¹. The time step for sampling runs was 4 fs via hydrogen mass repartitioning (HMR) [23].

5.2.3. Generation of Membrane-associated Bcl-x_L and Simulation Details

1-Palmitoyl-2-oleoylphosphatidylcholine (POPC) is the most abundant lipid in MOM and is used as a representative model for MOM [173–176]. Therefore, in the study POPC lipid was used to mimic the MOM. All protein associated membrane systems were generated by CHARMM-GUI Membrane Builder [177, 178] and each layer included 240 POPC lipids.

Prepared systems (Bcl-x_L and deamidated Bcl-x_L) were oriented with respect to the membrane (if needed) to avoid the IDR insertion into the membrane. A 50Å water thickness was added on both top and bottom of each system. 0.15 M KCl was added into the system in order to mimic physiological conditions. In all simulations Amberff14SB [142] and Lipid14 [179] force fields were used for protein and membrane, respectively. Moreover, the TIP3P [143] explicit water model was used. A minimization followed by a six-step equilibration protocol was conducted/applied for all initial systems. The minimization and the first five steps in the equilibrium runs were repeated using the same protocols as in the water system simulations. A sixth stage was added and consisted in letting the systems equilibrate without restraints for 4 ns at 300 K using the Berendsen thermostat86 with a coupling time of 1.0 ps. The area per lipid (APL) was calculated in order to check membrane equilibration and its compliance with known experimental APL (Figure A.11). Finally, microsecond long MD simulations with Langevin thermostat with a gamma of 1.0 ps⁻¹ were performed for each system at 300K (above phase transition temperature of POPC). Additionally, the cpptraj [145] module of Amber18 was used for the analyses of the MD trajectories.

5.3. Results and Discussion

Limited structural information about full-length Bcl-x_L (FL) is available and the impact of the deamidation in the membrane associated Bcl-x_L is not well understood. Relations/interactions between the IDR, the C-tail, and the membrane need to be unraveled to understand their roles on the structure and function of Bcl-x_L. In this context, full-length Bcl-x_L was explored in water and membrane prior to and after deamidation by considering both Asp and iso-Asp mutations (DM1 and DM2, respectively). The studied systems were tabulated in Table 5.1. We primarily focused on the conformational and dynamic changes in the binding groove upon deamidation in the IDR, as well as their environmental impacts. The findings are discussed in water and membrane environments. Mainly, the stability of each system, hydrogen bond interactions and principal component analysis are investigated to identify/detect conformational differences during simulations.

Table 5.1. Summary of the initial system setup.

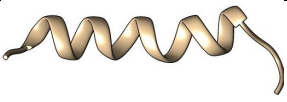
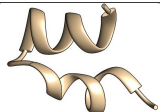
Water system	Water	Na+	Total atoms	Simulation box (\AA^3)	Simulation time
Bcl-x _L (FL-wat)	71146	11	217032	130.383×130.383×130.383	1 μ s×4, 2 μ s×1
DM1-Bcl-x _L (DM1-wat)	71144	13	217024	130.383×130.383×130.383	1 μ s×2, 2 μ s×3
DM2-Bcl-x _L (DM2-wat)	71144	13	217024	130.383×130.383×130.383	1 μ s×2, 2 μ s×3
Membrane system	Water	K+/Cl-	Total atoms	Simulation box (\AA^3)	Simulation time
FL-memb					
FL-C1-memb	84338	245/234	321396	129.445 × 129.439 × 207.818	1.5 μ s
FL-C2-memb	72640	209/198	286230	129.445 × 129.349 × 184.544	1.5 μ s
FL-C3-memb	73052	211/200	287470	129.445 × 129.349 × 185.787	1 μ s
DM1-memb					
DM1-C1-memb	84414	246/233	321620	129.445 × 129.439 × 207.818	1 μ s
DM1-C2-memb	72585	212/199	286065	129.445 × 129.349 × 184.544	1 μ s
DM1-C3-memb	72998	213/200	287306	129.445 × 129.349 × 185.787	1 μ s
DM2-memb					
DM2-C1-memb	84414	246/233	321620	129.445 × 129.439 × 207.818	1 μ s
DM2-C2-memb	72585	212/199	286065	129.445 × 129.349 × 184.544	1 μ s
DM2-C3-memb	72998	213/200	287306	129.445 × 129.349 × 185.787	1 μ s
Water thickness in membrane systems is 50 \AA .					
Wat and memb refer to water and membrane systems, respectively.					

5.3.1. Evaluation of the C-terminal Tail

Subsequent to 20 μ s long REMD simulation between 270 K and 468.7 K, the frames at 293.6K were extracted from REMD trajectories. Energy of each frame in Table 5.2 was calculated by *esander* in the *cpptraj* [145] module of Amber18. Secondary structure analysis was performed using the Definition of Secondary Structure Prediction (DSSP) algorithm, [146] and successive helix residues were identified. In the scope of this study, the C-tail candidates were selected in the aspect of minimum energy, secondary structure, and helix content criteria to better represent the C-tail behavior in full-length systems (Table 5.2). The tail candidates were evaluated under three groups, namely helix (three helical tails), min energy structure (hairpin) and random coil with min. energy. In the first group, the C-tail having the helix (criteria $h > 16$) with minimum energy was selected as the first candidate. Two candidates were available for maximum helix content ($h=22$) and were selected as sec-

ond and third candidates. Then, the C-tail with minimum energy was used as a 4th candidate. Lastly, minimum energy random coil was used 5th candidate in the study. For the sake of completeness, we continued with five tails. Additionally, some recent studies showed that the C-tail formed a transmembrane α -helix inside the lipid membrane with various helix content/long (h18 to h22) [96, 110]. Thus, helical models were used in membrane systems.

Table 5.2. Representative C-tail candidates used in the study.

C-tail candidates	Tail structure	Criteria	Energies of C-tail (kcal/mol)	Full Length ID
C1 (h17)		min. energy successive helix 16	-496.8658	FL-C1
C2 (h22-m1)		max successive helix	-484.9407	FL-C2
C3 (h22-m2)		max successive helix	-464.8594	FL-C3
C4 (min)		min. energy	-559.3848	FL-C4
C5 (coil)		min energy random coil	-487.6524	FL-C5

5.3.2. Stability of Bcl-x_L Systems prior to and subsequent to Deamidation

Prior to comprehensive investigation of all systems (FL, DM1, DM2) in water and membrane, stability of each system was initially analyzed using the backbone root mean-square deviation (RMSD) analysis with respect to the initial/built structure. The core helices and (< 3.0) are stable during the simulations (Figure 5.3). The IDR is highly flexible in all systems (Figure A.12). Figure 5.4 depicts that the C-tails inside the membrane considerably lower RMSD values than the C-tail in water and are not flexible as expected due to the surrounding lipids. Additionally, the stability of the helical contents and structural behavior of the studied systems were also evaluated using the Definition of Secondary Structure Prediction analysis [146] (Figure A.13). In general, α 1- α 8 preserved their helical structures.

Partial unfolding in the helical tails were observed in all water systems, especially deamidated systems. In membrane, helical tails preserved during the simulations. Furthermore, helical tendency was seen in the IDR in line with previous studies [96, 140].

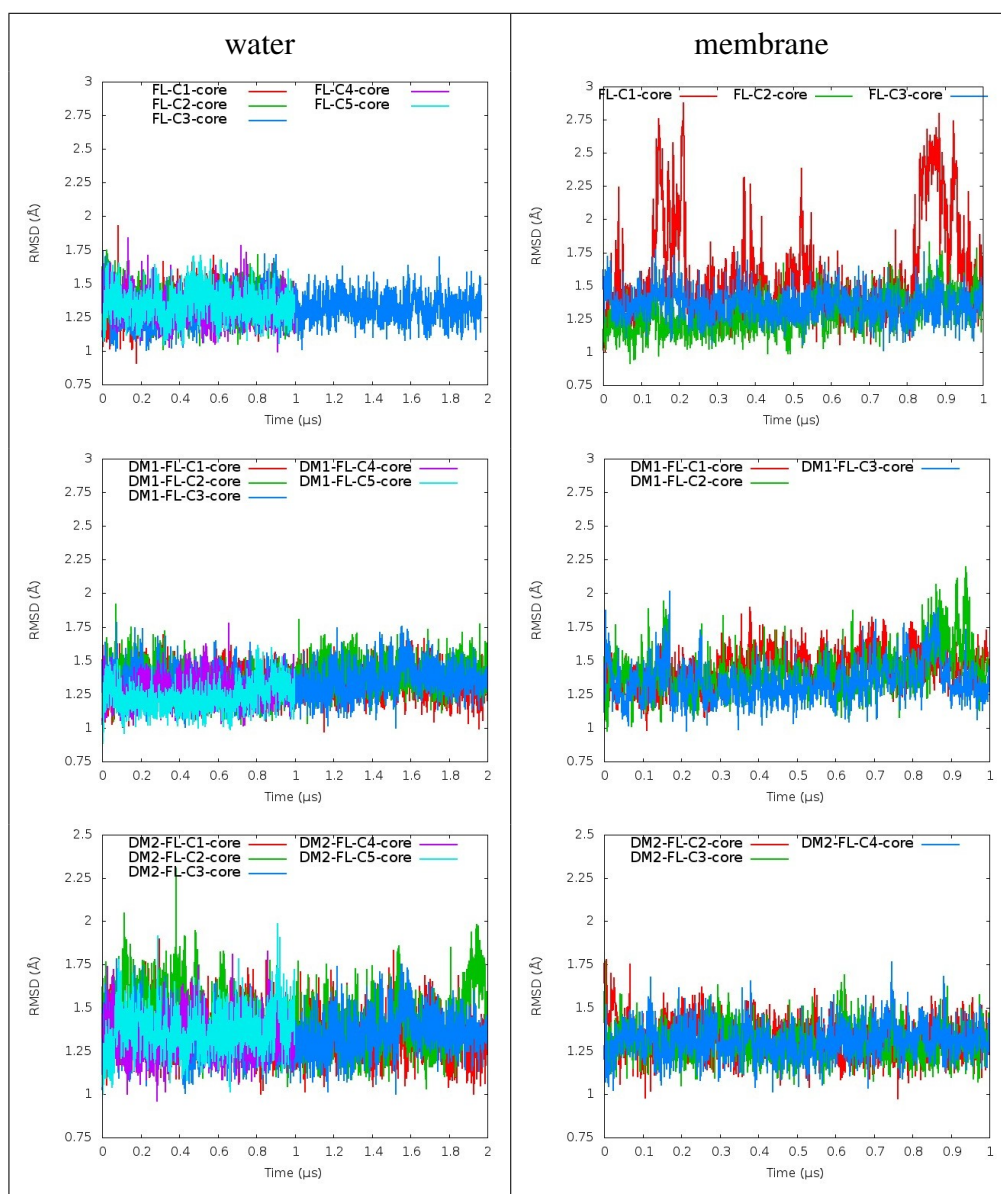


Figure 5.3. Backbone RMSD plots for core helices of FL, DM1 and DM2-Bcl-x_L simulations with respect to initial/built structures (Every 20 frames).

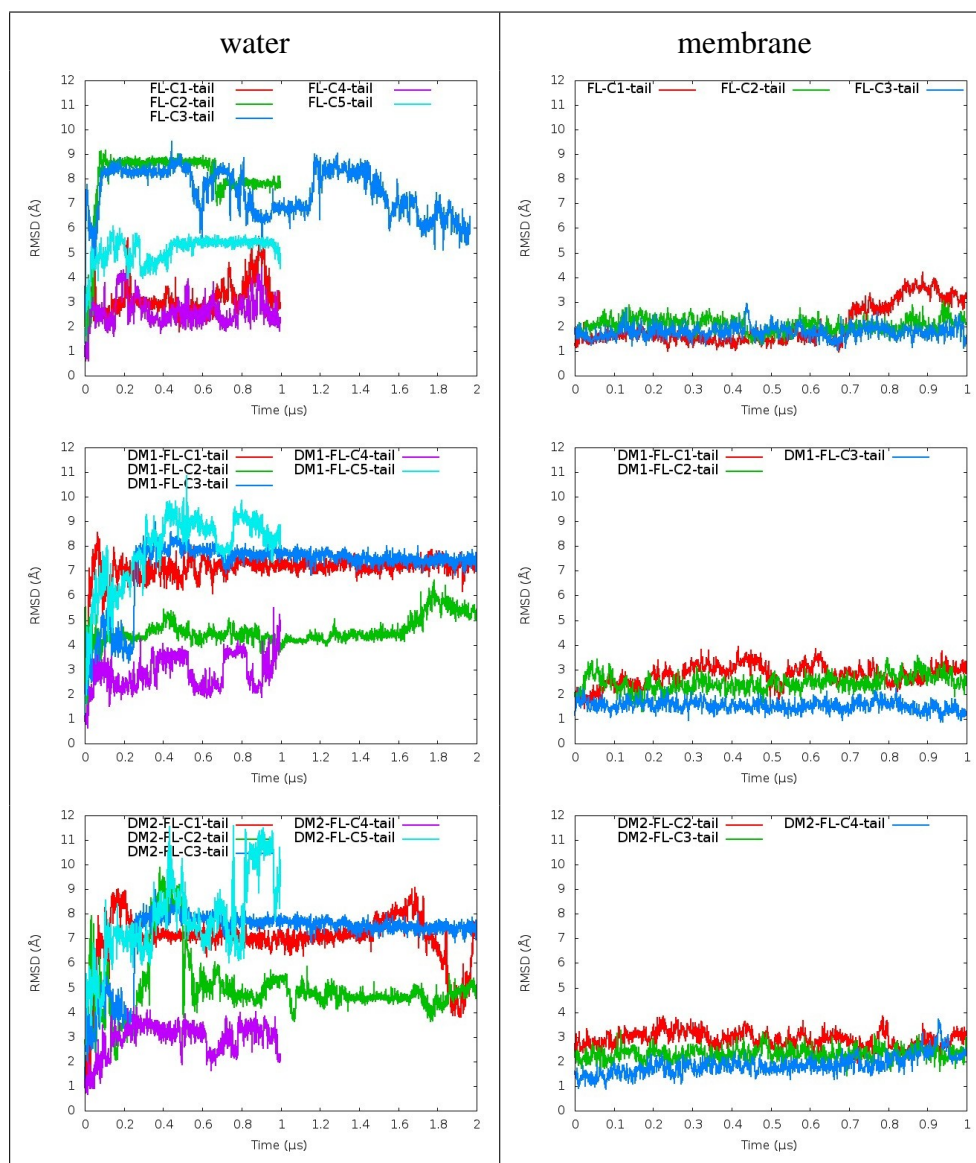


Figure 5.4. Backbone RMSD plots for the C-tails of FL, DM1 and DM2-Bcl- x_L simulations with respect to initial/built structures (Every 20 frame).

5.3.3. Bcl- x_L and Deamidated Bcl- x_L in Water

Structural behaviors of Bcl- x_L bearing the C-tail (FL) in water were evaluated before and after deamidation to identify the changes during simulations and to understand the structural consequences. Moreover, water system was considered as a reference to assess the outcomes of membrane systems. Structurally, the C-tails did not preserve their initial extended forms, which do not make contact with the protein head before the simulations. The C-tails approached the protein head during the simulations. Additionally, the C-tails are

highly dynamic in water and the flexible junction connecting $\alpha 8$ and $\alpha 9$ (J89) contributes the C-tail to move in various orientations. Notably, as depicted in Figure 5.5 the C-tails of deamidated models aligned/positioned towards different region of the protein core/head. This observation pertains to almost all C-tails (except the systems bearing C2 tail). The C-tails in native form positioned differently with respect to deamidated ones (for all snapshots see: Figure A.14).

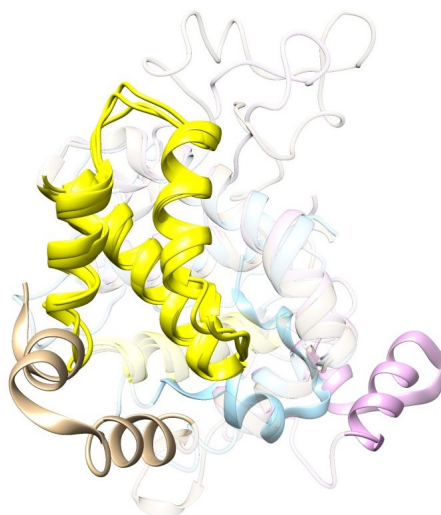


Figure 5.5. Representative positions of the C-tails among Bcl-x_L and deamidated Bcl-x_L in water. (Yellow color presents the binding groove. Tan, blue, and pink colors denote the C-tails of FL-C3, DM1-C3, and DM2-C3, respectively. Water was not shown for clarity.)

H-bond interactions were examined during the simulations in order to detect persistent (long-lived) and transient (short-lived) but consistently re-occurring interactions. Temporary (short-lived) interactions among the C-tail-protein head (C-tail-loop and C-tail-BG (mostly $\alpha 2$ and J23)), and tail-junction of $\alpha 8$ and $\alpha 9$ (J89) were observed during the simulations. In general, the terminal residues, that is, N211, R212, W213, R232 and K233 residues in the C-tail drive the H-bond interactions with the protein head.

Yao et al mentioned that the C-tail interactions with G94 in $\alpha 2$, G138 in $\alpha 5$ and G196 in J78 in the BG indicate close conformation of the BG with the C-tail [110]. When we checked these interactions for all water systems, we observed transient interactions (short-lived) with the C-tail residues and the BG residues (G138 in $\alpha 5$ and/or G196 in J78). We also examined the adjacent residues of G94, G138 and G196 to check the possibility to

shift the interactions. In the adjacent residues we detected persistent and/or transient (short-lived) interactions with the C-tail, but the C-tails did not fully cover the BG (Figure 5.6). Instead, the C-tail interacts with outer side residues in the BG or approaches to the bottom side of the BG. Additionally, in DM1 simulations, the C-tail mostly interacts more with the loop than with the BG. We suggest that these interactions could be an indicator of a C-tail approach to the BG (not only on the inner side but also on outer residues of the BG). This may cause/trigger the pseudo-inhibitor activity in water by inhibiting/preventing the binding affinity of pro-apoptotics and BOPs.

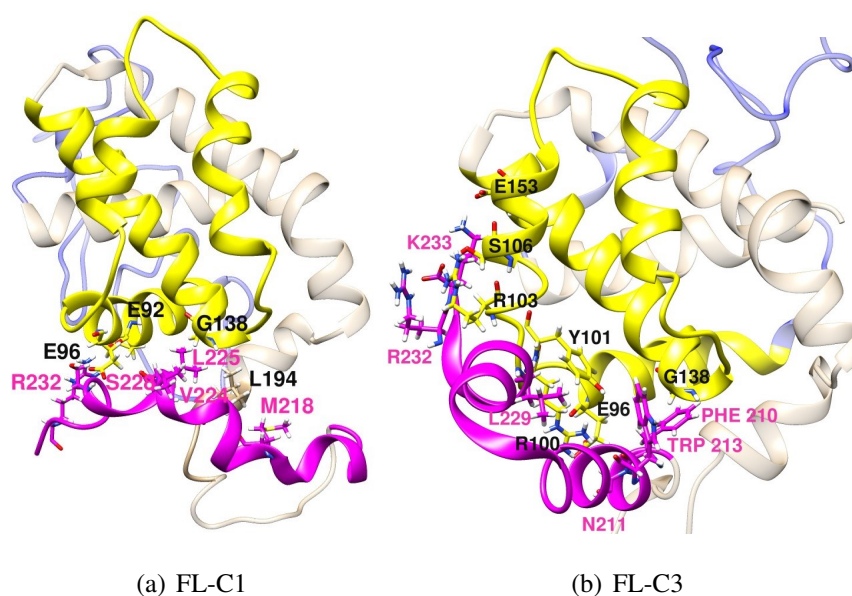


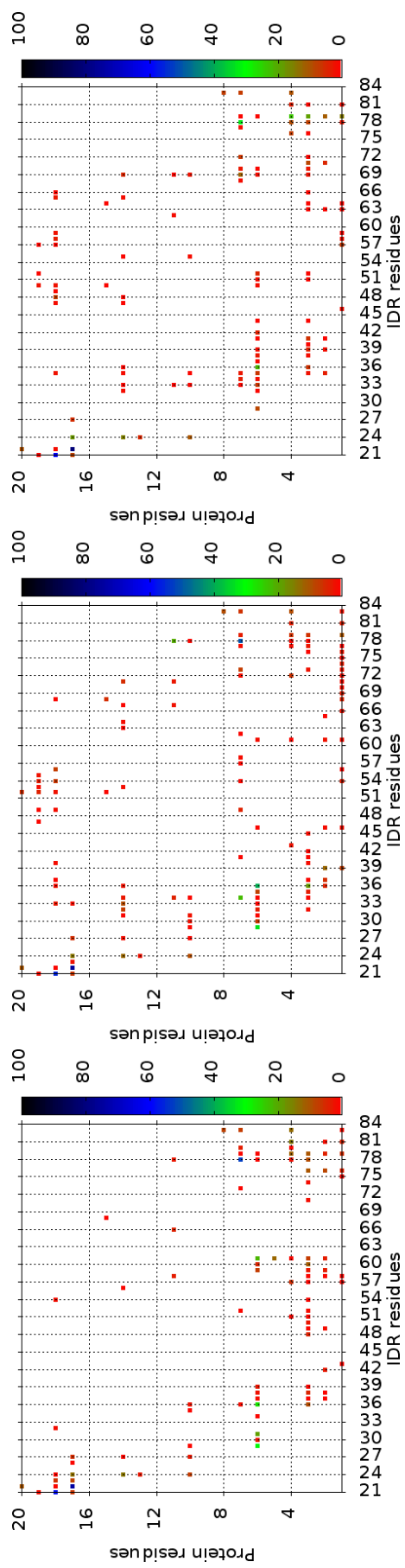
Figure 5.6. Representative orientations of the BG and the C-tail residues in water. (Blue color denotes loop region (IDR). Magenta and yellow colors present the C-tail and the BG, respectively.)

5.3.3.1. Intrinsically Disordered Region (IDR, loop). The loop behavior was also investigated throughout the simulations. The initial extended structure of the loop was not preserved during the simulations. In water systems, the loop transiently interacts with the protein core (protein excluding the loop and the C-tail) and the C-tail. In general, the loop approaches $\alpha 1$, $\alpha 2$, $\alpha 6$, $\alpha 7$, and J89. H-bond interactions between protein (Δ IDR)-IDR in Figures 5.7 and 5.8 showed the transient interaction between the IDR and protein and depicted that deamidation altered the interaction pattern between protein and the IDR and conformational

behavior of the IDR. Remarkably, the C-tail of Bcl-x_L interacted less with the IDR compared to the deamidated ones (Figure 5.8). Deamidated IDR transiently interact with the C-tail. In deamidated systems, the increase in negative charge residues in the IDR could facilitate the C-tail-loop interaction and mediate the position of the C-tail (residues 210-233). These observations suggest that the differences in the C-tail and the loop movements can affect membrane localization behavior/affinity and can alter the accessibility of the BG for pro-apoptotic proteins or BOPs.

Additionally, in the FL simulation, N52 and N66 did not interact with the C-tail residues, both D52 and D66 in DM1 and only iso-D66 in DM2 interact with the C-tail (Figure 5.8). R232 and R209 transiently interacted with D52 and D66 in DM1. In DM2 simulations, isoD66-R232 and isoD66-K233 transient interactions were detected. This could indicate that deamidation may invoke loop-C-tail interactions.

Notably, transient D52-R102 interaction in the DM1 simulation urged us to re-visit the experimental work of Follis et al [106]. They displayed that negatively charged residues (D61, E62, D52 and D66) interacted with positively charged arginines (R100, R102, R103; known as Arg cluster.) in junction 23 connecting $\alpha 2$ and $\alpha 3$ (J23). In order to follow this interaction, radial distribution functions (RDF) were computed between side chain oxygen atoms of residues 52 and 66 and the hydrogen atoms of the guanidinium moieties in the Arg cluster (Figure 5.9) both in water and membrane systems. This interaction was only detected in DM1-C3 in water in the range of 1.0-3.0 Å. Through the distance analysis the frequency of this interaction was also followed (Figure 5.10) and approximately after 1.5 μ s transient but consistently re-occurring R102-D52 interaction was inspected on DM1-C3.



(a) FL

(b) DM1

(c) DM2

Figure 5.7. H-bond interactions plots for $\alpha 1$ residues of the protein-IDR residues of FL, DM1, and DM2. The color bar shows overall contact percentage during the simulations.

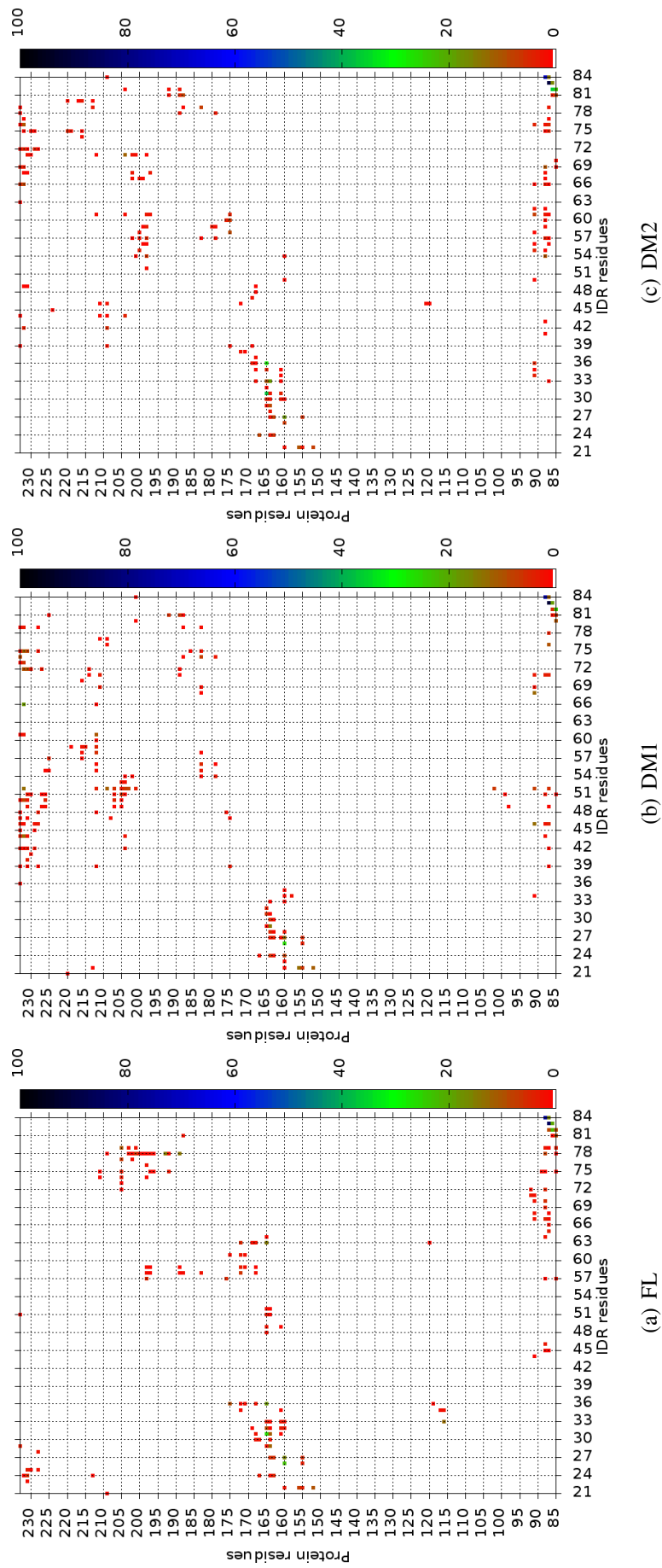


Figure 5.8. H-bond interactions plots for the protein (α 2-C-terminal residues)-IDR residues of FL, DMI, and DM2 simulations. The color bar shows overall contact percentage during the simulations.

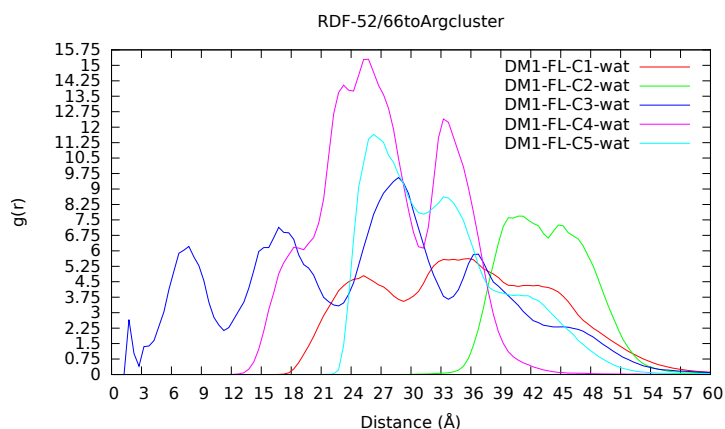


Figure 5.9. Radial distribution function, $g(r)$, vs the distance between side chain oxygen atoms of residues 52 and 66 and H atoms of the guanidinium moieties in Arg cluster in DM1-wat simulations.

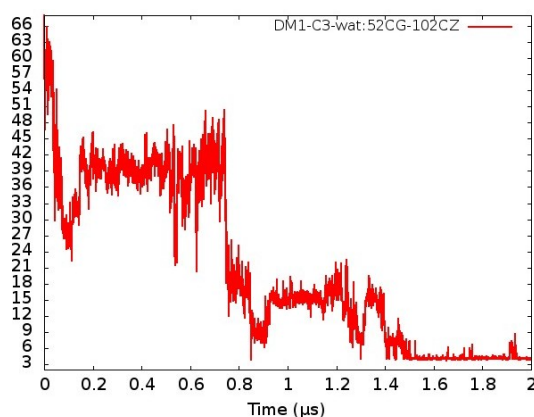


Figure 5.10. Distance plot between Asn52@CG and CZ atoms of guanidinium moieties of R102 in the simulation of DM1-C3) in water (Every 15 frames).

5.3.3.2. Deamidation Impact on the Binding Groove (BG). Impact of deamidation on the BG were examined more closely through the H-bond analysis in order to detect key H-bond interactions before and after deamidation. Remarkably, R103-Q111 (42.9 % in DM2-C2 and 25.6 % in DM2-C5) and R103-E129 (21.6 % in DM2-C2) were detected in two out of five iso-Asp mutated (DM2-wat) simulations. These interactions cover the top side of the BG. Distance analysis in Figure 5.11 also showed that while R103@CZ-Q111@CD interaction was seen in DM2-wat, this interaction was not available in FL-wat simulations. Additionally, in the models bearing the C1 tail, particularly (FL-C1 and DM1-C1) R103-D133 (43.7% -

25.2%) and R103-E129 (30.6% - 15.8%) interactions were detected. However, the R103-D133 and R103-E129 interactions decreased half-fold in DM1-C1. Transient (short-lived) R103-D133 interactions were observed in DM2 (three out of five) as well.

Taken together, considerable/subtle differences were observed in the behavior of the IDR and the C-tail upon deamidation. The BG is not fully closed by the C-tail. Instead, the dynamic C-tail approaches the bottom and side of the BG. Intriguingly, the C-tail mostly prefers to interact with the IDR in DM1 simulations. In general, R103 interactions with Q111 and D129 in the binding groove are key interactions as particularly detected in DM2 simulations. Conformational changes upon deamidation will be further investigated by means of PCA in the following section.

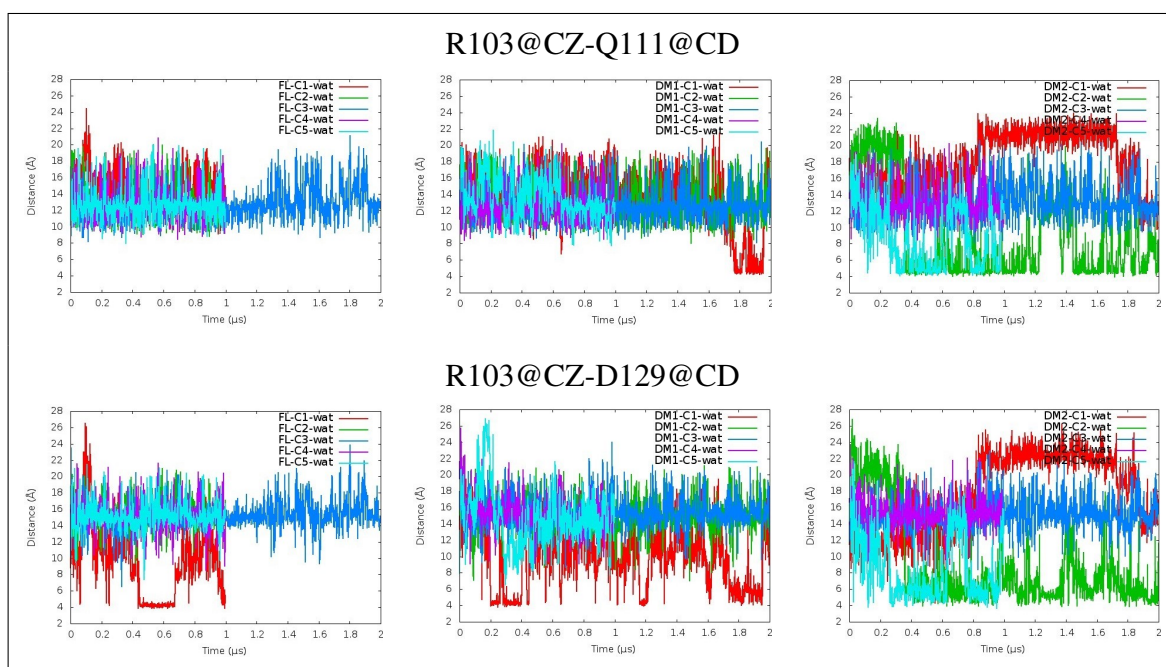


Figure 5.11. Distance evolution plots for key H-bonded residues in the BG of FL-wat, DM1-wat and DM2-wat in water (Every 30 frames).

5.3.4. Bcl-x_L and Deamidated Bcl-x_L in Membrane

Membrane insertion related conformational changes in protein and protein-membrane interactions (PMI) are important in order to fully understand the structure and function re-

lationship of Bcl-x_L upon deamidation. As discussed earlier, deamidation and membrane mediated impacts on the protein head still remain unclear. In this section, we focused to detect the deamidation-induced conformational changes on the protein, particularly the BG. Since previous studies showed that the C-tail forms an α -helix inside the membrane, Bcl-x_L with three helical models (C1-C3) were investigated in this section [94, 96, 110].

In line with the experimental study of Yao et al [94, 110], the head of Bcl-x_L preserved its fold during the simulations. The head of deamidated systems also maintained their folds. In addition, we also examined the possible behavior of the membrane-inserted non-canonical model of Bcl-x_L suggested by Vasquez-Montes et al [169, 170]. In all simulations α 6 did not enter the membrane while α 1 stayed intact with the protein head.

5.3.4.1. Structural Behavior and Interactions of the C-tail in Membrane. As mentioned, Bcl-x_L anchors to the membrane through its C-tail. After association of the C-tails of Bcl-x_L and deamidated Bcl-x_L to the POPC membrane, we observed that all C-tails stayed/remained inside the membrane during the simulations. The tails have smoother/ordered α -helices inside the membrane through interaction with POPC side chains. N-terminal (N211, R212, W213: upper leaflet) and C-terminal (S231, R232, and K233: lower leaflet) tail residues also transiently and/or persistently interact with the phosphatidylcholine head (PC head) during the simulations. These interactions/residues confirm that the C-tails stay inside the membrane and help to sustain the secondary structure by stabilizing the C-tail helices in the membrane in good agreement with the computational study of Maity et al [168]. Additionally, R232 and K233 also protrude from the membrane in most of the simulations (Figure 5.12).

The tilt angle of the C-tail is also one of the important factors that affect the protein's position and movement above the membrane. Tilt angle calculations of Yao et al. [110] and Ryzhov et al. [171] displayed that the C-tail helix (α 9) spanning 213-233 and 207-230 (after 1 μ s MD simulations) tilted approximately by 25° to 36° relative to the membrane, respectively. The C-tails before and after deamidation were inspected through the simulations in order to detect helix tilt in the lipid bilayer/membrane (Figure 5.13). In general, average tilt angle is 21° and the C-tail helix spans around residues 210-231. DM1 models are slightly

more tilted compared to the FL and DM2 simulations/models.

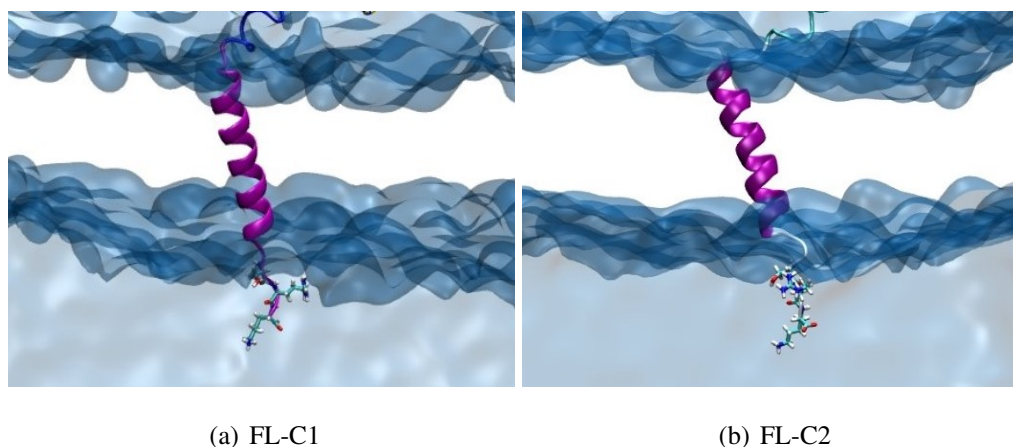


Figure 5.12. The representative snapshots of membrane-embedded C-tails and its water interactions. (POPC bilayer was not shown for clarity. Snapshots taken at 1.5 μs . The water surface was generated using the VMD quicksurf presentation.)

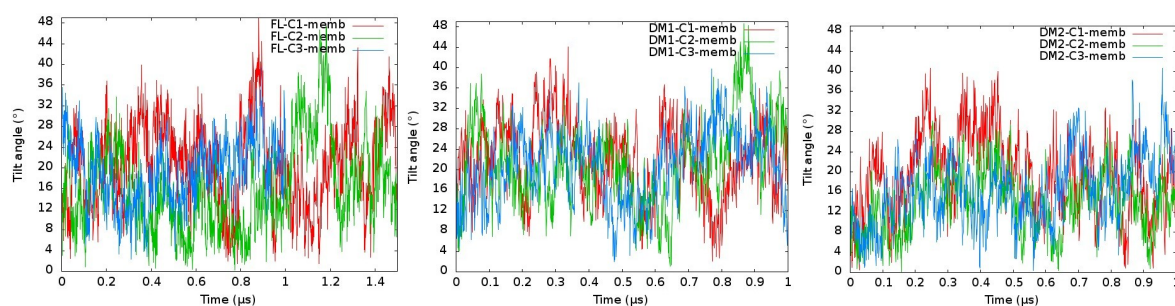


Figure 5.13. The tilt angle evolution plots for the C-tails of FL, DM1, and DM2 simulations with respect to the membrane plane simulations in membrane during simulations (Every 5 frame).

More importantly, the junction 89 connecting $\alpha 8$ and $\alpha 9$ (J89) facilitates the flexible orientation/movement of the protein head during the simulations in line with the experimental results of Ryzhov et al., which observed higher NMR peak intensity at residues 199-205 [171]. The flexibility of J89 triggers the protein head to lean towards the membrane leading to interactions with phosphatidylcholine heads (PC head).

5.3.4.2. Intrinsically Disordered Region (IDR). The role of the IDR in the loss of apoptotic function of Bcl-x_L was investigated in membrane systems. Membrane association of the C-tails resulted in a limited movement of the IDR towards the protein head due to the orientation of the BG towards membrane. The IDR above the membrane has less accessible area to move compared to the water systems. The IDRs approach the side of $\alpha 6$ (right side) and $\alpha 8$ due to the lean/approach of BG from $\alpha 3$ and J23 sides to the membrane. Direction of the IDR mostly shifted to $\alpha 1$, $\alpha 6$ - $\alpha 8$, and J67. Figures 5.14 and 5.8 illustrated that interaction pattern was changed upon deamidation. Notably, deamidated systems transiently interact with the residues in J89. However, no IDR-J89 interaction was observed in Bcl-x_L (Figure 5.8). Furthermore, the IDR also transiently interacts with PC head of the POPC membrane. Remarkably, the deamidated IDR interacts with the PC heads more than Bcl-x_L. The increase in negative charge affects membrane interactions and in turn the BG movement.

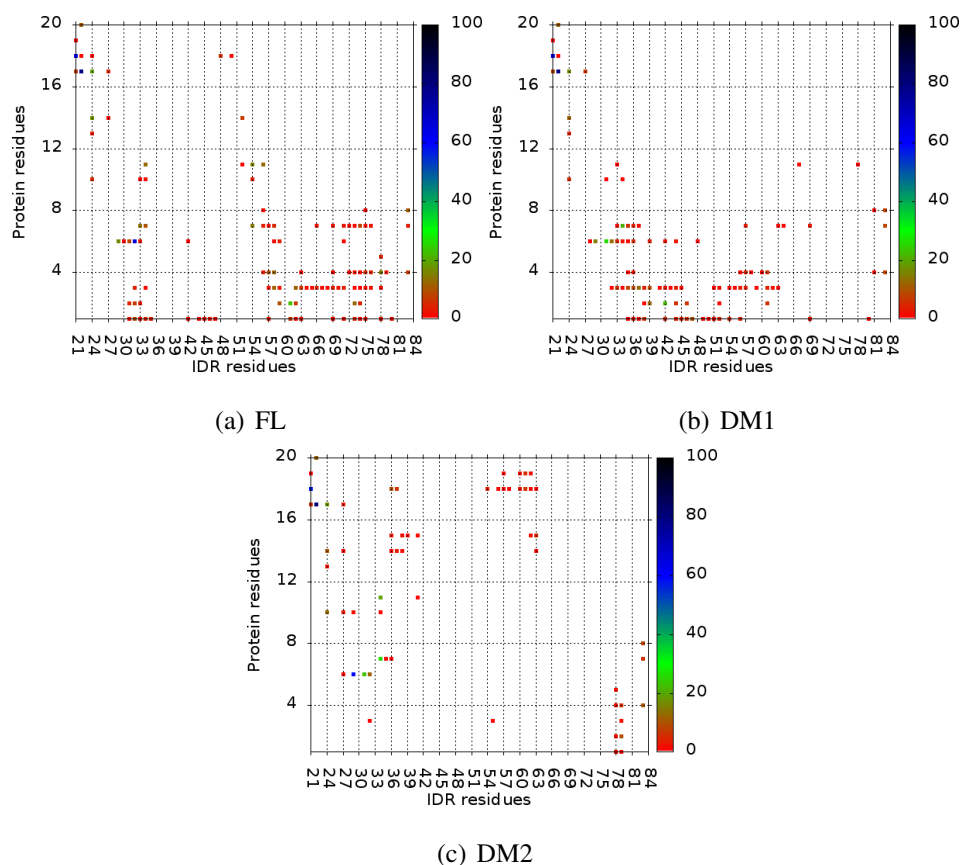


Figure 5.14. H-bond interactions plots for $\alpha 1$ residues of the protein-IDR residues of FL, DM1, and DM2 in membrane. The color bar shows overall contact percentage during the simulations.

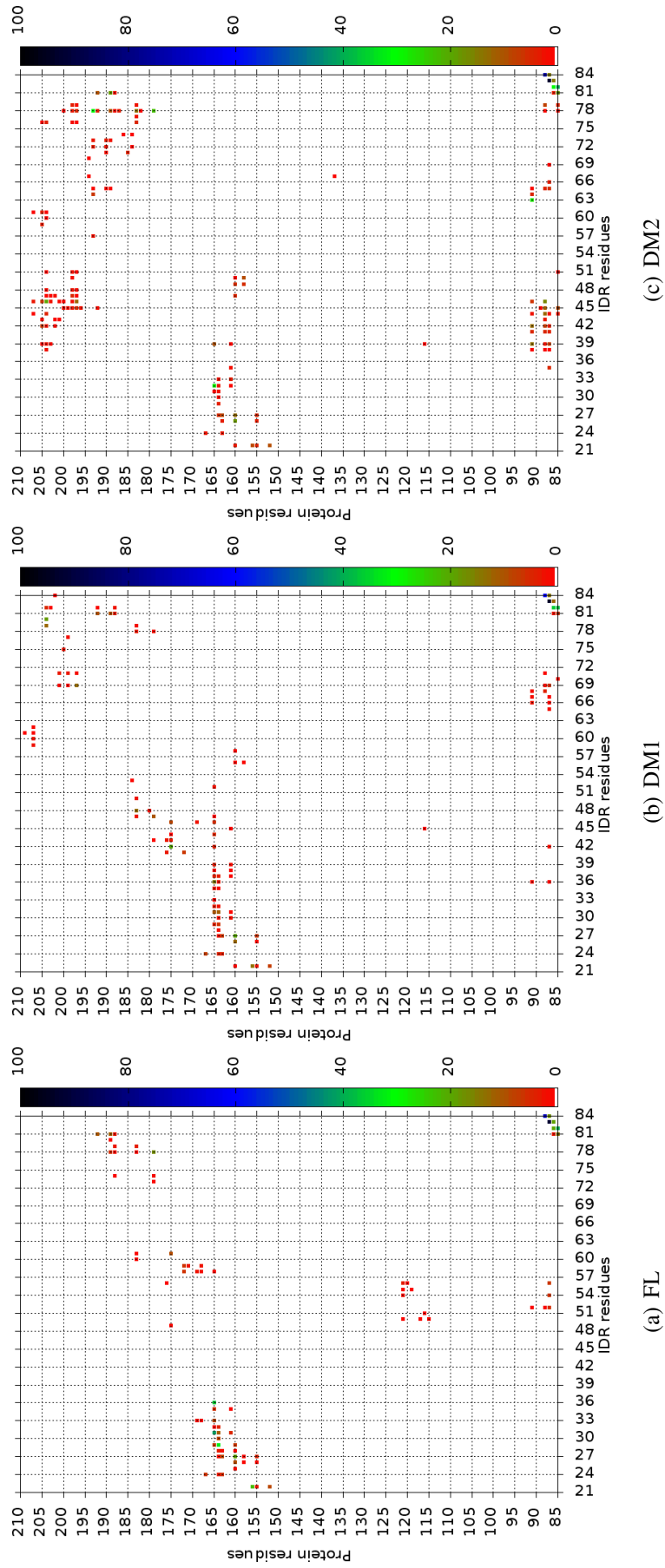


Figure 5.15. H-bond interactions plots for the protein (α 2-C-terminal residues)-IDR residues of FL, DM1, and DM2 simulations. The color bar shows overall contact percentage during the simulations in membrane.

5.3.4.3. Deamidation Impact on the Binding Groove (BG). Influence of the IDR and the membrane insertion on the binding groove were also scrutinized in order to understand their potential roles on the BG. Previously, in the experimental study of Raltchev et al. they reported that the binding groove is in close proximity to the membrane suggesting that the BG loosely interacts with the membrane and awaits binding partners [96]. In line with the experimental studies, [94, 96, 110] we also observed that the BG loosely interacts with the membrane and mostly stays open. The protein head, particularly the BG is highly dynamic during the simulations. Initially the BG is perpendicular to the membrane, and the BG is open (Figure 5.16). After a short while the BG specifically leans towards the membrane from $\alpha 2$, $\alpha 3$, and J23 sites in most of the simulations (Figure 5.17). Transient interactions of the BG, particularly J23, $\alpha 2$, and $\alpha 3$ with the PC polar heads of the membrane were detected (Figures 5.17 and 5.18). Ryzhov also confirmed the BG and lipids interaction and observed mostly $\alpha 2$ - $\alpha 4$ reflecting the BG is less in contact with the cytosol [171]. We also observed short-lived interactions between the bottom side of the BG ($\alpha 2$ - $\alpha 4$) and the PC head in Bcl-x_L (FL) simulations. During the simulations the bottom of the BG closes too much to the membrane from time to time by preventing the possible bindings partners, namely proapoptotic proteins and BOPs, particularly in Bcl-x_L simulations. Intriguingly, unlike the BG of Bcl-x_L, the BG in DM1 simulations moves above the membrane and minimally/rarely gets contact with the membrane. Due to the increase in negative charge in the IDR, in two out of three DM1 simulations the IDR interacts with the membrane and may push up the BG above (Figure 5.18). The fact that the BG has less contact with the membrane may contribute the change in the BG-BG residue interactions.

Remarkably, transient J23 residues (R100-R103)-C-tail interactions in Bcl-x_L are considerably higher than the deamidated ones. H-bond interactions among the J23 residues, particularly the Arg cluster (R100, R102, and R103) and the PC heads reach a maximum, up to 38.7 %. In deamidated simulations Arg cluster tends to interact with $\alpha 3$, $\alpha 4$, and J45 in order to narrow the BG instead of interacting with the membrane. This outcome suggests that the PC head interactions with the Arg cluster could prevent the narrowing of the BG and render the BG open.

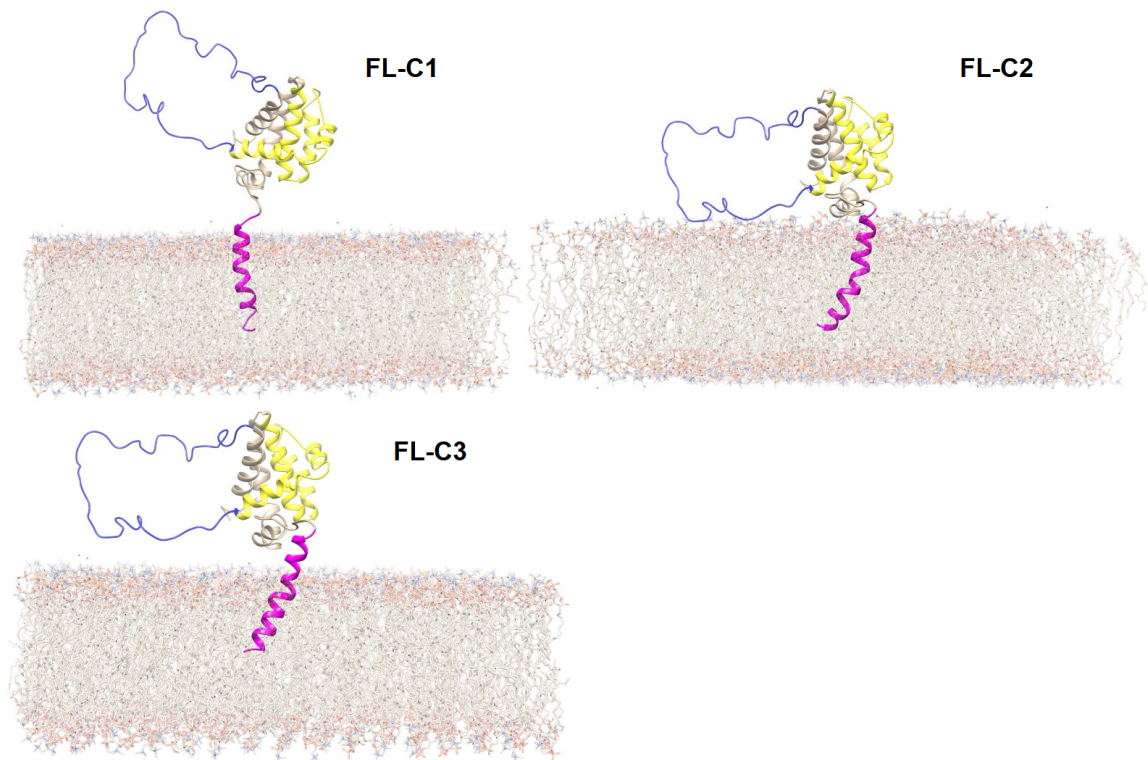


Figure 5.16. Initial structures of FL models in membrane. (Blue color denotes the IDR. Magenta and yellow colors present the C-tail and the BG, respectively. Water was not shown for clarity.)

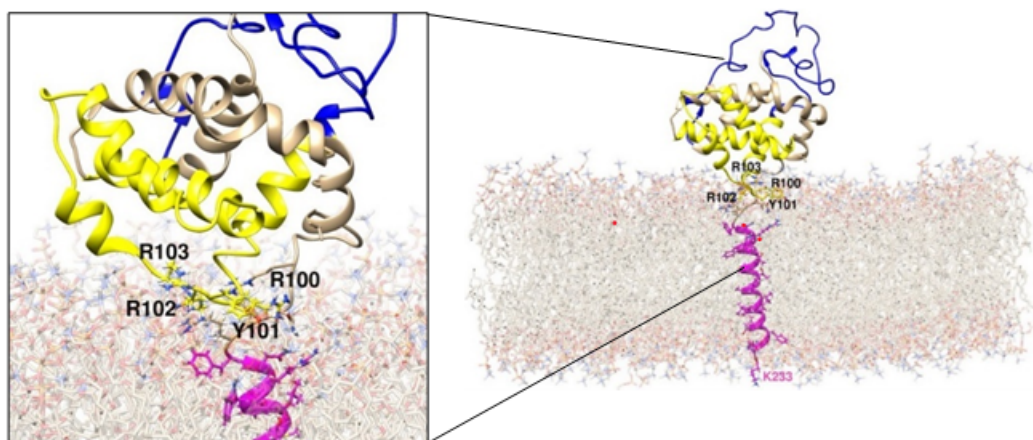


Figure 5.17. Representative orientation of the BG of FL-C3 toward the membrane.

Key H-bond interactions in the BG were also detected and followed during the simulations (Figure 5.19). Remarkably, in all simulations of DM1s on membrane, R103-D133 (in the range 27.4-55.8%), R103-E129 (in the range of 10.6-65.3 %) interactions were detected. Particularly, the R103-D133 interaction in DM1 contributes to the narrowing of the bottom

side of the binding groove. Distance analysis also depicted larger R102-D133 distances in Bcl-x_L (2 out of 5) and DM2 compared to DM1 simulations (Figure 5.19). Taken together, R103-D133 and R103-E129 are the key interactions, leading to the narrowing and the covering of the BG. These outcomes also stress that deamidation in the IDR allosterically affect the BG groove and alters the interaction pattern. Consequently, it may impair its function.

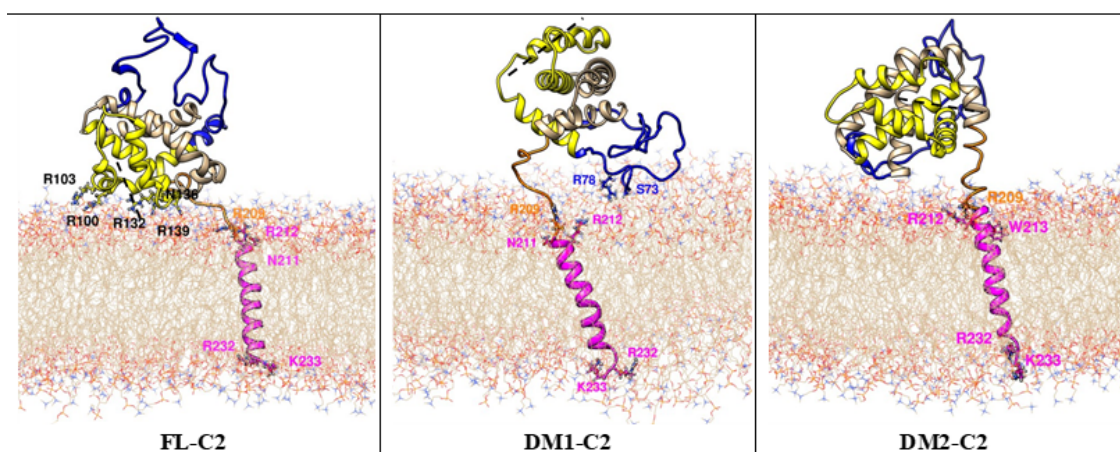


Figure 5.18. Representative protein head-membrane interactions in the simulations. (Blue color denotes the IDR and orange for J89. Magenta and yellow colors present C-tail and the BG, respectively. The black dashed line presents the position of the BG.)

Radius of gyration (R_g) analysis was also performed to further monitor time evolution of the narrowing of the bottom side of the BG using the backbone atoms of J23 and J45 residues during the simulations. Figure 5.20 shows that FL-memb R_g's generally fluctuate in the range of 6.0-11.5 Å. Compared to FL-memb, the R_g seems to reach a stable trend in DM1-memb and DM2-memb. In DM1 simulations, the R_g is lower compared with the others indicating a narrowing of J23 and J45. The R_g's of the DM2 simulations are also slightly lower (in general range of 5.5-10.0 Å) than with Bcl-x_L. The R_g outcomes also confirm the allosteric effect of deamidation.

In 2017, Priya et al claimed that R103 and R139 cover the bottom part of the BG by behaving like a gate [138]. In our study, we suggest that R103 interactions play major role to cover the inner side of the BG, especially for the deamidated systems. Taken together,

deamidation in IDR indicates that R103-D133, R103-E129 and R103-Q111 interactions collectively provide/contribute closure and narrowing of the BG in membrane systems. These results may also indicate that deamidation in membrane environment allosterically affects the BG of Bcl-x_L in terms of the change in the interaction pattern (i.e., protein-membrane interactions and the IDR interaction) and narrowing of the BG. Notably, compared to the water environment, Bcl-x_L shows crucial differences in the BG upon deamidation. This could indicate that the increase in negative charges in the IDR and membrane association collectively impacts on the structure of the protein.

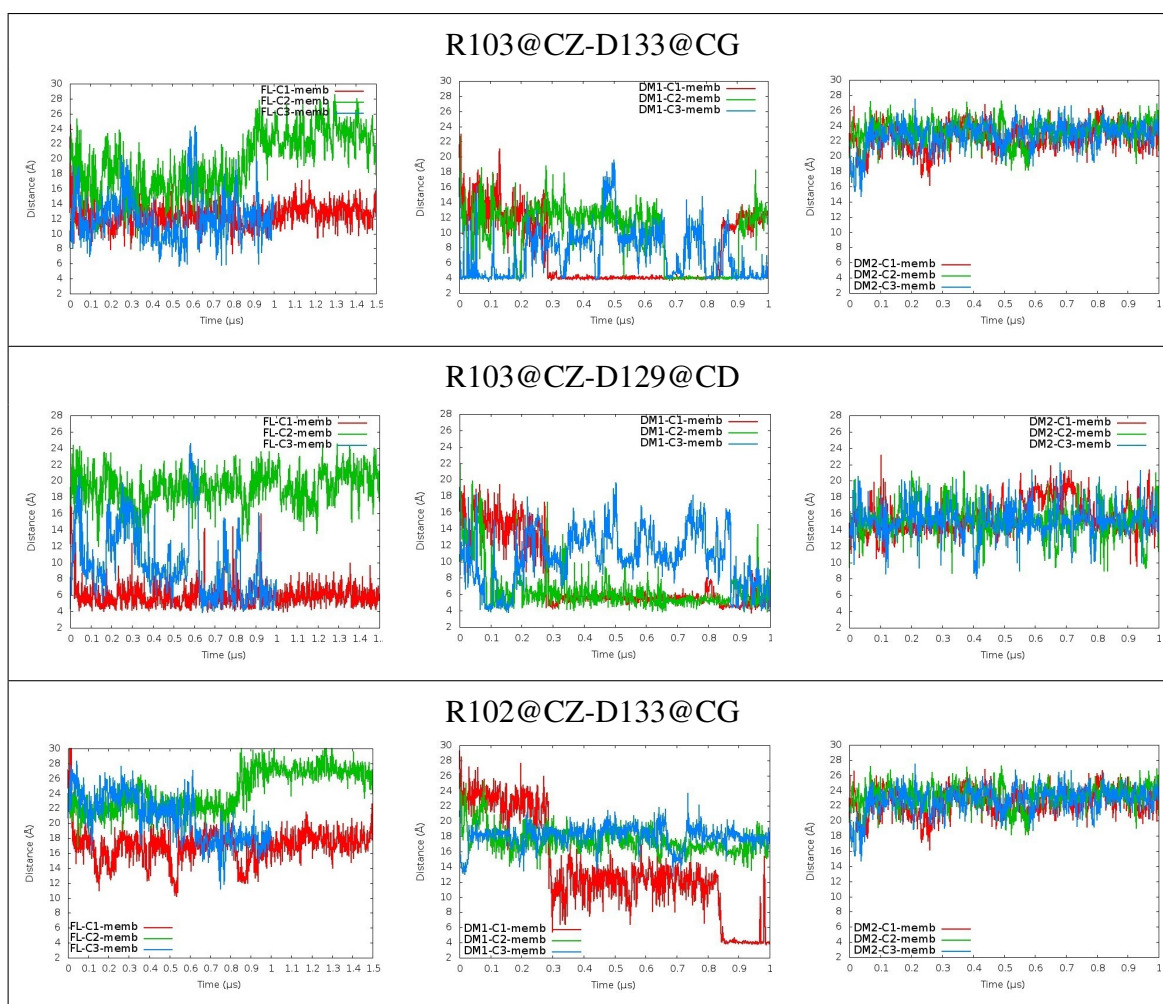


Figure 5.19. Distance evolution plots for key H-bonded residues in the BG of FL-memb, DM1-memb and DM2-memb in membrane (Every 30 frames).

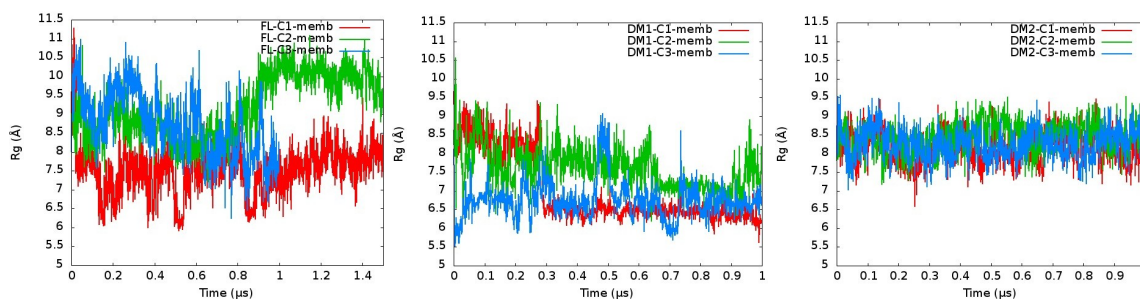


Figure 5.20. Rg as a function of time for the backbone atoms of J23 and J45 of FL, DM1 and DM2 simulations in membrane (Every 20 frames).

Overall, the BG is mostly oriented towards the membrane from the $\alpha 3$ and J23 sites, but in DM1 simulations it is oriented to the opposite direction and is in less contact with the membrane. The Arginine cluster in J23, particularly R103 interactions, plays an essential role on the narrowing of the BG. During DM1 simulations, the narrowing of the bottom side of the BG was observed and these results suggest that deamidation allosterically affects the BG and this may imply the loss of Bcl-x_L function upon deamidation.

5.3.5. Principal Components Analysis (PCA)

The essential dynamics and the dominant motions of the BG in the water and in membrane systems were scrutinized using principle component analysis (PCA) in order to get insights into the structural/conformational differences in both environments [26]. Basically, PCA converts cartesian coordinates into dominant motions. The changes in their conformations and the dominant motions of Bcl-x_L prior to and subsequent to deamidation were investigated by examining the overlaps of the distributions. PCA was comparatively investigated in three groups by combining all independent simulations (24 in total (15 in water and 9 in membrane systems)). The combined 24 independent simulations were separately projected for each system (WT, DM1 and DM2 in water and membrane). Since approximately 80 % of the cumulative variance was reached by the first four PCs, only the first four PCs were depicted herein (Figure 5.21).

PC scatter plots in Figure 5.22 illustrate that the water and membrane models overlap less with each other and cover different conformational spaces. This outcome indicates that

the simulation environment considerably affects the essential dynamics, which results in dissimilar motions and conformational differences. Moreover, the findings also indicate that the conformational transitions from water to the membrane environment. In addition, DM2-wat explores/scans larger area than DM2-memb. Conformational distributions in membrane environment are considerably reduced in DM2-memb implying a rigidity and less flexibility of the iso-Asp deamidated Bcl-x_L in membrane.

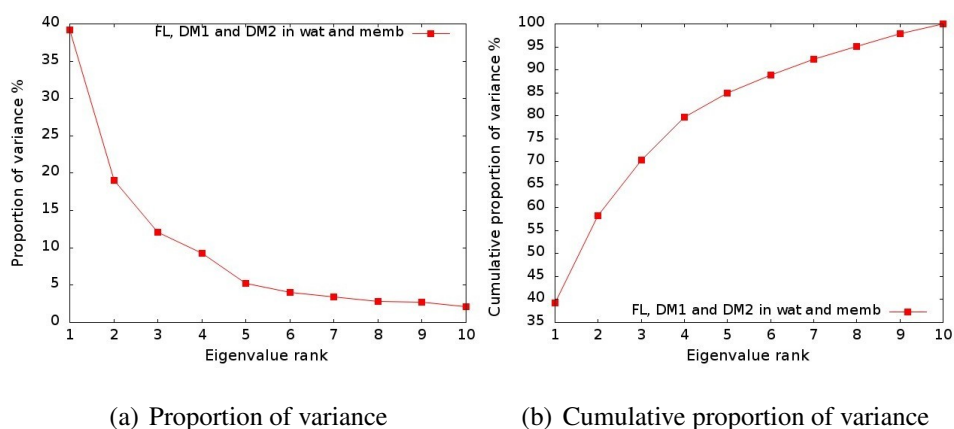


Figure 5.21. a) Proportion of variance b) Cumulative sum of total variance captured by the first 10 PCs for the combined clusters (FL, DM1, and DM2).

In water, deamidated and FL simulations display notable differences (Figure 5.23). Deamidated proteins explore larger and distinct areas than FL-wat. Particularly, DM2-wat simulations scan considerably different and larger areas indicating considerable changes in conformations and overall motions. In membrane, larger differences were observed between Bcl-x_L and deamidated Bcl-x_L systems. FL-memb, DM1-memb, and DM2-memb explore distinct areas and the deamidated systems are less flexible and overlap less compared to FL-memb (Figure 5.23). FL-memb scans larger conformational area/distributions. Deamidated systems cover limited areas, particularly D2-memb, which indicate a less flexible BG. These findings suggest that deamidation and membrane integration allosterically effects the dynamics of the BG leading to conformational differences. Moreover, the essential dynamics of the systems are also environment dependent and show different behaviors.

Taken together, considerable differences in PC distributions between water and membrane environments highlight the structural differences upon membrane integration.

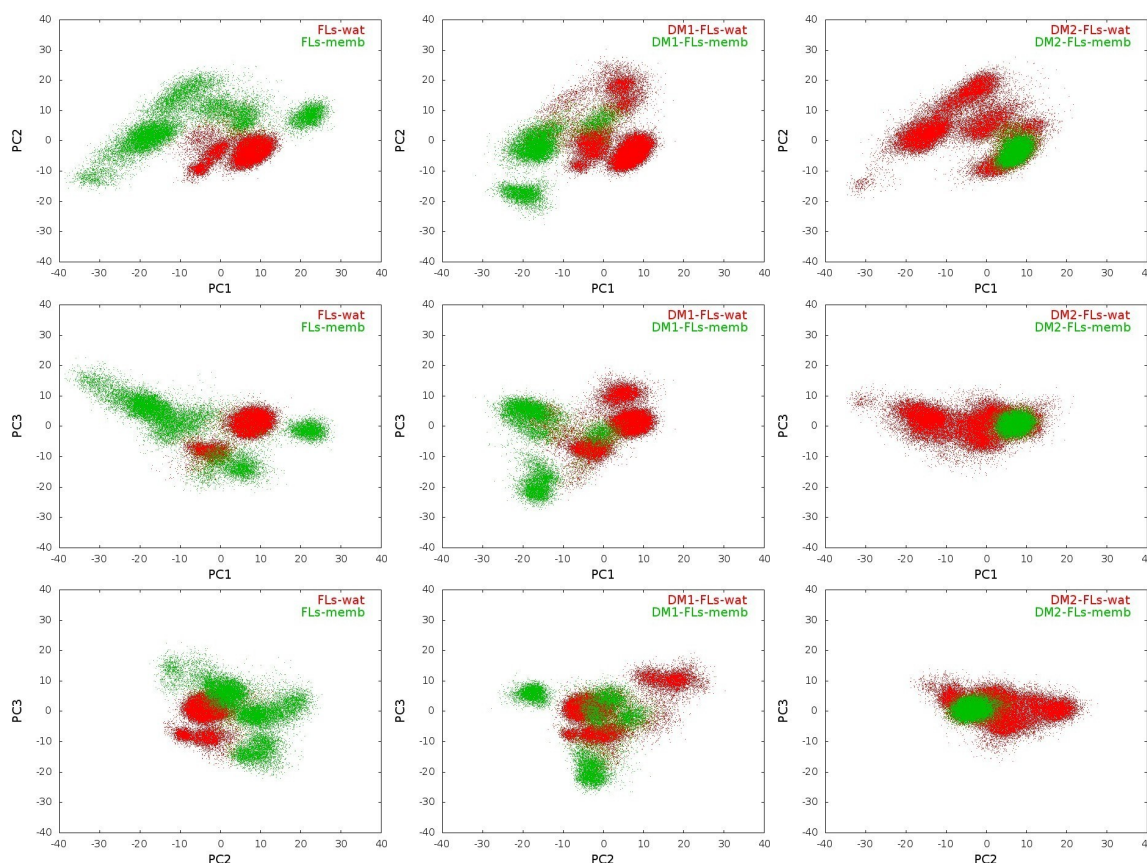


Figure 5.22. PC scatter plots for top three PC modes of all MD runs onto all MD runs.

(Every 5 points were plotted.)

5.4. Conclusions

In recent years full-length Bcl-x_L was experimentally evaluated but structural understanding of full-length Bcl-x_L before and after deamidation in the membrane has been missing. In this study, the conformational/structural role of deamidation on the tertiary structure of membrane-anchored Bcl-x_L was deciphered using MD simulations by considering systems both in water and in membrane environments. We mainly focused on the conformational changes and essential dynamics of Bcl-x_L upon membrane insertion and deamidation. While the C-tail is more flexible as expected in water and interacts with the head of the protein, it is more stable in membrane through the interaction with the lipids. In membrane, the C-tails were tilted to the membrane normal and $\alpha 2$, $\alpha 3$, and J23 in the BG were oriented towards the membrane while the BG interacted loosely with membrane.

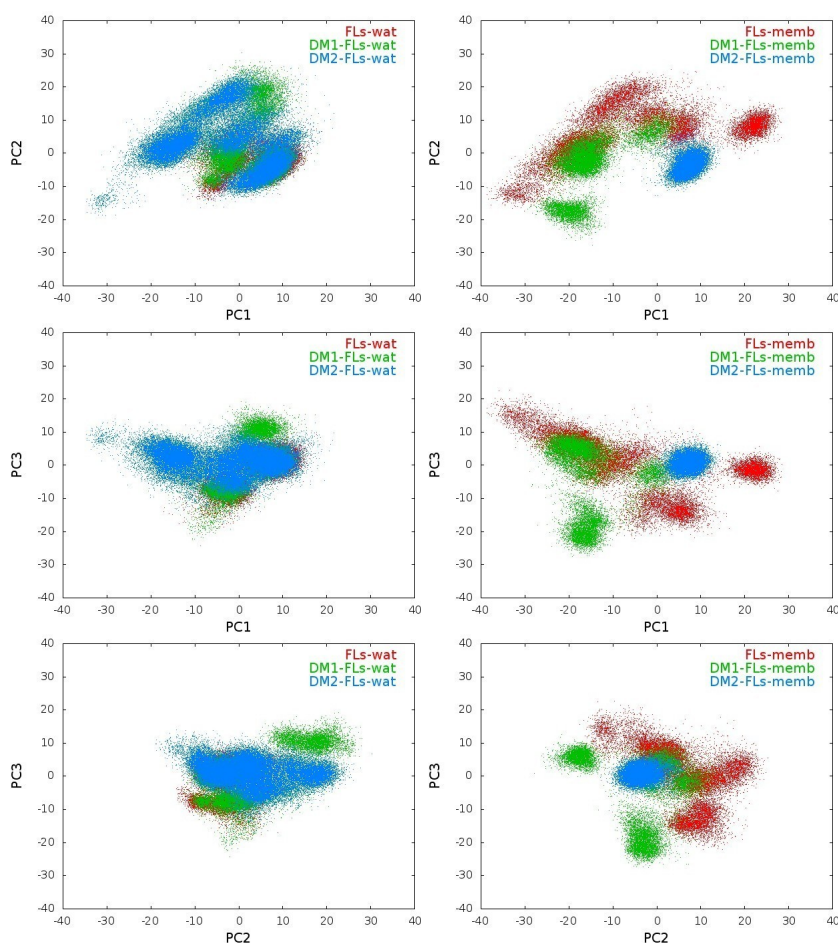


Figure 5.23. PC scatter plots for top three PC modes of water (left) and membrane systems (right) onto all MD runs. (Every 5 points were plotted.)

Remarkably, asparagine deamidation to aspartate/iso-aspartate in membrane systems seems to allosterically trigger the changes in the binding groove. PCA illustrated the conformational transitions between water and membrane systems. PCA suggests that the simulation environment considerably affects the essential dynamics implying conformational differences. Our findings suggest that interaction pattern change, flexibility of the J89, protein orientation towards membrane and protein-membrane interaction play a pivotal role on the structural differences of the protein upon deamidation. Furthermore, the pivotal differences could be collective/cooperative consequences of membrane association and deamidation. In other words, allosteric effect could arise from both deamidation in the IDR and in the membrane environment. In addition, unlike the outcome of Vasquez-Montes et al., we did not observe Bcl-x_L refolding and the release of BH4 domain in membrane during the simulations. Analysis of this study is still in progress. Initial results were shared herein. We

have planned to perform further analysis for further rationalization and clarification of the computational findings. We believe that this study will provide a valuable contribution with potential implications towards developing anticancer therapeutics by presenting insights into the consequences of deamidation on the structure and function of Bcl-x_L. Further studies will focus on understanding complex systems (Bcl-x_L + BOPs/pro-apoptotics) in order to provide comprehensive insight and full perspective on the impact of Bcl-x_L deamidation.

6. INVESTIGATION of Bcl-x_L-BH3-only PEPTIDE COMPLEX

6.1. Introduction

BH3-only proteins (BOPs) are divided into two groups, namely activator and sensitizer (Figure 6.1). Andrews and coworkers described BOPs as orchestrators of apoptosis in their review. [156] While activator BH3-only proteins (BIM, BID and PUMA) directly induce apoptosis, sensitizers (BAD, NOXA, etc.) indirectly induce cell death. BOPs only consist of a BH3 domain and this domain plays a pivotal role for their interactions with the BCL2 family proteins and for the regulation of MOMP. Since full-length of BH3-only proteins are not available except BID, BH3 peptides derived from each of the BH3-only proteins were used in the literature. Literature results showed that BH3 peptides mimic the corresponding full length protein and induce BAX and BAK oligomerization and MOMP [64, 153, 180]. BH3 domains of activator BH3-only proteins/peptides interact with the binding groove of Bcl-x_L and lose their functions. In addition, they directly promote MOMP by activating Bak and Bax. [181] As mentioned in the previous chapter, the binding groove of Bcl-x_L accommodates BH3-only peptides. Rajan et al reported crystal structures of Bcl-x_L in complex with BID and BIM peptides (4QVE and 4QVF, respectively) and showed that BH3-only peptides bind the binding groove of Bcl-x_L and formed alpha helical conformations. Furthermore, owing to their sequence variations of the peptides, different interaction modes and conformational changes were observed [149]. Additionally, Bcl-x_L is a potential target for Bcl-x_L inhibitors design, known as BH3-mimetics. For instance, Navitoclax targeting BCL-2, Bcl-W and Bcl-x_L and Venetoclax (Venclexta and Venclyxto) for BCL-2 are already in the market [182].

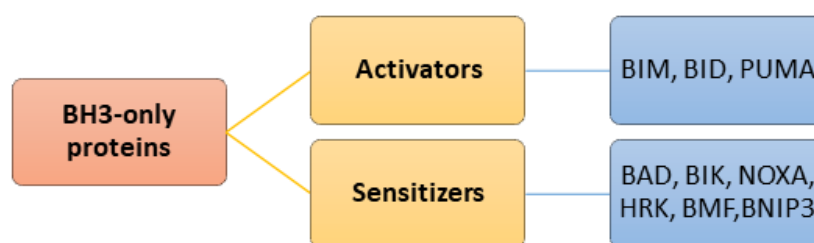


Figure 6.1. The BOP family.

In 2013, Maity et al. investigated dynamics of Bcl-x_L (PDB ID: 1BXL_{NMR}, Δ45-84) in water and the pre-equilibrated DOPC membrane by means of MD simulations (1.6 μs in total) [99]. Simulation results showed that the C-tail covered the binding groove in water after 60 ns of simulation. When BAK peptide was also included in the water system, the C-tail was displaced with BH3-only peptide. In membrane, BAK reduced its binding affinity due to conformational changes in the binding groove. Contrary to Maity et al, In 2015 Yao et al showed that membrane-anchored Bcl-x_L has a higher affinity to the BID peptide when compared to Bcl-x_L in water [110]. Due to the competition between the C-tail and the BID peptide in water, the C-tail behaved as a pseudo-inhibitor by binding to the binding groove of Bcl-x_L and showed cytoprotective activity. Moreover, Pécot et al. [183] reported that the BH3 binding affinity of membrane-associated Bcl-x_L was enhanced compared to its counterpart in water since there was no competition between C-tail of membrane-anchored Bcl-x_L and the BH3 peptides to interact with the binding groove of Bcl-x_L. There is an obvious contradiction between the results of Maity et al., Yao et al., and Pécot et al. in the binding affinity of the peptide to the membrane-bound Bcl-x_L. The reason for the contradiction could be that Maity et al. used modified Bcl-x_L structure, which lacks a real C-tail. The C-tail they use in their study is histidine tagged in order to facilitate purification. In this context, further investigation is needed to clarify the reason of binding affinity variations when Bcl-x_L is bounded to the membrane. Additionally, in previous studies, the Bcl-x_L structures in complex systems did not include the IDR. Yet recent studies emphasized the importance of the IDR as mentioned in the previous chapter. For this reason, in order to give further insights on these complex systems, we considered the impact of the IDR on complex systems.

In this study, the structural behaviors of BH3-only peptide in water was investigated and compared with some complex systems. In the second part of the study, we focused on the Bcl-x_L-BIM peptide complex (PDB ID: 4QVF_{X-RAY}) and the Bcl-x_L-BID peptide complex (PDB ID: 4QVE_{X-RAY}). In this context, since Bcl-x_L in the experimental complexes does not have the IDR we modified the models to include the IDR. The IDR was extracted from a Bcl-x_L (PDB ID: 1LXL_{NMR}) structure and added to the complex models.

6.2. Methodology

Initial structures (4QVF, [149] 4QVE, [149] and 1LXL [2]) were provided from the Protein Data Bank (Homo sapiens). The Bcl-x_L ΔC+BIM peptide complex I and Bcl-x_L ΔC+*BID* peptide complex II systems were prepared as follows: 4QVF and 1LXL were used to prepare complex system I (Bcl-x_L ΔC+BIM peptide). To prepare the complex system II, 4QVE and 1LXL were used (Bcl-x_L ΔC+*BID* peptide). Missing residues and loop sections were provided from 1LXL. For proper addition of the residues, 1LXL were fitted and added to 4QVF and 4QVE using Profit (Version 3.1) [184] and the tleap module from Amber, respectively. All MD simulations were performed using the Amberff14SB [142] force field implemented in the Amber18 program package [141] and solvation was carried out using the TIP3P [143] explicit water model forming cubic boxes. Counter ions (sodium or chloride) were added into each system to neutralize charges. The same MD protocol as the one described in chapter 4 was used in this study.

6.3. Results and Discussion

First, we concentrated on the understanding of the structural behavior of the *BID* and *BIM* peptides in water (unbounded state). Then, initial analysis results of the complex systems (bounded state) were discussed herein. The studied systems were tabulated in Table 6.1. As mentioned above, our complex systems include Bcl-x_L with the IDR and a BH3-only peptide.

Table 6.1. Initial structure set up.

Initial Structure	Water	Na ⁺	Total atoms	Simulation time
BH3-only peptide (Simulation box = 74.505x74.505x74.505 Å ³)				
BIM	13372	2	40547	1 μs
BID	13403	2	40563	1 μs
Bcl-x _L -BH3-peptide complex (Simulation box = 111.757x111.757x111.757 Å ³)				
Bcl-x _L -BIM complex	44265	15	136360	1 μs
Bcl-x _L -BID complex	44234	15	136344	1 μs

6.3.1. Stability of BH3-only Peptides in Water

Figure 6.2 displays that BH3-only peptides show higher RMSD values indicating instability of the peptides in water. Additionally, secondary structure analysis results also displayed reduction of helix length (partial unfolding) (Figure 6.3). Literature data demonstrated that hydrophobic residues tend to cluster in order to minimize solvent exposure and this leads to the reduction of helix length and partial to complete loss of helical character [64, 185–187].

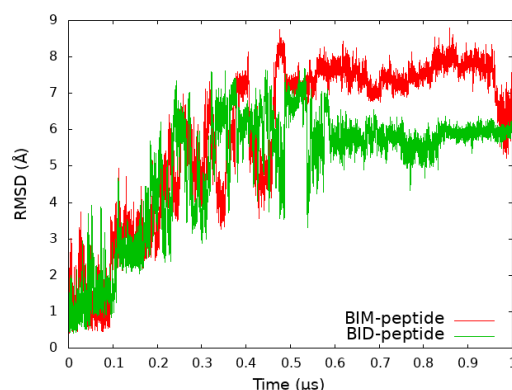


Figure 6.2. Backbone RMSD plot for BH3-only peptides with respect to X-Ray structures.

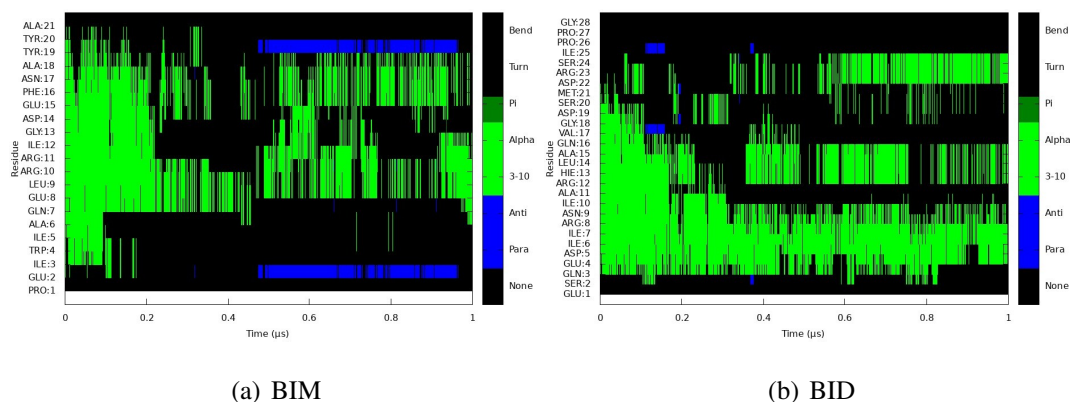


Figure 6.3. Secondary structure plots of a) BIM b) BID peptides.

6.3.2. Analysis of Complex Systems

As seen in Figure 6.4 when the BH3-only peptides binds to Bcl-x_L, they form helices. Figure 6.5 shows that the core helices are stable and that the loop regions display a higher

RMSD for complex systems. Secondary structure analysis in Figure 6.6 also demonstrates that the BH3 peptide is considerably stable in contact with Bcl-x_L.

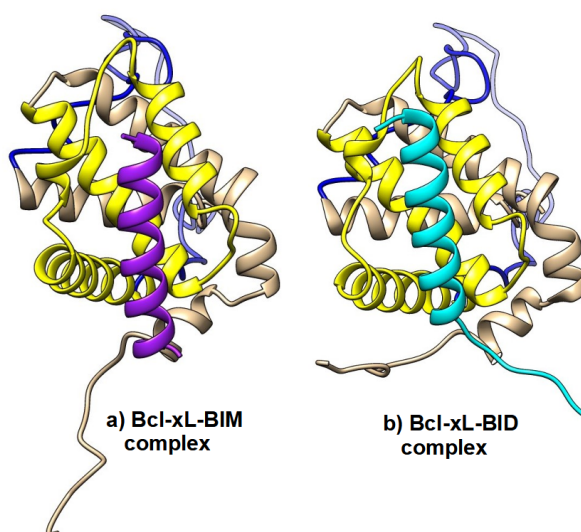


Figure 6.4. Representative structure of a) Bcl-x_L-BIM complex b) Bcl-x_L-BID complex. (Blue and yellow colors refer to the IDR and the the binding groove. BIM peptide in purple, BID peptide in cyan.)

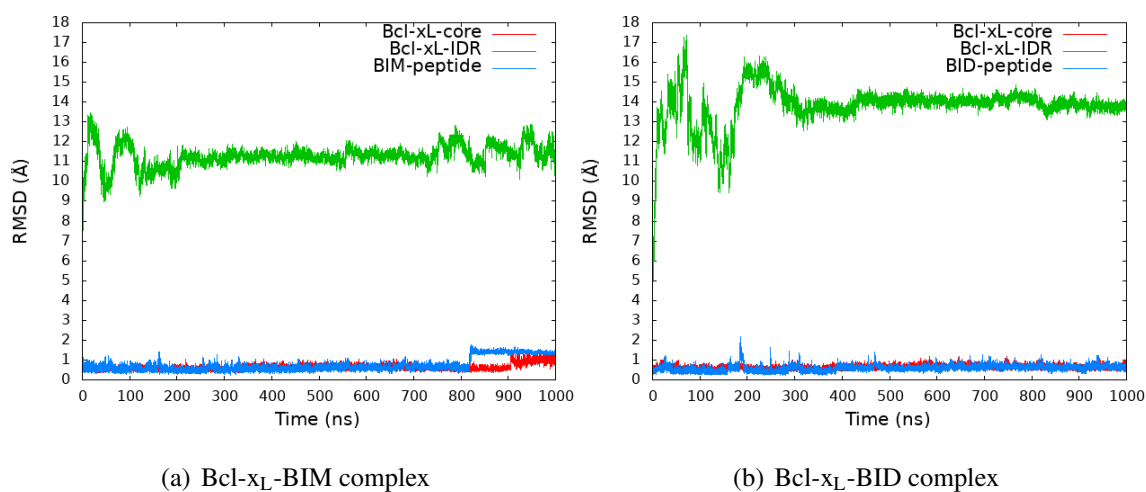


Figure 6.5. Backbone RMSD plots of a) Bcl-x_L-BIM complex b) Bcl-x_L-BID complex with respect to the built structures.

Investigation of the Bcl-x_L-BOP complexes both prior to and following deamidation is underway and aims to give insight into the interactions between Bcl-x_L and BH3-only peptides.

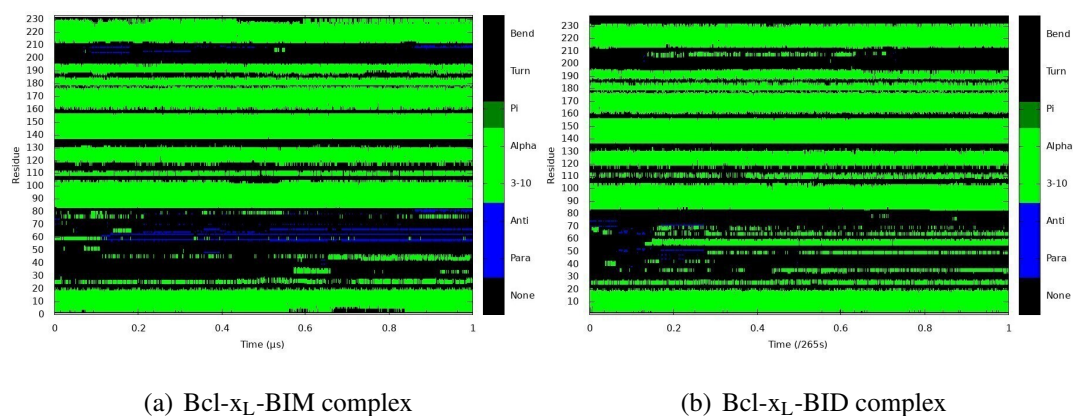


Figure 6.6. Secondary structure plots of a) Bcl-x_L-BIM complex b) Bcl-x_L-BID complex.

6.4. Conclusions

MD simulations confirmed that unbound BH3-only peptides are dynamic in water compared to their corresponding complex systems (bound state). Disruption of helicity (short helices) are observed and the peptides are unstable in water in line with previous studies. They are significantly more stable when in contact with Bcl-x_L. Analysis results of complex systems showed that BH3 peptides preserved their helical shapes, yet loop regions were highly flexible. As a future work we will investigate BH3-bound Bcl-x_L (complex systems) in membrane environment before and after deamidation. Understanding of the interactions in the complex systems will pave the way to design future Bcl-x_L inhibitors.

7. KETENIMINIUM CHEMISTRY

7.1. Introduction

Keteniminium salts (KIs) are versatile and reactive intermediates in organic chemistry [9,188]. Historically, the pioneers of the use and synthesis of KI are Viehe and Ghosez [3,4]. KIs are an improved alternative to their ketene analogues, due to their higher reactivity and high electrophilicity. Furthermore, KIs do not undergo undesired side reactions, such as dimerization or polymerization, as readily as ketenes [5, 7, 188–191]. KIs are mainly categorized in two groups, namely classical (aldo-KI and keto-KI) and activated keteniminium ions as depicted in Figure 7.1.

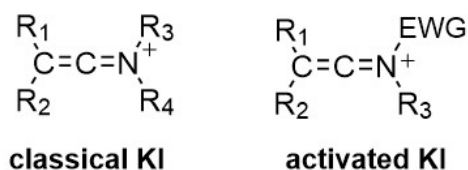


Figure 7.1. General structures of KIs.

Keteniminium salts have a wide range of synthetic applications [9, 188]. They are mostly used as key intermediates in electrocycloaddition reactions, [192,193] intermolecular and intramolecular cycloaddition reactions, [189, 194, 195] [1,5]-sigmatropic hydrogen shifts, [196, 197] and Claisen rearrangements [198] (Figure 7.2). KIs were shown to undergo [2 + 2] cycloadditions with alkynes and are also used as dienophiles in Diels-Alder reactions [194, 199, 200]. [2 + 2] cycloaddition products of KI and alkenes can also undergo nucleophilic addition on the cyclobutyliminium ion to produce highly stereoselective quaternary centers [201]. In the following section we will describe three computational/experimental studies involving KIs.

7.1.1. Formation of Keteniminium Salts

As mentioned above, the formation reaction of KIs was first mentioned by Viehe and coworkers in 1967 [10]. However, some drawbacks limit the use of this procedure, such as

the initial formation of a highly reactive and sensitive ynamine and a side reaction of the KI formed with its precursor. In the following years, various alternative formation reactions of KIs, allowing a broader use of these intermediates, have been disclosed in Figure 7.3, namely, reactions of α -haloenamines with Lewis acids, [4–6] triflation of amides, [7] methylation of ketenimines, [8] and protonation of ynamines [9, 10] and ynamides [11–13]. Particularly, in 1981, Ghosez and coworkers [7] reported the synthetically most useful and commonly used formation method by activation of amides with triflic anhydride. In context of this study, we focused on the KI formation reaction from the reaction of tertiary amides (Ghosez’s KI formation) since it requires milder conditions and is the synthetically most used KI formation method. The effect of substituents on starting amide reactivity was investigated by considering the mechanism of amide triflation. A broad range of substituents were selected, and energetic analysis was performed to assess relative reactivities and their effect on the ease of KI formation. Furthermore, reactivity of experimentally available starting amides with different substituents was computationally investigated with various aspects, namely FMO, and reactivity descriptors.

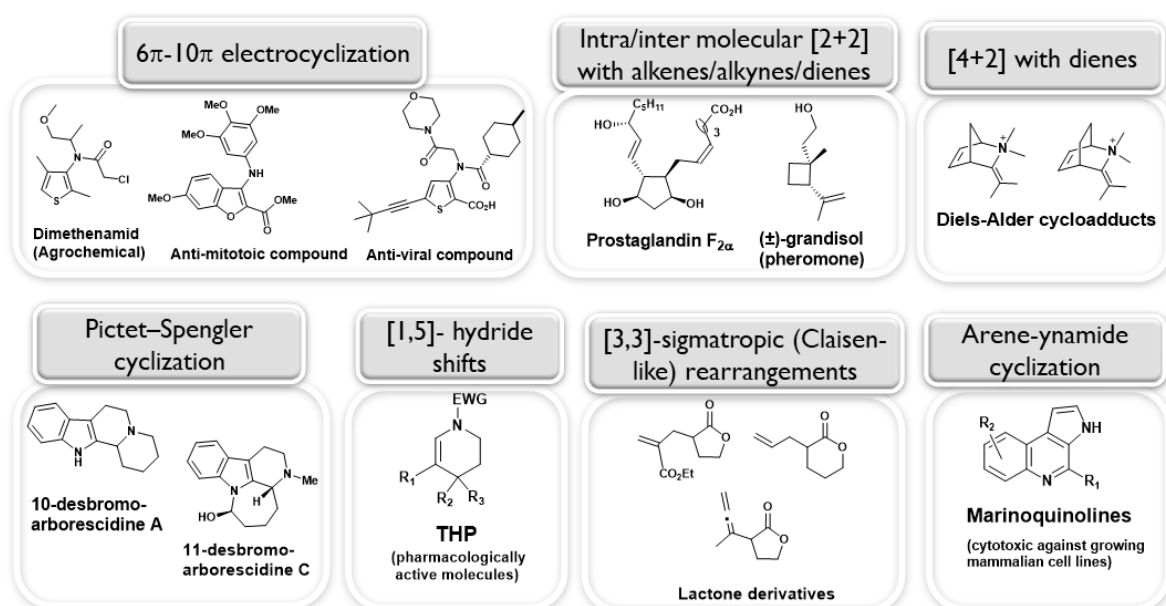


Figure 7.2. Summary of the reactions involving KIs.

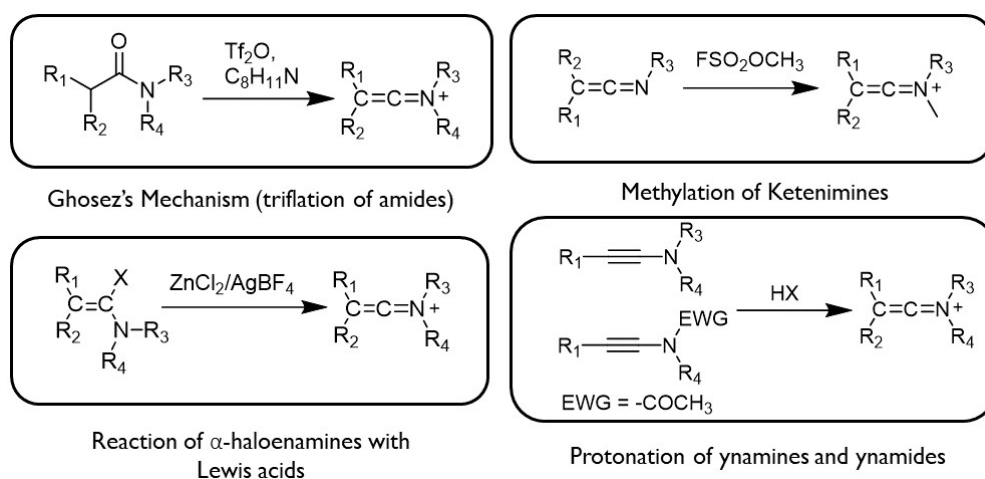


Figure 7.3. Various formation reactions of KI.

7.1.1.1. Methodology. A density functional theory (DFT) study was performed where KI formation reactions were modeled using a hybrid meta-generalized gradient-approximation (HM-GGA) via the M06-2X functional [39, 50]. M06-2X was selected for its well-known performance in functional organic systems and its inclusion of dispersion effects [202, 203]. The 6-31+G(d,p) basis set was employed for all atoms, except sulfur for which the 6-311++G(3df,3pd) extra basis set was used for higher accuracy [204, 205]. The effect of the solvent environment was modelled by means of the self-consistent reaction field (SCRF) theory [58] using the IEF-PCM approach [59, 206] as implemented in the Gaussian 16 (G16, Revision A.03) program package [207]. Geometry optimizations were performed in chloroform (CHCl₃, $\epsilon=4.7113$) and dichloromethane (CH₂Cl₂, DCM, $\epsilon=8.93$) taking into account the experimental conditions for each reaction. All free energy values are relative to the corresponding separate reactants and are reported at 298 K and 1 atm. Free energy of reactions (ΔG_{rxn}) was calculated using product complex (PC). Intrinsic reaction coordinate [208–212] (IRC) calculations were performed for all systems in order to verify and track each transition state (TS) leading to its corresponding reactant, intermediate and product. Distortion/interaction energy [213–215] was conducted for further investigation of substituent effects using the M06-2X/6-31+G(d,p) in CHCl₃. Frontier molecular orbitals (FMO) [216, 217] and reactivity descriptors [73, 74] were performed using the 6-311++G(d,p) basis set and the 6-311++G(3df,3pd) extra basis set was used for sulfur atoms. FMO and the descriptors were analyzed and calculated using Multiwfn (version 3.7) [218]. HOMO and LUMO orbitals were visualized using Chemission (version 4.60) developed by

Skripnikov [219]. CYLview (version 1.0b) was used for the illustration of the studied structures [220].

7.1.1.2. Results and Discussion. As discussed above, KI formation from the reaction of tertiary amides with triflic anhydride and collidine was mostly used method [7]. The reaction mechanism consists of three consecutive steps as depicted in Figure 7.4. The first step is the electrophilic activation of the amide with triflic anhydride, providing a transient O-triflyliminium triflate, which at the second step, upon reaction with collidine, gives the corresponding α -trifloylenamine. Then the enamine undergoes elimination to access the desired keteniminium salt in the final step. Computed data shows that the first step, which is the electrophilic activation of the starting amide, is the rate-determining step (RDS) (Figure 7.4). This indicates that the reactivity of the amide towards Tf_2O directly affects the overall KI formation process. Therefore, substituent effects on the C3 and N1 atoms of the amide leading to the corresponding KI were further investigated in this section. Various amides, leading to experimentally accessible KIs, were selected. The effects of substituents on the reactivity of the starting amides and KI were inspected under three subsections by means of energetic, frontier molecular orbitals (FMO), and reactivity descriptors.

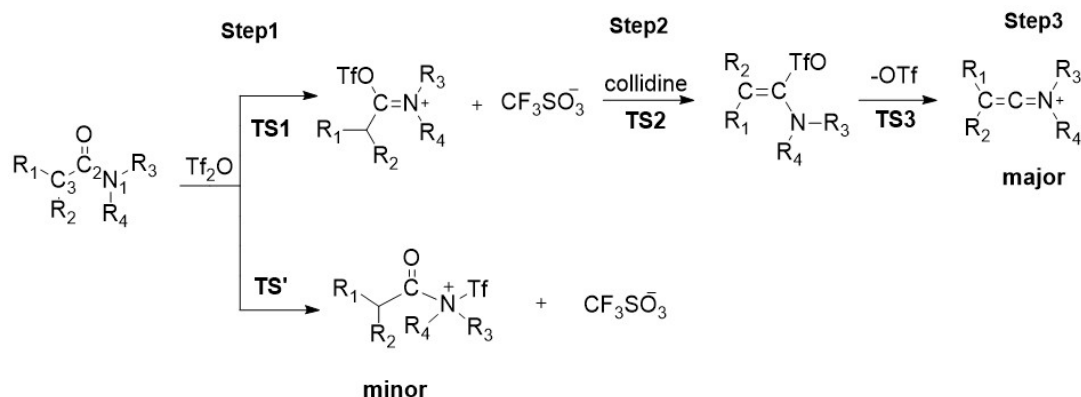


Figure 7.4. Ghosez's KI formation reaction from amides with triflic anhydride.

7.1.1.3. Energetics Analysis of KI Formation. The energetic cost of the formation reactions of KIs with various substituents and their relative reactivities were examined in two groups according to the substituent placement, namely C3 and N1 substituents (Figure 7.4) as mentioned previously. In general, EDGs were shown to decrease activation barrier when com-

pared to EWG substituted amides, regardless of the position of the substituent. Blue colored substituents in Table 7.1 represent EDG while red colored substituents represent EWG groups. The reported barriers herein belong to the RDS.

7.1.1.4. Amide Reactivity. In the pursuit of energetic analysis of the substituted starting amides and their contribution to formation reactions of KI, the substituent effects on amide reactivity were examined by means of several analysis techniques, namely, Frontier Molecular Orbitals (FMO) and Reactivity Descriptors. The highest occupied molecular orbitals (HOMOs) and reactivity indices of the amides under study were inspected to rationalize the calculated order of activation barriers by using Multiwfn (version 3.7) [218]. Table 7.2 reveals that while EDGs raise the HOMO energy levels by enriching carbonyl oxygen with electrons, EWGs lower the HOMO energy level in line with the activation barriers (Table 7.1). Intriguingly, the amides bearing heteroatoms (9a, 11a-13a and 16a-17a) also increase the HOMO level due to the electron-donating ability of lone pairs on the heteroatoms. Figure 7.5 depicted that lone pairs of the heteroatoms provide remarkable contributions to the HOMO level and raise the HOMO level. However, smaller HOMO lobes of carbonyl oxygen in the amides (9a and 11a-13a) clarify the higher barriers in the range of 30.5-32.2 kcal/mol compared to larger HOMO lobes of 1a and 5a ($\Delta G^\ddagger = 29.8$ and 27.7 kcal/mol, respectively).

Conceptual DFT is a powerful tool to predict chemical reactivity by way of employing global and local reactivity descriptors [72–74]. In line with the HOMO energy levels, EDGs also enhances the nucleophilicity index (Nu), which is a measure of the nucleophilicity of the amides. The nucleophilicity of the amides bearing EDGs are higher than those having EWGs with both C3 and N substituted amides. EDGs increase the nucleophilicity of the amides and improves the ease for KI formation. Notably, EWGs on nitrogen (4b and 5b) dramatically decrease both HOMO energy levels and nucleophilicity indices in line with higher activation barriers ($\Delta G^\ddagger \approx 33.6$ kcal/mol). Moreover, Fukui, local nucleophilicity indices and dual descriptors were analyzed for the amides with heteroatoms, the descriptors are higher on hetero atoms than the carbonyl oxygen, showing the reason of decrease in nucleophilicity and increase in HOMO levels for these systems (Table 7.3). Taken together, the outcomes of HOMO levels and nucleophilicity indices are in line with the energetic results.

Table 7.1. Gibbs free energies of activation (ΔG^\ddagger) and reaction (ΔG_{rxn}) for the RDS of Ghosez's reaction with C3 and N substituted amides.

Entry	C3-substituted Amide	ΔG^\ddagger	ΔG_{rxn}	Entry	C3-substituted Amide	ΔG^\ddagger	ΔG_{rxn}
1a		29.8	9.2	10a		31.3	4.8
2a		27.9	7.5	11a		30.1	13.1
3a		28.0	8.9	12a		30.9	11.7
4a		28.6	8.5	13a		30.5	9.2
5a		27.7	5.5	14a		28.5	12.5
6a		27.9	6.7	15a		29.7	14.9
7a		29.6	1.2	16a		28.8	7.7
8a		30.5	11.1	17a		30.1	12.3
9a		28.1	10.7	18a		29.5	7.8
Entry	N-substituted Amide	ΔG^\ddagger	ΔG_{rxn}	Entry	N-substituted Amide	ΔG^\ddagger	ΔG_{rxn}
1a		29.8	9.2	3b		30.6	11.4
1b		30.1	9.9	4b		33.5	22.6
2b		32.6	11.1	5b		33.7	18.7

Table 7.2. Calculated HOMO energy, nucleophilicity index, and local nucleophilicity indices for the substituted amides for the substituted amides.
(M06-2X/6-311++G(d,p)//M06-2X/6-31+G(d,p) in CHCl₃.)

C3 substituted amides										
		O (C=O)			N1		O (C=O)			N ₁
Amide	HOMO	Nu	Nu _k	Nu _k	Amide	HOMO	Nu	Nu _k	Nu _k	
1a	-8.095	2.509	0.4811	0.4685	10a	-8.291	2.314	0.4463	0.4280	
2a	-8.081	2.524	0.4715	0.4751	11a	-7.890	2.715	0.0880	0.0299	
3a	-8.123	2.482	0.4713	0.4658	12a	-7.804	2.801	0.0591	0.0143	
4a	-8.136	2.469	0.4753	0.4506	13a	-6.784	3.821	0.0604	0.0355	
5a	-8.120	2.485	0.4938	0.4597	14a	-8.357	2.248	0.4627	0.4240	
6a	-8.091	2.514	0.4779	0.4709	15a	-8.380	2.225	0.4536	0.4009	
7a	-8.132	2.473	0.4745	0.4634	16a	-8.031	2.574	0.0886	0.0250	
8a	-8.202	2.403	0.4577	0.4474	17a	-7.780	2.824	0.0757	0.0082	
9a	-7.587	3.018	0.0715	0.0296	18a	-6.827	3.778	0.1137	0.0181	
N substituted amides										
1b	-8.279	2.326	0.4811	0.4685						
1a	-8.095	2.509	0.4865	0.4811						
2b	-8.363	2.242	0.4392	0.4260						
3b	-8.361	2.244	0.4497	0.4369						
4b	-8.944	1.661	0.3628	0.3352						
5b	-8.779	1.826	0.3701	0.3749						

Higher Fukui indices (f^-) and local nucleophilicity index (Nu_k) on carbonyl oxygen of the amides in Tables 7.2 and 7.3 indicates higher nucleophilicity of this oxygen, in turn, higher reactivity of the carbonyl oxygen leading to KIs. More importantly, the differences in local reactivity descriptor values between carbonyl oxygen and nitrogen results encourage us to investigate the side reaction barriers of the amides with selected substituents. The amides with smaller (1a, 2a, 10a, and 1b) and larger (5a, 9a, 15a and 4b) Nu_k were selected to get insight into the effect of the substituents on the side reaction. Table 7.4 depicted the activation barriers differences between the main and the side reaction for the selected amides. Free energy of activation differences shows the amides bearing EWGs tend to decrease the activation barriers of the amides leading to KIs (major product). Intriguingly, the TSs (TS-

15a and TS-4b) of Ghosez reaction with 15a and 4b leading to KIs (KI-15a and KI-4b) are kinetically favored over those of their side reactions by 2.8 and 2.6 kcal/mol, respectively. The differences in activation barriers may indicate that kinetic product can be changed by using the suitable substituents. Additionally, contrary to 1a and 1b, which lead to keto-KI, the use of the amide leading to aldo-KI may increase the activation barrier of the side reaction and, thus, decrease the formation of N-sulfonylated minor product.

7.1.1.5. KI Reactivity. Finally, we evaluated how reactivity of the amides correlates to the reactivity of the resulting KIs. Therefore, FMO and reactivity descriptor analysis on all KI's studied was performed.

The substituent effects on the lowest unoccupied molecular orbital (LUMO) energies and electrophilicity of the KIs were analyzed to investigate the relationship with amide reactivity and predict electrophilic behaviors of resulting KIs (Table 7.5). Notably, KI reactivity is inversely correlated to the activation barriers for the formation of KI. Unlike amide reactivity, electrophilicity of KI impacts on KI reactivity. EWGs lower the LUMO level leading to decrease in the HOMO-LUMO gap and increases the reactivity of the KIs leading to lower energy barrier. In line with the LUMO energy level, electrophilicity index (ω) of the KIs with EWG is higher than KI with EDGs due to rendering central carbon of KI more electrophilic and increasing reactivity of KIs. This intriguing reverse connection will be further investigated in an upcoming paper to give comprehensive insight on the KI reactivity.

7.1.2. [2 + 2] Cycloaddition Reactions

Due to the limited general methods to attain substituted aminocyclobutanes and aminocyclobutenes, a straightforward general access from the corresponding iminium salts has gained considerable attention. Inter and intramolecular [2 + 2] cycloaddition reactions of KI with alkenes or alkynes are extensively used methods to access cyclobutanones/cyclobutenones and various complex compounds in organic synthesis that can be derived from them. In this context, a DFT study was performed in order to investigate the experimentally observed reactivity differences in the [2 + 2] cycloaddition reactions.

Table 7.3. Calculated condensed fukui (f-) and condensed dual descriptors (CDD) for the heteroatom substituted amides.

C-subs. amide	X=S,O,N			O (carbonyl oxygen)		N ₁ atom	
	f-	CDD	Nu _k	f-	CDD	f-	CDD
1a	-	-	-	0.1917	-0.1742	0.1867	-0.1844
2a	-	-	-	0.1868	-0.1726	0.1882	-0.1858
3a	-	-	-	0.1899	-0.1818	0.1877	-0.1844
4a	-	-	-	0.1925	-0.1750	0.1825	-0.1783
5a	-	-	-	0.1987	-0.1808	0.1850	-0.1839
6a	-	-	-	0.1901	-0.1724	0.1873	-0.1853
7a	-	-	-	0.1919	-0.1819	0.1874	-0.1833
8a	-	-	-	0.1905	-0.1713	0.1862	-0.1816
9a	0.0515	-0.0093	0.1554	0.0237	-0.0085	0.0098	-0.0069
10a	-	-	-	0.1929	-0.1758	0.1850	-0.1798
11a	0.4378	-0.3318	1.1885	0.0324	-0.0071	0.0110	-0.0045
12a	0.1122	-0.0956	0.3142	0.0211	-0.0085	0.0051	-0.0037
13a	0.1469	-0.1453	0.5612	0.0158	-0.0056	0.0093	-0.0080
14a	-	-	-	0.2058	-0.1713	0.1886	-0.1842
15a	-	-	-	0.2039	-0.0996	0.1802	-0.1490
16a	0.4956	-0.3821	1.2759	0.0344	-0.0089	0.0097	-0.0033
17a	0.1104	-0.0921	0.3118	0.0268	-0.0100	0.0029	0.0002
18a	0.1430	-0.1330	0.5402	0.0301	-0.0141	0.0048	-0.0034
N-subs. amide	O (carbonyl oxygen)		N1 atom				
	f-	CDD	f-	CDD			
1a	0.1917	-0.1742	0.1867	-0.1844			
1b	0.2091	-0.1918	0.2068	-0.1998			
2b	0.1959	-0.1832	0.1900	-0.1899			
3b	0.2004	-0.1809	0.1947	-0.1955			
4b	0.2184	-0.2006	0.2018	-0.1917			
5b	0.2027	-0.1642	0.2053	-0.1898			

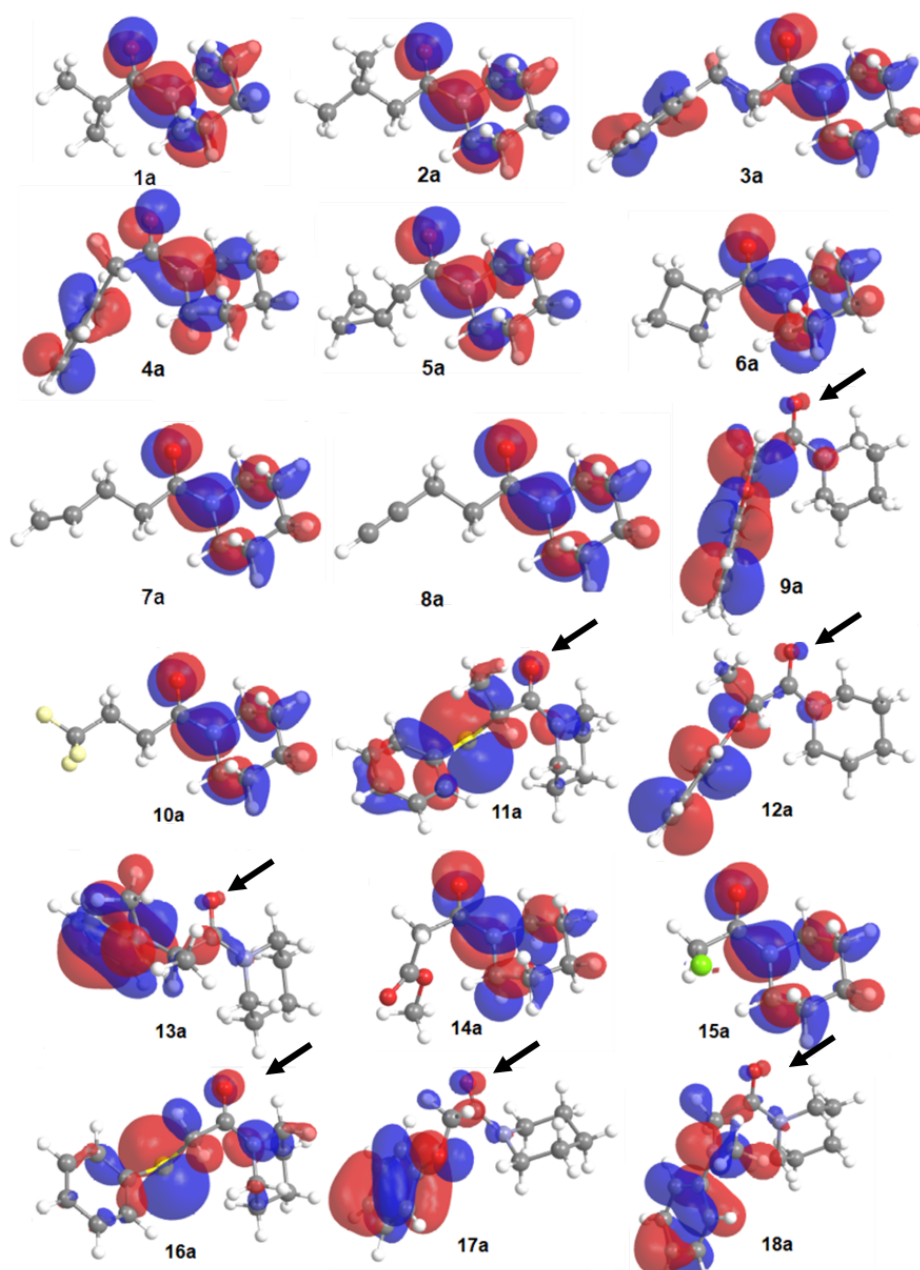


Figure 7.5. HOMO orbitals of C_3 -substituted amides.

(M06-2X/6-311++G(d,p)//M06-2X/6-31+G(d,p) in $CHCl_3$, extra basis set for S atom;
iso-surface value = 0.03 au.)

N-allyl groups are known to be easily cleaved under mild conditions to provide free amines [221]. Although allylic double bond in keteniminium salt is expected to be deactivated by the electron withdrawing effect of the iminium cation, the compatibility of *N*-allylic groups in the [2 + 2] cycloadditions of keteniminium salts was initially assessed to rule out the possibility of an intermolecular competitive reaction. Preliminary experimental results

based on a competition reaction highlighted the lower reactivity of the allylammonium salt 3, which is used to mimic the keteniminium *N*-allyl group (Figure 7.7) [222]. When KI 1 was added to a 1:1 mixture of alkene 2 and 3, cyclobutaniminium 4 resulting from the [2 + 2] cycloaddition of 1 and 2, was exclusively observed and no trace of 5 was detected confirming our suggestions that the positively charged nitrogen atom in KIs would considerably decrease the reactivity of the adjacent *N*-allyl groups toward electrophiles (Figure 7.7).

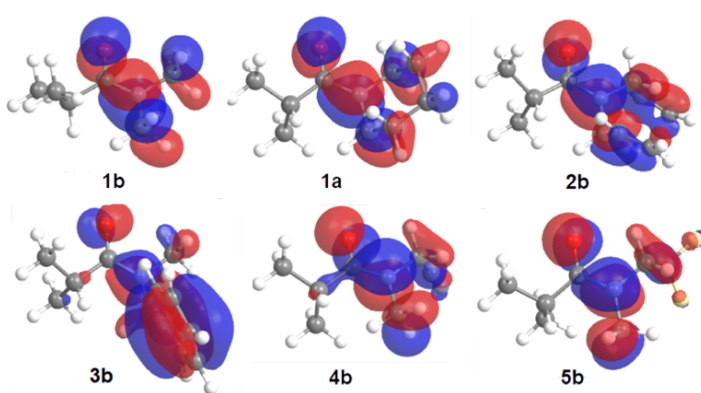


Figure 7.6. HOMO orbitals of N-substituted amides.

(M06-2X/6-311++G(d,p)//M06-2X/6-31+G(d,p) in CHCl₃; iso-surface value = 0.03 au.)

Table 7.4. Calculated activation barrier differences between main reaction leading to KI major product and side reaction leading N-sulfonylated minor product. (Prime sign (') refers to TS of side reaction.)

	ΔG^\ddagger	$\Delta\Delta G^\ddagger$		ΔG^\ddagger	$\Delta\Delta G^\ddagger$
TS-1a	29.8	1.8	TS-12a	30.9	-0.2
TS-1a'	28.0		TS-12a'	31.1	
TS-2a	27.9	0.7	TS-15a	29.7	-2.8
TS-2a'	27.2		TS-15a'	32.5	
TS-5a	27.7	0.1	TS-1b	30.1	2.6
TS-5a'	27.6		TS-1b'	27.5	
TS-9a	28.1	-0.3	TS-4b	33.5	-2.5
TS-9a'	28.4		TS-4b'	36.0	
TS-10a	31.3	-0.5	TS-5b	33.7	-4.2
TS-10a'	31.8		TS-5b'	37.9	

Table 7.5. Calculated LUMO energy and electrophilicity index for the substituted KIs.

M06-2X/6-311++G(d,p)/M06-2X/6-31+G(d,p) in CHCl₃. Units in eV.

Entry	KI	LUMO	ω	Entry	KI	LUMO	ω
C3 substitution							
KI-1a		-1.547	2.437	KI-10a		-2.012	2.818
KI-2a		-1.681	2.552	KI-11a		-2.009	2.795
KI-3a		-1.822	2.495	KI-12a		-1.999	2.798
KI-4a		-1.691	2.488	KI-13a		-1.759	2.591
KI-5a		-1.712	2.544	KI-14a		-2.176	2.964
KI-6a		-1.864	2.685	KI-15a		-2.637	3.376
KI-7a		-1.727	2.526	KI-16a		-2.107	2.890
KI-8a		-1.926	2.720	KI-17a		-2.246	3.022
KI-9a		-1.821	2.668	KI-18a		-1.717	2.520
N substitution							
KI-1b		-1.620	2.504	KI-3b		-1.512	1.782
KI-1a		-1.547	2.437	KI-4b		-2.070	2.894
KI-2b		-1.719	2.549	KI-5b		-2.045	2.860

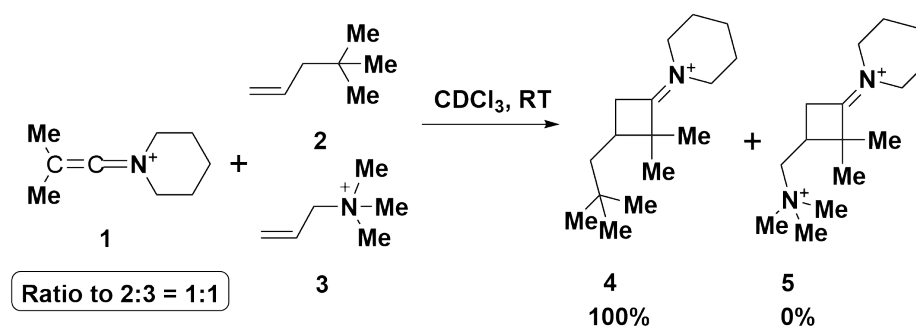


Figure 7.7. Competition reaction between allylammonium 3 and corresponding alkene 2 in a [2 + 2] cycloaddition with KI 1.

This study aimed to elucidate the reaction mechanism for [2 + 2] cycloaddition reaction of KI and olefins and rationalize the experimental data by means of DFT calculations. Two alkene (olefin) derivatives in Figure 7.7 were studied in order to determine the substituent effect on the cycloaddition reactions [222].

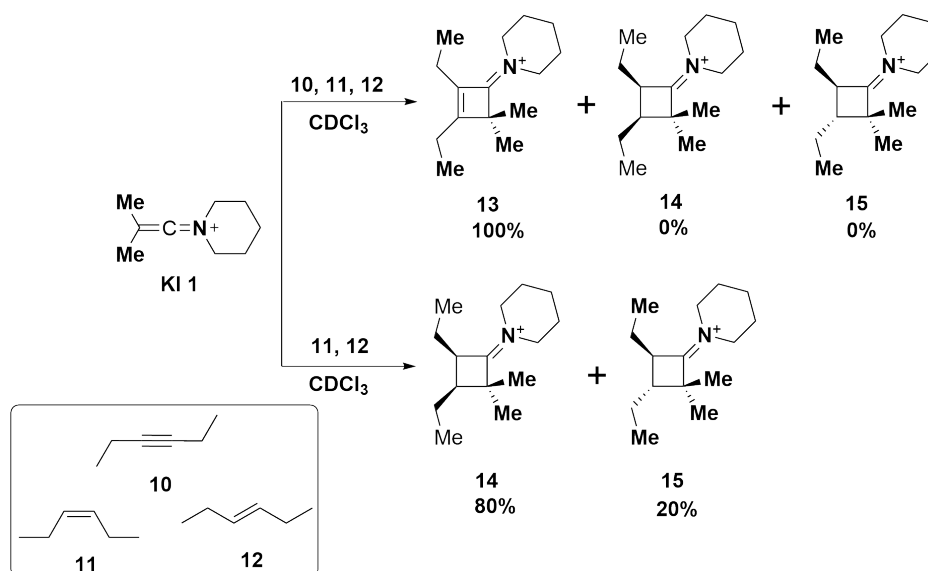


Figure 7.8. Competition reaction experiment between 10, 11, and 12 in a [2 + 2] cycloaddition with KI 1.

Secondly, alkynes are usually much more reactive species than the corresponding alkenes toward electrophiles as verified in the competition reaction depicted in Figure 7.8. When keteniminium 1 was added to a 1:1:1 mixture of 10, 11, and 12, the [2 + 2] cycloaddition occurred, in 15 minutes, exclusively with alkyne 10. However, upon mixing keteni-

minium salt 1 with alkenes 11 and 12 (1:1 ratio), the [2 + 2] cycloaddition was completed in 1 h giving 14:15 in a 80:20 ratio, also evidencing that cis-alkenes react faster than trans-alkenes [222]. We aimed to validate and rationalize the experimental data by means DFT calculations.

7.1.2.1. Methodology. Density functional theory calculations utilizing the meta-hybrid GGA M06-2X were performed. M06-2X was chosen for its well-known performance in organic systems with dispersion effects. The effect of the solvent environment was taken into account by means of the self-consistent reaction field (SCRF) theory. Geometry optimizations were employed in chloroform (CHCl_3 , $\epsilon=4.7113$) within the integral equation formalism-polarizable continuum (IEF-PCM) model as implemented in the Gaussian 09 (G09) program package [223]. Intrinsic reaction coordinate calculations were performed to trace each transition state (TS) to its corresponding reactant, intermediate or product. All free energies are reported at 298K and 1 atm. CYLview software [220] was used for visualization of the computed structures.

7.1.2.2. Results and Discussion. A computational study was performed to rationalize the experimentally observed reactivity difference in the [2 + 2] cycloaddition of keteniminium 1 with olefins 2 and 3 (Figure 7.7) [222]. All possible reaction pathways for the [2 + 2] cycloaddition of keteniminium 1 with alkenes 2 and 3 were computationally explored (Figure 7.9). The conformational space, including spatial orientations within pre-reactive complexes (PRCs), were thoroughly investigated. Calculations verified a stepwise reaction mechanism, where the initial transition state TS1 leads to a highly strained cyclopropane-like intermediate INT; this is incidentally the rate-determining step (Figure 7.10). Figure 7.10 depicts transition state geometries for the rate-determining step and the corresponding intermediates. The reaction path subsequently bifurcates, resulting in two transition states TS2, which lead to two cyclobutaniminiums. The major product is determined by the steric clash of substituent groups in TS2 (Figure 7.9). In line with the experiment, cyclobutaniminium 4, which results from the [2 + 2] cycloaddition of 1 and 2, is both the kinetic and the thermodynamic product in the competition reaction between allylammonium 3 and corresponding alkene 2 (Figure 7.10). The free energy of activation for the cycloaddition of 1 and 3 ($\Delta G^\ddagger =$

42.5 kcal/mol) is significantly high, validating the assumption that alkylammonium 3 is unreactive towards cycloaddition with 1 due to the electron withdrawing nature of the cationic quaternary amine.

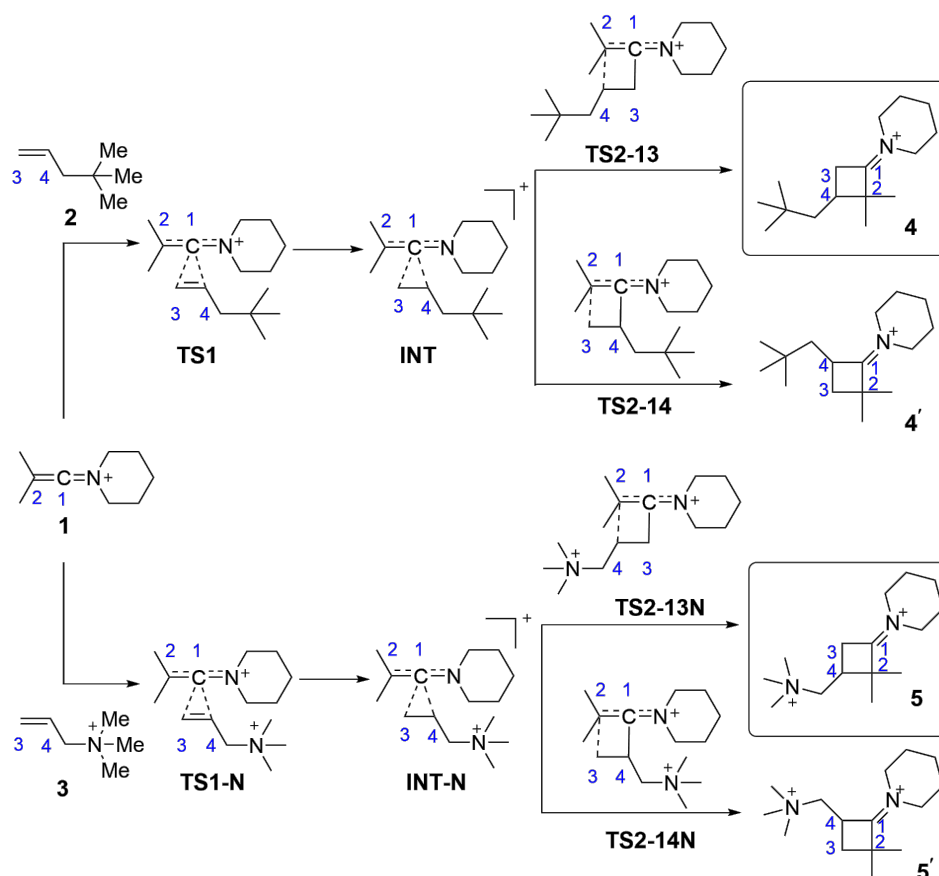


Figure 7.9. Possible reaction mechanisms for the [2 + 2] cycloaddition of keteniminium 1 with olefins 2 and 3.

Frontier Molecular Orbital analysis [216,217] and Natural Population Analysis (NPA) [61] were carried out at the same level of theory. FMO was investigated in order to evaluate the reactivity difference between 2 and 3 (Figure 7.10). The HOMO-LUMO gap between HOMO of 2 and LUMO of 1 (4.01 eV) is considerably smaller than the corresponding gap for 3 and 1 (8.81 eV) (Figure 7.11). The small gap between 1 and 2 implies high reactivity and larger orbital interaction and is consistent with experimental data. Moreover, FMO analysis shows the cationic center has significantly lowered the HOMO of 3, rendering it unreactive.

Similarly, NPA results reveal, as expected, a considerably larger negative charge on carbon C3 of 2 (-0.456), compared to that of 3 (-0.362), indicating higher reactivity in the

former alkene (Table 7.6). Note that electron density distributions on carbons C3 and C4 are approximately equal in allylammonium 3, whereas C3 has a significantly higher negative charge than C4 in 2. The difference in the charge distributions is reflected in the critical distances in Figure 7.10, where INT and INT-N bond lengths are shown to be significantly different. Moreover, NPA charges on the allylic double bond of *N,N*-diallyl-ket closely resemble those of allylammonium 3 (Table 7.6), which was specifically chosen to mimic the reactivity of *N*-allyl substituents. Thus keteniminium *N*-allyl substituents are predicted to be similarly unreactive toward cycloaddition.

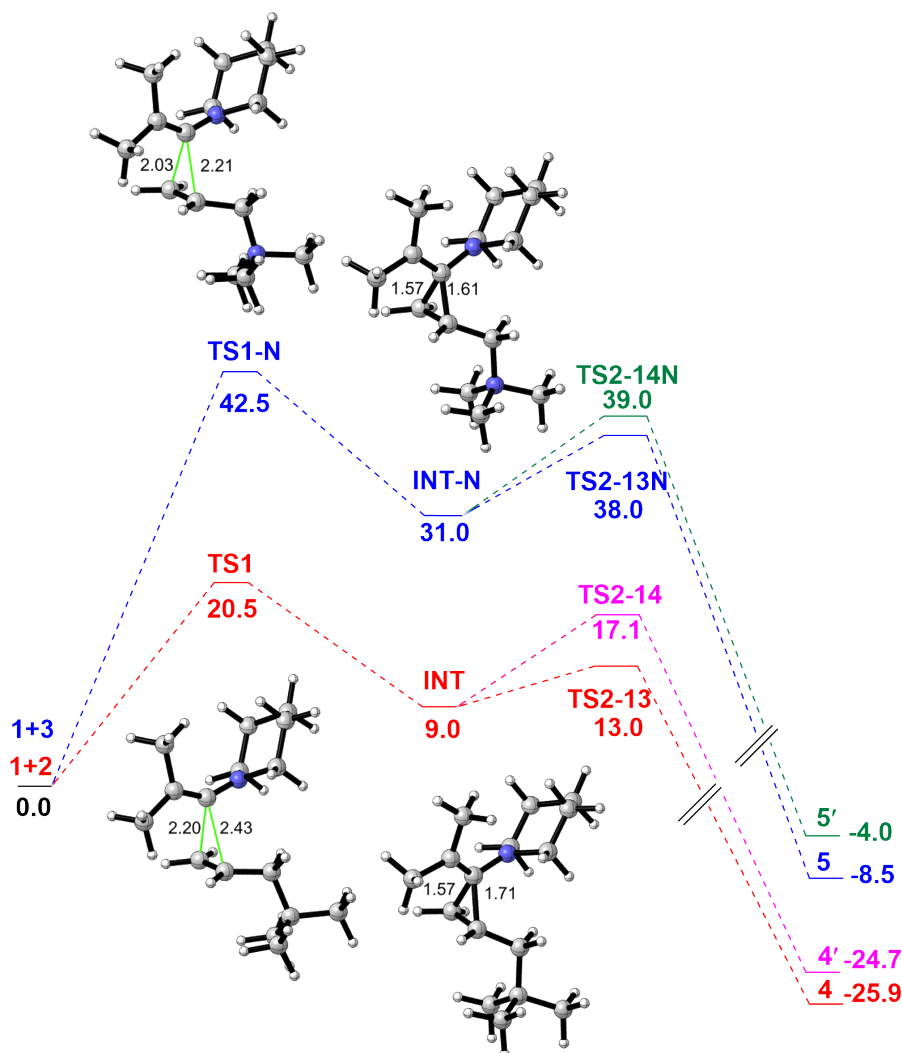


Figure 7.10. Free energy profile for the [2 + 2] cycloaddition reaction of KI 1 with alkenes 2 and 3. Optimized TS1s and intermediates. Free energies in kcal/mol; M06-2X/6-31+G(d,p) with IEF-PCM in CHCl₃.

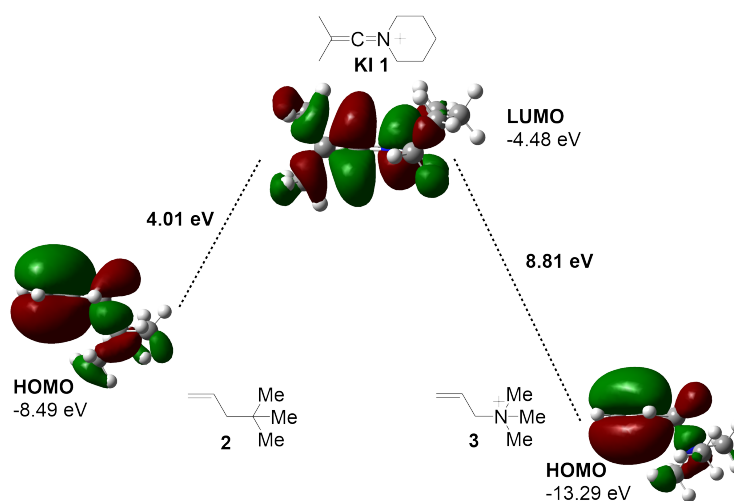


Figure 7.11. HOMO-LUMO gaps between KI 1 and alkenes 2 and 3.

M06-2X/6-31+G(d,p); iso-surface value = 0.02 au.

Table 7.6. Natural Population Analysis (NPA) of alkenes 2, 3, and *N,N*-diallyl keteniminium. M06-2X/6-31+G(d,p).

	NPA		
	C3	C4	C5
2	-0.456	-0.223	-0.498
3	-0.362	-0.319	-0.291
<i>N,N</i>-diallyl-ket	-0.376	-0.298	-0.295

The competition reaction depicted in Figure 7.8 was modeled at the same level of theory to understand the difference in reactivity of alkyne 10, alkenes 11 and 12 toward cycloaddition with KI 1 [222]. Reaction barriers were compared to identify the most feasible reaction, revealing alkyne 10 as the most reactive reaction partner and cyclobuteniminium 13, the major product of the competition reaction, as both the kinetic and the thermodynamic product (Table 7.7), with highly exergonic reaction energies. Both the reaction mechanisms and the energetic results are in good agreement with a recent study by Domingo et. al. [224] which investigated the reaction mechanism for the [2 + 2] cycloaddition of KIs with

acetylene and propyne at the MPWB1K/6-311G(d,p) level of theory [225]. Note that unlike the cycloaddition of alkylammonium 3, which is predicted to have a very high activation barrier ($\Delta G^\ddagger = 42.5$ kcal/mol, Figure 7.10) and therefore, deemed unlikely, alkenes 11 and 12 (Table 7.7) have comparable activation barriers with alkene 2 and are experimentally reported to react with KI 1 at different reaction rates that are fully consistent with the computed relative barriers, depicting *cis*-alkene 11 to be slightly more reactive than *trans*-alkene 12. Note that 11 leads to one product due to symmetry.

Table 7.7. Free energies of activation (ΔG^\ddagger) and reaction (ΔG_{rxn}) (kcal/mol) for the [2 + 2] cycloaddition reaction of KI 1 with alkyne 10, alkenes 11 and 12. M06-2X/6-31+G(d,p) with IEF-PCM in CHCl_3 .

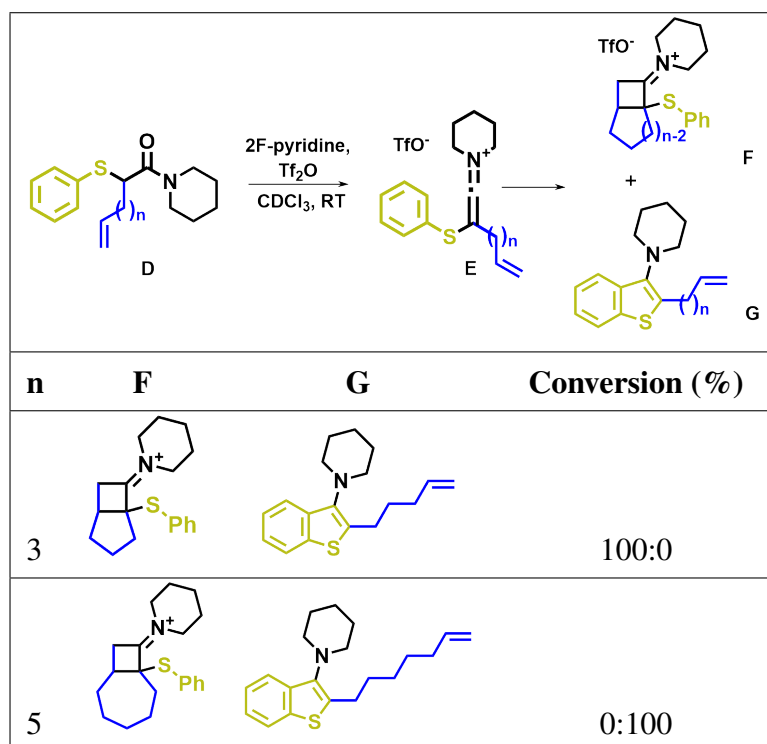
Reaction	ΔG^\ddagger_1	ΔG^\ddagger_2		ΔG_{rxn}	
		i	ii	i	ii
KI 1 + alkyne 10	17.0	11.4	12.2	-41.4	-39.7
KI 1 + <i>cis</i> -alkene	19.8	15.7		-23.2	
KI 1+ <i>trans</i> -alkene	21.2	17.8	19.3	-25.5	-25.6

7.1.3. Intramolecular Competition Reactions

This section includes computational rationalization of the experimental competition studies, which were given below. Firstly, intramolecular competition reactions were performed to investigate which type of reactivity involving a KI is favored between a [2 + 2] cycloaddition on a C=C double bond and a 6π -electrocyclization. Hence, three amides bearing different terminal olefins and a S-Ph moiety were synthesized by our experimental collaborators. Indeed, once the KI E is formed, it can either evolve through a [2 + 2] cycloaddition giving the cyclobutaniminium F or through a 6π -electrocyclization giving the benzothio-*phene* G. Interestingly, the experimental results were highly dependent on the length of the chain (Table 7.8). When $n=3$, the [2 + 2] intramolecular cycloaddition was favored and gave exclusively product $F_{n=3}$ with a 4-5 bicyclic system. For $n=4$, crude NMR revealed a 9:1 ratio of products F/G where the 4-6 bicyclic system $F_{n=4}$ was the major compound underlining the preference of the [2 + 2] intramolecular cycloaddition. This trend was then reversed with longer chain ($n=5$) and the formation of the 7-membered ring was not observed. Only

the formation of the benzothiophene $G_n=5$ was detected in the crude NMR. These interesting results experimentally proved that the kinetics of both reactions are very close and they can be switched from one mechanism to another only by modification of the length of the side chain containing the $C=C$ double bond. In order to rationalize and validate the experimental outcomes, intramolecular competition reactions between 6π -electrocyclization and [2 + 2] cycloaddition reactions bearing the various carbon chain lengths were computationally investigated (Table 7.8) [226].

Table 7.8. Intramolecular competition reaction between a 6π electrocyclization and [2 + 2] cycloaddition.



Secondly, competition reactions proved that the formation of thiophene 9 was the fastest pathway in all cases, with an isolation yield ranging from 77% to 84%. No benzothiophenes 15 or [2 + 2] cycloaddition adducts 14 were detected in the crude mixture. Such a difference of reactivity between a vinyl sulfide and a phenyl sulfide is not surprising, as the latter would require a higher energy to break the aromaticity of the phenyl ring during the cyclization step. A DFT study was performed in order to elucidate the favorable formation of the thiophene in Figure 7.12 [227]. Note that, electrocyclization reactions of KIs were further discussed in the following chapter.

Lastly, the effect of alkyl chain length (addition of one more methylene group (-CH₂-) in intramolecular [2 + 2] reaction were experimentally examined in order to discern which cycle (five or six) was easier to form in 16. Internal competition reaction was performed and cyclobutane iminium 17 was the only intermediate formed and no trace of 18 was detected (confirmation by ROESY correlations on the product resulting from the reduction of the iminium). In order to explore and rationalize the reactivity differences in the intramolecular [2 + 2] cycloaddition reaction a computational study was performed at the M06-2X/6-31+G(d,p) in CHCl₃ (Figure 7.13) [195].

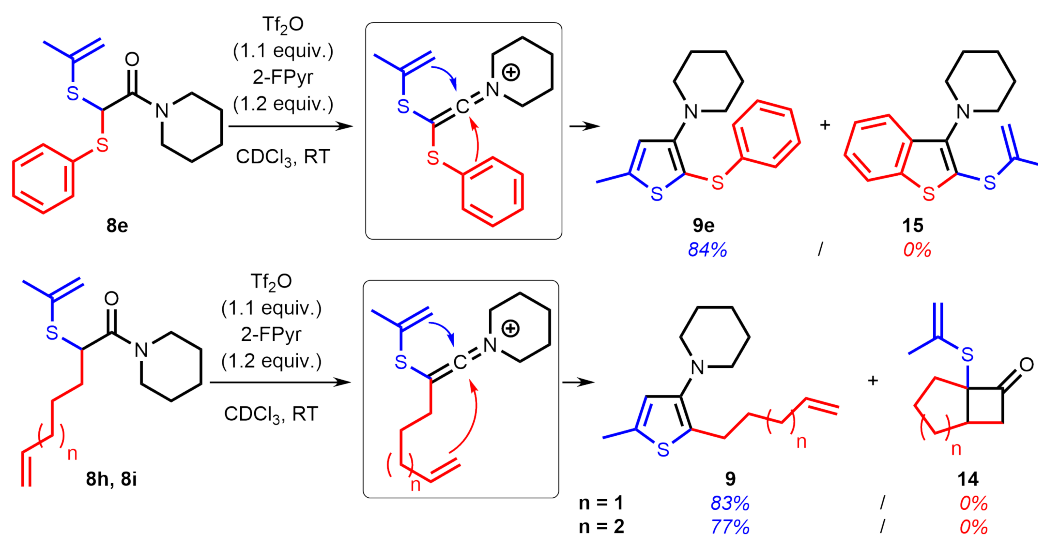


Figure 7.12. Intramolecular competition reactions between formation of thiophene, benzothiophene, and [2 + 2]-cycloadduct.

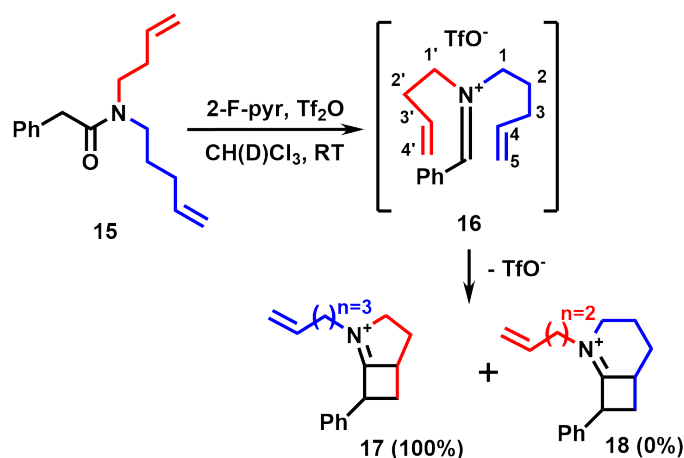


Figure 7.13. Intramolecular competition reaction to access five vs six membered rings.

7.1.3.1. Methodology. All optimizations were carried out the widely used hybrid meta-GGA functional, at the M06-2X/6-31+G(d,p) level of theory using IEF-PCM [59, 206] with the Gaussian software package (G09 [223] for the first and third study). The meta-GGA M06-2X was utilized due to its well-known effectiveness in organic systems with dispersive effects [39, 50, 228].

In the first study, 6-311++G(3df,3pd) extra basis was used for the sulfur atom in order to provide more accurate results [204, 205]. For each transition state (TS), corresponding reactant and products were verified through IRC calculations [208–212]. Additionally, BMK [229] and MPW1K [51] kinetic functionals were employed for energy refinements to provide accurate evaluation of the activation barriers [204, 230].

In the second study, all optimizations were performed using in Gaussian 16 (G16, Revision A.03) [207]. 6-311++G(3df,3pd) extra basis set was used for the sulfur atoms to attain more accurate results [204, 205]. In order to evaluate the activation barriers accurately energy refinements were performed with hybrid-GGA MPW1K, range-separated CAM-B3LYP [231] and double hybrid B2PLYP [52] functionals.

7.1.3.2. Results and Discussion. In the first competition reaction, a DFT study was performed to investigate the intramolecular competition reaction between 6π -electrocyclization and [2 + 2] cycloaddition reactions bearing the various carbon chain lengths ($n = 3$ and 5) in Table 7.8 [226]. Previous computational studies revealed that the [2 + 2] cycloaddition is a stepwise reaction, where the rate-determining step (RDS) is the initial addition of the central carbon atom of the KI onto the π -system, corresponding to TS-i. [195, 201, 224] Therefore, TS-i was used for comparison in the competition reactions. The computed data showed that the activation barrier for the [2 + 2] cycloaddition reaction of E ($n = 3$) ($\Delta G^\ddagger = 10.8$ kcal/mol) is significantly lower than the electrocyclization reaction ($\Delta G^\ddagger = 21.4$ kcal/mol) reflecting the higher conversion of Fn=3 (100%). Moreover, the [2 + 2] cycloaddition reaction of E ($n = 3$) is also highly exergonic ($\Delta G_{\text{rxn}} = -34.5$ kcal/mol) compared to electrocyclization of En=3 ($\Delta G_{\text{rxn}} = 8.2$ kcal/mol). Hence, the cycloaddition reaction of En=3 is favored both kinetically and thermodynamically, validating the experimentally observed outcome. BMK

and MPW1K results ($\Delta G^\ddagger = 10.3$ kcal/mol and 8.4, respectively) are consistent with the M06-2X results (Figure 7.14 and Table 7.9). In the case of $E_n=5$, BMK and MPW1K considerably lowered the activation barrier of electrocyclization reaction ($\Delta G^\ddagger = 16.1$ kcal/mol and 14.0, respectively) and the computational data is in agreement with the experimental observations. Figure 7.14 shows that even if the [2 + 2] cycloaddition reaction of E ($n = 5$) leads to thermodynamically more stable product, due to the higher difference in Gibbs free energy of activation ($\Delta\Delta G^\ddagger = 5.5$ kcal/mol) the electrocyclization reaction is kinetically favored over the cycloaddition reaction in line with the experimental results. $E_n=5$ affords the kinetic product $G_n=5$ (100%) as the major product of the competition reaction. Figure 7.15 demonstrates transition state structures for the studied systems. Consequently, computational findings allowed us to determine favorable kinetic and thermodynamic pathways and investigate the effect of chain length on the competition reaction.

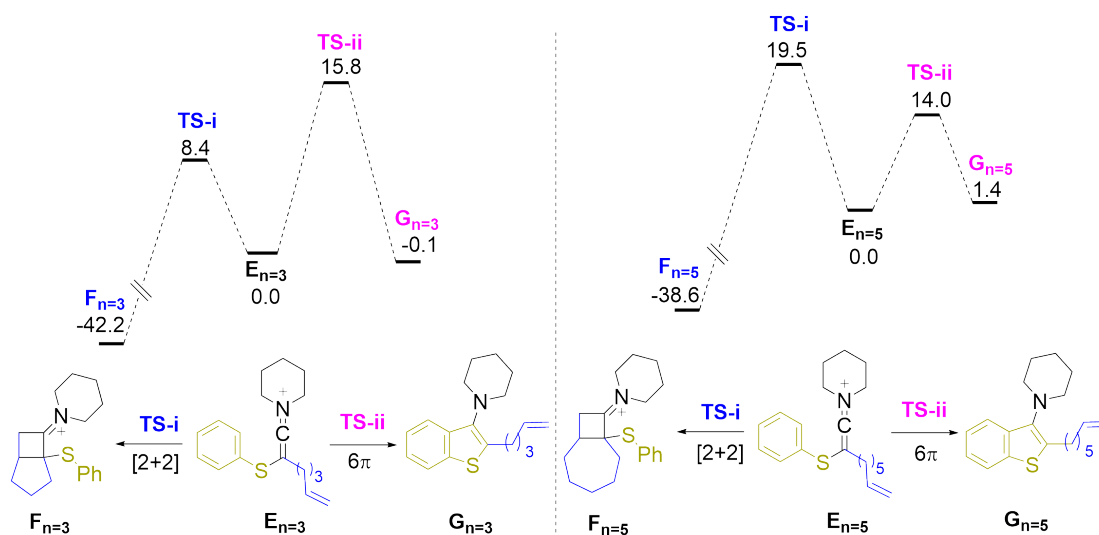


Figure 7.14. Free energy profiles for the competition reactions. 298 K and 1 atm; free energies in kcal/mol; MPW1K/6-31+G(d,p)//M06-2X/6-31+G(d,p) with IEF-PCM in CHCl_3 ; 6-311++G(3df,3pd) extra basis set for sulfur atom.

In the second competition reaction, a DFT study was performed to investigate the reactivity differences of the intramolecular competition reactions between formation of thiophene, benzothiophene and [2 + 2]-cycloadduct, and rationalize the favorable formation of the thiophene in Figure 7.12 [227]. Table 7.10 displays Gibbs free energies of activation (ΔG^\ddagger) and reaction (ΔG_{rxn}), respectively. Energies in kcal/mol at 298 K and 1 atm. Regardless of the level of theory similar barrier trends were observed. In the cy-

cycloaddition reaction of 8h, only the first transition state (TS1) results were presented, since previous studies disclosed that the rate-determining step of the stepwise [2 + 2] cycloaddition reaction is the initial addition of the central carbon atom of the KI onto the π -system of pentenyl [195, 201, 224, 226, 232]. In the competition reaction of 8e, due to the disruption of the aromaticity, the activation barrier for the formation of benzothiophene ($\Delta G^\ddagger = 16.4$ kcal/mol) is significantly higher than the barrier of the formation of thiophene ($\Delta G^\ddagger = 8.3$ kcal/mol). The formation of thiophene is both kinetically and thermodynamically favored in line with the experimentally observed findings (100%) (Figure 7.12 and Table 7.10). Similarly, in the case of 8h, energetic analysis showed that 8h undergoes 6π -electrocyclization reaction rather than the cycloaddition reaction. The activation barrier for the electrocyclization is considerably lower than the cycloaddition reaction validating the experimental outcome. Major product of the competition reaction for 8h is the kinetic product 9h (100%). Consistent with the experimental studies, the formation of thiophene (9e and 9h) is preferred over both the formations of the benzothiophene 15e and [2 + 2]-cycloadduct 14h.

Table 7.9. Gibbs free energies of activation (ΔG^\ddagger) and reaction (ΔG_{rxn}) (kcal/mol) for the competition reaction.

	BMK/6-31+G(d,p)				MPW1K/6-31+G(d,p)				Exp.
	Path i	Path ii	Path i	Path ii	Path i	Path ii	Path i	Path ii	
	ΔG^\ddagger		ΔG_{rxn}		ΔG^\ddagger		ΔG_{rxn}		
n=3	10.3	18.3	-42.0	3.9	8.4	15.8	-42.2	-0.1	100:0
n=5	19.4	16.1	-39.8	4.8	19.5	14.0	-38.6	1.4	0:100

Additionally, in our previous study, competition reaction between 6π -electrocyclization reaction to give benzothiophene and [2 + 2] cycloaddition reaction to give the cyclobutan-iminium were investigated at the same level of theory (MPW1K/6-31+G(d,p)//M06-2X/6-31+G(d,p)) [226]. In that study, due to the significantly lower activation barrier, the cycloaddition reaction ($\Delta G^\ddagger = 8.4$ kcal/mol) was favored both kinetically and thermodynamically over 6π -electrocyclization leading to the formation of benzothiophene ($\Delta G^\ddagger = 15.8$ kcal/mol). Taken together, in the light of both experimental and computational studies, it can be deduced that the ease of formation of the major product is follows: thiophene > [2 + 2]-cycloadduct > benzothiophene, respectively.

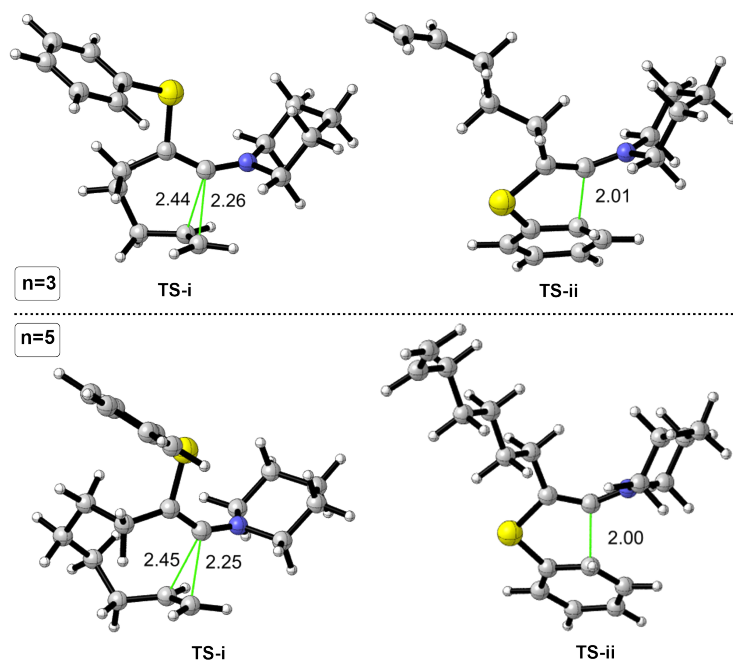


Figure 7.15. Optimized TSs for the intramolecular [2 + 2] cycloaddition and 6 π electrocyclization of En=3 and En=5. M06-2X/6-31+G(d,p) with IEF-PCM in CHCl₃; 6-311++G(3df,3pd) basis set for sulfur atom; critical distances in Å.

Table 7.10. Gibbs free energies of activation (ΔG^\ddagger) and reaction (ΔG_{rxn}) for the competition reactions.

		MPW1K/6-31+G(d,p)	CAM-B3LYP/6-31+G(d,p)	B2PLYP/6-31+G(d,p)	Exp.
 8e	ΔG^\ddagger	8.3	10.0	13.4	100
	ΔG_{rxn}	-30.8	-25.4	-20.6	
	ΔG^\ddagger	16.4	19.2	23.7	
 8h	ΔG_{rxn}	2.5	7.2	11.4	0
	ΔG^\ddagger	9.3	10.8	13.9	
	ΔG_{rxn}	-27.3	-22.5	-18.0	
	ΔG^\ddagger	11.0	13.5	16.7	0
	ΔG_{rxn}	-39.5	-30.7	-26.7	

In order to explore the intramolecular competition reaction of keteniminium 16 (Figure 7.13), a computational study was performed at the M06-2X/6-31+G(d,p) level of theory in CHCl₃ [195]. Previous computational works [222, 224] revealed the first step (binding of the central carbon of the KI to the olefin) in intermolecular [2 + 2] cycloadditions of

keteniminiums to be rate determining. Herein, the reaction profile for the intramolecular [2 + 2] reaction was re-examined to verify the step that will determine the ultimate outcome. It was shown that the first step of the reaction is still rate-determining. Moreover, computed data revealed that first transition state 16-5ring leading to 17 is favored over that of its counterpart, 16-6ring leading to 18, by 2.3 kcal/mol, while product stabilities favored 18 by 8.3 kcal/mol. Optimized transition state geometries for the first TSs leading to 17 and 18 are depicted in Figure 7.16. In line with the experimental findings, the difference in activation barriers for the first step indicate 17 is the kinetic product and the competition reaction is dictated by kinetic rather than thermodynamic factors.

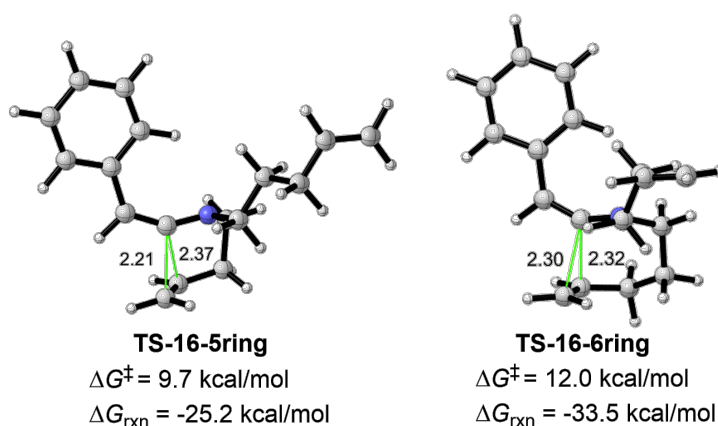


Figure 7.16. Optimized TS structures for the intramolecular cycloaddition of 16. M06-2X/6-31+G(d,p) with IEF-PCM in CHCl_3 ($\epsilon=4.7113$); critical distances in Å.

7.2. General Conclusions

In this chapter, formations of KIs, [2 + 2] cycloaddition reactions, and intramolecular competition reactions of KIs were investigated and general conclusions were presented herein.

In KI formation study, the reactivity of the starting nucleophilic amides towards the electrophilic triflic anhydride directly affects the ease of formation of the KI. EDGs on both C3 and N1 atoms of the starting amide generally lowers the activation barriers of the RDS. Additionally, the energetic findings were supported with distortion/interaction model, FMO, and reactivity descriptors. Lastly, reverse relationship was observed between amide and KI reactivities. While nucleophilicity of the amides affect the reactivity, electrophilicity of

the KIs plays a pivotal role on KI reactivity. In an upcoming paper/As a future work, this relationship will be further investigated.

In [2 + 2] cycloaddition study, DFT calculations rationalize the experimentally observed reactivity difference in the [2 + 2] cycloaddition of keteniminium and olefins. The reaction takes place with stepwise fashion. Each reaction (mechanism) involves an initial transition state (TS1) leading to an intermediate which follows a bifurcated path resulting in two transition states (TS2), and two products. The major product is determined by the steric clash of substituent groups in TS2. TS1 is the rate determining step (RDS). Computed data also verified the compatibility/use of *N*-allyl KI in [2 + 2] cycloaddition reactions.

In the intramolecular competition studies, favorable kinetic and thermodynamic pathways were determined and the computed data displayed the effect of chain length on the competition reaction between [2 + 2] cycloaddition and electrocyclization reactions. DFT calculations have verified the ease of the formation of thiophene for the competition reactions. This can be emphasized that the ease of formation of the major product is follows: thiophene > [2 + 2]-cycloadduct > benzothiophene, respectively. Lastly, in intramolecular [2 + 2] cycloaddition study, computed data have verified that the [2 + 2] cycloaddition step is driven by kinetic and not thermodynamic factors confirming all experimental observations.

8. KETENIMINIUM SALTS: REACTIVITY AND PROPENSITY TOWARD ELECTROCYCLIZATION REACTIONS

8.1. Introduction

Electrocyclization is a powerful method to build complex structural motifs. Recently we reported an efficient access to naphthylamines using intramolecular $6\pi/10\pi$ electrocyclization of keteniminium salts, [192] where the electrocyclizations of KIs were compared with ketenes, allenes, and trienes (Figure 8.1a). The computed data showed that keteniminium salts -both kinetically and thermodynamically- undergo electrocyclization more readily than ketenes, allenes, and trienes. Besides, naphthylamines, (benzo)thiophenes, (benzo)furans and indoles are also core scaffolds for several bioactive compounds used in various areas, such as agrochemicals, [233] pharmaceuticals, [234] antimitotic agents, [235] inhibitors of tubulin polymerization, [236] tumor growth, [237,238] and anti-viral [239,240] compounds (Figure 8.2).

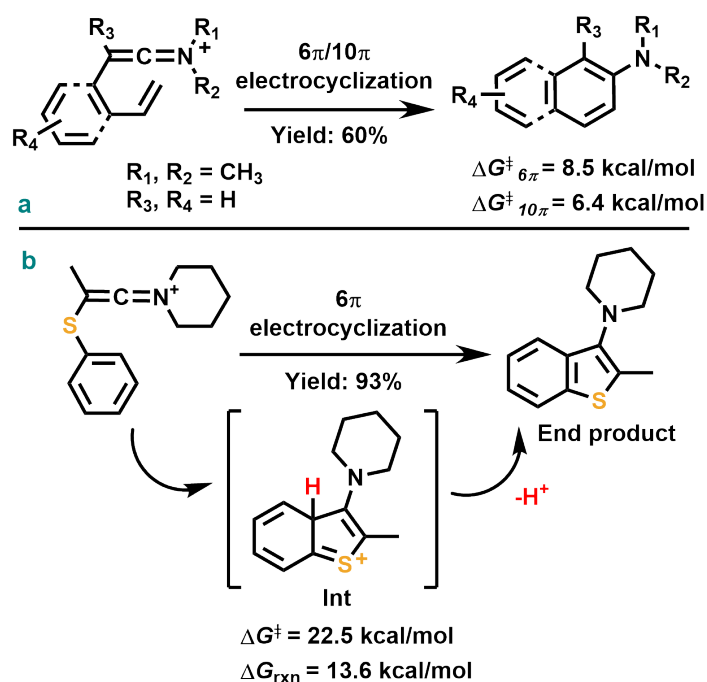


Figure 8.1. Access to (hetero)cyclic compounds using KI intermediates.

(M06-2X/6-31+G(d,p) in gas phase.)

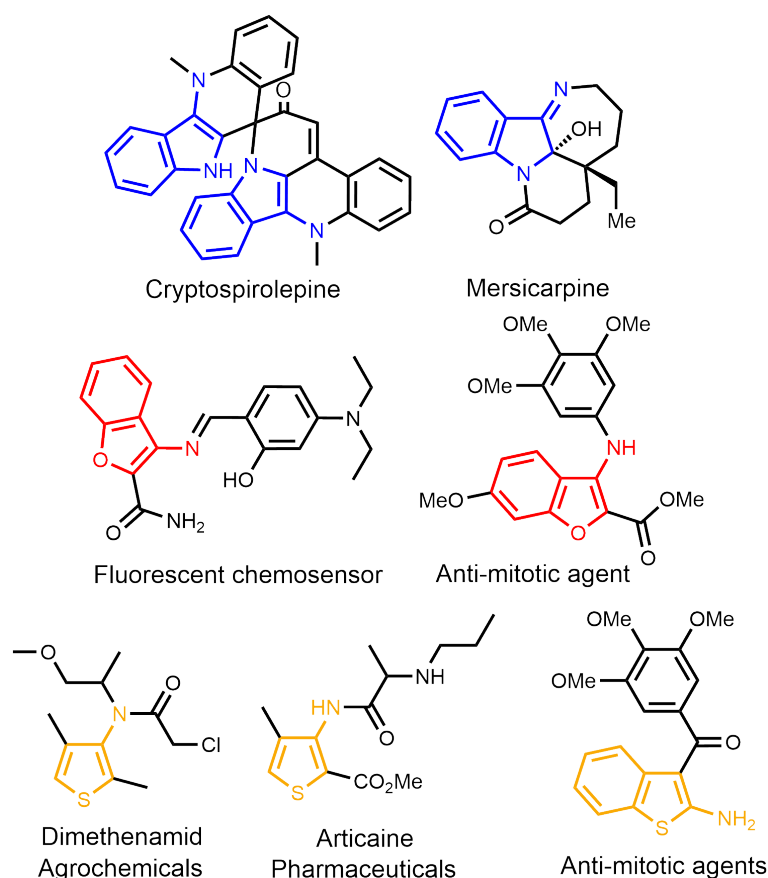


Figure 8.2. Illustration of bioactive heterocyclic compounds.

Our previous study has described an efficient access to 3-aminobenzothiophene derivatives through the 6π -electrocyclization of the corresponding KI (Figure 8.1b) [193]. These derivatives were obtained with the use of various N-substituents, particularly *N*-allyl and *N*-diallyl protecting groups under mild conditions. In addition, several plausible pathways for the cyclization of KI were computationally examined, namely a 6π -electrocyclization, a stepwise cationic cyclization involving a KI and a ‘direct’ cationic cyclization without formation of a keteniminium salt [193]. 6π -electrocyclization was suggested as the prevailing mechanism due to the higher activation barrier of the cationic ring closure proceeding without the formation of a keteniminium salt ($\Delta\Delta G^\ddagger \approx 8.0$ kcal/mol, M06-2X/6-31+G(d,p)). Accordingly, 6π -electrocyclization initially leads to an intermediate (Int) bearing a H atom. Upon deprotonation, aromaticity is established and the end product is obtained (Figure 8.1a). The present study aims to extend this knowledge to assess the ease of formation of a variety of heterocyclic systems, by means of computationally analyzing the relative barriers of 6π -electrocyclizations of keteniminiums, leading to pyrroles 9, furans 10, thiophenes 11 as

well as indoles 13, benzofurans 14, and benzothiophenes 15 (Table 8.1) [241]. Moreover, the true nature of the cyclization mechanism of KIs will be thoroughly scrutinized via a range of different analysis techniques. Furthermore, we focus on reactivity differences among keteniminium derivatives bearing different substituents and heteroatoms. This knowledge will allow substituent modifications to obtain more reactive/activated KI to access the desired heterocyclic compounds. We aim to examine a plethora of substituents including electron donating group (EDG) and electron withdrawing group (EWG). The molecular systems under investigation in this study were divided into two groups, namely Group I and Group II as tabulated in Table 8.1.

Table 8.1. Electrocyclization reactions of KI leading to (hetero)cyclic systems.

Keteniminium Salt			Target Compounds		
X	Group I		X		
N-Me	Enamine	1	N-Me	Pyrrole	9
O	Enol ether	2	O	Furan	10
S	Vinyl sulfide	3	S	Thiophene	11
C=C	Butadiene	4	C=C	Benzene	12
X	Group II		X		
N-Me	Aniline	5	N-Me	Indole	13
O	Phenyl ether	6	O	Benzofuran	14
S	Phenyl sulfide	7	S	Benzothiophene	15
C=C	Styrene	8	C=C	Naphthalene	16

8.2. Methodology

A density functional theory (DFT) study has been conducted in order to explore and compare the ease of formation of different heterocyclic systems via electrocyclization reac-

tions of keteniminium ions. All reactions were modeled using M06-2X, a hybrid meta-GGA known for its good performance in organic systems with dispersion effects [39, 50, 228]. The 6-31+G(d,p) basis set was employed for all calculations. Ultrafine grid was applied for highly accurate integral evaluation (see Appendix, Table S1 for a DFT survey) [242]. For systems bearing sulfur atoms, namely vinyl sulfide and phenyl sulfide substituted KIs leading to thiophenes 11 and benzothiophenes 15, respectively, the 6-311++G(3df,3pd) basis set was employed on sulfur atoms for more accurate results [205, 243]. All geometry optimizations and frequency calculations were performed in chloroform (CHCl_3 , $\epsilon = 4.7113$) using IEF-PCM [59, 206] with the Gaussian 09 (G09) program package [223]. All free energies are reported at 1 atm and 298 K. Furthermore, energy refinements were conducted with hybrid-GGA MPW1K, [51] range-separated ω B97XD and double hybrid B2PLYP [52] functionals to establish hierarchy in the “Jacob’s Ladder” to accurately evaluate the barriers. Frequency calculations were utilized to define stationary points as minima (ground states) or first order saddle points (transition states). Intrinsic reaction coordinate (IRC) calculations were conducted to verify that each transition state (TS) leads to its corresponding reactant and product [208–212]. Additionally, Frontier Molecular Orbital (FMO) [216, 217] analysis, as well as nucleus-independent chemical shift (NICS) [63, 64] analysis were performed using the 6-311++G(d,p) basis set. The NICS values were computed using ghost atoms (Bq) at the center and 1 Å below and above the ring critical points (RCP) by the GIAO [244, 245] (gauge-independent atomic orbital) method. The (3,+1) ring critical points were defined using the XAIM program developed by Bader [69]. ACID calculations (anisotropy of the current-induced density) were performed with the code provided by Herges and coworkers [65, 66]. Natural Bond Orbital (NBO 6.0) [246] and the quantum theory of atoms in molecules (QTAIM) calculations were performed at the M06-2X/ATZ2P in CHCl_3 with no frozen core and good numerical quality with the Amsterdam Density Functional package (ADF) [247, 248].

8.3. Results and Discussion

In an effort to assess and compare the ease of electrocyclization reactions of keteniminium ions depicted in Table 8.1, a thorough DFT study was executed [241]. Firstly,

a detailed structural and energetic analysis comparatively assessing relative reactivities of keteniminiums was performed. Secondly, the true nature of the reaction mechanism was explored by means of several analysis techniques. Thirdly, the effect of various substituents on the reactivity of keteniminium ions towards 6π -electrocyclization reactions was elucidated. Finally, computational predictions were experimentally confirmed for a selection of KI.

8.3.1. Structure, Energetics and Reactivity of Keteniminium Ions in Electrocyclization Reactions

Structural features of keteniminium ions (Table 8.1), comparative energetics and relative reactivities in electrocyclization reactions are detailed in this section.

8.3.1.1. Structural Features of Keteniminium Ions. Conformational spaces were scanned for each KI depicted in Table 8.1 and surprisingly, minimum energy conformers of enamine 1 and aniline 5 showed a non-linear orientation for C3=C2=N1 atoms (KI-1:134.2° and KI-4:132.6°, respectively) when compared to systems containing O and S heteroatoms (Figure 8.3). Linear conformers (C3=C2=N1 bond angles 180°) of enamine 1 and aniline 5 were found to be considerably higher in energy ($\Delta G_{rel} = 7.8$ and 9.5 kcal/mol, respectively, M06-2X/6-31+G(d,p) in CHCl₃) (Figures 8.4a and 8.5a). Upon closer inspection of the C4-X-C3 angles of the non-linear conformers of KI-1 and KI-4, it was revealed that when X=N, the nitrogen atom (Nx) bears sp² character and has trigonal planar geometry. Whereas, C4-X-C3 angles for linear conformers (Figures 8.4a and 8.5a) illustrate that the nitrogen atom (Nx) exhibits trigonal pyramidal geometry and sp³ character. This points to a Nx=C3-C2=N1 type conjugated structure that competes with the expected Nx-C3=C2=N1 form of the keteniminium, for KI-1 and KI-4. As expected, the C4-X-C3 angles of keteniminiums with X=O, S atoms (KI-2, KI-3, KI-5, and KI-6) are bent and the C3=C2=N1 structure is linear (Figure 8.3). Additionally, non-covalent interactions, [62] more particularly CH- π and cation- π interactions, were also considered for Group II keteniminium ions (Figure 8.3 and Figure A.15). CH- π interactions were shown to contribute to the stabilities of KI-4 (CH... π distance = 3.41 Å and 3.67 Å) and KI-6 (CH... π distance = 3.43 Å and 3.51 Å). However, directionality plays an important role in CH- π interactions, [249] and the ring orientation

must allow the interaction of the CH with the aromatic quadrupole moment, as such, even a CH $\cdots\pi$ distance of 3.48 Å (in KI-4) may not constitute a CH– π interaction (see NCIPLOT in Figure A.15). Moreover, large CH $\cdots\pi$ distances (as in KI-5) have much less stabilizing effects and do not qualify as CH– π interactions.

8.3.1.2. Effect of Nx-substituents on Enamine and Aniline Bearing Keteniminium Ions. The linearity of the KI is clearly affected by the substituents on the aniline and enamine nitrogen (Nx). In order to elucidate the effect of the Nx-substituent, the N-methyl group in enamine 1 and aniline 5 were replaced by electron withdrawing fluorocarbons (–CF₃ and –CH₂CF₃) and a tosyl group (–Ts). Structural features are illustrated in Figures (Figures 8.4 and 8.5, and indicate that for both enamine and aniline systems, electron withdrawing groups (EWG) increase linearity in the reactant conformers and lower $\Delta\Delta G_{rel}$, albeit still favoring the non-linear conformation. The computed data reveals that linearity can be somewhat restored in keteniminiums bearing aniline and enamine moieties by reducing the electron density on the Nx nitrogen atom via electron-withdrawing substituents. This verifies that the loss of linearity in these KI's originates from the willingness of the Nx lone pair to compete for a double bond, forming the conjugated structure Nx=C3–C2=N1, where the C3–C2 bond is no longer a double bond and the C3–C2–N1 moiety is no longer linear.

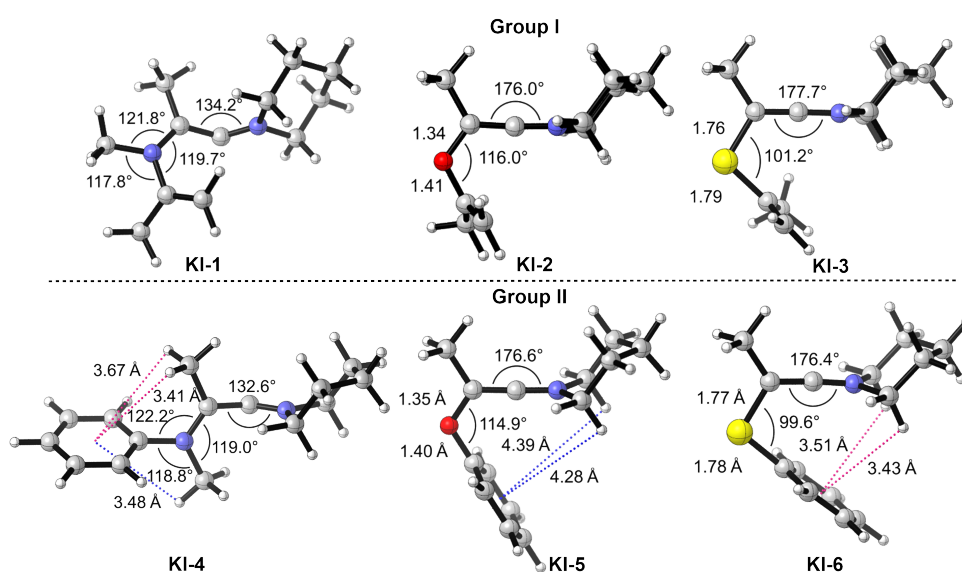


Figure 8.3. Optimized structures of KIs. (M06-2X/6-31+G(d,p) in CHCl₃, extra basis set for sulfur atoms; pink and blues colors denote CH– π , non-CH– π interactions, respectively.)

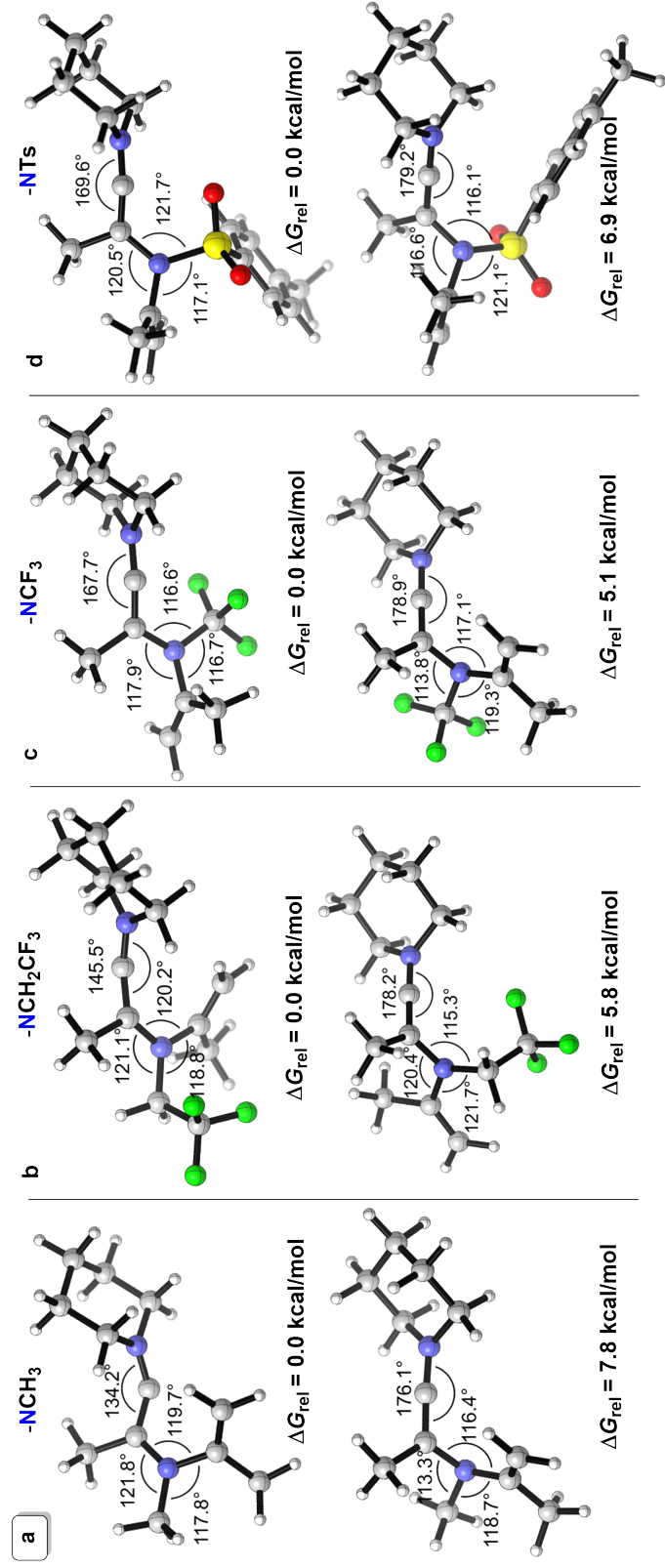


Figure 8.4. Optimized structures for KIs of Nx-substituted enamine derivatives in Group I. M06-2X/6-31+G(d,p) in CHCl₃, extra basis set for S atom.

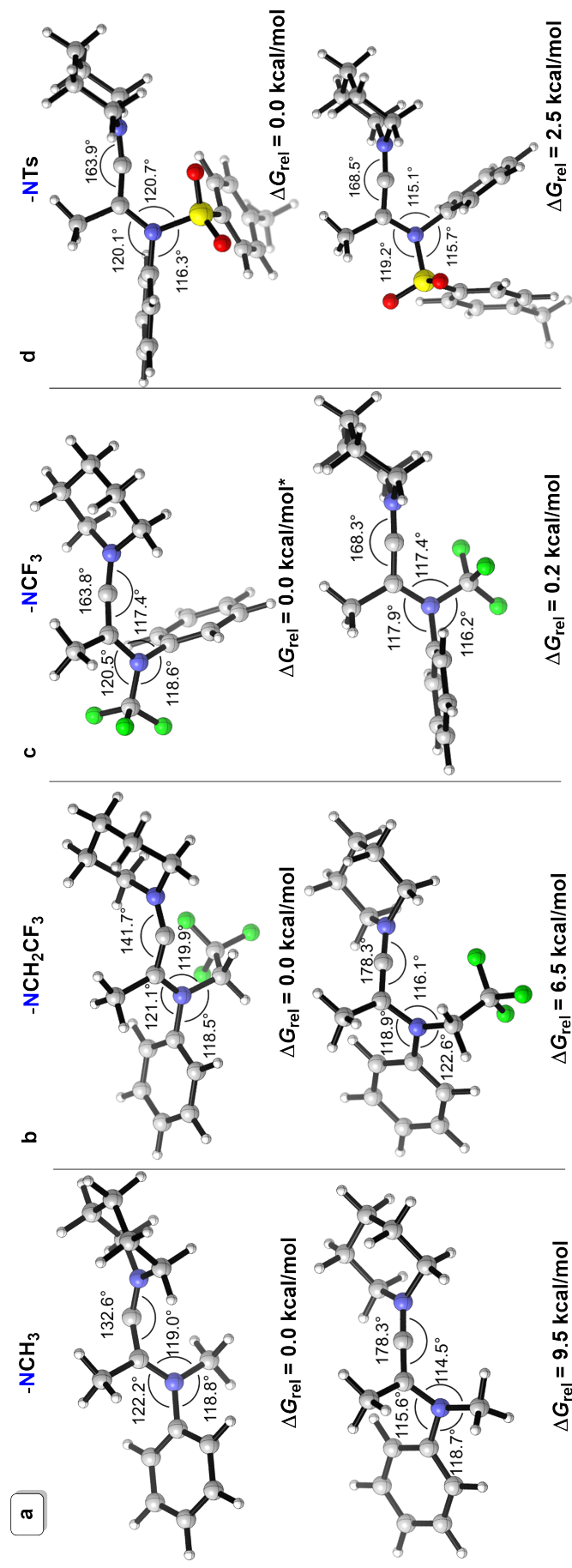


Figure 8.5. Optimized structures for KIs of Nx-substituted aniline derivatives in Group II. M06-2X/6-31+G(d,p) in CHCl₃, extra basis set for S atom. *To overcome imaginary frequency M06-2X/6-31+G(d,p)//B3LYP/6-31+G(d,p) in CHCl₃.

8.3.2. Energetic Analysis of Electrocyclization Reactions Involving Keteniminium Ions

A level of theory study was performed to assess the energetic cost of electrocyclization reactions involving keteniminium ions illustrated in Table 8.1. The effect of the heteroatom (X) was further scrutinized by adding a non-hetero 'ethylene' group as X to fully assess the ease of formation of (hetero)cyclic systems. Evolution of bond distances (Table A.4) were examined throughout the electrocyclization reaction coordinate for all hetero-systems. C3–C2 and Nx–C3 bond lengths of non-linear enamine 1 and aniline 5 show partial double bond character and closely resemble bond lengths of the TS, whereas C3–C2 bonds of the linear conformers in question are double bonds and Nx–C3 bond lengths display single bond character (Table A.4). This validates that the electrocyclization reactions leading to pyrrole 9 and indole 13 proceed from a non-linear pre-reactive conformer (PRC), as such all Gibbs free energies of activation and reaction for these system were calculated from the PRC. Computed free energies of activation (ΔG^\ddagger) and reaction (ΔG_{rxn}) are presented in Table 8.2. All energies for the formation of pyrrole (entry1) and indole (entry 5) are relative to the pre-reactive conformer (PRC). Electrocyclization reactions involving vinylic double bonds (Group I) were shown to have significantly lower activation barriers in the range of 4.8-15.5 kcal/mol (B2PLYP/6-31+G(d,p)//M06-2X/6-31+G(d,p)) compared to their phenylic counterparts (Group II), which have barriers varying between 16.4 and 25.5 kcal/mol, due to the disruption of aromaticity in the latter. It should be noted that similar barrier trends were observed regardless of the level of theory.

Among Group I molecules, formation of the pyrrole derivative 9 has the lowest activation barrier (TS1, $\Delta G^\ddagger = 3.0$ kcal/mol, M06-2X/6-31+G(d,p) in CHCl_3) and is, therefore, predicted to undergo electrocyclization most readily. Similarly, in the second group, the indole derivative 13 has the lowest free energy barrier (10.8 kcal/mol, M06-2X/6-31+G(d,p) in CHCl_3), predicting a higher ease of formation when compared to benzofuran 14 and benzothiophene 15. The same reactivity pattern is observed in both groups; thiophene 11 (benzothiophene 15) being the least reactive, followed by furan 10 (benzofuran 14).

Structural features of transition states disclose further information on the extent of the reaction (Figure 4). Critical distances in the range of 2.19-2.42 Å reveal the reactant-like

nature of the transition states for Group I resulting in more exothermic reactions and lower free energies of activation. Whereas, for Group II, much shorter C–C critical distances (in the range of 1.98-2.10 Å) highlight the product-like nature of the transition states (TSs), leading to significantly higher free energies of activation and endothermic reactions. Only aniline substituted KI leading to indole 13 results in a slightly exothermic reaction ($\Delta G_{\text{rxn}} = -4.9$ kcal/mol, M06-2X/6-31+G(d,p)) in Group II. Hence, early TS characteristics verify higher reactivity of Group I. Additionally, the C3=C2=N1 bond angle is significantly smaller for enamine and aniline containing systems (134.5° and 133.5° for TS1 and TS4, respectively) compared to others.

Table 8.2. Free energy barriers (ΔG^\ddagger), and reaction free energies (ΔG_{rxn}) for electrocyclization reactions of KIs. Free energies in kcal/mol.

		M06-2X		MPW1K		ω B97XD		B2PLYP	
Entry	Group	ΔG^\ddagger	ΔG_{rxn}	ΔG^\ddagger	ΔG_{rxn}	ΔG^\ddagger	ΔG_{rxn}	ΔG^\ddagger	ΔG_{rxn}
1	pyrrole	3.0	-37.8	1.9	-42.4	2.9	-39.3	4.8	-34.3
2	furan	6.0	-23.8	4.8	-27.8	5.5	-26.6	10.1	-19.1
3	thiophene	11.4	-22.2	9.9	-27.4	10.9	-25	15.5	-16.9
4	benzene	9.2	-34.8	10.4	-38	8.0	-37.6	14.5	-29.3
5	indole	10.8	-4.9	10.1	-8.3	11.6	-5.8	16.4	0.5
6	benzofuran	17.0	8.0	15.5	4.2	16.1	5.3	22.4	12.7
7	benzothiophene	21.0	9.0	18.6	3.9	20.4	6.9	25.5	13.8
8	naphthalene	14.8	1.7	17	1.6	13.7	-0.3	21.9	10.9

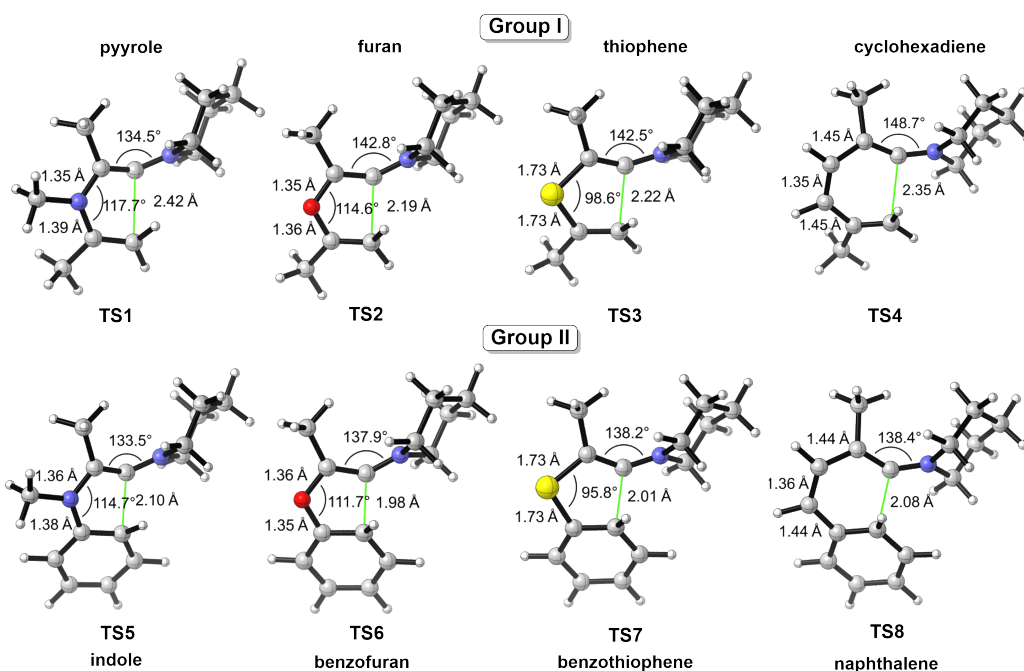


Figure 8.6. Optimized transition state structures. M06-2X/6-31+G(d,p) in CHCl_3 , extra basis set for sulfur atom.

In our recent work, an efficient access to 3-aminobenzothiophene with various substituents was reported (Figure 8.2b) [193]. In that study, benzothiophene 15 (entry 7) was successfully synthesized at room temperature (RT) and computationally optimized at the same level of theory (M06-2X/6-31+G(d,p)) in gas phase ($\Delta G^\ddagger_{\text{gas}} = 22.5$ kcal/mol) [193]. Current data ($\Delta G^\ddagger_{\text{solvent}} = 21.0$ kcal/mol, M06-2X/6-31+G(d,p), Table 8.2) is in line with the previously reported result. More recently, intramolecular competition reactions of vinyl sulfide and phenyl sulfide were modelled in CHCl_3 at the MPW1K/6-31+G(d,p)//M06-2X/6-31+G(d,p) level of theory to investigate the favorable formation of thiophene derivatives [227]. Consistent with experimental findings, the electrocyclization reactions leading to thiophene formation ($\Delta G^\ddagger = 8.3$ kcal/mol, M06-2X/6-31+G(d,p)) was shown to be both kinetically and thermodynamically favored over the formation of benzothiophene ($\Delta G^\ddagger = 16.4$ kcal/mol, M06-2X/6-31+G(d,p)) [227].

Similar to the outcome of the aforementioned intramolecular competition reaction, [227] the free energy of activation for electrocyclization of vinyl sulfide 3 ($\Delta G^\ddagger = 9.9$ kcal/mol, MPW1K/6-31+G(d,p)//M06-2X/6-31+G(d,p), Table 8.2) is shown to be notably lower than that of phenyl sulfide 7 ($\Delta G^\ddagger = 18.6$ kcal/mol, MPW1K/6-31+G(d,p)//M06-2X/6-31+G(d,p).

Considering homocyclization (entries 4 and 8 in Table 8.2), reaction barriers (TS4, $\Delta G^\ddagger = 9.2$ kcal/mol and TS8, $\Delta G^\ddagger = 14.8$ kcal/mol, M06-2X/6-31+G(d,p)) remain between the lowest and highest values and the computational findings for entry 4 in Table 8.2 are in line with our previous study [192] ($\Delta G^\ddagger_{\text{gas}} = 8.5$ kcal/mol, $\Delta G_{\text{rxn}} = -44.5$ kcal/mol, M06-2X/6-31+G(d,p) in gas phase). Hence, in light of previous experimental and computational studies, the computational results presented herein suggest the likelihood of formation of all heterocyclic systems depicted in Table 8.1 via electrocyclization of their corresponding KI derivatives. Lastly, the energetic consequences of electron-withdrawing Nx-substituents ($-\text{CF}_3$, $-\text{CH}_2\text{CF}_3$, $-\text{Ts}$) on electrocyclization of keteniminiums bearing enamine and aniline moieties (Figures 8.4 and 8.5) were investigated (see Appendix, Figure A.16). Computed data show that EWGs, in particular $-\text{CF}_3$ and $-\text{Ts}$, significantly increase the activation barriers and decrease product stabilities.

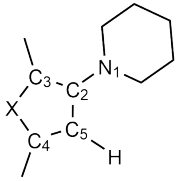
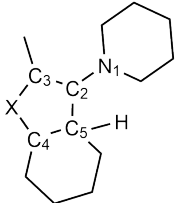
8.3.3. Population Analysis and Local Reactivity Descriptors

Prior to analyzing the nature of the heterocyclic electrocyclization reactions we investigated the effect of different heteroatoms on the KI reactivity by means of population analysis and local descriptors for all KI's listed in Table 8.1.

8.3.3.1. Population Analysis. In order to gain insight into the electrostatic nature of the electrocyclization reaction and rationalize the calculated order of activation barriers, NBO 6.0 analysis was performed as shown in Table 8.3. Note that 6π -electrocyclization initially leads to an intermediate (Int) where C5 bears a H atom. Upon deprotonation of C5, aromaticity is established and the end product is obtained. Population analysis results depict considerably larger negative charges on carbon C5, indicating its reactivity towards the positively charged carbon C2. NPA results show that carbon C5 of enamine 1, enol ether 2 and vinyl sulfide 3 substituted KIs leading to pyrrole 9, furan 10 and thiophene 11, respectively, bear approximately two-fold larger negative charges compared to carbon C5 of aniline 5, phenyl ether 6 and phenyl thioether 7 substituted KIs, implying lower reactivity of the aromatic ring, as expected. Additionally, higher negative charges on carbon C5 were detected in N-heteroatom substituted KIs (enamine 1 and aniline 5) decreasing consistently through O

and S heteroatom substituted KIs. Sulfur shows a tendency to donate electrons to the delocalization hence, its positive charge. Evaluation of the NPA charges indicate the keteniminium nature of the reacting species.

Table 8.3. Evolution of NPA atomic charges throughout the electrocyclization reaction.
M062X/6-31+G(d,p)//M062X/6-31+G(d,p) in CHCl₃.

									
X= N-Me, O, S									
Group I					Group II				
Enamine					Aniline				
Charges	KI	KI-PRC	TS	Int	Charges	KI	KI-PRC	TS	Int
N1	-0.297	-0.330	-0.358	-0.446	N1	-0.298	-0.323	-0.385	-0.478
C2	0.460	0.216	0.247	0.241	C2	0.455	0.186	0.248	0.235
C3	0.159	0.260	0.208	0.054	C3	0.157	0.278	0.197	0.150
X=N-Me	-0.492	-0.394	-0.366	-0.265	X=N-Me	-0.476	-0.381	-0.343	-0.286
C4	0.232	0.204	0.244	0.428	C4	0.176	0.133	0.217	0.332
C5	-0.536	-0.410	-0.451	-0.509	C5	-0.273	-0.226	-0.288	-0.361
Enol ether					Phenyl ether				
Charges	KI	TS	Int		Charges	KI	TS	Int	
N1	-0.290	-0.364	-0.443		N1	-0.285	-0.389	-0.478	
C2	0.325	0.282	0.204		C2	0.336	0.254	0.188	
C3	0.323	0.307	0.186		C3	-0.319	0.322	0.296	
X=O	-0.492	-0.455	-0.366		X=O	-0.491	-0.443	-0.400	
C4	0.309	0.454	0.696		C4	0.265	0.402	0.528	
C5	-0.436	-0.522	-0.556		C5	-0.259	-0.231	-0.404	
Vinyl sulfide					Phenyl sulfide				
Charges	KI	TS	Int		Charges	KI	TS	Int	
N1	-0.303	-0.366	-0.412		N1	-0.304	-0.391	-0.464	
C2	0.412	0.352	0.298		C2	0.417	0.326	0.261	
C3	-0.193	-0.216	-0.332		C3	-0.186	-0.197	-0.216	
X=S	0.310	0.457	0.733		X=S	0.334	0.460	0.603	
C4	-0.161	-0.216	-0.045		C4	-0.204	-0.110	-0.077	
C5	-0.355	-0.458	-0.520		C5	-0.214	-0.314	-0.366	

8.3.3.2. Local Reactivity Descriptors. In order to predict local reactivities and rationalize the calculated order of barrier heights for the heterocyclic electrocyclization reactions, the electrophilic Parr function P_k^+ proposed by Domingo et al [79] and the Fukui function f_k^+ proposed by Yang and Mortier [80] were calculated.

P_k^+ for carbon atoms C2 and C5, in keteniminium ions of Group I and II, were calculated using NBO atomic spin density with the UM062X/6-31+G(d,p)//M062X/6-31+G(d,p) in CHCl_3 . The calculation of Fukui indices were performed with M062X/DZP//M062X/6-31+G(d,p) in CHCl_3 . The computed P_k^+ and f_k^+ for C2 and C5 are tabulated in Table 3. Analysis of the Parr and Fukui functions stress that C2 carbon is the most electrophilic center for all reactants in the following order: enamine > enol ether > vinyl sulfide (Group I); aniline > phenyl enol ether > phenyl sulfide (Group II). These findings are directly correlated to the activation barriers and reveal that higher P_k^+ and f_k^+ in C2 leads to lower activation barriers. There was no apparent correlation found for C5.

Table 8.4. Calculated P_k^+ and f_k^+ for the C2 and C5 carbon atoms of Groups I and II KIs.

Reactants	P_k^+		f_k^+	
	C2	C5	C2	C5
Enamine 1	0.714	0.015	0.448	0.002
Enol Ether 2	0.663	0.001	0.439	0.008
Vinyl sulfide 3	0.608	0.005	0.388	0.006
Aniline 5	0.692	-0.001	0.449	0.003
Phenyl Enol Ether 6	0.659	0.002	0.439	0.005
Phenyl sulfide 7	0.592	0.002	0.372	0.006

8.3.4. Nature of the Electrocyclization Reaction of Keteniminium Ions

The structural, energetic and population analysis of keteniminium cyclizations reactions detailed in the previous section does not indicate/validate the pericyclic character of the reactions studied. Herein, we decided to further investigate the true nature of the cyclization reactions under investigation. According to Berney and coworkers, pseudo-pericyclic reac-

tions possess lower activation barriers than pericyclic ones. [250] The significantly lower activation barriers (Table 8.2) for the formation of pyrrole 9 and indole 13 and the non-linear nature of the C3–C2–N1 structure in keteniminiums KI-1 and KI-4 (Figure 8.4) encouraged us to investigate the nature of the reaction in further detail. Therefore, we set out to perform FMO (data not presented here, see Appendix, Figure A.19), AIM, NICS and ACID analysis, for all systems under study, in order to distinguish between pericyclic and (non-planar)-pseudopericyclic reactions.

8.3.4.1. Atoms in molecules (AIM) Analysis. Atoms-in-molecules (AIM) analysis for transition state structures is a useful method to distinguish the nature of a reaction through the presence/absence of critical points [69]. AIM analysis were performed for transition states (TSs) of Groups I and II; findings indicate that new bond critical points (BCPs, (3,-1)) in TSs were formed as well as ring critical points (RCP) (3,+1), supporting a pericyclic type reaction as illustrated in Figure 8.7. Moreover, the AIM analysis displays lower density values for Group I when compared to Group II, signifying that newly formed C2–C5 bonds of Group I are weaker, indicative of early transition states and exothermic reactions.

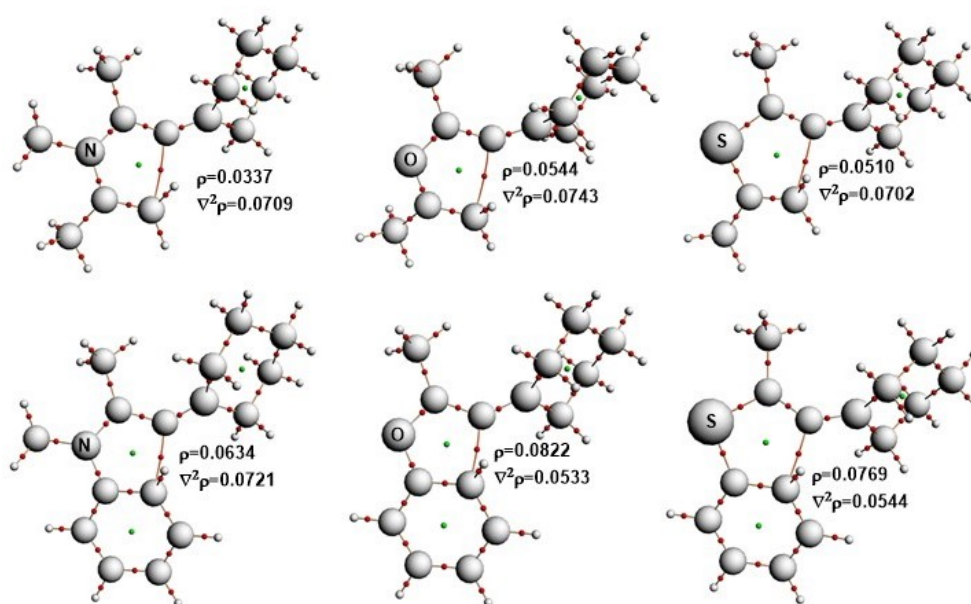


Figure 8.7. AIM analysis of the TS structures for Groups I and II. (Values in a.u., M06-2X/ATZ2P//M06-2X/6-31+G(d,p) in CHCl_3 .)

8.3.4.2. Nucleus-Independent Chemical Shifts (NICS) Analysis. Pericyclic ring closure reactions possess aromatic transition state (TS) structures according to Woodward–Hoffmann rules [251]. NICS introduced by Schleyer et al [63] is a magnetic measure/indicator of aromaticity, particularly for the evaluation of TS aromaticities. In the present study, NICS(-1) values, which are points placed 1 Å below the RCP (since the cyclization occurs along this trajectory, (Figure 8.8), were considered in order to account for π -electron contribution and to avoid the additional sigma (σ) electron contribution in NICS(0). Negative NICS values indicate aromaticity; calculated NICS(-1) values graphed in Figure 8.9 clearly show minima for TSs compared to their corresponding reactants and products, indicating aromaticity in the TS. The aromatic character of the TS confirms the pericyclic ring closure classified as electrocyclization. [252] Moreover, notably, NICS values of TSs in Group II are lower than the corresponding TSs in Group I. This points to larger aromatic stabilization of the TSs in Group II and is in agreement with our previous work [193] that proposed larger number of electrons (10π rather than 6π) contribute to the transition state. However, it is important to note that despite the larger aromatic stabilization of the TS, initial disruption of aromaticity still affords larger activation barriers for Group II.

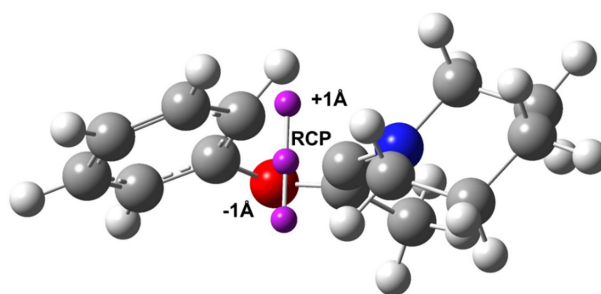


Figure 8.8. One of the representative image of points (Bq ghost atoms) for NICS calculations.

8.3.4.3. Anisotropy of the Induced Current Density Analysis. Herges and Geuenich developed the anisotropy of the induced current density (ACID) method in order to quantify and visualize electronic delocalization and conjugation [65]. This method is also used for the measurement of aromaticity in order to differentiate the type of the reactions, namely peri-

cyclic and pseudopericyclic reactions [65–68]. Lemal and coworkers defined the pseudo-electrocyclic reaction as a disconnection in the cyclic array [253]. In the present study, ACID analysis was carried out to conclusively elucidate the nature of cyclization reactions in Groups I and II. The continuous set of gauge transformation (CSGT) [254, 255] method was applied for the ACID calculations. ACID plots in Figure 8.10 indicate that TS structures do not display any disconnection at isosurface value of 0.03 au. Additionally, diatropic ring currents are known to be present in aromatic systems, where the magnetic field vector is orthogonal to the ring plane leading to clock-wise current. Diatropic ring currents were observed in all ACID isosurfaces of TSs analyzed, indicating the pericyclic nature of the reactions.

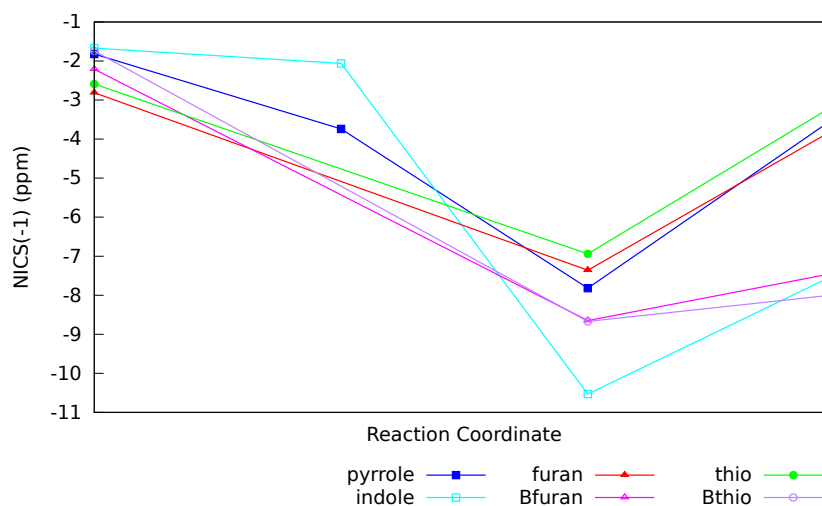


Figure 8.9. Variation of NICS along the reaction coordinates 1 \AA below the RCPs for Groups I and II. (M06-2X/6-311++G(d,p)//M06-2X/6-31+G(d,p) in CHCl_3). Note that the electrocyclization initially leads to an intermediate (Int) where C5 bears a H atom. Upon deprotonation of C5, aromaticity is established, and the end product is obtained.

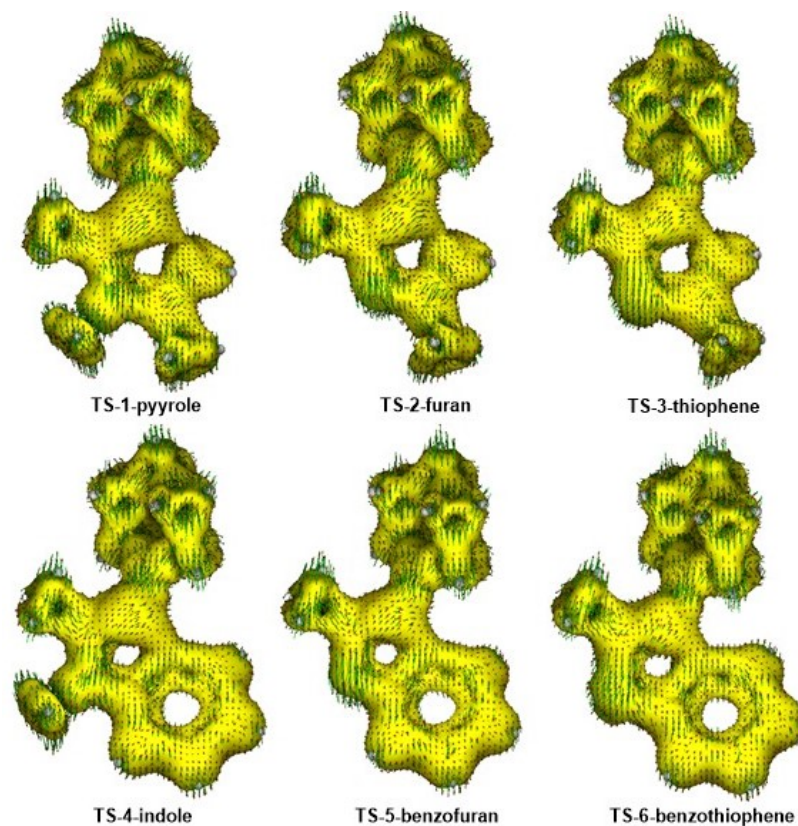


Figure 8.10. ACID plots for the transition states of Groups I and II.
(M06-2X/6-311++G(d,p)//M06-2X/6-31+G(d,p) in CHCl_3 , extra basis set for S atom,
isosurface value 0.03 a.u.)

Moreover, critical isosurface values (CIV) were calculated in order to quantify the delocalization and pinpoint critical values for the topology change from cyclic to noncyclic. Higher CIVs indicate strong delocalization and aromaticity, confirming the pericyclic character of the reaction. CIVs of TSs (TS1-3) in Group I are 0.034, 0.035, and 0.037, respectively; CIVs in Group II are 0.061, 0.053, 0.054 for TS4-6, respectively. Large CIVs both in Group I and II indicate pericyclic character of the reactions (CIV is usually ≤ 0.02 for a typical pseudopericyclic reaction).⁷⁸ Additionally, larger CIVs in Group II are associated with short C2–C5 bond distances (1.98–2.10 Å) leading to higher electron delocalization compared to Group I (2.19–2.42 Å). This outcome is in line with the higher densities and shorter critical distances observed for Group II in AIM analysis. Moreover, higher CIVs for Group II are consistent with larger NICS values, once again pointing towards a 10π -electrocyclization reaction for Group II. Briefly, $6\pi/10\pi$ -electrocyclizations for Groups I/II are characterized as pericyclic reactions, through FMO, QTAIM, NICS and ACID analysis.

8.3.5. Understanding Effect of Substituents on Keteniminium Reactivity

To evaluate the effect of substituents on keteniminium reactivity, a variety of substituted keteniminiums that are experimentally accessible have been selected [193, 227, 256]. Free energy of activation barriers (ΔG^\ddagger) and reaction free energies (ΔG_{rxn}) for $6\pi/10\pi$ -electrocyclizations of keteniminiums in Groups I and II (Table 8.1), are tabulated in Tables 8.5 and 8.6, respectively. Although M06-2X data are tabulated herein, energy refinements at MPW1K, ω B97XD and B2PLYP levels of theory were also performed for all systems (see Appendix, Table S3-8). To be able to systematically check the effect of substituents on vinylic and phenylic moieties, methyl substitution was chosen for the alpha position (C3-Me), for all systems. The effect of substituents at the alpha position will be systematically investigated in a subsequent study. Generally speaking, regardless of the substituents, electrocyclizations of Group I were found to be highly exergonic, making these reactions thermodynamically more favorable. This is also in line with their lower free energies of activation (Table 8.5). Computed data reveal that Group I products are both kinetically and thermodynamically more favored over their Group II counterparts. While the formation of the indole systems in Group II was also found to be slightly exergonic except in the case of ortho- CF_3 and ortho and para -Cl substituents (Table 8.6, entries 8 and 13, respectively). However, electrocyclizations yielding benzothiophenes and benzofurans, showed endergonic reactions, making them less favorable. Substituent positions in Tables 8.5 and 8.6 were given in Figure 8.11.

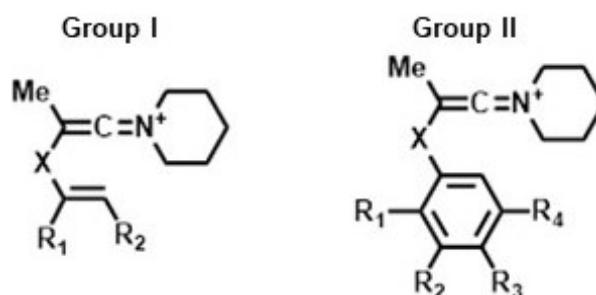


Figure 8.11. R group positions for Groups I and II.

Table 8.5. Effect of substituents on free energy barriers (ΔG^\ddagger), and reaction free energies (ΔG_{rxn}) of 6π -electrocyclizations of KI-Group I.
(Free energies in kcal/mol.)

Entry	Enamine		Enol ether		Vinyl sulfide				
	R1	R2	ΔG^\ddagger	ΔG_{rxn}	ΔG^\ddagger	ΔG_{rxn}	Yield% [227]		
1	CH3	H	3.0	-37.8	6.0	-23.8	11.4	-22.2	80%
2	H	CH3 (<i>E</i>)	2.8	-29.8	10.6	-14.0	14.5	-14.5	
3	H	CH3 (<i>Z</i>)	7.0	-33.0	15.6	-14.1	20.2	-15.0	
4	H	H	2.9	-35.1	10.5	-16.1	14.3	-18.5	
5	Ph	H	3.8	-35.0	8.3	-23.9	13.5	-22.1	95%
6	H	Ph (<i>E</i>)	2.6	-30.6	9.4	-13.4	13.1	-13.8	72% <i>E/Z</i> :80:20
7	H	Ph (<i>Z</i>)	5.4	-31.1	15.1	-11.5	18.7	-14.0	10% <i>E/Z</i> 13:87
8	CO2Me	H	6.4	-31.8	12.8	-12.7	15.7	-18.0	47%
9	H	CO2Me (<i>E</i>)	6.0	-24.7	12.6	-8.3	15.4	-10.7	56% <i>E/Z</i> :60:40
10	CO2Me	CO2Me	7.2	-26.7	16.9	-6.5	17.0	-13.5	58% <i>E/Z</i> :67:33
11	CN	H	5.3	-32.4	15.9	-9.3	20.0	-14.0	36%
12	H	CN (<i>E</i>)	7.0	-19.3	15.3	-1.7	16.1	-6.7	
13	H	CN (<i>Z</i>)	8.0	-22.9	20.1	-1.0	21.1	-7.1	54% <i>E/Z</i> :100:0

Table 8.6. Effect of substituents on free energy barriers (ΔG^\ddagger) and reaction free energies (ΔG_{rxn}) of 10π -electrocyclizations of KI-Group II.
(Free energies in kcal/mol.)

Entry	Aniline				Phenyl ether				Phenyl sulfide				
	R1	R2	R3	R4	ΔG^\ddagger	ΔG_{rxn}	Yield% [257]	ΔG^\ddagger	ΔG_{rxn}	Yield% [257]	ΔG^\ddagger	ΔG_{rxn}	Yield% [193]
1	H	H	H	H	10.8	-4.9	84%	17.0	8.0	69%	21.0	9.0	93%
2	H	CH3	H	CH3	9.2	-4.7		13.6	4.8	93%	18.8	8.5	78%
3	CH3	H	H	H	15.2	-1.9		16.3	6.3		19.3	7.6	
4	H	CH3	H	H	8.9	-7.5		14.6	4.4		18.9	7.1	
5	H	H	CH3	H	10.4	-4.9		16.6	7.0		21.7	10.4	
6	H	H	CF3	H	10.1	-3.8		18.1	9.6		22.8	11.5	80%
7	H	CF3	H	H	9.6	-3.5		19.6	11.7		20.7	11.5	
8	CF3	H	H	H	17.2	1.5		18.9	11.9		21.5	10.8	88%
9	H	H	CN	H	9.9	-3.9		19.3	12.2		22.0	12.3	47%
10	H	CN	H	H	10.5	-3.1		19.8	12.0		22.4	12.0	
11	H	Cl	H	H	10.0	-6.0		18.5	9.3		21.2	9.3	
12	H	H	Cl	H	11.0	-4.1		17.5	10.1		22.1	11.7	
13	Cl	H	Cl	H	17.8	2.8		20.5	13.3	91%	22.9	13.0	89%

8.3.5.1. Role of the Substituents in Group I. While each substituent has a different effect on the reactivity itself, the position of the R group plays a potent role on the ease of electrocyclization. In case of R1 and R2, calculations in Table 8.5 demonstrate a general trend, where R1 and R2 with electron donating capabilities (EDG) allow the electrocyclization reaction to proceed with more ease by increasing the electron density around C5 carbon. Moreover, EWG groups ($-\text{CO}_2\text{Me}$, $-\text{CN}$) increase the activation barriers. For all systems, the Z isomer appears to have a higher activation barrier, caused by the steric clash between Z orientation of substituents and the piperidine group (Figure 8). Hence, electrocyclization of E isomers are favored. Activation barriers for Z isomers are also in $\text{CH}_3 < \text{Ph} < \text{CN}$ order.

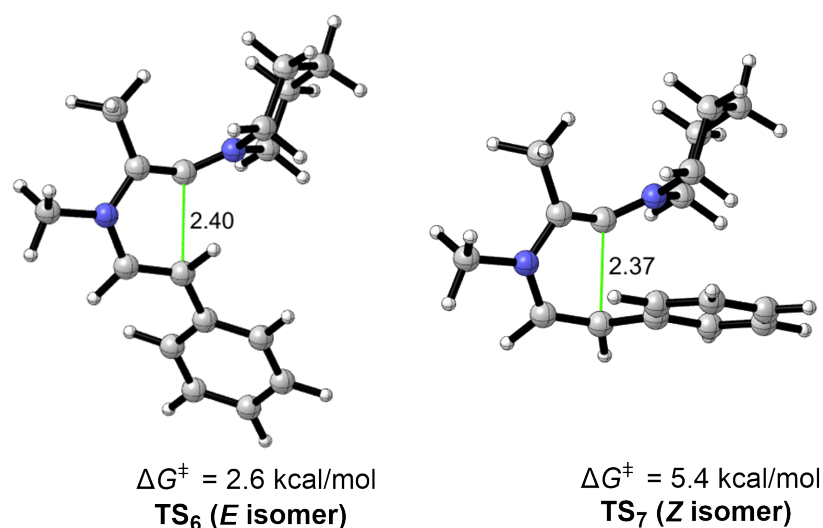


Figure 8.12. Optimized TS structures for the E and Z isomers (entries 6 and 7 in Table 8.5) of enamine systems (Group I). M06-2X/6-31+G(d,p) with IEF-PCM in CHCl_3 ; critical distances in Å.

In case of R1 substituent: For enamine systems, the activation free energy barriers are in order $\text{CH}_3 \approx \text{H} < \text{Ph} < \text{CN} < \text{CO}_2\text{Me}$. On the other hand, the activation barriers leading to furans and thiophenes have increasing orders as follows: $\text{CH}_3 < \text{Ph} < \text{H} < \text{CO}_2\text{Me} < \text{CN}$. Due to the steric hindrance between N–Me and R1, electron donating groups in R1 position slightly increase the barriers compared to furan and thiophene cases, causing the difference in order of reactivities. Apart from electron withdrawing effect, due to steric hindrance, electrocyclization of $-\text{CO}_2\text{Me}$ substituted KI, leading to pyrrole, shows the highest free energy of activation. In electrocyclizations of corresponding KIs leading to furan and thiophene, the highest barriers belong to the cyano ($-\text{CN}$) substituted KI.

In case of R2 substituent: In case of enamine, the effect of the R2 is similar among methyl (-CH₃), phenyl (-Ph) and hydrogen (-H). Similar trends are also consistently observed for enol ether and vinyl sulfide counterparts, except for the phenyl moiety showing the lowest activation barriers. Similar to the R1 effect, EWGs increase the activation barriers for all systems in CO₂Me < CN order. Overall, among Group I ions, activation barriers of all enamine derivatives are significantly lower, followed by enol ether and vinyl sulfide derivatives, respectively.

8.3.5.2. Role of the Substituents in Group II. For Group II, -CH₃, -CF₃, -Cl, -CN were placed in ortho (o-), para (p-) and meta (m-) positions as depicted in Table 5. The activation barriers of ortho-substituted KIs leading to indoles show an increase in the order: H < CH₃ < CF₃ < Cl, whereas activation barriers for KIs leading to benzofuran and benzothiophene are as follows: CH₃ < H < CF₃ < Cl. The differences stem from the steric hindrance between N-Me and the substituents at o-position. In case of para-substituents, for all systems, the activation barriers are more or less the same. Regarding meta-substituents, the activation barriers of KIs leading to indole are close. The relative order of meta-substituents for electrocyclizations to benzofuran and benzothiophene are CH₃ < H < Cl < CF₃ ≈ CN and CH₃ < CF₃ ≈ H ≈ Cl < CN, respectively. Similar to Group I, activation barrier trends in Group II follow: indole < benzofuran < benzothiophene.

Ultimately, the substitution patterns investigated herein illustrate that the pyrrole systems are the most reactive with the lowest activation barriers, whereas the benzothiophenes are the least reactive with free energies of activation as high as 22.9 kcal/mol (Table 8.6, entry 13). Due to the disruption of aromaticity, free energies of activation for Group II are significantly higher compared to Group I. All in all, it is important to note that among all six heterocyclic systems, the highest barrier (21.0 kcal/mol) is for the formation of 'parent' benzothiophene (Table 5, entry 1), which was already successfully synthesized.¹⁷ Accordingly, the formation of all heterocyclic systems via the 6π/10π-electrocyclization are suggested to be plausible in the light of computational and experimental findings [193, 227, 256].

8.4. Conclusions

In the study on electrocyclization of KI's, structural and energetic analysis, nature of the reactions and the reactivity differences leading to six different heterocyclic systems were computationally examined. The computational results reveal that the 6π -electrocyclization of enamine substituted KI 1 leading to 3-aminopyrroles 9 is favored in Group I, when lowest activation and reaction free energies are considered. Aniline substituted keteniminiums 5 leading to 3-aminoindoles 13 has the lowest free energy of activation in Group II, compared to phenyl ether and phenyl sulfide substituted keteniminiums furnishing the corresponding 3-aminobenzofurans 14 and 3-aminobenzothiophenes 15, respectively. The aromatic moiety in Group II decreases the reactivity compared to the systems in Group I, as expected due to the disruption of the aromaticity in the transition state for cyclization. Notably, the pericyclic nature of the reaction was validated by means of AIM, NICS, ACID analysis, also pointing towards a 10π -electrocyclization for Group II rather than the 6π -electrocyclization observed in Group I. Lastly, among all six heterocyclic systems, the highest barrier is for the formation of benzothiophene 15, which was previously shown to readily form at RT. In line with computational findings, experimental results show that electrocyclization reactions of selected systems in Group II were achieved under mild conditions, suggesting the likelihood of formation of all heterocyclic systems studied herein from their corresponding keteniminium derivatives. Overall, this study is expected to contribute to the understanding of reactivity differences of keteniminium ions and further aid synthetic applications.

9. CONCLUDING REMARKS

This dissertation presents the outcomes of deamidation's impact on the structure and function of Bcl-x_L and the chemistry of KI's including its formation and subsequent reactions.

In the first part of the thesis, we explored deamidation-induced conformational changes in Bcl-x_L to gain insight into its loss of function by performing microsecond-long molecular dynamics (MD) simulations. MD simulation outcomes showed that the IDR motion and interaction patterns have changed notably upon deamidation. Principal component analysis (PCA) demonstrates significant differences between wild type and deamidated Bcl-x_L and suggests that deamidation affects the structure and dynamics of Bcl-x_L. The combination of clustering analysis, H-bond analysis, and PCA revealed changes in conformation, interaction and dynamics upon deamidation. Differences in contact patterns and essential dynamics that lead to a narrowing in the binding groove (BG) are clear indications of deamidation-induced allosteric effects. In line with previous studies, we show that the intrinsically disordered region plays a very important role in the loss of apoptotic function of Bcl-x_L, while providing a unique perspective on the underlying mechanism of Bcl-x_L deamidation-induced cell death. Additionally, we emphasized the importance of using full-length Bcl-x_L in membrane environment as well as the impact of an important post-translational modification, i.e., deamidation. The findings suggest that change in interaction pattern, protein orientation towards membrane and protein-membrane interaction play pivotal role on the structural differences of the protein upon deamidation. Lastly, MD simulations confirmed that unbounded BH3-only peptides are dynamic in water compared to bound state (complex systems). As a future work, complex systems (Bcl-x_L-BH3-only peptides) will be investigated before and after deamidation both in water and membrane environments.

In the second part of the thesis, keteniminium (KI) chemistry was examined including its formation and subsequent reactions (electrocyclization and cycloaddition reactions). A wide range of substituents was examined to give insight on their potential contributions to the ease of formation of KIs. The computed data revealed that the reactivity of the start-

ing nucleophilic amides towards the electrophilic triflic anhydride directly affected the ease of formation of the keteniminium salt. Additionally, DFT calculations were performed to rationalize the experimentally observed reactivity difference in the [2 + 2] cycloaddition of keteniminiums with alkene and alkyne reactant partners. Calculations verified that the [2 + 2] cycloaddition reactions of keteniminiums with alkenes/alkynes have a stepwise reaction mechanism. In the competition reactions, computational findings also allowed us to determine favorable kinetic and thermodynamic pathways and investigate the effect of chain length on the competition reaction. Lastly, a study on electrocyclization presents structural and energetic analysis and the reactivity differences among keteniminium derivatives bearing different substituents leading to six different heterocyclic systems by means of DFT. The electrocyclization of enamines leading to 3-aminopyrroles was shown to be both kinetically and thermodynamically most favorable. Compared to the systems in Group I, the aromatic moiety in Group II diminishes the reactivity due to the aromaticity disruption in the transition state for cyclization. This study provides insight on reactivity of keteniminium derivatives bearing different substituents and heteroatoms towards electrocyclization reactions. In addition, the true nature of the cyclization mechanism of keteniminium salts were disclosed via a range of different analysis techniques, pointing towards a 10π -electrocyclization for Group II rather than the 6π -electrocyclization observed in Group I.

Taken together, this dissertation provides a unique perspective on the underlying mechanism of Bcl-x_L deamidation-induced cell death. Keteniminium studies will also contribute to the understanding of keteniminium chemistry (formation, reactivity differences, etc.) and further aid synthetic applications.

REFERENCES

1. Boise, L. H., M. González-García, C. E. Postema, L. Ding, T. Lindsten, L. A. Turka, X. Mao, G. Nuñez and C. B. Thompson, "Bcl-x, a Bcl-2-related Gene that Functions as a Dominant Regulator of Apoptotic Cell Death", *Cell*, Vol. 74, No. 4, pp. 597–608, 1993.
2. Muchmore, S. W., M. Sattler, H. Liang, R. P. Meadows, J. E. Harlan, H. S. Yoon, D. Nettlesheim, B. S. Chang, C. B. Thompson, S.-L. Wong, S.-C. Ng and S. W. Fesik, "X-ray and NMR Structure of Human Bcl-xL, An Inhibitor of Programmed Cell Death", *Nature*, Vol. 381, No. 6580, pp. 335–341, 1996.
3. Viehe, H. G., R. Buijle, R. Fuks, R. Merényi and J. M. F. Oth, "Acylation, Alkylation, and Protonation of Alkynylamines", *Angewandte Chemie International Edition in English*, Vol. 6, No. 1, pp. 77–78, 1967.
4. Ghosez, L., B. Haveaux and H. G. Viehe, "Alkyl and Aryl α -Chloro Enamines", *Angewandte Chemie International Edition in English*, Vol. 8, No. 6, pp. 454–455, 1969.
5. Marchand-Brynaert, J. and L. Ghosez, "Cycloadditions of Keteneimmonium Cations to Olefins and Dienes. A New Synthesis of Four-Membered Rings", *Journal of the American Chemical Society*, Vol. 94, No. 8, pp. 2870–2872, 1972.
6. Sidani, A., J. Marchand-Brynaert and L. Ghosez, "A Convenient Procedure for the Synthesis of Cyclobutanones", *Angewandte Chemie International Edition in English*, Vol. 13, No. 4, p. 267, 1974.
7. Falmagne, J.-B., J. Escudero, S. Taleb-Sahraoui and L. Ghosez, "Cyclobutanone and Cyclobutenone Derivatives by Reaction of Tertiary Amides with Alkenes or Alkynes", *Angewandte Chemie International Edition in English*, Vol. 20, No. 10, pp. 879–880, 1981.

8. Deyrup, J. A. and G. S. Kuta, "Deprotonation of a Hindered Keteniminium Salt", *The Journal of Organic Chemistry*, Vol. 43, No. 3, pp. 501–505, 1978.
9. Evano, G., M. Lecomte, P. Thilmann and C. Theunissen, "Keteniminium Ions: Unique and Versatile Reactive Intermediates for Chemical Synthesis", *Synthesis*, Vol. 49, No. 15, pp. 3183–3214, 2017.
10. Viehe, H. G., "Synthesis and Reactions of the Alkynylamines", *Angewandte Chemie International Edition in English*, Vol. 6, No. 9, pp. 767–778, 1967.
11. DeKorver, K. A., H. Li, A. G. Lohse, R. Hayashi, Z. Lu, Y. Zhang and R. P. Hsung, "Ynamides: A Modern Functional Group for the New Millennium", *Chemical Reviews*, Vol. 110, No. 9, pp. 5064–5106, 2010.
12. Evano, G., A. Coste and K. Jouvin, "Ynamides: Versatile Tools in Organic Synthesis", *Angewandte Chemie International Edition*, Vol. 49, No. 16, pp. 2840–2859, 2010.
13. Zhou, B., T.-D. Tan, X.-Q. Zhu, M. Shang and L.-W. Ye, "Reversal of Regioselectivity in Ynamide Chemistry", *ACS Catalysis*, Vol. 9, No. 7, pp. 6393–6406, 2019.
14. Alder, B. J. and T. E. Wainwright, "Phase Transition for A Hard Sphere System", *The Journal of Chemical Physics*, Vol. 27, No. 5, pp. 1208–1209, 1957.
15. Alder, B. J. and T. E. Wainwright, "Studies in Molecular Dynamics. I. General Method", *The Journal of Chemical Physics*, Vol. 31, No. 2, pp. 459–466, 1959.
16. Stillinger, F. H. and A. Rahman, "Improved Simulation of Liquid Water by Molecular Dynamics", *The Journal of Chemical Physics*, Vol. 60, No. 4, pp. 1545–1557, 1974.
17. McCammon, J. A., B. R. Gelin and M. Karplus, "Dynamics of Folded Proteins", *Nature*, Vol. 267, No. 5612, pp. 585–590, 1977.
18. Darden, T., D. York and L. Pedersen, "Particle Mesh Ewald: an $N \cdot \log(N)$ Method for Ewald Sums in Large Systems", *The Journal of Chemical Physics*, Vol. 98, No. 12, pp.

10089–10092, 1993.

19. Essmann, U., L. Perera, M. L. Berkowitz, T. Darden, H. Lee and L. G. Pedersen, “A Smooth Particle Mesh Ewald Method”, *The Journal of Chemical Physics*, Vol. 103, No. 19, pp. 8577–8593, 1995.
20. Berendsen, H. J. C., J. P. M. Postma, W. F. van Gunsteren, A. DiNola and J. R. Haak, “Molecular Dynamics with Coupling to an External Bath”, *The Journal of Chemical Physics*, Vol. 81, No. 8, pp. 3684–3690, 1984.
21. Andersen, H. C., “Molecular Dynamics Simulations at Constant Pressure and/or Temperature”, *The Journal of Chemical Physics*, Vol. 72, No. 4, pp. 2384–2393, 1980.
22. Ryckaert, J. P., G. Ciccotti and H. J. Berendsen, “Numerical Integration of the Cartesian Equations of Motion of a System with Constraints: Molecular Dynamics of n-Alkanes”, *Journal of Computational Physics*, Vol. 23, No. 3, pp. 327–341, 1977.
23. Hopkins, C. W., S. Le Grand, R. C. Walker and A. E. Roitberg, “Long-Time-Step Molecular Dynamics through Hydrogen Mass Repartitioning”, *Journal of Chemical Theory and Computation*, Vol. 11, No. 4, pp. 1864–1874, 2015.
24. Sugita, Y. and Y. Okamoto, “Replica-exchange Molecular Dynamics Method for Protein Folding”, *Chemical Physics Letters*, Vol. 314, No. 1-2, pp. 141–151, 1999.
25. Hansmann, U. H., “Parallel Tempering Algorithm for Conformational Studies of Biological Molecules”, *Chemical Physics Letters*, Vol. 281, No. 1-3, pp. 140–150, 1997.
26. Amadei, A., A. B. Linssen and H. J. Berendsen, “Essential Dynamics of Proteins”, *Proteins: Structure, Function, and Bioinformatics*, Vol. 17, No. 4, pp. 412–425, 1993.
27. Bakan, A., L. M. Meireles and I. Bahar, “ProDy: Protein Dynamics Inferred from Theory and Experiments”, *Bioinformatics*, Vol. 27, No. 11, pp. 1575–1577, 2011.
28. Humphrey, W., A. Dalke and K. Schulten, “VMD: Visual Molecular Dynamics”, *Jour-*

- nal of Molecular Graphics*, Vol. 14, No. 1, pp. 33–38, 2 1996.
29. Shao, J., S. W. Tanner, N. Thompson and T. E. Cheatham, “Clustering Molecular Dynamics Trajectories: 1. Characterizing the Performance of Different Clustering Algorithms”, *Journal of Chemical Theory and Computation*, Vol. 3, No. 6, pp. 2312–2334, 2007.
 30. Jain, A. K., M. N. Murty and P. J. Flynn, “Data Clustering”, *ACM Computing Surveys*, Vol. 31, No. 3, pp. 264–323, 1999.
 31. Pople, J. A. and G. A. Segal, “Approximate Self-Consistent Molecular Orbital Theory. II. Calculations with Complete Neglect of Differential Overlap”, *The Journal of Chemical Physics*, Vol. 43, No. 10, pp. S136–S151, 1965.
 32. Pople, J. A., D. L. Beveridge and P. A. Dobosh, “Approximate Self-Consistent Molecular-Orbital Theory. V. Intermediate Neglect of Differential Overlap”, *The Journal of Chemical Physics*, Vol. 47, No. 6, pp. 2026–2033, 1967.
 33. Pople, J. A., D. P. Santry and G. A. Segal, “Approximate Self-Consistent Molecular Orbital Theory. I. Invariant Procedures”, *The Journal of Chemical Physics*, Vol. 43, No. 10, pp. S129–S135, 1965.
 34. Dewar, M. J. and W. Thiel, “Ground States of Molecules. 38. The MNDO Method. Approximations and Parameters”, *Journal of the American Chemical Society*, Vol. 99, No. 15, pp. 4899–4907, 1977.
 35. Dewar, M. J., E. G. Zoebisch, E. F. Healy and J. J. Stewart, “AM1: A New General Purpose Quantum Mechanical Molecular Model”, *Journal of the American Chemical Society*, Vol. 107, No. 13, pp. 3902–3909, 1985.
 36. Stewart, J. J. P., “Optimization of Parameters for Semiempirical Methods II. Applications”, *Journal of Computational Chemistry*, Vol. 10, No. 2, pp. 221–264, 3 1989.

37. Stewart, J. J., "Optimization of Parameters for Semiempirical Methods V: Modification of NDDO Approximations and Application to 70 Elements", *Journal of Molecular Modeling*, Vol. 13, No. 12, pp. 1173–1213, 2007.
38. Sousa, S. F., P. A. Fernandes and M. J. Ramos, "General Performance of Density Functionals", *The Journal of Physical Chemistry A*, Vol. 111, No. 42, pp. 10439–10452, 2007.
39. Zhao, Y. and D. G. Truhlar, "Density Functionals with Broad Applicability in Chemistry", *Accounts of Chemical Research*, Vol. 41, No. 2, pp. 157–167, 2008.
40. Ceperley, D. M. and B. J. Alder, "Ground State of the Electron Gas by a Stochastic Method", *Physical Review Letters*, Vol. 45, No. 7, pp. 566–569, 1980.
41. Perdew, J. P. and A. Zunger, "Self-interaction Correction to Density-functional Approximations for Many-Electron Systems", *Physical Review B*, Vol. 23, No. 10, pp. 5048–5079, 1981.
42. Ortiz, G. and P. Ballone, "Correlation Energy, Structure Factor, Radial Distribution Function, and Momentum Distribution of the Spin-polarized Uniform Electron Gas", *Physical Review B*, Vol. 50, No. 3, pp. 1391–1405, 1994.
43. Paier, J., R. Hirschl, M. Marsman and G. Kresse, "The Perdew-Burke-Ernzerhof Exchange-correlation Functional Applied to the G2-1 Test Set Using a Plane-wave Basis Set", *Journal of Chemical Physics*, Vol. 122, No. 23, p. 234102, 2005.
44. Cramer, C. J., *Essentials of Computational Chemistry: Theories and Models, 2nd Edition* — Wiley, Wiley, 2nd edn., 2004.
45. Lee, C., W. Yang and R. G. Parr, "Development of the Colle-Salvetti Correlation-energy Formula into a Functional of the Electron Density", *Physical Review B*, Vol. 37, No. 2, pp. 785–789, 1988.

46. Becke, A. D., “Density-functional Exchange-energy Approximation with Correct Asymptotic Behavior”, *Physical Review A*, Vol. 38, No. 6, pp. 3098–3100, 1988.
47. Miehlich, B., A. Savin, H. Stoll and H. Preuss, “Results Obtained with the Correlation Energy Density Functionals of Becke and Lee, Yang and Parr”, *Chemical Physics Letters*, Vol. 157, No. 3, pp. 200–206, 1989.
48. Guidon, M., J. Hutter and J. Vandevondele, “Auxiliary Density Matrix Methods for Hartree-Fock Exchange Calculations”, *Journal of Chemical Theory and Computation*, Vol. 6, No. 8, pp. 2348–2364, 2010.
49. Becke, A. D., “Density-functional Thermochemistry. III. The Role of Exact Exchange”, *The Journal of Chemical Physics*, Vol. 98, No. 7, pp. 5648–5652, 1993.
50. Zhao, Y. and D. G. Truhlar, “The M06 Suite of Density Functionals for Main Group Thermochemistry, Thermochemical Kinetics, Noncovalent Interactions, Excited States, and Transition Elements: Two New Functionals and Systematic Testing of Four M06-class Functionals and 12 Other Function”, *Theoretical Chemistry Accounts*, Vol. 120, No. 1-3, pp. 215–241, 2008.
51. Lynch, B. J., P. L. Fast, M. Harris and D. G. Truhlar, “Adiabatic Connection for Kinetics”, *The Journal of Physical Chemistry A*, Vol. 104, No. 21, pp. 4811–4815, 2000.
52. Grimme, S., “Semiempirical Hybrid Density Functional with Perturbative Second-order Correlation”, *Journal of Chemical Physics*, Vol. 124, No. 3, p. 034108, 2006.
53. Barone, V. and M. Cossi, “Quantum Calculation of Molecular Energies and Energy Gradients in Solution by a Conductor Solvent Model”, *The Journal of Physical Chemistry A*, Vol. 102, No. 11, pp. 1995–2001, 1998.
54. Cancès, E., B. Mennucci and J. Tomasi, “A New Integral Equation Formalism for the Polarizable Continuum Model: Theoretical Background and Applications to Isotropic and Anisotropic Dielectrics”, *The Journal of Chemical Physics*, Vol. 107, No. 8, pp.

- 3032–3041, 1997.
55. Marenich, A. V., C. J. Cramer and D. G. Truhlar, “Universal Solvation Model Based on Solute Electron Density and on a Continuum Model of the Solvent Defined by the Bulk Dielectric Constant and Atomic Surface Tensions”, *The Journal of Physical Chemistry B*, Vol. 113, No. 18, pp. 6378–6396, 2009.
 56. Klamt, A. and G. Schüürmann, “COSMO: A New Approach to Dielectric Screening in Solvents with Explicit Expressions for the Screening Energy and its Gradient”, *J. Chem. Soc., Perkin Trans. 2*, Vol. 0, No. 5, pp. 799–805, 1993.
 57. Miertuš, S., E. Scrocco and J. Tomasi, “Electrostatic Interaction of a Solute with a Continuum. A Direct Utilizaion of AB Initio Molecular Potentials for the Prevision of Solvent Effects”, *Chemical Physics*, Vol. 55, No. 1, pp. 117–129, 1981.
 58. Tomasi, J., B. Mennucci and R. Cammi, “Quantum Mechanical Continuum Solvation Models”, *Chemical Reviews*, Vol. 105, No. 8, pp. 2999–3094, 2005.
 59. Mennucci, B. and J. Tomasi, “Continuum Solvation Models: A New Approach to the Problem of Solute’s Charge Distribution and Cavity Boundaries”, *The Journal of Chemical Physics*, Vol. 106, No. 12, pp. 5151–6158, 1997.
 60. Leach, A. R., *Molecular Modelling: Priciples and Applications*, Pearson, 2nd edn edn., 2001.
 61. Reed, A. E., R. B. Weinstock and F. Weinhold, “Natural Population Analysis”, *The Journal of Chemical Physics*, Vol. 83, No. 2, pp. 735–746, 1985.
 62. Contreras-García, J., E. R. Johnson, S. Keinan, R. Chaudret, J. P. Piquemal, D. N. Beratan and W. Yang, “NCIPLOT: A Program for Plotting Noncovalent Interaction Regions”, *Journal of Chemical Theory and Computation*, Vol. 7, No. 3, pp. 625–632, 2011.

63. Schleyer, P. V. R., C. Maerker, A. Dransfeld, H. Jiao and N. J. R. van Eikema Hommes, “Nucleus-Independent Chemical Shifts: A Simple and Efficient Aromaticity Probe”, *Journal of the American Chemical Society*, Vol. 118, No. 26, pp. 6317–6318, 1996.
64. Chen, Z., C. S. Wannere, C. Corminboeuf, R. Puchta and P. v. R. Schleyer, “Nucleus-Independent Chemical Shifts (NICS) as an Aromaticity Criterion”, *Chem. Rev.*, Vol. 105, pp. 3842–3888, 2005.
65. Herges, R. and D. Geuenich, “Delocalization of Electrons in Molecules”, *The Journal of Physical Chemistry A*, Vol. 105, No. 13, pp. 3214–3220, 2001.
66. Geuenich, D., K. Hess, F. Köhler and R. Herges, “Anisotropy of the Induced Current Density (ACID), a General Method to Quantify and Visualize Electronic Delocalization”, *Chemical Reviews*, Vol. 105, No. 10, pp. 3758–3772, 2005.
67. Cabaleiro-Lago, E. M., J. Rodríguez-Otero, S. M. Varela-Varela, A. Peña-Gallego and J. M. Hermida-Ramón, “Are Electrocyclization Reactions of (3 Z)-1,3,5-Hexatrienone and Nitrogen Derivatives Pseudopericyclic? A DFT Study”, *The Journal of Organic Chemistry*, Vol. 70, No. 10, pp. 3921–3928, 5 2005.
68. Peña-Gallego, A., J. Rodríguez-Otero and E. M. Cabaleiro-Lago, “A DFT Study of the [4+2] Cycloadditions of Conjugated Ketenes (Vinylketene, Imidoylketene and Formylketene) with Formaldimine. The Pericyclic or Pseudopericyclic Character from Magnetic Properties”, *Tetrahedron*, Vol. 63, No. 23, pp. 4937–4943, 2007.
69. Bader, R. F. W., *Atoms in Molecules: A Quantum Theory*, Oxford University Press, Oxford, 1990.
70. Rode, J. E. and J. C. Dobrowolski, “An Ab Initio Study on the Allene–Isocyanic Acid and Ketene–Vinylimine [2 + 2] Cycloaddition Reaction Paths”, *The Journal of Physical Chemistry A*, Vol. 110, No. 10, pp. 3723–3737, 3 2006.
71. Musavi, S. M., J. Amani and N. Omidian, “Changing the Regioselectivity and Asyn-

- chronicity of the Possible Concerted [2+2] and [4+2] Cycloadditions of Ketene and Halogenated Ketenes with cyclopentadiene: A DFT Survey”, *Tetrahedron*, Vol. 70, No. 3, pp. 708–719, 2014.
72. Geerlings, P., F. De Proft and W. Langenaeker, “Conceptual Density Functional Theory”, *Chemical Reviews*, Vol. 103, No. 5, pp. 1793–1874, 2003.
73. Domingo, L. R., E. Chamorro and P. Pérez, “Understanding the Reactivity of Captodative Ethylenes in Polar Cycloaddition Reactions. A Theoretical Study”, *The Journal of Organic Chemistry*, Vol. 73, No. 12, pp. 4615–4624, 2008.
74. Soto-Delgado, J., L. R. Domingo and R. Contreras, “Quantitative Characterization of Group Electrophilicity and Nucleophilicity for Intramolecular Diels-Alder Reactions”, *Organic and Biomolecular Chemistry*, Vol. 8, No. 16, pp. 3678–3683, 2010.
75. Parr, R. G., R. A. Donnelly, M. Levy and W. E. Palke, “Electronegativity: The Density Functional Viewpoint”, *The Journal of Chemical Physics*, Vol. 68, No. 8, pp. 3801–3807, 1978.
76. Domingo, L. R., M. J. Aurell, P. Pérez and R. Contreras, “Quantitative Characterization of the Global Electrophilicity Power of Common Diene/Dienophile Pairs in Diels-Alder Reactions”, *Tetrahedron*, Vol. 58, No. 22, pp. 4417–4423, 2002.
77. Domingo, L. R., M. J. Aurell, P. Pérez and R. Contreras, “Quantitative Characterization of the Local Electrophilicity of Organic Molecules. Understanding the Regioselectivity on Diels-Alder Reactions”, *Journal of Physical Chemistry A*, Vol. 106, No. 29, pp. 6871–6875, 2002.
78. Parr, R. G. and W. Yang, “Density Functional Approach to the Frontier-Electron Theory of Chemical Reactivity”, *Journal of the American Chemical Society*, Vol. 106, No. 14, pp. 4049–4050, 1984.
79. Domingo, L. R., P. Pérez and J. A. Sáez, “Understanding the Local Reactivity in Po-

- lar Organic Reactions through Electrophilic and Nucleophilic Parr Functions”, *RSC Advances*, Vol. 3, No. 5, pp. 1486–1494, 2013.
80. Yang, W. and W. J. Mortier, “The Use of Global and Local Molecular Parameters for the Analysis of the Gas-Phase Basicity of Amines”, *Journal of the American Chemical Society*, Vol. 108, No. 19, pp. 5708–5711, 1986.
81. Igney, F. H. and P. H. Krammer, “Death and Anti-death: Tumour Resistance to Apoptosis”, *Nature Reviews Cancer*, Vol. 2, No. 4, pp. 277–288, 2002.
82. Trapani, J. A. and M. J. Smyth, “Functional Significance of the Perforin/Granzyme Cell Death Pathway”, *Nature Reviews Immunology*, Vol. 2, No. 10, pp. 735–747, 2002.
83. Martinvalet, D., P. Zhu and J. Lieberman, “Granzyme A Induces Caspase-Independent Mitochondrial Damage, a Required First Step for Apoptosis”, *Immunity*, Vol. 22, No. 3, pp. 355–370, 3 2005.
84. Singh, R., A. Letai and K. Sarosiek, “Regulation of Apoptosis in Health and Disease: the Balancing Act of BCL-2 Family Proteins”, *Nature Reviews Molecular Cell Biology*, Vol. 20, No. 3, pp. 175–193, 2019.
85. Adams, J. M. and S. Cory, “The BCL-2 Arbiters of Apoptosis and Their Growing Role as Cancer Targets”, *Cell Death and Differentiation*, Vol. 25, No. 1, pp. 27–36, 2018.
86. Brunelle, J. K. and A. Letai, “Control of Mitochondrial Apoptosis by the Bcl-2 Family”, *Journal of Cell Science*, Vol. 122, No. 4, pp. 437–441, 2009.
87. Tait, S. W. G. and D. R. Green, “Mitochondria and Cell Death: Outer Membrane Permeabilization and Beyond”, *Nature Reviews Molecular Cell Biology*, Vol. 11, No. 9, pp. 621–632, 2010.
88. Chipuk, J. E., L. Bouchier-Hayes and D. R. Green, “Mitochondrial Outer Membrane Permeabilization during Apoptosis: the Innocent Bystander Scenario.”, *Cell death and*

- differentiation*, Vol. 13, No. 8, pp. 1396–402, 2006.
89. Warren, C. F. A., M. W. Wong-Brown and N. A. Bowden, “BCL-2 Family Isoforms in Apoptosis and Cancer”, *Cell Death & Disease*, Vol. 10, No. 3, p. 177, 2019.
 90. Birkinshaw, R. W. and P. E. Czabotar, “The BCL-2 Family of Proteins and Mitochondrial Outer Membrane Permeabilisation”, *Seminars in Cell & Developmental Biology*, Vol. 72, pp. 152–162, 2017.
 91. Takehara, T. and H. Takahashi, “Suppression of Bcl-xL Deamidation in Human Hepatocellular Carcinomas”, *Cancer research*, Vol. 63, No. 12, pp. 3054–7, 2003.
 92. Leech, S. H., R. A. Olie, O. Gautschi, A. P. Simões-Wüst, S. Tschopp, R. Häner, J. Hall, R. A. Stahel and U. Zangemeister-Wittke, “Induction of Apoptosis in Lung-cancer Cells following Bcl-xL Anti-sense Treatment.”, *International journal of cancer*, Vol. 86, No. 4, pp. 570–6, 2000.
 93. Aritomi, M., N. Kunishima, N. Inohara, Y. Ishibashi, S. Ohta and K. Morikawa, “Crystal Structure of Rat Bcl-xL”, *Journal of Biological Chemistry*, Vol. 272, No. 44, pp. 27886–27892, 1997.
 94. Yao, Y., D. Nisan, A. Antignani, A. Barnes, N. Tjandra, R. J. Youle, F. M. Marassi and L. M. Fujimoto, “Characterization of the Membrane-inserted C-terminus of Cytoprotective BCL-XL”, *Protein Expression and Purification*, Vol. 122, pp. 56–63, 2016.
 95. Lee, E. F. and W. D. Fairlie, “The Structural Biology of Bcl-xL”, *International Journal of Molecular Sciences*, Vol. 20, No. 9, p. 2234, 2019.
 96. Raltchev, K., J. Pipercevic and F. Hagn, “Production and Structural Analysis of Membrane-Anchored Proteins in Phospholipid Nanodiscs”, *Chemistry - A European Journal*, Vol. 24, No. 21, pp. 5493–5499, 2018.
 97. Liu, X., A. Beugelsdijk and J. Chen, “Dynamics of the BH3-Only Protein Binding

- Interface of Bcl-xL”, *Biophysical Journal*, Vol. 109, No. 5, pp. 1049–1067, 2015.
98. Liu, X., Z. Jia, J. Chen, J. Phys and B. Chem, “Enhanced Sampling of Intrinsic Structural Heterogeneity of the BH3-Only Protein Binding Interface of Bcl-xL”, *The Journal of Physical Chemistry B*, Vol. 121, No. 39, pp. 9160–9168, 2017.
 99. Maity, A., S. Yadav, C. S. Verma and S. Ghosh Dastidar, “Dynamics of Bcl-xL in Water and Membrane: Molecular Simulations”, *PLoS ONE*, Vol. 8, No. 10, p. e76837, 2013.
 100. Hill, R. B., K. R. MacKenzie and M. C. Harwig, “The Tail-End Is Only the Beginning: NMR Study Reveals a Membrane-Bound State of BCL-XL”, *Journal of Molecular Biology*, Vol. 427, No. 13, pp. 2257–2261, 2015.
 101. Chang, B. S., A. J. Minn, S. W. Muchmore, S. W. Fesik and C. B. Thompson, “Identification of a Novel Regulatory Domain in Bcl-xL and Bcl-2”, *EMBO Journal*, Vol. 16, No. 5, pp. 968–977, 1997.
 102. Kharbanda, S., S. Saxena, K. Yoshida, P. Pandey, M. Kaneki, Q. Wang, K. Cheng, Y.-N. Chen, A. Campbell, T. Sudha, Z.-M. Yuan, J. Narula, R. Weichselbaum, C. Nalin and D. Kufe, “Translocation of SAPK/JNK to Mitochondria and Interaction with Bcl-xL in Response to DNA Damage”, *Journal of Biological Chemistry*, Vol. 275, No. 1, pp. 322–327, 1 2000.
 103. Zheng, J. H., A. Viacava Follis, R. W. Kriwacki and T. Moldoveanu, “Discoveries and Controversies in BCL-2 Protein-mediated Apoptosis”, *The FEBS Journal*, Vol. 283, No. 14, pp. 2690–2700, 2016.
 104. Clem, R. J., E. H.-Y. Cheng, C. L. Karp, D. G. Kirsch, K. Ueno, A. Takahashi, M. B. Kastan, D. E. Griffin, W. C. Earnshaw, M. A. Veluona and J. M. Hardwick, “Modulation of Cell Death by Bcl-xL through Caspase Interaction”, *Proceedings of the National Academy of Sciences*, Vol. 95, No. 2, pp. 554–559, 1998.
 105. Basañez, G., J. Zhang, B. N. Chau, G. I. Maksaev, V. A. Frolov, T. A. Brandt, J. Burch,

- J. M. Hardwick and J. Zimmerberg, “Pro-apoptotic Cleavage Products of Bcl-xL form Cytochrome c-conducting Pores in Pure Lipid Membranes”, *Journal of Biological Chemistry*, Vol. 276, No. 33, pp. 31083–31091, 2001.
106. Follis, A. V., F. Llambi, H. Kalkavan, Y. Yao, A. H. Phillips, C.-G. Park, F. M. Marassi, D. R. Green and R. W. Kriwacki, “Regulation of Apoptosis by an Intrinsically Disordered Region of Bcl-xL”, *Nature Chemical Biology*, Vol. 14, No. 5, pp. 458–465, 2018.
107. Beaumatin, F., M. El Dhaybi, C. Bobo, M. Verdier and M. Priault, “Bcl-xL Deamidation and Cancer: Charting the Fame Trajectories of Legitimate Child and Hidden Siblings”, *Biochimica et biophysica acta. Molecular cell research*, Vol. 1864, No. 10, pp. 1734–1745, 2017.
108. Letai, A. and O. Kutuk, “Regulation of Bcl-2 Family Proteins by Posttranslational Modifications”, *Current Molecular Medicine*, Vol. 8, No. 2, pp. 102–118, 2008.
109. Kale, J., E. J. Osterlund and D. W. Andrews, “BCL-2 Family Proteins: Changing Partners in the Dance towards Death”, *Cell Death and Differentiation*, Vol. 25186, No. 10, pp. 65–80, 2017.
110. Yao, Y., L. M. Fujimoto, N. Hirshman, A. A. Bobkov, A. Antignani, R. J. Youle and F. M. Marassi, “Conformation of BCL-XL upon Membrane Integration”, *Journal of Molecular Biology*, Vol. 427, No. 13, pp. 2262–2270, 2015.
111. Borrás, C., C. Mas-Bargues, A. Román-Domínguez, J. Sanz-Ros, L. Gimeno-Mallench, M. Inglés, J. Gambini and J. Viña, “BCL-xL, a Mitochondrial Protein Involved in Successful Aging: From *C. elegans* to Human Centenarians”, *International Journal of Molecular Sciences*, Vol. 21, No. 2, p. 418, 2020.
112. Walsh, G. and R. Jefferis, “Post-translational Modifications in the Context of Therapeutic Proteins”, *Nature Biotechnology*, Vol. 24, No. 10, pp. 1241–1252, 2006.

113. Walsh, G., “Post-translational Modifications of Protein Biopharmaceuticals”, *Drug Discovery Today*, Vol. 15, No. 17-18, pp. 773–780, 2010.
114. Han, Z.-J., Y.-H. Feng, B.-H. Gu, Y.-M. Li and H. Chen, “The Post-translational Modification, SUMOylation, and Cancer (Review)”, *International Journal of Oncology*, Vol. 52, No. 4, pp. 1081–1094, 2018.
115. Bobo, C., C. Céré, M. Dufossée, A. Dautant, V. Moreau, S. Manon, F. Beaumatin and M. Priault, “Improved Electrophoretic Separation to Assist the Monitoring of Bcl-xL Post-Translational Modifications”, *International Journal of Molecular Sciences*, Vol. 20, No. 22, p. 5571, 2019.
116. Deverman, B. E., B. L. Cook, S. R. Manson, R. A. Niederhoff, E. M. Langer, I. Rosová, L. A. Kulans, X. Fu, J. S. Weinberg, J. W. Heinecke, K. A. Roth and S. J. Weintraub, “Bcl-xL Deamidation Is a Critical Switch in the Regulation of the Response to DNA Damage”, *Cell*, Vol. 111, No. 1, pp. 51–62, 2002.
117. Beaumatin, F., M. E. Dhaybi, J.-p. Lasserre, B. Salin, M. P. Moyer, M. Verdier, S. Manon and M. Priault, “N52 Monodeamidated Bcl-xL Shows Impaired Oncogenic Properties in Vivo and in Vitro”, *Oncotarget*, Vol. 7, No. 13, pp. 17129–17143, 2016.
118. Zhao, R., D. Oxley, T. S. Smith, G. A. Follows, A. R. Green and D. R. Alexander, “DNA Damage–Induced Bcl-xL Deamidation Is Mediated by NHE-1 Antiport Regulated Intracellular pH”, *PLoS Biology*, Vol. 5, No. 1, p. e1, 2006.
119. Seng, N., J. Megyesi, A. Tarcsafalvi and P. Price, “Mimicking Cdk2 Phosphorylation of Bcl-xL at Ser73 Results in Caspase Activation and Bcl-xL Cleavage”, *Cell Death Discovery*, Vol. 2, No. 1, p. 16001, 2016.
120. Fujita, N., A. Nagahashi, K. Nagashima, S. Rokudai and T. Tsuruo, “Acceleration of Apoptotic Cell Death after the Cleavage of Bcl-XL Protein by Caspase-3-like Proteases”, *Oncogene*, Vol. 17, No. 10, pp. 1295–1304, 1998.

121. Robinson, N. E. and A. B. Robinson, "Molecular Clocks.", *Proceedings of the National Academy of Sciences of the United States of America*, Vol. 98, No. 3, pp. 944–9, 2001.
122. Robinson, N. E., Z. W. Robinson, B. R. Robinson, A. B. A. L. Robinson, J. A. Robinson, M. L. Robinson and A. B. A. L. Robinson, "Structure-dependent Nonenzymatic Deamidation of Glutaminyl and Asparaginyl Pentapeptides", *Journal of Peptide Research*, Vol. 63, No. 5, pp. 426–436, 2004.
123. Tonie Wright, H. and D. W. Urry, "Nonenzymatic Deamidation of Asparaginyl and Glutaminyl Residues in Protein", *Critical Reviews in Biochemistry and Molecular Biology*, Vol. 26, No. 1, pp. 1–52, 1991.
124. Geiger, T. and S. Clarke, "Deamidation, Isomerization, and Racemization at Asparaginyl and Aspartyl Residues in Peptides. Succinimide-linked Reactions that Contribute to Protein Degradation.", *Journal of Biological Chemistry*, Vol. 262, No. 2, pp. 785–794, 1987.
125. Catak, S., G. Monard, V. Aviyente and M. F. Ruiz-López, "Reaction Mechanism of Deamidation of Asparaginyl Residues in Peptides: Effect of Solvent Molecules", *The Journal of Physical Chemistry A*, Vol. 110, No. 27, pp. 8354–8365, 2006.
126. Cory, S. and J. M. Adams, "The Bcl2 Family: Regulators of the Cellular Life-or-death Switch", *Nature Reviews Cancer*, Vol. 2, No. 9, pp. 647–656, 2002.
127. Cheng, E. H.-Y., M. C. Wei, S. Weiler, R. A. Flavell, T. W. Mak, T. Lindsten and S. J. Korsmeyer, "BCL-2, BCL-XL Sequester BH3 Domain-Only Molecules Preventing BAX- and BAK-Mediated Mitochondrial Apoptosis", *Molecular Cell*, Vol. 8, No. 3, pp. 705–711, 2001.
128. Leber, B., J. Lin and D. W. Andrews, "Still Embedded Together Binding to Membranes Regulates Bcl-2 Protein Interactions.", *Oncogene*, Vol. 29, No. 38, pp. 5221–5230, 2010.

129. Levine, B., S. C. Sinha and G. Kroemer, “Bcl-2 Family Members: Dual Regulators of Apoptosis and Autophagy”, *Autophagy*, Vol. 4, No. 5, pp. 600–606, 2008.
130. Borrás, C., K. M. Abdelaziz, J. Gambini, E. Serna, M. Inglés, M. de la Fuente, I. Garcia, A. Matheu, P. Sanchís, A. Belenguer, A. Errigo, J. A. Avellana, A. Baretino, C. Lloret-Fernández, N. Flames, G. Pes, L. Rodríguez-Mañas and J. Viña, “Human Exceptional Longevity: Transcriptome from Centenarians is Distinct from Septuagenarians and Reveals a Role of Bcl-xL in Successful Aging”, *Aging*, Vol. 8, No. 12, pp. 3185–3208, 2016.
131. Yosef, R., N. Pilpel, R. Tokarsky-Amiel, A. Biran, Y. Ovadya, S. Cohen, E. Vadai, L. Dassa, E. Shahar, R. Condiotti, I. Ben-Porath and V. Krizhanovsky, “Directed Elimination of Senescent Cells by Inhibition of BCL-W and BCL-XL”, *Nature Communications*, Vol. 7, No. 1, p. 11190, 2016.
132. Vicencio, J. M., L. Galluzzi, N. Tajeddine, C. Ortiz, A. Criollo, E. Tasdemir, E. Morselli, A. Ben Younes, M. C. Maiuri, S. Lavandro and G. Kroemer, “Senescence, Apoptosis or Autophagy? When a Damaged Cell Must Decide Its Path – A Mini-Review”, *Gerontology*, Vol. 54, No. 2, pp. 92–99, 2008.
133. Dho, S. H., B. E. Deverman, C. Lapid, S. R. Manson, L. Gan, J. J. Riehm, R. Aurora, K.-S. S. Kwon and S. J. Weintraub, “Control of Cellular Bcl-xL Levels by Deamidation-Regulated Degradation”, *PLoS Biology*, Vol. 11, No. 6, pp. 12201901–14924, 2013.
134. Deverman, B. E., B. L. Cook, S. R. Manson, R. A. Niederhoff, E. M. Langer, I. Rosová, L. A. Kulans, X. Fu, J. S. Weinberg, J. W. Heinecke, K. A. Roth and S. J. Weintraub, “Bcl-xL Deamidation Is a Critical Switch in the Regulation of the Response to DNA Damage”, *Cell*, Vol. 115, No. 4, p. 503, 2003.
135. Ahn, J. S., J. Li, E. Chen, D. G. Kent, H. J. Park and A. R. Green, “JAK2V617F Mediates Resistance to DNA Damage-induced Apoptosis by Modulating FOXO3A Localization and Bcl-xL Deamidation”, *Oncogene*, Vol. 35, No. 17, pp. 2235–2246,

2016.

136. Fares, M., M. Abedi-Valugerdi, M. Hassan and Z. Potáčová, “DNA Damage, Lysosomal Degradation and Bcl-xL Deamidation in Doxycycline- and Minocycline-induced Cell Death in the K562 Leukemic Cell Line”, *Biochemical and Biophysical Research Communications*, Vol. 463, No. 3, pp. 268–274, 2015.
137. Asakura, T., K. Maeda, H. Omi, H. Matsudaira and K. Ohkawa, “The Association of Deamidation of Bcl-xL and Translocation of Bax to the Mitochondria through Activation of JNK in the Induction of Apoptosis by Treatment with GSH-conjugated DXR”, *International Journal of Oncology*, Vol. 33, No. 2, pp. 389–395, 2008.
138. Priya, P., A. Maity and S. Ghosh Dastidar, “The Long Unstructured Region of Bcl-xL Modulates Its Structural Dynamics”, *Proteins: Structure, Function, and Bioinformatics*, Vol. 85, No. 8, pp. 1567–1579, 2017.
139. Ryzhov, P., Y. Tian, Y. Yao, A. A. Bobkov, W. Im and F. M. Marassi, “Conformational States of the Cytoprotective Protein Bcl-xL”, *Biophysical Journal*, Vol. 119, No. 7, pp. 1324–1334, 2020.
140. Tanriver, G., G. Monard and S. Catak, “Impact of Deamidation on the Structure and Function of Antiapoptotic Bcl-xL”, *Journal of Chemical Information and Modeling*, Vol. 62, No. 1, pp. 102–115, 2022.
141. Case, D. A., S. R. Brozell, D. S. Cerutti, I. T. E. Cheatham, V. W. D. Cruzeiro, T. A. Darden, R. E. Duke, D. Ghoreishi, H. Gohlke, A. W. Goetz, D. Greene, R. Harris, N. Homeyer, S. Izadi, A. Kovalenko, T. S. Lee, S. LeGrand, P. Li and P. A. Lin, “Amber 2018”, *University of California: San Francisco*, 2018.
142. Maier, J. A., C. Martinez, K. Kasavajhala, L. Wickstrom, K. E. Hauser and C. Simmerling, “ff14SB: Improving the Accuracy of Protein Side Chain and Backbone Parameters from ff99SB”, *Journal of Chemical Theory and Computation*, Vol. 11, No. 8, pp. 3696–3713, 2015.

143. Jorgensen, W. L., J. Chandrasekhar, J. D. Madura, R. W. Impey and M. L. Klein, "Comparison of Simple Potential Functions for Simulating Liquid Water", *The Journal of Chemical Physics*, Vol. 79, No. 2, pp. 926–935, 1983.
144. Izaguirre, J. A., D. P. Catarello, J. M. Wozniak and R. D. Skeel, "Langevin Stabilization of Molecular Dynamics", *The Journal of Chemical Physics*, Vol. 114, No. 5, pp. 2090–2098, 2001.
145. Roe, D. R. and T. E. Cheatham, "PTRAJ and CPPTRAJ: Software for Processing and Analysis of Molecular Dynamics Trajectory Data", *Journal of Chemical Theory and Computation*, Vol. 9, No. 7, pp. 3084–3095, 2013.
146. Kabsch, W. and C. Sander, "Dictionary of Protein Secondary Structure: Pattern Recognition of Hydrogen-bonded and Geometrical Features", *Biopolymers*, Vol. 22, No. 12, pp. 2577–2637, 1983.
147. Pettersen, E. F., T. D. Goddard, C. C. Huang, G. S. Couch, D. M. Greenblatt, E. C. Meng and T. E. Ferrin, "UCSF Chimera-A Visualization System for Exploratory Research and Analysis", *Journal of Computational Chemistry*, Vol. 25, No. 13, pp. 1605–1612, 2004.
148. Goddard, T. D., C. C. Huang, E. C. Meng, E. F. Pettersen, G. S. Couch, J. H. Morris and T. E. Ferrin, "UCSF ChimeraX: Meeting Modern Challenges in Visualization and Analysis", *Protein Science*, Vol. 27, No. 1, pp. 14–25, 2018.
149. Rajan, S., M. Choi, K. Baek and H. S. Yoon, "BH3 Induced Conformational Changes in Bcl-XL Revealed by Crystal Structure and Comparative Analysis", *Proteins: Structure, Function, and Bioinformatics*, Vol. 83, No. 7, pp. 1262–1272, 2015.
150. Lee, E. F., N. A. Smith, T. P. Soares da Costa, N. Meftahi, S. Yao, T. J. Harris, S. Tran, A. Pettikiriarachchi, M. A. Perugini, D. W. Keizer, M. Evangelista, B. J. Smith and W. D. Fairlie, "Structural Insights into BCL2 Pro-Survival Protein Interactions with the Key Autophagy Regulator BECN1 Following Phosphorylation by STK4/MST1",

Autophagy, Vol. 15, No. 5, pp. 785–795, 2019.

151. Priyadarshi, A., A. Roy, K. S. Kim, E. E. K. Kim and K. Y. Hwang, “Structural Insights into Mouse Anti-apoptotic Bcl-xl Reveal Affinity for Beclin 1 and Gossypol”, *Biochemical and Biophysical Research Communications*, Vol. 394, No. 3, pp. 515–521, 2010.
152. Bhola, P. D. and A. Letai, “Mitochondria-Judges and Executioners of Cell Death Sentences”, *Molecular Cell*, Vol. 61, No. 5, pp. 695–704, 2016.
153. Letai, A., M. C. Bassik, L. D. Walensky, M. D. Sorcinelli, S. Weiler and S. J. Korsmeyer, “Distinct BH3 Domains either Sensitize or Activate Mitochondrial Apoptosis, Serving as Prototype Cancer Therapeutics”, *Cancer Cell*, Vol. 2, No. 3, pp. 183–192, 2002.
154. Leber, B., J. Lin and D. W. Andrews, “Embedded Together: The Life and Death Consequences of Interaction of the Bcl-2 Family with Membranes”, *Apoptosis*, Vol. 12, No. 5, pp. 897–911, 2007.
155. Llambi, F., T. Moldoveanu, S. W. Tait, L. Bouchier-Hayes, J. Temirov, L. L. McCormick, C. P. Dillon and D. R. Green, “A Unified Model of Mammalian BCL-2 Protein Family Interactions at the Mitochondria”, *Molecular Cell*, Vol. 44, No. 4, pp. 517–531, 2011.
156. Shamas-Din, A., H. Brahmabhatt, B. Leber and D. W. Andrews, “BH3-only Proteins: Orchestrators of Apoptosis”, *Biochimica et Biophysica Acta - Molecular Cell Research*, Vol. 1813, No. 4, pp. 508–520, 2011.
157. Shamas-Din, A., S. Bindner, W. Zhu, Y. Zaltsman, C. Campbell, A. Gross, B. Leber, D. W. Andrews and C. Fradin, “tBid Undergoes Multiple Conformational Changes at the Membrane Required for Bax Activation”, *Journal of Biological Chemistry*, Vol. 288, No. 30, pp. 22111–22127, 2013.

158. Chi, X., J. Kale, B. Leber and D. W. Andrews, “Regulating Cell Death At, On, and In Membranes.”, *Biochimica et biophysica acta*, Vol. 1843, No. 9, pp. 2100–13, 2014.
159. Hsu, Y. T., K. G. Wolter and R. J. Youle, “Cytosol-to-membrane Redistribution of Bax and Bcl-XL during Apoptosis”, *Proceedings of the National Academy of Sciences of the United States of America*, Vol. 94, No. 8, pp. 3668–3672, 1997.
160. Todt, F., Z. Cakir, F. Reichenbach, R. Youle and F. Edlich, “The C-terminal Helix of Bcl-xL Mediates Bax Retrotranslocation from the Mitochondria”, *Cell Death and Differentiation*, Vol. 20, No. 10, pp. 333–342, 2013.
161. Hausmann, G., L. A. O’Reilly, R. van Driel, J. G. Beaumont, A. Strasser, J. M. Adams and D. C. Huang, “Pro-Apoptotic Apoptosis Protease-Activating Factor 1 (Apaf-1) Has a Cytoplasmic Localization Distinct from Bcl-2 or Bcl-XL”, *Journal of Cell Biology*, Vol. 149, No. 3, pp. 623–634, 2000.
162. Nijhawan, D., M. Fang, E. Traer, Q. Zhong, W. Gao, F. Du and X. Wang, “Elimination of Mcl-1 Is Required for the Initiation of Apoptosis Following Ultraviolet Irradiation”, *Genes & Development*, Vol. 17, No. 12, pp. 1475–1486, 2003.
163. Edlich, F., S. Banerjee, M. Suzuki, M. M. Cleland, D. Arnoult, C. Wang, A. Neutzner, N. Tjandra and R. J. Youle, “Bcl-xL Retrotranslocates Bax from the Mitochondria into the Cytosol”, *Cell*, Vol. 145, No. 1, pp. 104–116, 2011.
164. Kaufmann, T., S. Schlipf, J. Sanz, K. Neubert, R. Stein and C. Borner, “Characterization of the Signal that Directs Bcl-xL, but not Bcl-2, to the Mitochondrial Outer Membrane”, *Journal of Cell Biology*, Vol. 160, No. 1, pp. 53–64, 2003.
165. Suzuki, M., R. J. Youle and N. Tjandra, “Structure of Bax: Coregulation of Dimer Formation and Intracellular Localization”, *Cell*, Vol. 103, No. 4, pp. 645–654, 2000.
166. Eswar, N., B. Webb, M. A. Marti-Renom, M. Madhusudhan, D. Eramian, M. Shen, U. Pieper and A. Sali, “Comparative Protein Structure Modeling Using Modeller”,

Current Protocols in Bioinformatics, Vol. 15, No. 1, pp. 1–5, 2006.

167. Maity, A., S. Sinha, D. Ganguly and S. Ghosh Dastidar, “C-Terminal Tail Insertion of Bcl-xL in Membrane Occurs via Partial Unfolding and Refolding Cycle Associating Micro-solvation”, *Phys Chem Chem Phys*, Vol. 18, No. 34, pp. 24095–24105, 2016.
168. Maity, A., S. Sinha and S. Ghosh Dastidar, “Dissecting the Thermodynamic Contributions of the Charged Residues in the Membrane Anchoring of Bcl-xl C-Terminal Domain”, *Chemistry and Physics of Lipids*, Vol. 218, pp. 112–124, 2019.
169. Vasquez-Montes, V., M. Vargas-Uribe, N. K. Pandey, M. V. Rodnin, R. Langen and A. S. Ladokhin, “Lipid-modulation of Membrane Insertion and Refolding of the Apoptotic Inhibitor Bcl-xL”, *Biochimica et Biophysica Acta - Proteins and Proteomics*, Vol. 1867, No. 7-8, pp. 691–700, 2019.
170. Vasquez-Montes, V., A. Kyrychenko, M. Vargas-Uribe, M. V. Rodnin and A. S. Ladokhin, “Conformational Switching in Bcl-xL: Enabling Non-Canonical Inhibition of Apoptosis Involves Multiple Intermediates and Lipid Interactions”, *Cells*, Vol. 9, No. 3, p. 539, 2020.
171. Ryzhov, P., Y. Yao, B. B. Verdugo, G. Salvesen and F. M. Marassi, “Membrane-Mediated Conformational Changes of Cytoprotective BCL-XI Regulate its Activity”, *Biophysical Journal*, Vol. 118, No. 3, p. 211a, 2020.
172. Patriksson, A. and D. van der Spoel, “A Temperature Predictor for Parallel Tempering Simulations”, *Physical Chemistry Chemical Physics*, Vol. 10, No. 15, pp. 2073–2077, 2008.
173. Cathcart, K., A. Patel, H. Dies, M. Rheinstädter and C. Fradin, “Effect of Cholesterol on the Structure of a Five-Component Mitochondria-Like Phospholipid Membrane”, *Membranes*, Vol. 5, No. 4, pp. 664–684, 2015.
174. Horvath, S. E. and G. Daum, “Lipids of Mitochondria”, *Progress in Lipid Research*,

- Vol. 52, No. 4, pp. 590–614, 2013.
175. Daum, G. and J. E. Vance, “Import of Lipids into Mitochondria”, *Progress in Lipid Research*, Vol. 36, No. 2-3, pp. 103–130, 1997.
176. Goossens, K. and H. De Winter, “Molecular Dynamics Simulations of Membrane Proteins: An Overview”, *Journal of Chemical Information and Modeling*, Vol. 58, No. 11, pp. 2193–2202, 2018.
177. Lee, J., X. Cheng, J. M. Swails, M. S. Yeom, P. K. Eastman, J. A. Lemkul, S. Wei, J. Buckner, J. C. Jeong, Y. Qi, S. Jo, V. S. Pande, D. A. Case, C. L. Brooks, A. D. MacKerell, J. B. Klauda and W. Im, “CHARMM-GUI Input Generator for NAMD, GROMACS, AMBER, OpenMM, and CHARMM/OpenMM Simulations Using the CHARMM36 Additive Force Field”, *Journal of Chemical Theory and Computation*, Vol. 12, No. 1, pp. 405–413, 2016.
178. Jo, S., J. B. Lim, J. B. Klauda and W. Im, “CHARMM-GUI Membrane Builder for Mixed Bilayers and Its Application to Yeast Membranes”, *Biophysical Journal*, Vol. 97, No. 1, pp. 50–58, 2009.
179. Dickson, C. J., B. D. Madej, A. A. Skjevik, R. M. Betz, K. Teigen, I. R. Gould, R. C. Walker, A. A. Skjevik, R. M. Betz, K. Teigen, I. R. Gould, R. C. Walker, g. A. Skjevik, R. M. Betz, K. Teigen, I. R. Gould and R. C. Walker, “Lipid14: The Amber Lipid Force Field”, *Journal of Chemical Theory and Computation*, Vol. 10, No. 2, pp. 865–879, 2014.
180. Liu, X., S. Dai, Y. Zhu, P. Marrack and J. W. Kappler, “The Structure of a Bcl-xL/Bim Fragment Complex”, *Immunity*, Vol. 19, No. 3, pp. 341–352, 2003.
181. Wilfling, F., A. Weber, S. Potthoff, F.-N. Vögtle, C. Meisinger, S. A. Paschen and G. Häcker, “BH3-only Proteins Are Tail-anchored in the Outer Mitochondrial Membrane and Can Initiate the Activation of Bax”, *Cell Death & Differentiation*, Vol. 19, No. 8, pp. 1328–1336, 2012.

182. Ashkenazi, A., W. J. Fairbrother, J. D. Levenson and A. J. Souers, “From Basic Apoptosis Discoveries to Advanced Selective BCL-2 Family Inhibitors”, *Nature Reviews Drug Discovery*, Vol. 16, No. 4, pp. 273–284, 2017.
183. Pécot, J., L. Maillet, J. Le Pen, C. Vuillier, S. d. C. Trécesson, A. Fétiveau, K. A. Sarosiek, F. J. Bock, F. Braun, A. Letai, S. W. Tait, F. Gautier and P. P. Juin, “Tight Sequestration of BH3 Proteins by BCL-xL at Subcellular Membranes Contributes to Apoptotic Resistance”, *Cell Reports*, Vol. 17, No. 12, pp. 3347–3358, 2016.
184. Martin, A. C. R. and C. T. Porter, “ProFit, version 3.1”, *University College London*, 2009.
185. Modi, V., D. Lama and R. Sankararamakrishnan, “Relationship between Helix Stability and Binding Affinities: Molecular Dynamics Simulations of Bfl-1/A1-binding Pro-apoptotic BH3 Peptide Helices in Explicit Solvent”, *Journal of Biomolecular Structure and Dynamics*, Vol. 31, No. 1, pp. 65–77, 2013.
186. Lama, D. and R. Sankararamakrishnan, “Molecular Dynamics Simulations of Pro-apoptotic BH3 Peptide Helices in Aqueous Medium: Relationship between Helix Stability and Their Binding affinities to the Anti-apoptotic Protein Bcl-XL”, *Journal of Computer-Aided Molecular Design*, Vol. 25, No. 5, pp. 413–426, 2011.
187. Yao, Y., A. A. Bobkov, L. A. Plesniak and F. M. Marassi, “Mapping the Interaction of Pro-Apoptotic tBID with Pro-Survival BCL-XL”, *Biochemistry*, Vol. 48, No. 36, pp. 8704–8711, 2009.
188. Madelaine, C., V. Valerio and N. Maulide, “Revisiting Keteniminium Salts: More than the Nitrogen Analogs of Ketenes”, *Chemistry - An Asian Journal*, Vol. 6, No. 9, pp. 2224–2239, 9 2011.
189. Snider, B. B., “Intramolecular Cycloaddition Reactions of Ketenes and Keteniminium Salts with Alkenes”, *Chemical Reviews*, Vol. 88, No. 5, pp. 793–811, 1988.

190. Ghosez, L., F. Mahuteau-Betzer, C. Genicot, A. Vallribera and J.-F. Cordier, "Enantioselective Vicinal Bis-Acylation of Olefins", *Chemistry - A European Journal*, Vol. 8, No. 15, pp. 3411–3422, 2002.
191. Mahuteau-Betzer, F., P.-Y. Ding and L. Ghosez, "First [4+2] Cycloadditions Involving the Olefinic Bond of an 'Aldoketeniminium Salt' (=N-Alk-1-enylideneaminium Salt)", *Helvetica Chimica Acta*, Vol. 88, No. 7, pp. 2022–2031, 2005.
192. Villedieu-Percheron, E., S. Catak, D. Zurwerra, R. Staiger, M. Lachia and A. De Mesmaeker, " $6\pi/10\pi$ -Electrocyclization of Ketene-iminium Salts for the Synthesis of Substituted Naphthylamines", *Tetrahedron Letters*, Vol. 55, No. 15, pp. 2446–2449, 2014.
193. Lumbroso, A., J. Behra, A. Kolleth, P.-Y. Dakas, U. Karadeniz, S. Catak, S. Sulzer-Mossé and A. De Mesmaeker, "Access to Functionalized 3-Amino-benzothiophenes using Keteniminium Intermediates", *Tetrahedron Letters*, Vol. 56, pp. 6541–6545, 2015.
194. Lumbroso, A., S. Catak, S. Sulzer-Mossé and A. De Mesmaeker, "Synthesis of Cyclobuteniminium Salts Derived from Aldo-keteniminium salts and Study of Their Reactivity in Diels-Alder Reaction", *Tetrahedron Letters*, Vol. 55, No. 49, pp. 6721–6725, 2014.
195. Kolleth, A., A. Lumbroso, G. Tanriver, S. Catak, S. Sulzer-Mossé and A. De Mesmaeker, "Synthesis of 4-membered Ring Alkaloid Analogues via Intramolecular [2+2] Cycloaddition Involving Keteniminium Salt Intermediates", *Tetrahedron Letters*, Vol. 58, No. 30, pp. 2904–2909, 2017.
196. Lecomte, M. and G. Evano, "Harnessing the Electrophilicity of Keteniminium Ions: A Simple and Straightforward Entry to Tetrahydropyridines and Piperidines from Ynamides", *Angewandte Chemie - International Edition*, Vol. 55, No. 14, pp. 4547–4551, 2016.
197. Xu, L., P. Yang and L. Wang, "Direct Functionalization of Benzylic and Non-

- benzylic C(sp³)-H Bonds via Keteniminium Ion Initiated Cascade [1,5]-hydrogen Transfer/Cyclization”, *Organic Chemistry Frontiers*, Vol. 5, No. 11, pp. 1854–1858, 2018.
198. Peng, B., D. H. O’Donovan, I. D. Jurberg and N. Maulide, “Dual Nucleophilic/Electrophilic Capture of In Situ Generated Iminium Ethers: Towards the Synthesis of Functionalized Amide Building Blocks”, *Chemistry - A European Journal*, Vol. 18, No. 51, pp. 16292–16296, 2012.
199. Lumbroso, A., S. Catak, S. Sulzer-Mossé and A. De Mesmaeker, “Cycloaddition of Keteniminium with Terminal Alkynes toward Cyclobuteniminium and Their Use in Diels-Alder Reactions”, *Tetrahedron Letters*, Vol. 55, No. 37, pp. 5147–5150, 2014.
200. Emamian, S., S. j. Hosseini and K.-s. Ravani, “Ionic Diels–Alder Reaction of 3-bromofuran toward the Highly Electron Deficient Cyclobuteniminium Cation: a Regio- and Stereoselectivity, and Molecular Mechanism Study Using DFT”, *RSC Advances*, Vol. 5, No. 119, pp. 98538–98548, 2015.
201. Kolleth, A., A. Lumbroso, G. Tanriver, S. Catak, S. Sulzer-Mossé and A. De Mesmaeker, “New Access to Quaternary Aminocyclobutanes via Nucleophilic Addition on Cyclobutaniminium Salts”, *Tetrahedron Letters*, Vol. 57, No. 31, pp. 3510–3514, 2016.
202. Catak, S., K. Hemelsoet, L. Hermosilla, M. Waroquier and V. Van Speybroeck, “Competitive Reactions of Organophosphorus Radicals on Coke Surfaces”, *Chemistry - A European Journal*, Vol. 17, No. 43, pp. 12027–12036, 2011.
203. Goossens, H., J. M. Winne, S. Wouters, L. Hermosilla, P. J. De Clercq, M. Waroquier, V. Van Speybroeck and S. Catak, “Possibility of [1,5] Sigmatropic Shifts in Bicyclo[4.2.0]octa-2,4-dienes”, *Journal of Organic Chemistry*, Vol. 80, No. 5, pp. 2609–2620, 2015.
204. Hermosilla, L., S. Catak, V. Van Speybroeck, M. Waroquier, J. Vandenberg, F. Motmans, P. Adriaensens, L. Lutsen, T. Cleij and D. Vanderzande, “Kinetic and Mech-

- anistic Study on p- Quinodimethane Formation in the Sulfinyl Precursor Route for the Polymerization of Poly(p-phenylenevinylene) (PPV)”, *Macromolecules*, Vol. 43, No. 18, pp. 7424–7433, 2010.
205. Schuchardt, K. L., B. T. Didier, T. Elsethagen, L. Sun, V. Gurumoorthi, J. Chase, J. Li and T. L. Windus, “Basis Set Exchange: A Community Database for Computational Sciences”, *Journal of Chemical Information and Modeling*, Vol. 47, No. 3, pp. 1045–1052, 2007.
206. Tomasi, J., B. Mennucci and E. Cancès, “The IEF Version of the PCM Solvation Method: an Overview of a New Method Addressed to Study Molecular Solutes at the QM Ab Initio Level”, *Journal of Molecular Structure: THEOCHEM*, Vol. 464, No. 1-3, pp. 211–226, 1999.
207. Frisch, M. J., G. W. Trucks, H. B. Schlegel, G. E. Scuseria, M. A. Robb, J. R. Cheeseman, G. Scalmani, V. Barone, G. A. Petersson, H. Nakatsuji, X. Li, M. Caricato, A. V. Marenich, J. Bloino, B. G. Janesko, R. Gomperts, B. Mennucci, H. P. Hratchian, J. V. Ortiz, A. F. Izmaylov, J. L. Sonnenberg, D. Williams-Young, F. Ding, F. Lipparini, F. Egidi, J. Goings, B. Peng, A. Petrone, T. Henderson, D. Ranasinghe, V. G. Zakrzewski, J. Gao, N. Rega, G. Zheng, W. Liang, M. Hada, M. Ehara, K. Toyota, R. Fukuda, J. Hasegawa, M. Ishida, T. Nakajima, Y. Honda, O. Kitao, H. Nakai, T. Vreven, K. Throssell, J. A. Montgomery Jr., J. E. Peralta, F. Ogliaro, M. J. Bearpark, J. J. Heyd, E. N. Brothers, K. N. Kudin, V. N. Staroverov, T. A. Keith, R. Kobayashi, J. Normand, K. Raghavachari, A. P. Rendell, J. C. Burant, S. S. Iyengar, J. Tomasi, M. Cossi, J. M. Millam, M. Klene, C. Adamo, R. Cammi, J. W. Ochterski, R. L. Martin, K. Morokuma, O. Farkas, J. B. Foresman and D. J. Fox, “Gaussian 16, Revision A.03”, *Gaussian Inc. Wallingford CT*, 2016.
208. Fukui, K., “The Path of Chemical Reactions - The IRC Approach”, *Accounts of Chemical Research*, Vol. 14, No. 12, pp. 363–368, 1981.
209. Hratchian, H. P. and H. B. Schlegel, “Accurate Reaction Paths Using a Hessian Based Predictor-corrector Integrator”, *Journal of Chemical Physics*, Vol. 120, No. 21, pp.

- 9918–9924, 2004.
210. Hratchian, H. P. and H. B. Schlegel, “Using Hessian Updating to Increase the Efficiency of a Hessian Based Predictor-Corrector Reaction Path Following Method”, *Journal of Chemical Theory and Computation*, Vol. 1, No. 1, pp. 61–69, 2005.
211. Hehre, W. J., R. Ditchfield and J. A. Pople, “Self—Consistent Molecular Orbital Methods. XII. Further Extensions of Gaussian—Type Basis Sets for Use in Molecular Orbital Studies of Organic Molecules”, *The Journal of Chemical Physics*, Vol. 56, No. 5, pp. 2257–2261, 1972.
212. Gonzalez, C. and H. B. Schlegel, “Reaction Path Following in Mass-Weighted Internal Coordinates”, *J. Phys. Chem*, Vol. 94, No. 14, pp. 5523–5527, 1990.
213. Bickelhaupt, F. M. and K. N. Houk, “Analyzing Reaction Rates with the Distortion/Interaction-Activation Strain Model”, *Angewandte Chemie - International Edition*, Vol. 56, No. 34, pp. 10070–10086, 2017.
214. Fernández, I. and F. M. Bickelhaupt, “The Activation Strain Model and Molecular Orbital Theory: Understanding and Designing Chemical Reactions”, *Chem. Soc. Rev.*, Vol. 43, No. 14, pp. 4953–4967, 2014.
215. van Zeist, W.-J. and F. M. Bickelhaupt, “The Activation Strain Model of Chemical Reactivity”, *Organic & Biomolecular Chemistry*, Vol. 8, No. 14, p. 3118, 2010.
216. Fukui, K., T. Yonezawa and H. Shingu, “A Molecular Orbital Theory of Reactivity in Aromatic Hydrocarbons”, *The Journal of Chemical Physics*, Vol. 20, No. 4, pp. 722–725, 1952.
217. Fukui, K., “Role of Frontier Orbitals in Chemical Reactions.”, *Science*, Vol. 218, No. 4574, pp. 747–754, 1982.
218. Lu, T. and F. Chen, “Multiwfn: A Multifunctional Wavefunction Analyzer”, *Journal of*

Computational Chemistry, Vol. 33, No. 5, pp. 580–592, 2012.

219. Skripnikov, L. V., “Chemissian, version 4.60”, *Visualization Computer Program*, 2018.
220. Legault, C. Y., “CYLview, version 1.0b”, *Université de Sherbrooke*, 2009.
221. Garro-Helion, F., A. Merzouk and F. Guibé, “Mild and Selective Palladium(0)-Catalyzed Deallylation of Allylic Amines. Allylamine and Diallylamine as Very Convenient Ammonia Equivalents for the Synthesis of Primary Amines”, *Journal of Organic Chemistry*, Vol. 58, No. 22, pp. 6109–6113, 1993.
222. Kolleth, A., A. Lumbroso, G. Tanriver, S. Catak, S. Sulzer-Mossé and A. De Mesmaeker, “Synthesis of Amino-cyclobutanes via [2+2] Cycloadditions Involving Keteniminium Intermediates”, *Tetrahedron Letters*, Vol. 57, No. 25, pp. 2697–2702, 2016.
223. Frisch, M. J., G. W. Trucks, H. B. Schlegel, G. E. Scuseria, M. A. Robb, J. R. Cheeseman, G. Scalmani, V. Barone, B. Mennucci, G. A. Petersson, H. Nakatsuji, M. Caricato, X. Li, H. P. Hratchian, A. F. Izmaylov, J. Bloino, G. Zheng, J. L. Sonnenberg, M. Hada, M. Ehara, K. Toyota, R. Fukuda, J. Hasegawa, M. Ishida, T. Nakajima, Y. Honda, O. Kitao, H. Nakai, T. Vreven, J. A. Montgomery Jr., J. E. Peralta, F. Ogliaro, M. Bearpark, J. J. Heyd, E. Brothers, K. N. Kudin, V. N. Staroverov, R. Kobayashi, J. Normand, K. Raghavachari, A. Rendell, J. C. Burant, S. S. Iyengar, J. Tomasi, M. Cossi, N. Rega, J. M. Millam, M. Klene, J. E. Knox, J. B. Cross, V. Bakken, C. Adamo, J. Jaramillo, R. Gomperts, R. E. Stratmann, O. Yazyev, A. J. Austin, R. Cammi, C. Pomelli, J. W. Ochterski, R. L. Martin, K. Morokuma, V. G. Zakrzewski, G. A. Voth, P. Salvador, J. J. Dannenberg, S. Dapprich, A. D. Daniels, O. Farkas, J. B. Foresman, J. V. Ortiz, J. Cioslowski and D. J. Fox, “Gaussian 09, Revision E.01”, *Gaussian Inc. Wallingford CT*, 2013.
224. Domingo, L. R., M. Ríos-Gutiérrez and P. Pérez, “A DFT Study of the Ionic [2+2] Cycloaddition Reactions of Keteniminium Cations with Terminal Acetylenes”, *Tetrahedron*, Vol. 71, No. 16, pp. 2421–2427, 2015.

225. Domingo, L. R., M. Ríos-Gutiérrez and J. A. Sáez, “Unravelling the Mechanism of the Ketene-imine Staudinger Reaction. An ELF Quantum Topological Analysis”, *RSC Advances*, Vol. 5, No. 47, pp. 37119–37129, 2015.
226. Kolleth, A., S. Müller, A. Lumbroso, G. Tanriver, S. Catak, S. Sulzer-Mossé and A. De Mesmaeker, “Access to 3-Aminobenzothiophenes and 3-Aminothiophenes Fused to 5-membered Heteroaromatic Rings through 6π -electrocyclization Reaction of Keteniminium salts”, *Tetrahedron Letters*, Vol. 59, No. 34, pp. 3242–3248, 2018.
227. Dagoneau, D., A. Kolleth, A. Lumbroso, G. Tanriver, S. Catak, S. Sulzer-Mossé and A. De Mesmaeker, “Straightforward Synthesis of 3-Aminothiophenes Using Activated Amides”, *Helvetica Chimica Acta*, Vol. 102, No. 4, p. e1900031, 2019.
228. Catak, S., M. D’hooghe, N. De Kimpe, M. Waroquier and V. Van Speybroeck, “Intramolecular π – π Stacking Interactions in 2-Substituted N,N-Dibenzylaziridinium Ions and Their Regioselectivity in Nucleophilic Ring-Opening Reactions”, *The Journal of Organic Chemistry*, Vol. 75, No. 3, pp. 885–896, 2010.
229. Boese, A. D. and J. M. Martin, “Development of Density Functional for Thermochemical Kinetics”, *Journal of Chemical Physics*, Vol. 121, No. 8, pp. 3405–3416, 2004.
230. Boydas, E., G. Tanriver, M. D’Hooghe, H.-J. Ha, V. Van Speybroeck and S. Catak, “Theoretical Insight into the Regioselective Ring-expansions of Bicyclic Aziridinium Ions”, *Organic and Biomolecular Chemistry*, Vol. 16, No. 5, pp. 796–806, 2018.
231. Yanai, T., D. P. Tew and N. C. Handy, “A New Hybrid Exchange-correlation Functional using the Coulomb-attenuating Method (CAM-B3LYP)”, *Chemical Physics Letters*, Vol. 393, No. 1-3, pp. 51–57, 2004.
232. Kolleth, A., A. Lumbroso, G. Tanriver, S. Catak, S. Sulzer-Mossé and A. De Mesmaeker, “New Access to Quaternary Aminocyclobutanes via Nucleophilic Addition on Cyclobutaniminium Salts”, *Tetrahedron Letters*, Vol. 57, No. 31, pp. 3510–3514, 2016.

233. Boeger P, "Finding the Target Site of Chloroacetamides: A Thorny Subject", *Journal of Pesticide Science*, Vol. 22, p. 257–262, 1997.
234. Snoeck, M., "Articaine: A Review of Its Use for Local and Regional Anesthesia", *Local and Regional Anesthesia*, Vol. 5, pp. 23–33, 2012.
235. Tackie, A. N., G. L. Boye, M. H. Sharaf, P. L. Schiff, R. C. Crouch, T. D. Spitzer, R. L. Johnson, J. Dunn, D. Minick and G. E. Martin, "Cryptospirolepine, A Unique Spiro-nonacyclic Alkaloid Isolated from *Cryptolepis Sanguinolenta*", *Journal of Natural Products*, Vol. 56, No. 5, pp. 653–670, 1993.
236. Romagnoli, R., P. G. Baraldi, M. D. Carrion, C. L. Cara, D. Preti, F. Fruttarolo, M. G. Pavani, M. A. Tabrizi, M. Tolomeo, S. Grimaudo, A. Di Cristina, J. Balzarini, J. A. Hadfield, A. Brancale and E. Hamel, "Synthesis and Biological Evaluation of 2- and 3-Aminobenzo[b]thiophene Derivatives as Antimitotic Agents and Inhibitors of Tubulin Polymerization", *Journal of Medicinal Chemistry*, Vol. 50, No. 9, pp. 2273–2277, 2007.
237. Papakyriakou, A., P. Kefalos, P. Sarantis, C. Tsiamantas, K. P. Xanthopoulos, D. Vourloumis and D. Beis, "A Zebrafish In Vivo Phenotypic Assay to Identify 3-Aminothiophene-2-Carboxylic Acid-Based Angiogenesis Inhibitors", *ASSAY and Drug Development Technologies*, Vol. 12, No. 9-10, pp. 527–535, 12 2014.
238. Silva, Y., C. Reyes, G. Rivera, M. Alves, E. Barreiro, M. Moreira and L. Lima, "3-Aminothiophene-2-Acylhydrazones: Non-Toxic, Analgesic and Anti-Inflammatory Lead-Candidates", *Molecules*, Vol. 19, No. 6, pp. 8456–8471, 2014.
239. Court, J. J., C. Poisson, A. Ardzinski, D. Bilimoria, L. Chan, K. Chandupatla, N. Chauret, P. N. Collier, S. K. Das, F. Denis, W. Dorsch, G. Iyer, D. Lauffer, L. L'Heureux, P. Li, B. S. Luisi, N. Mani, S. Nanthakumar, O. Nicolas, B. G. Rao, S. Ronkin, S. Selliah, R. S. Shawgo, Q. Tang, N. D. Waal, C. G. Yannopoulos and J. Green, "Discovery of Novel Thiophene-Based, Thumb Pocket 2 Allosteric Inhibitors of the Hepatitis C NS5B Polymerase with Improved Potency and Physicochemical Profiles", *Journal of*

Medicinal Chemistry, Vol. 59, No. 13, pp. 6293–6302, 2016.

240. Li, P., W. Dorsch, D. J. Lauffer, D. Bilimoria, N. Chauret, J. J. Court, S. K. Das, F. Denis, N. Mani, S. Nanthakumar, O. Nicolas, B. G. Rao, S. Ronkin, S. Selliah, R. S. Shawgo, R. Stearns, Q. Tang, N. D. Waal and J. Green, “Discovery of Novel Allosteric HCV NS5B Inhibitors. 2. Lactam-Containing Thiophene Carboxylates”, *ACS Medicinal Chemistry Letters*, Vol. 8, No. 2, pp. 251–255, 2017.
241. Tanriver, G., D. Dagoneau, U. Karadeniz, A. Kolleth, A. Lumbroso, S. Sulzer-Mossé, A. De Mesmaeker and S. Catak, “Keteniminium Salts: Reactivity and Propensity toward Electrocyclization Reactions”, *The Journal of Organic Chemistry*, Vol. 85, No. 2, pp. 449–463, 2020.
242. Bootsma, A. N. and S. E. Wheeler, “Popular Integration Grids Can Result in Large Errors in DFT-Computed Free Energies”, *ChemRxiv*, 2019.
243. Goossens, H., K. Vervisch, S. Catak, S. Stanković, M. D’hooghe, F. De Proft, P. Geerlings, N. De Kimpe, M. Waroquier and V. Van Speybroeck, “Reactivity of Activated versus Nonactivated 2-(Bromomethyl)aziridines with respect to Sodium Methoxide: A Combined Computational and Experimental Study”, *The Journal of Organic Chemistry*, Vol. 76, No. 21, pp. 8698–8709, 2011.
244. Ditchfield, R., “Self-consistent Perturbation Theory of Diamagnetism”, *Molecular Physics*, Vol. 27, No. 4, pp. 789–807, 1974.
245. Cheeseman, J. R., G. W. Trucks, T. A. Keith and M. J. Frisch, “A Comparison of Models for Calculating Nuclear Magnetic Resonance Shielding Tensors”, *The Journal of Chemical Physics*, Vol. 104, No. 14, pp. 5497–5509, 1996.
246. Glendening, E. D., C. R. Landis and F. Weinhold, “NBO 6.0 : Natural Bond Orbital Analysis Program”, *Journal of Computational Chemistry*, Vol. 34, No. 16, pp. 1429–1437, 6 2013.

247. te Velde, G., F. M. Bickelhaupt, E. J. Baerends, C. Fonseca Guerra, S. J. A. van Gisbergen, J. G. Snijders and T. Ziegler, "Chemistry with ADF", *Journal of Computational Chemistry*, Vol. 22, No. 9, pp. 931–967, 2001.
248. Fonseca Guerra, C., J. G. Snijders, G. te Velde and E. J. Baerends, "Towards an Order-N DFT Method", *Theoretical Chemistry Accounts: Theory, Computation, and Modeling (Theoretica Chimica Acta)*, Vol. 99, No. 6, pp. 391–403, 1998.
249. Nishio, M., "The CH/ π Hydrogen Bond in Chemistry. Conformation, Supramolecules, Optical Resolution and Interactions Involving Carbohydrates", *Physical Chemistry Chemical Physics*, Vol. 13, No. 31, p. 13873, 2011.
250. Birney, D. M. and P. E. Wagenseller, "An Ab Initio Study of the Reactivity of Formylketene. Pseudopericyclic Reactions Revisited", *Journal of the American Chemical Society*, Vol. 116, No. 14, pp. 6262–6270, 1994.
251. Hoffmann, R. and R. B. Woodward, "The Conservation of Orbital Symmetry", *Accounts of Chemical Research*, Vol. 1, No. 1, pp. 17–22, 1968.
252. Gupta, N., R. K. Bansal, M. Von Hopffgarten and G. Frenking, "1,5-electrocyclization versus 1,5-proton Shift in Imidazolium Allylides and 2-phospha-allylides: A DFT Investigation", *Journal of Physical Organic Chemistry*, Vol. 24, No. 9, pp. 786–797, 2011.
253. Ross, J. A., R. P. Seiders and D. M. Lemal, "An Extraordinarily Facile Sulfoxide Automerization", *Journal of the American Chemical Society*, Vol. 98, No. 14, pp. 4325–4327, 1976.
254. Keith, T. and R. Bader, "Calculation of Magnetic Response Properties Using Atoms in Molecules", *Chemical Physics Letters*, Vol. 194, No. 1-2, pp. 1–8, 1992.
255. Keith, T. A. and R. F. Bader, "Calculation of Magnetic Response Properties using A Continuous Set of Gauge Transformations", *Chemical Physics Letters*, Vol. 210, No.

- 1-3, pp. 223–231, 1993.
256. Dagoneau, D., A. Kolleth, P. Quinodoz, G. Tanriver, S. Catak, A. Lumbroso, S. Sulzer-Mossé and A. De Mesmaeker, “Keteniminium Salts as Key Intermediates for the Efficient Synthesis of 3-Amino-Indoles and -Benzofurans”, *Helvetica Chimica Acta*, Vol. 103, No. 1, p. e1900217, 2020.
257. Dagoneau, D., A. Kolleth, P. Quinodoz, G. Tanriver, S. Catak, A. Lumbroso, S. Sulzer-Mossé and A. De Mesmaeker, “Keteniminium Salts as Key Intermediates for the Efficient Synthesis of 3-Amino-Indoles and -Benzofurans”, *Helvetica Chimica Acta*, Vol. 103, No. 1, p. e1900217, 2020.
258. Kučerka, N., S. Tristram-Nagle and J. F. Nagle, “Structure of Fully Hydrated Fluid Phase Lipid Bilayers with Monounsaturated Chains”, *Journal of Membrane Biology*, Vol. 208, No. 3, pp. 193–202, 2006.

APPENDIX A: SUPPORTING INFORMATION

A.1. Supporting Information for Chapter 4.

Table A.1. Experimentally available structures.

Entry ID	Experimental Method	Resolution (Å)	core	loop	J89	C-tail	Remarks
1LXL	SOLUTION NMR		✓	✓	✓	x	
6ZHC	X-RAY DIFFRACTION	1.92	✓	x	x	x	complex
1MAZ	X-RAY DIFFRACTION	2.2	✓	x	x	x	
1R2D	X-RAY DIFFRACTION	1.95	✓	x	x	x	
2B48	X-RAY DIFFRACTION	3.45	✓	x	x	x	
1R2G	X-RAY DIFFRACTION	2.7	✓	x	x	x	mutant
1R2H	X-RAY DIFFRACTION	2.2	✓	x	x	x	mutant
1R2I	X-RAY DIFFRACTION	2	✓	x	x	x	mutant
1R2E	X-RAY DIFFRACTION	2.1	✓	x	x	x	mutant
3CVA	X-RAY DIFFRACTION	2.7	✓	x	x	x	mutant
2ME8	SOLUTION NMR		✓	✓	✓	x	complex
2ME9	SOLUTION NMR		✓	✓	✓	x	
2MEJ	SOLUTION NMR		✓	x	x	x	complex
7CA4	X-RAY DIFFRACTION	2.7	✓	x	x	x	
4HNJ	X-RAY DIFFRACTION	2.9	✓	x	x	x	complex,swap dimer
6BF2	SOLUTION NMR		✓	x	✓	x	mutant
4YJ4	X-RAY DIFFRACTION	2.1	✓	x	✓	x	complex,mutant
4CIN	X-RAY DIFFRACTION	2.693	✓	x	x	x	complex
identity cutoff:90 %							

A.1.1. Force Field Parameterization of Non-standard Iso-Aspartate

Amber force field for L-iso-ASP, which is a non-standard amino acid was parameterized with the antechamber and tleap modules as implemented in the Amber program package [141]. Terminal sides of iso-Asp were capped with ACE and NME (ACE-iso-ASP-NME). The optimization and single point calculation were performed at the HF/6-31G(d) level of theory using Gaussian 09 [223] (G09) program package (Rev E.01) (Figure A.1).

A.1.2. Secondary Structure Analysis

Secondary structure content were calculated using Definition of Secondary Structure Prediction (DSSP) algorithm [146]. Green color in the SS figures presents α helix and 3_{10} helix structures during the simulations.

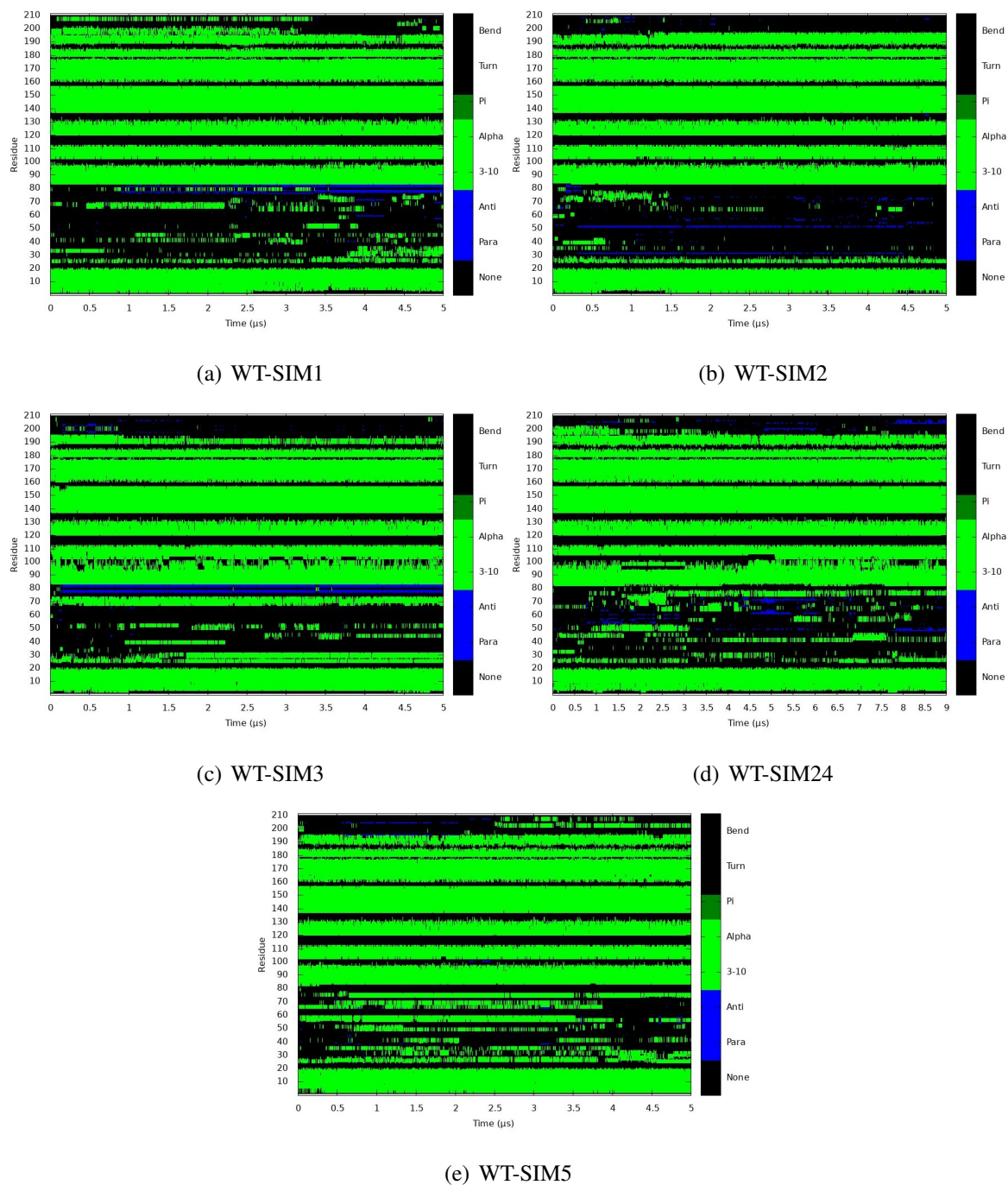


Figure A.2. Secondary structure plots for WT simulations.

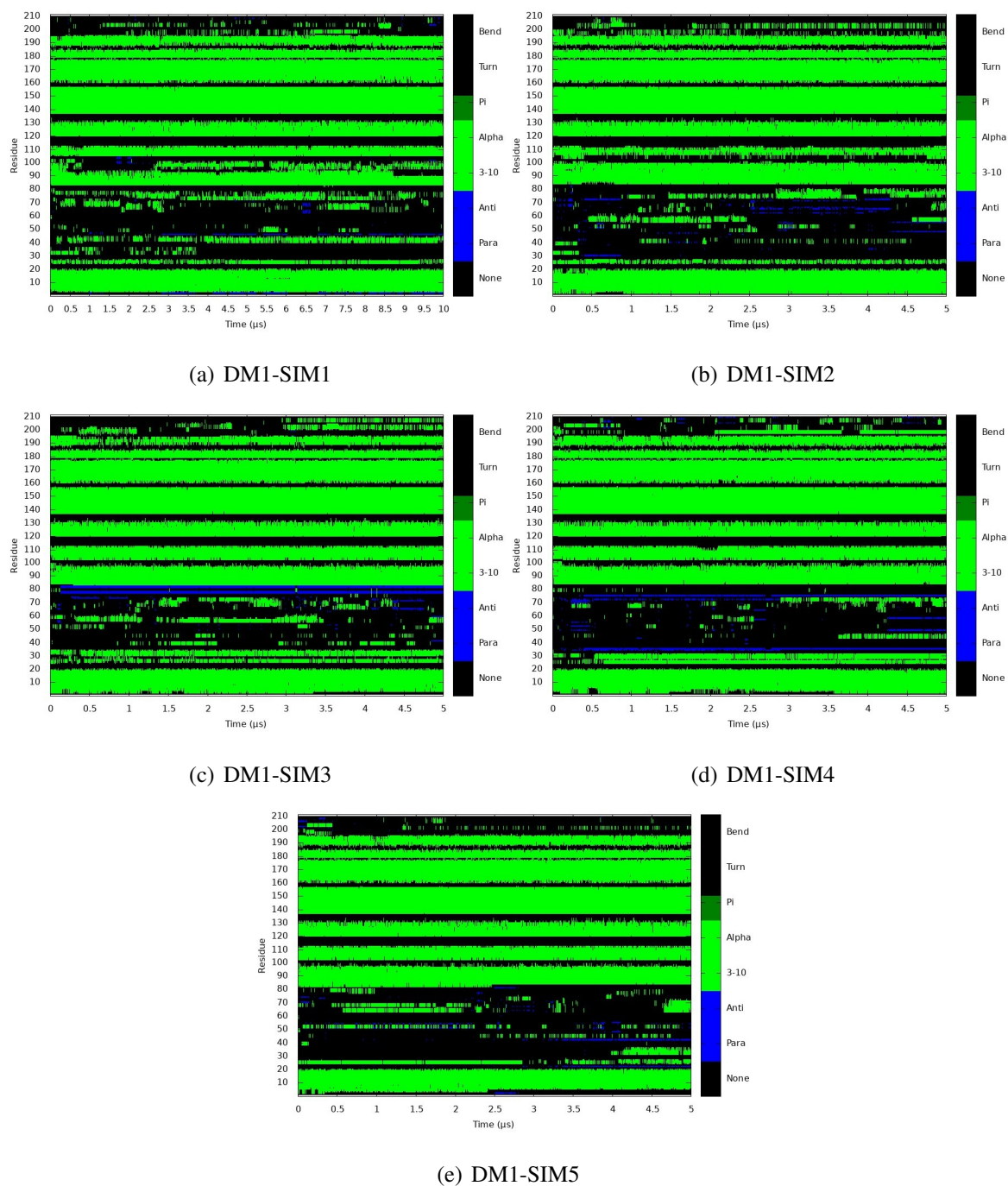


Figure A.3. Secondary structure plots for DM1 simulations.

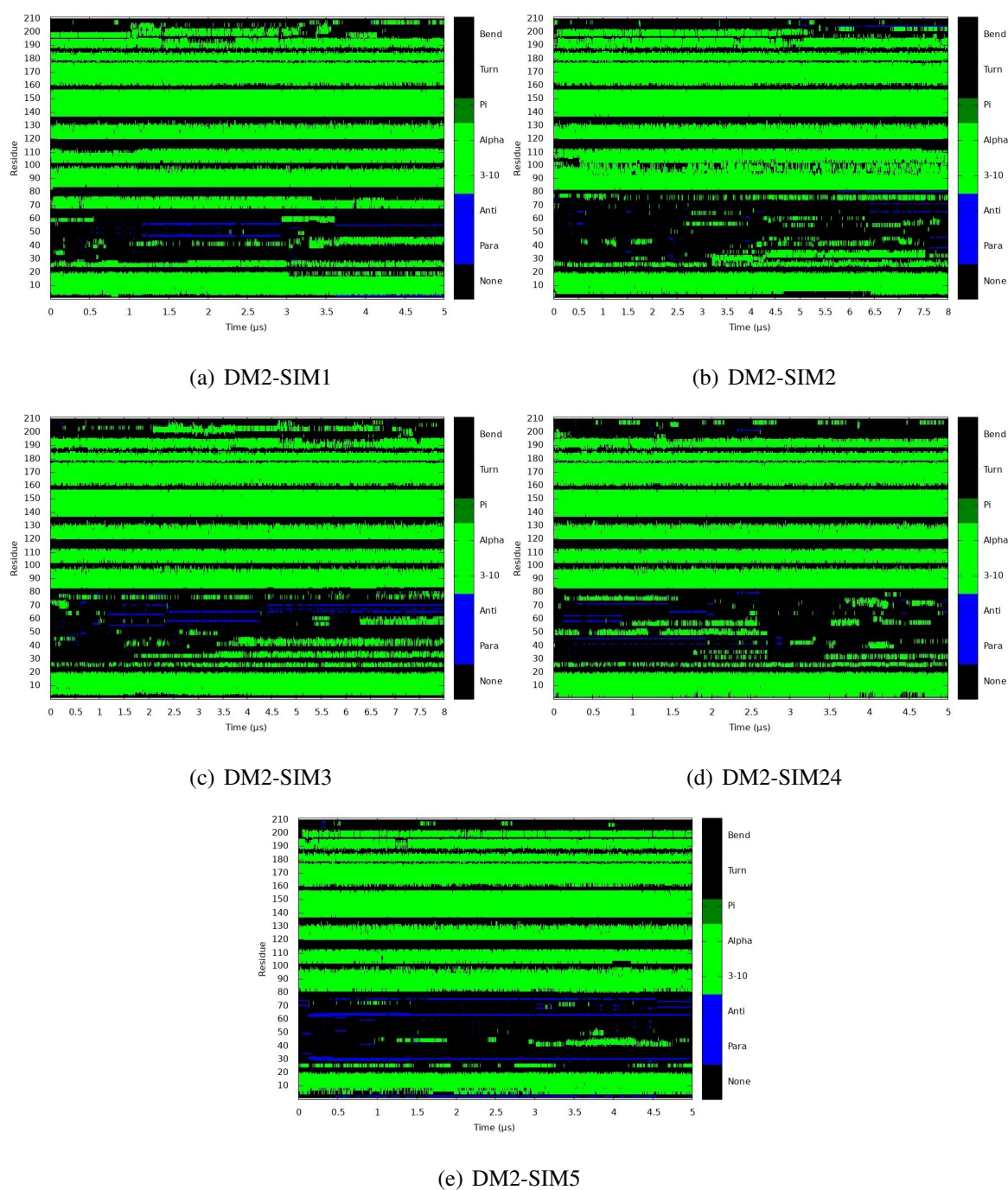


Figure A.4. Secondary structure plots for DM2 simulations.

A.1.3. B-factor Coloring

B-factor coloring is based on LIE calculations. In B-factor coloring, blue color represents stable interaction while red color represents unstable interactions.

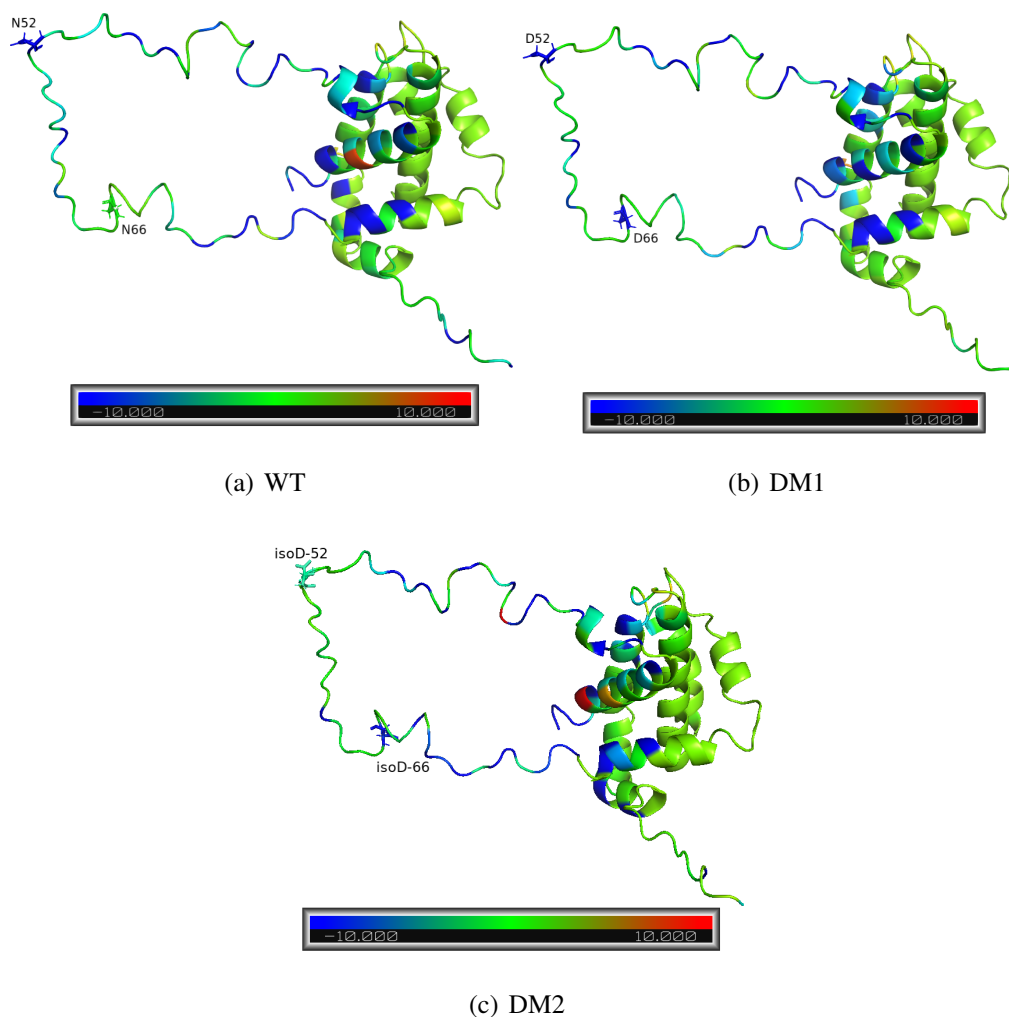


Figure A.5. B-factor coloring based on average LIE calculations between the IDR and protein (Δ IDR) for a) WT, b) DM1, and c) DM2.

A.1.4. Distance Analyses for the Combined Trajectories

Distance analysis results herein covers the analysis of the combined trajectories in each system (WT, DM1 and DM2). These results are consistent with the cluster data. In WT a slight narrowing of the binding groove was also detected but was less prominent compared to the DM1 case.

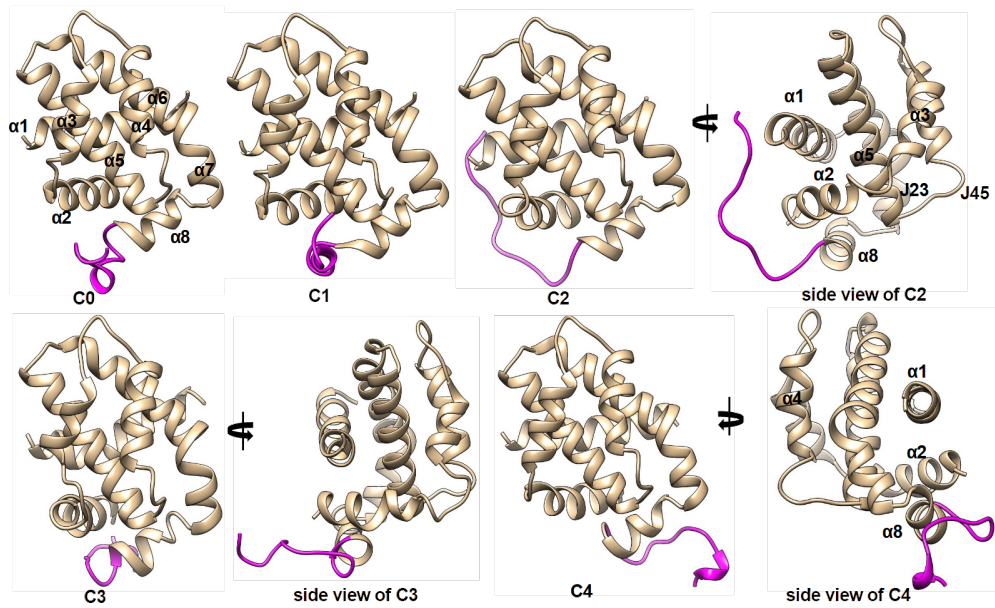


Figure A.6. Representative structures of clusters 0 – 4. (Magenta color refer to the C-terminal part.)

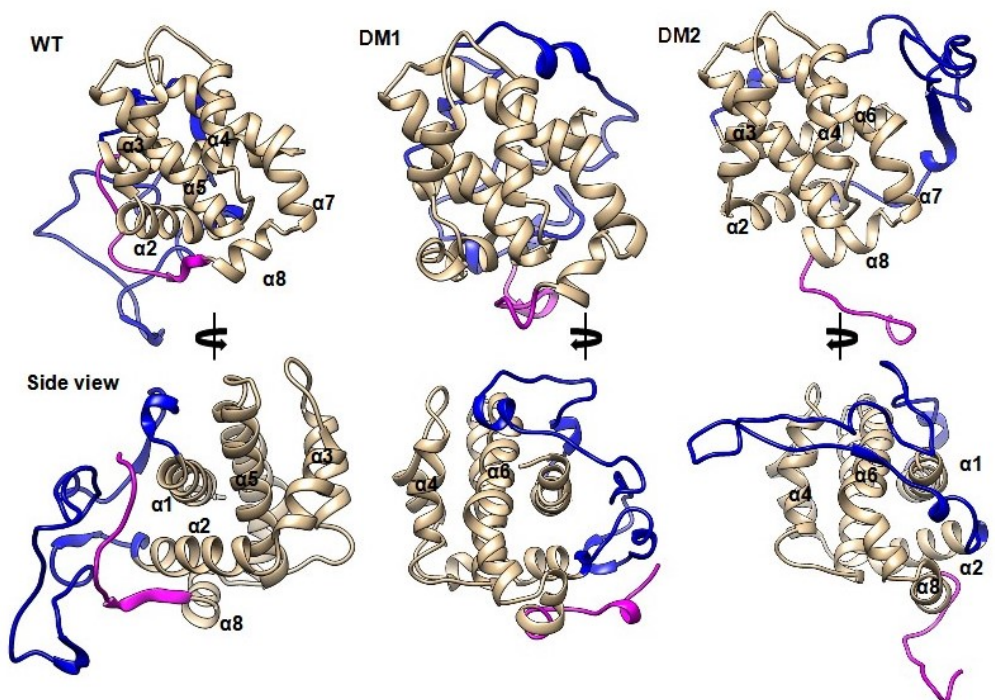


Figure A.7. Front and side views of representative snapshots of each system. (Blue and magenta colors refer to the IDR and the C-terminal part.)

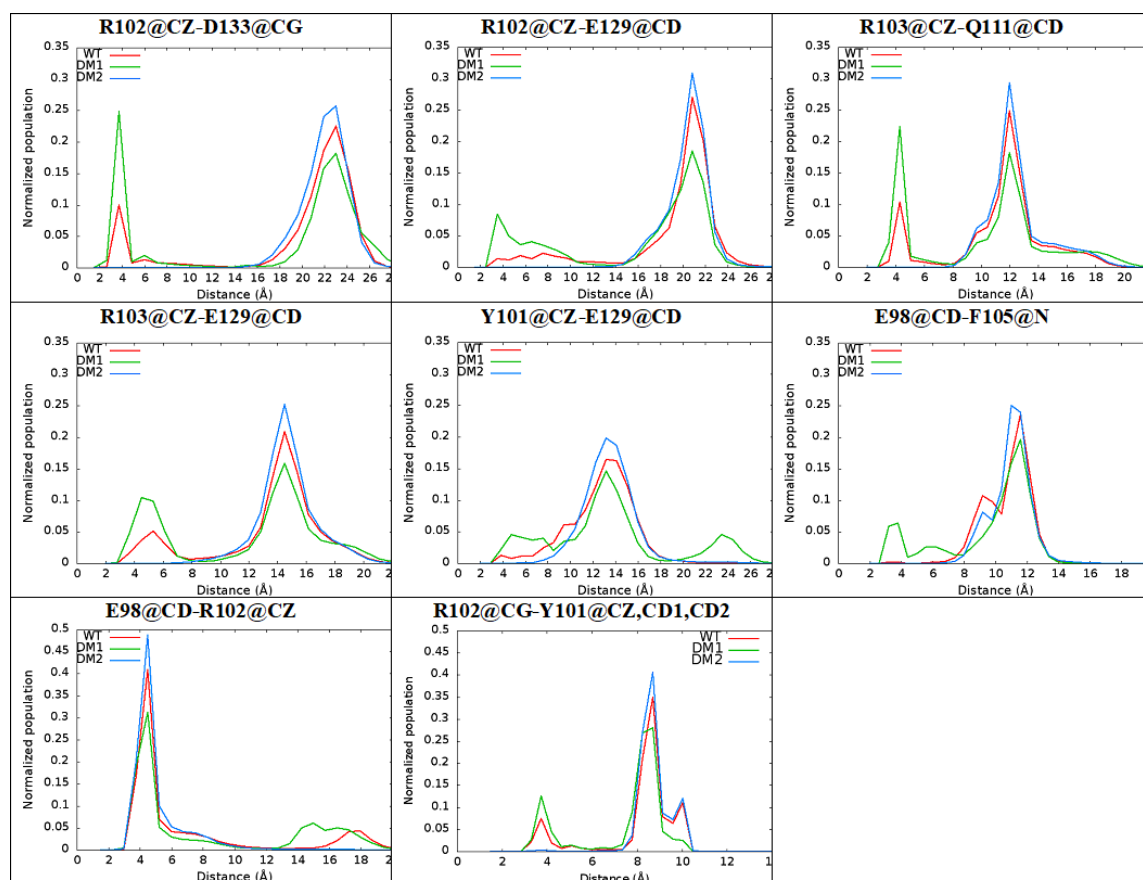
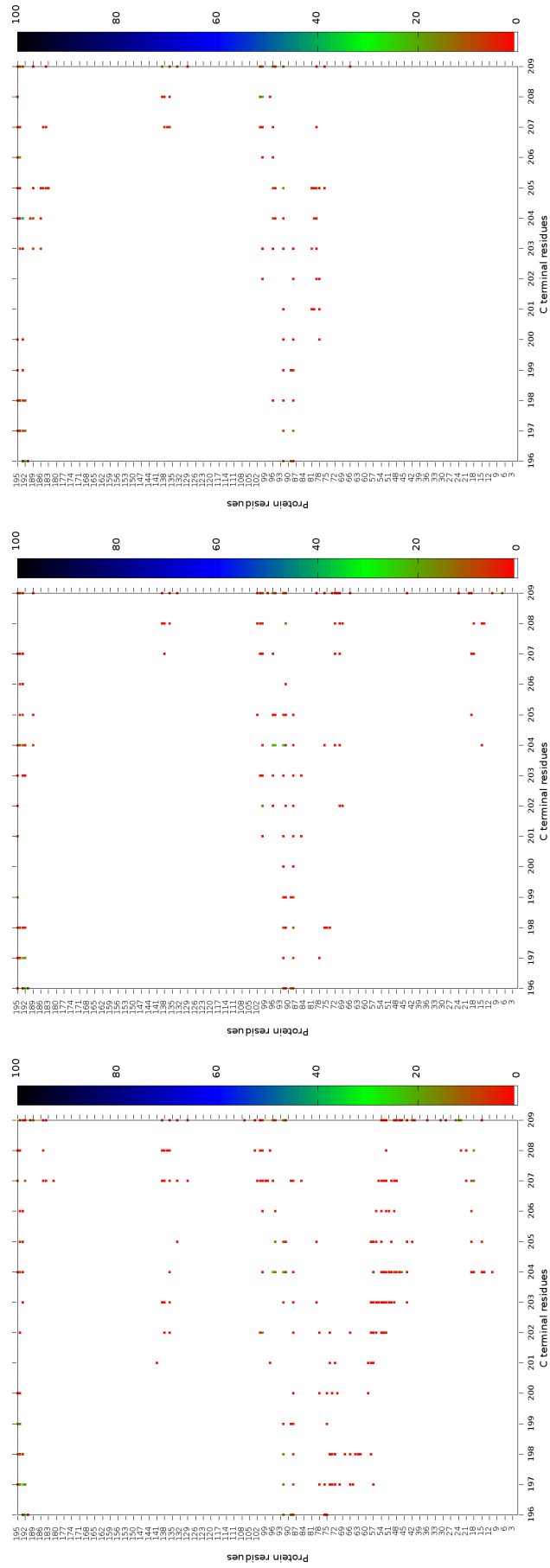


Figure A.8. Distance histogram for the key interactions in the binding groove of WT, DM1, and DM2 simulations.

A.1.5. Protein (Δ C terminal)-C terminal Interactions (residues 196-209) for the Combined Trajectories

In WT, C-terminal part (residues 196-209) is highly flexible/mobile, and it transiently interacts with the IDR and the residues among α 1- α 3 and α 5. In deamidated systems, the C terminal transiently interacts with the bottom side of the groove (particularly, α 2 and J23). The C-terminal-IDR interaction dramatically diminished compared to WT. Remarkably, the C-terminal residues in DM2 do not interact with α 1 and the IDR (except distal IDR residues). In DM2 the C-terminal transiently interacts with α 8.



(a) WT

(b) DM1

(c) DM2

Figure A.9. H-bond interaction plots for protein (Δ C terminal)-C terminal residues of WT, DM1, and DM2 simulations. The color bars show the contact percentage during the simulations.

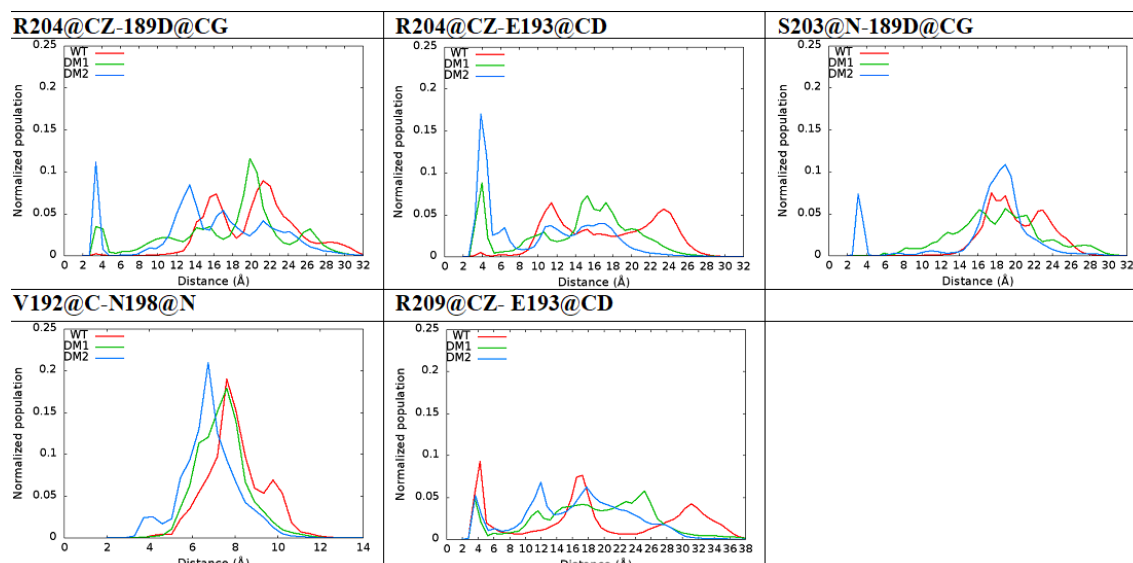


Figure A.10. Distance histogram for the key interactions in the selected H-bonded residues between the C-terminal and $\alpha 8$ of WT, DM1, and DM2 simulations.

A.2. Supporting Information for Chapter 5.

A.2.1. Area Per Lipid (APL)

Area per lipid of POPC (16:0 / 18:1) bilayer/membranes was calculated as shown in the formula below and found in the range of $65.8\text{-}66.4 \text{ \AA}^2$ within 3% of experimental values [179]. Note that the experimental APL for POPC is $68.3 \text{ \AA}^2/\text{lipid}$ and $64.3 \text{ \AA}^2/\text{lipid}$ [258]. APL was calculated as follows:

$$APL = (\text{boxX dimension}) \times (\text{boxY dimension}) \div (\text{number of phospholipids per layer}). \quad (\text{A.1})$$

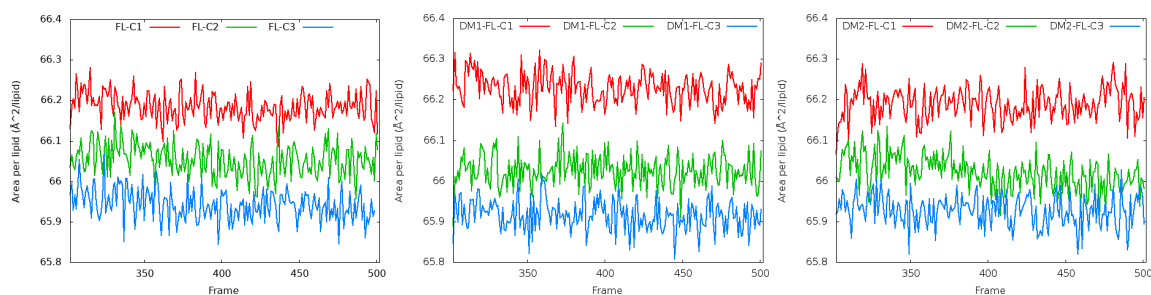


Figure A.11. APL plots for the POPC membranes in equilibrium runs.

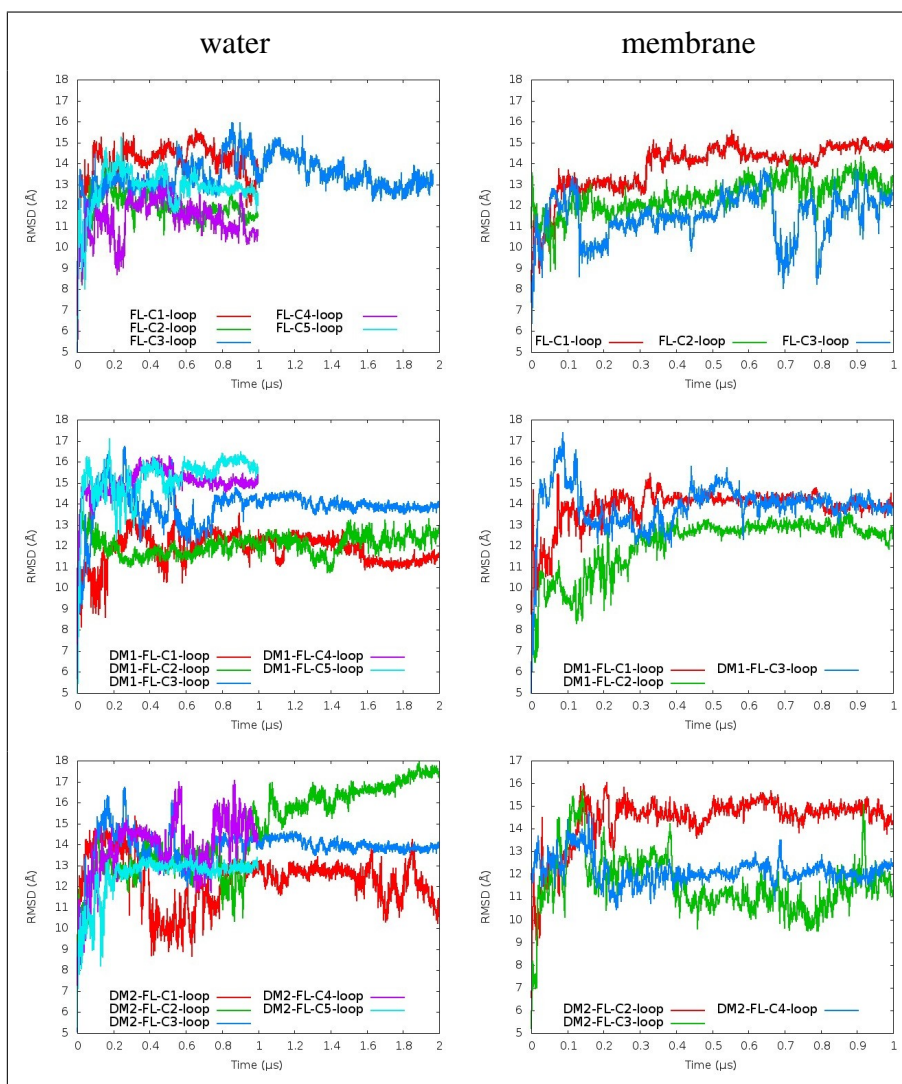


Figure A.12. Backbone RMSD plots for the IDR of FL, DM1 and DM2-Bcl- α_L simulations with respect to initial/built structures (Every 20 frames).

A.3. Supporting Information for Chapter 8

A.3.1. DFT Survey

Besides M06-2X, all calculation in Table A.3 were also performed at the hybrid-GGA B3LYP, hybrid-meta GGA MPWB1K and Second order Møller–Plesset perturbation (MP2). The calculations indicate that even though B3LYP, MPWB1K and MP2 lower the barriers compared to M06-2X optimizations, similar barrier trends were observed regardless of the level of theory. 6-311++G(3df,3pd) extra basis set was used for sulfur atom.

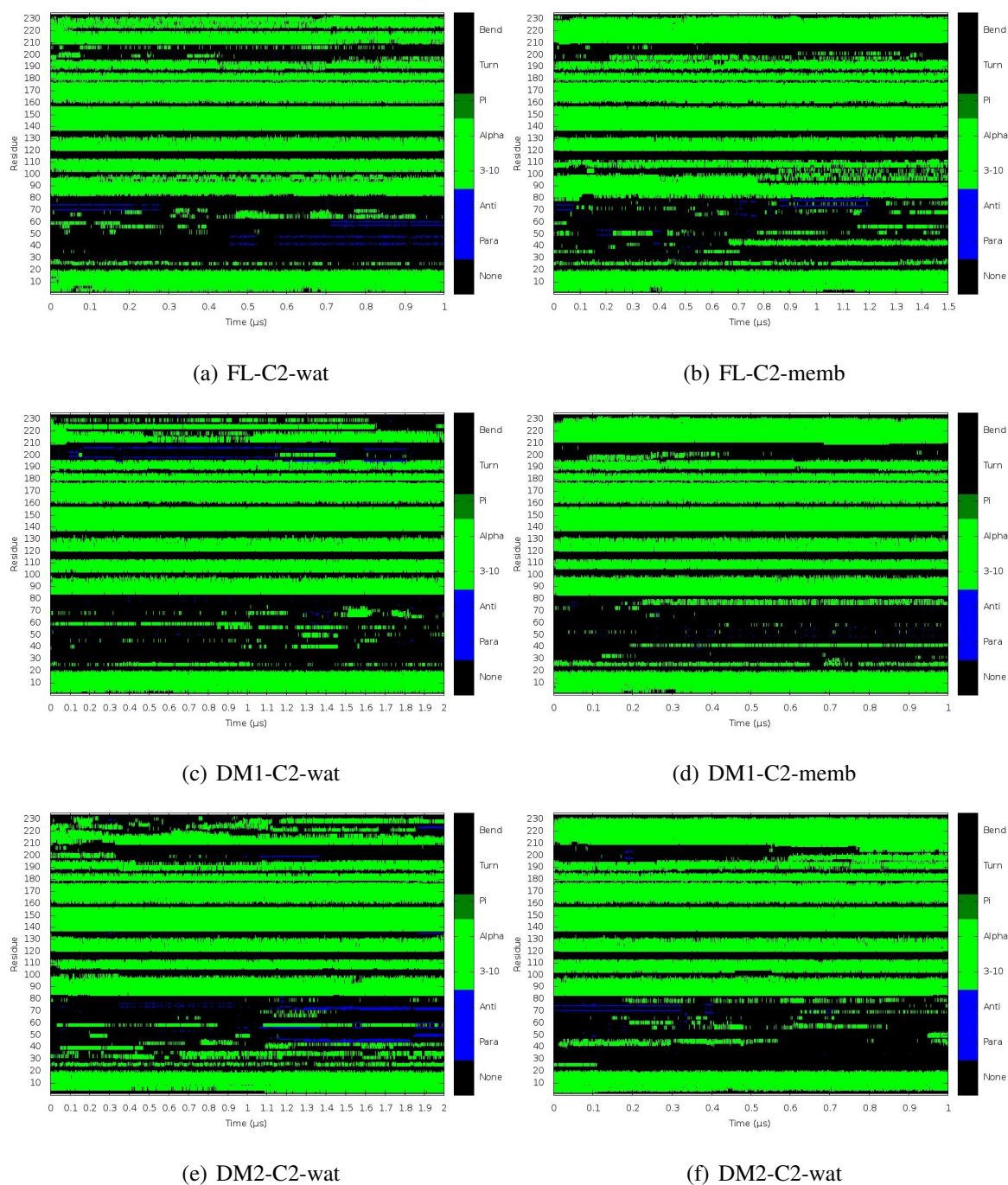


Figure A.13. Secondary structure evolution for the selected FL, DM1 and DM2 simulations in water (wat) and membrane (memb). (Green color presents α helix and 3_{10} helix structures during the simulations.)

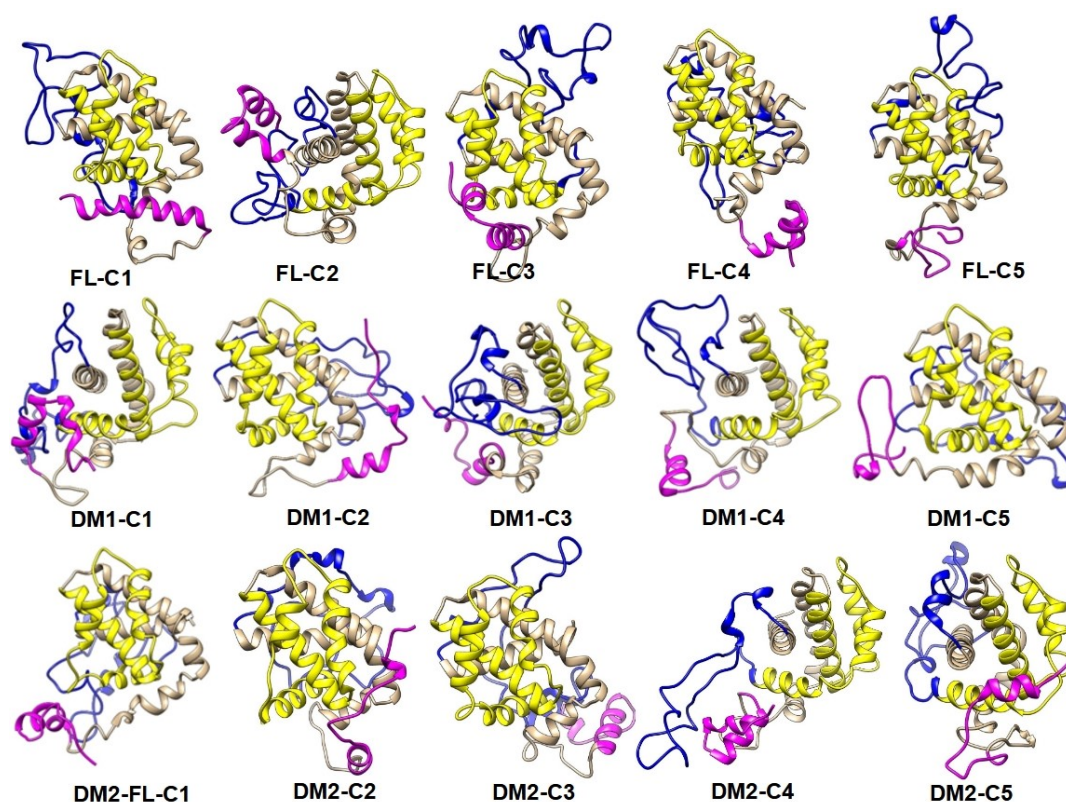


Figure A.14. FL models in water. (Snapshots belong to the last frame of each MD simulation. Blue color denotes loop region (IDR). Magenta and yellow colors present the C-tail and the binding groove, respectively. Water was not shown for clarity.)

Table A.3. Free energy barriers (ΔG^\ddagger), and reaction free energies (ΔG_{rxn}) for 6π -electrocyclization reactions of KIs.

	M06-2X/ 6-31+G(d,p)		B3LYP/ 6-31+G(d,p)		MPWB1K/ 6-31+G(d,p)		MP2/ 6-31+G(d,p)	
Group I	ΔG^\ddagger	ΔG_{rxn}	ΔG^\ddagger	ΔG_{rxn}	ΔG^\ddagger	ΔG_{rxn}	ΔG^\ddagger	ΔG_{rxn}
pyrrole	3.0	-37.8	2.2	-36.1	1.5	-43.0	*	-41.9
furan	6.0	-23.8	6.5	-20.5	5.5	-27.2	3.4	-22.9
thiophene	11.4	-22.2	10.6	-19.4	10.4	-26.8	8.2	-23.4
cyclohexadiene	9.2	-34.8	10.3	-28.6	10.5	-37.1	5.1	-36.6
Group II	ΔG^\ddagger	ΔG_{rxn}	ΔG^\ddagger	ΔG_{rxn}	ΔG^\ddagger	ΔG_{rxn}	ΔG^\ddagger	ΔG_{rxn}
indole	10.8	-4.9	10.2	-3.2	8.8	-9.1	6.1	-7.3
benzofuran	17.0	8.0	15.4	8.5	14.8	3.0	13.6	8.7
benzothiophene	21.0	9.0	20.4	10.6	18.8	4.3	16.0	9.3
naphthalene	14.8	1.7	18.1	8.6	16.2	0.8	6.2	-0.4

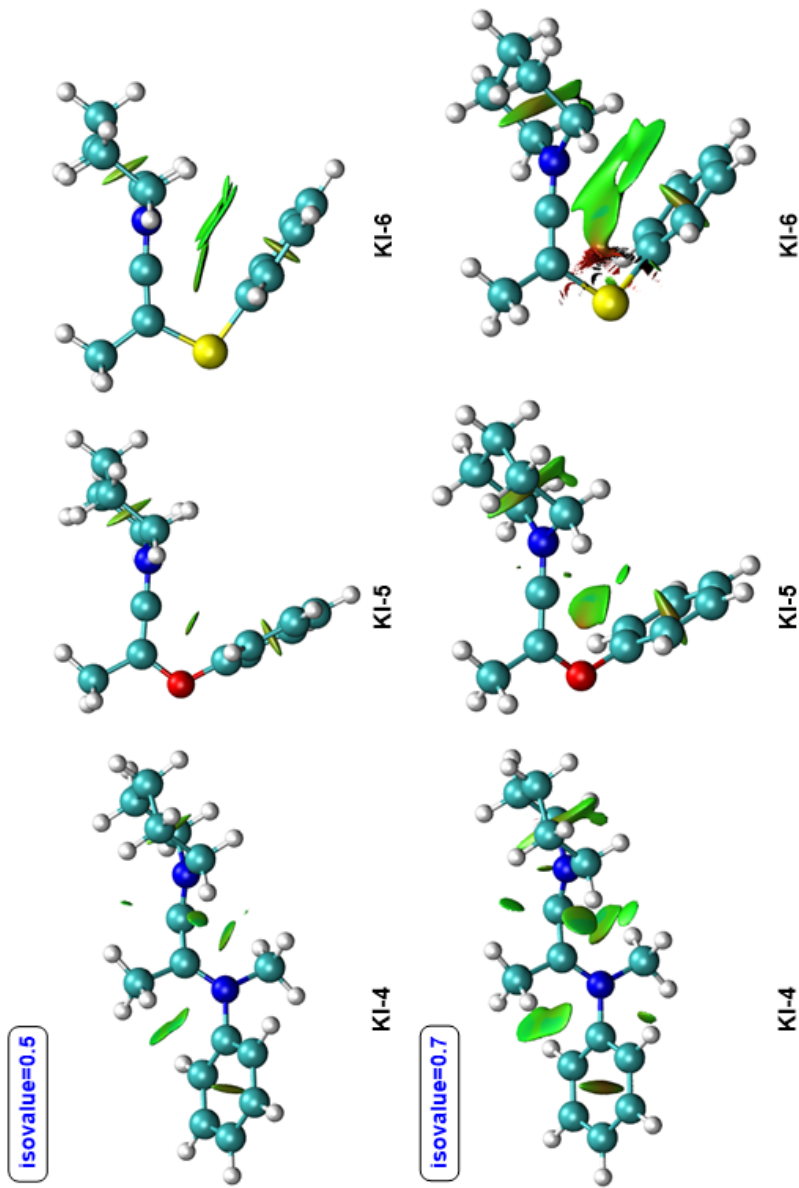
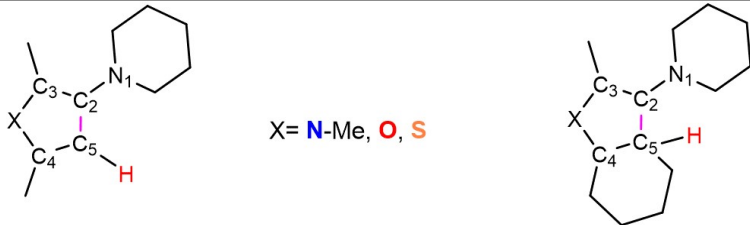


Figure A.15. The non-covalent interaction (NCI) plots of the optimized KI structures. NCI isosurface values= 0.5 and 0.7 au using SCF densities. NCI color scale is $-0.04 < \rho < 0.04$ au.

Note that the electrocyclization initially leads to an intermediate (Int) where C5 bears a H atom. Upon deprotonation of C5, aromaticity is established, and the end product is obtained.

Table A.4. Evolution of distances through the electrocyclization reaction (distances in Å).

											
Distance	KI ^a	KI-PRC	TS	Int	Distance	KI ^a	KI-PRC	TS	Int		
N1-C2	1.25	1.27	1.28	1.36	N1-C2	1.25	1.27	1.29	1.37		
C2-C3	1.31	1.39	1.38	1.37	C2-C3	1.31	1.39	1.38	1.37		
N-C3	1.42	1.34	1.35	1.44	N-C3	1.42	1.33	1.36	1.41		
N-C4	1.42	1.43	1.39	1.30	N-C4	1.42	1.44	1.38	1.32		
C4-C5	1.34	1.33	1.35	1.48	C4-C5	1.40	1.39	1.41	1.48		
C2-C5	3.34	2.88	2.42	1.51	C2-C5	3.62	4.33	2.10	1.53		
Distance	KI	TS	Int	Distance	KI	TS	Int	Distance	KI	TS	Int
N1-C2	1.25	1.28	1.36	N1-C2	1.25	1.30	1.37	N1-C2	1.25	1.30	1.36
C2-C3	1.32	1.34	1.36	C2-C3	1.32	1.35	1.36	C2-C3	1.30	1.35	1.37
O-C3	1.34	1.35	1.43	O-C3	1.35	1.36	1.40	S-C3	1.76	1.73	1.72
O-C4	1.41	1.36	1.27	O-C4	1.40	1.35	1.31	S-C4	1.79	1.73	1.62
C4-C5	1.33	1.36	1.48	C4-C5	1.39	1.41	1.46	C4-C5	1.33	1.36	1.49
C2-C5	3.11	2.19	1.51	C2-C5	3.22	1.98	1.54	C2-C5	3.54	2.22	1.51
N1-C2	1.25	1.28	1.35	N1-C2	1.25	1.30	1.36	C2-C5	3.30	2.01	1.54
C2-C3	1.30	1.34	1.39	C2-C3	1.30	1.35	1.37				
S-C3	1.76	1.73	1.72	S-C3	1.77	1.73	1.73				
S-C4	1.79	1.73	1.62	S-C4	1.78	1.73	1.67				
C4-C5	1.33	1.36	1.49	C4-C5	1.40	1.41	1.47				
C2-C5	3.54	2.22	1.51	C2-C5	3.30	2.01	1.54				

^a KI (Reactant) unless specified is linear.

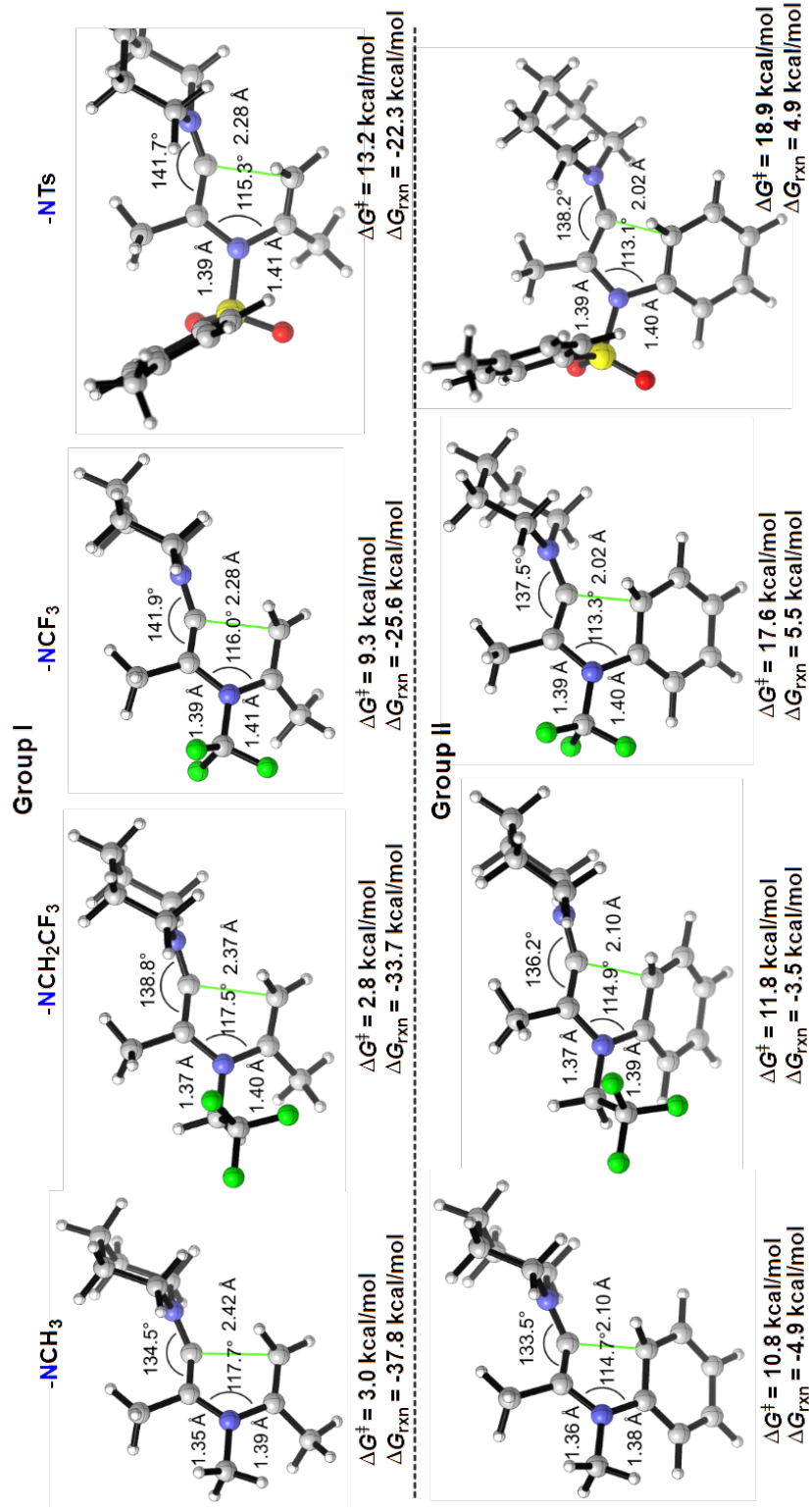


Figure A.16. Optimized TS structures. All energies for the formation of pyrrole and indole derivatives are relative to the pre-reactive conformer (PRC).

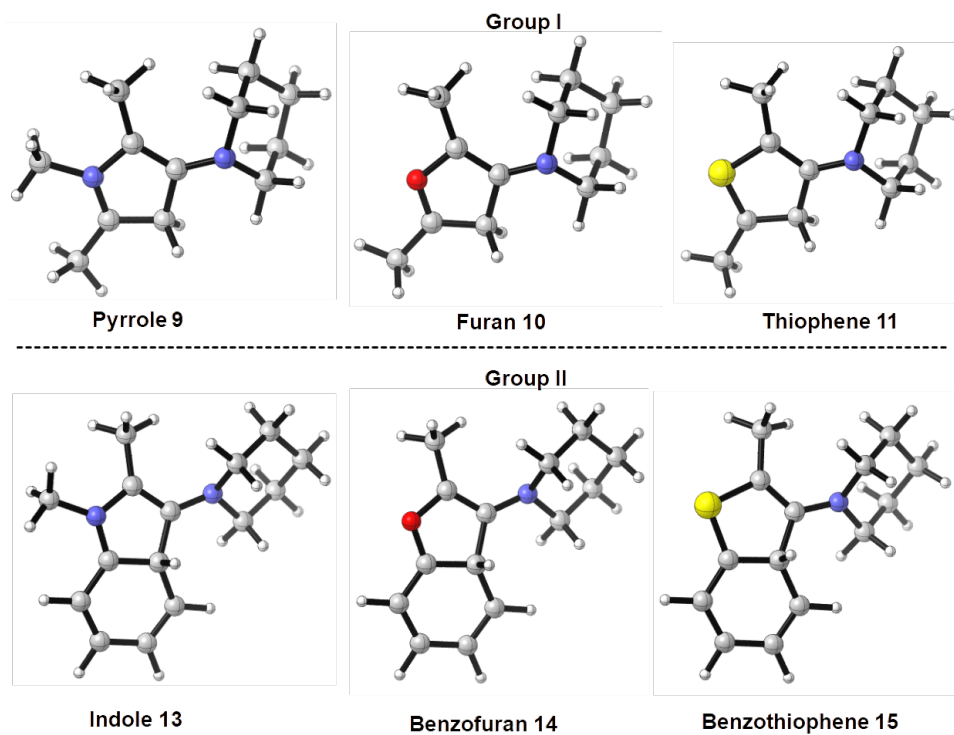


Figure A.17. Optimized INT structures.

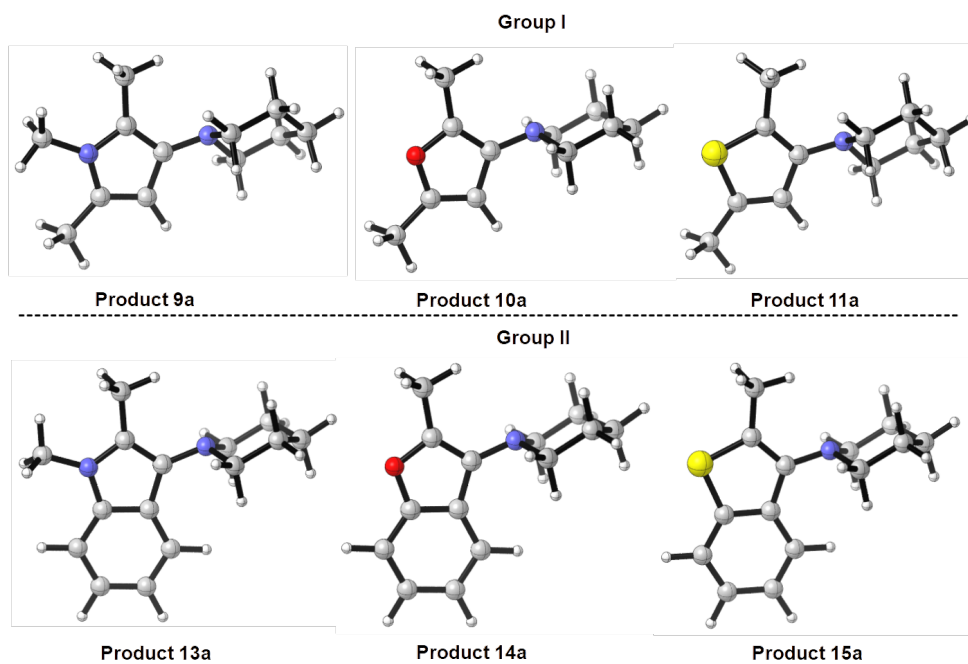


Figure A.18. Optimized end product structures.

M06-2X/6-31+G(d,p) in CHCl_3 , 6-311++G(3df,3pd) extra basis set for S atom were used in Figures A.16, A.17, and A.18.

A.3.2. Frontier Molecular Orbitals (FMO) Analysis

According to Woodward-Hoffmann rules, [251] pericyclic ring closure in $(4n+2)\pi$ systems proceeds through a concerted disrotatory motion. FMO analysis of the keteniminiums in Groups I and II show HOMOs of keteniminiums primed for a disrotatory closure.

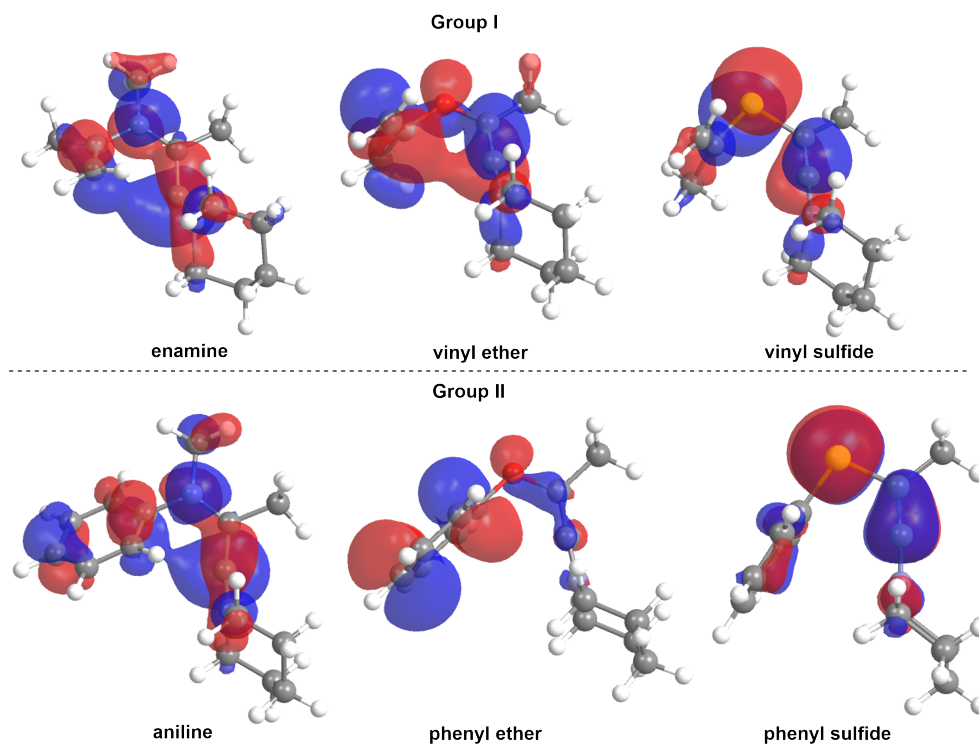


Figure A.19. HOMO of keteniminium ions.

(M06-2X/6-311++G(d,p)//M06-2X/6-31+G(d,p) in CHCl_3 , extra basis set for S atom;

iso-surface value = 0.03 au.)

APPENDIX B: ARTICLES

The first pages of the published articles were given herein. The articles were arranged by years of publication.

B.1. Impact of Deamidation on the Structure and Function of Anti-apoptotic Bcl-x_L (Article 1)



pubs.acs.org/jcim

Article

Impact of Deamidation on the Structure and Function of Antiapoptotic Bcl-x_L

Gamze Tanriver, Gerald Monard,* and Saron Catak*

Cite This: *J. Chem. Inf. Model.* 2022, 62, 102–115

Read Online

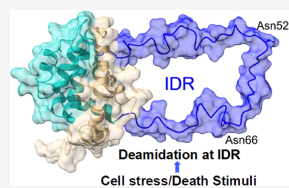
ACCESS |

Metrics & More

Article Recommendations

Supporting Information

ABSTRACT: Bcl-x_L is an antiapoptotic mitochondrial trans-membrane protein, which is known to play a crucial role in the survival of tumor cells. The deamidation of Bcl-x_L is a pivotal switch that regulates its biological function. The potential impact of deamidation on the structure and dynamics of Bcl-x_L is directly linked to the intrinsically disordered region (IDR), which is the main site for post-translational modifications (PTMs). In this study, we explored deamidation-induced conformational changes in Bcl-x_L to gain insight into its loss of function by performing microsecond-long molecular dynamics (MD) simulations. MD simulation outcomes showed that the IDR motion and interaction patterns have changed notably upon deamidation. Principal component analysis (PCA) demonstrates significant differences between wild-type and deamidated Bcl-x_L, and suggests that deamidation affects the structure and dynamics of Bcl-x_L. The combination of clustering analysis, H-bond analysis, and PCA revealed changes in conformation, interaction, and dynamics upon deamidation. Differences in contact patterns and essential dynamics that lead to a narrowing in the binding groove (BG) are clear indications of deamidation-induced allosteric effects. In line with previous studies, we show that the IDR plays a very important role in the loss of apoptotic functions of Bcl-x_L while providing a unique perspective on the underlying mechanism of Bcl-x_L deamidation-induced cell death.



INTRODUCTION

Bcl-2 family proteins (B-cell lymphoma-2), in combination with the mitochondrial outer membrane (MOM), control the fate of cells by regulating the mitochondrial pathway of apoptosis (programmed cell death).^{1–4} The Bcl-2 family includes proapoptotic (BAX, BAK, and BOK), antiapoptotic (Bcl-2, Bcl-x_L, Bcl-W, and MCL-1), and BH3-only proteins (BOP), such as BIM, BID, PUMA, and NOXA, and mediates the mitochondrial (intrinsic) apoptotic pathway in response to various apoptotic stimuli (cellular stress or damage signals). Bcl-2 family proteins maintain/preserve balance in healthy cells. When this balance is disrupted, elevated numbers of antiapoptotic proteins are observed in various cancer cells, such as chronic myelogenous leukemia (CML), pancreatic cancer, and ovarian and small-cell lung cancer.^{5–7}

Post-translational modification (PTM) is a regulatory mechanism in many biological processes. The most common modifications are acetylation, acylation, amidation, deamidation, phosphorylation, glycosylation, ubiquitination, nitrosylation, and SUMOylation.^{8–10} Among PTMs, deamidation is of particular interest to this study. Deamidation is a chemical reaction that spontaneously occurs in proteins with the potential to substantially modify their structure and compromise their function.¹¹ Asparagine (Asn) and glutamine (Gln), two of the 20 naturally occurring amino acids, are inherently unstable under physiological conditions.¹² Gln and Asn are known to spontaneously yet nonenzymatically

deamidate into a mixture of glutamyl (Glu) and iso-glutamyl (iso-Glu) and a mixture of aspartyl (Asp) and iso-aspartyl (iso-Asp) residues, respectively (Scheme 1).^{13,14,15} This, in turn, replaces a neutral residue with a negatively charged one and has the potential to cause severe electrostatic clashes, leading to structural deformations, which may eventually have dramatic biological consequences.

The deamidation rate is determined by the protein structure and environment; deamidation half times of proteins are shown to vary from a few hours to more than 100 years.¹⁶ Gln deamidation is usually substantially slower than Asn deamidation; hence, asparagine deamidation has more biologically relevant consequences. A notable example is the mitochondrial transmembrane protein, B-cell lymphoma-extra-large (Bcl-x_L),^{17,18} which functions as an antiapoptotic protein. Bcl-x_L belongs to the Bcl-2 family,⁴ which regulates the mitochondrial pathway of apoptosis in response to various apoptotic stimuli.¹⁹ Bcl-x_L indirectly binds to BH3-only proteins and prevents them from activating proapoptotic

Received: July 8, 2021

Published: December 23, 2021



B.2. Keteniminium Salts: Reactivity and Propensity Toward Electrocyclization Reactions (Article 2)

Keteniminium Salts: Reactivity and Propensity toward Electrocyclization Reactions

Gamze Tanriver,† Dylan Dagoneau,‡ Ulfet Karadeniz,† Amandine Kolleth,‡ Alexandre Lumbroso,‡ Sarah Sulzer-Mossé,‡ Alain De Mesmaeker,† and Saron Catak*†

†Department of Chemistry, Bogazici University, Bebek, 34342 Istanbul, Turkey

‡Crop Protection Research, Research Chemistry, Syngenta Crop Protection AG, Schaffhauserstrasse 101, CH-4332 Stein, Switzerland

Supporting Information

ABSTRACT: A predictive computational study was conducted in order to assess the efficiency of electrocyclization reactions of keteniminium salts, in an effort to form a variety of heterocyclic systems, namely, 3-amino(benzo)thiophenes, 3-amino(benzo)furans, 3-aminopyrroles, as well as 3-aminoindoles. A density functional theory (DFT) approach was utilized and the effect of heteroatoms (NMe, O, S) was thoroughly investigated by means of population analysis, QTAIM, NICS, ACID, and local reactivity descriptors (Parr and Fukui functions). The electrocyclization of enamines leading to 3-aminopyrroles was shown to be both kinetically and thermodynamically most favorable. Moreover, the pericyclic nature of the electrocyclizations was confirmed using FMO, QTAIM, NICS, and ACID methods. Additionally, substituent effects were investigated in order to give further insight on the reactivity of heteroatom containing keteniminium systems toward electrocyclization reactions. Finally, computational predictions were experimentally confirmed for a selection of keteniminium systems.

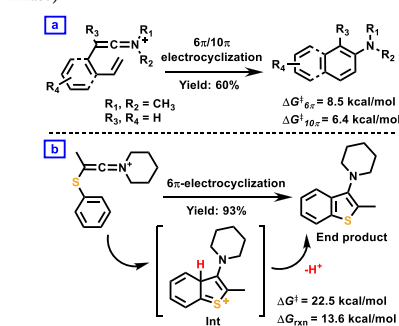
INTRODUCTION

Keteniminium salts (KI) are versatile and reactive intermediates in organic chemistry.^{1,2} Historically, the pioneers of the use and synthesis of KI are Viehe and Ghosez.^{3–4} These salts are an improved alternative to their ketene analogues, due to their higher reactivity and high electrophilicity. Furthermore, KI do not undergo undesired side reactions, such as dimerization or polymerization, as readily as ketenes.^{5–9}

Keteniminium salts have a wide range of synthetic applications.^{1,2,6,9–15} They are mostly used as key intermediates in electrocyclization reactions,^{16,17} intermolecular and intramolecular cycloaddition reactions,^{18–20} [1,5]-sigmatropic hydrogen shifts,^{21,22} and Claisen rearrangements.¹² KI were shown to undergo [2 + 2] cycloadditions with alkynes and are also used as dienophiles in Diels–Alder reactions.^{18,23,24} [2 + 2] cycloaddition products of KI and alkenes can also undergo nucleophilic addition on the cyclobutyliminium ion to produce highly stereoselective quaternary centers.²⁵

Electrocyclization is a powerful method to build complex structural motifs. Recently we reported an efficient access to naphthylamines using intramolecular 6π/10π-electrocyclization of keteniminium salts,¹⁶ where the electrocyclizations of KIs were compared with ketenes, allenes, and trienes (Scheme 1a). The computed data showed that keteniminium salts—both kinetically and thermodynamically—undergo electrocyclization more readily than ketenes, allenes, and trienes. Besides, naphthylamines, (benzo)thiophenes, (benzo)furans and indoles are also core scaffolds for several bioactive

Scheme 1. Access to (hetero)cyclic compounds using Keteniminium Intermediates (M06-2X/6-31+G(d,p) in Gas Phase)^{16,17}



compounds used in various areas such as agrochemicals,²⁶ pharmaceuticals,²⁷ antimitotic agents,²⁸ inhibitors of tubulin polymerization,²⁹ tumor growth,^{30,31} and antiviral^{32,33} compounds (Scheme 2).

Received: September 10, 2019

Published: December 2, 2019

B.3. Keteniminium Salts as Key Intermediates for the Efficient Synthesis of 3-Amino-Indoles and -Benzofurans (Article 3)



DOI: 10.1002/hlca.201900217

FULL PAPER

HELVETICA

Keteniminium Salts as Key Intermediates for the Efficient Synthesis of 3-Amino-Indoles and -Benzofurans

Dylan Dagoneau,^a Amandine Kolleth,^a Pierre Quinodoz,^a Gamze Tanriver,^b Saron Catak,^b Alexandre Lumbroso,^a Sarah Sulzer-Mossé,^a and Alain De Mesmaeker^{*a}

^a Syngenta Crop Protection AG, Crop Protection Research, Research Chemistry, Schaffhauserstrasse 101, CH-4332, Stein, Switzerland, e-mail: alain.de_mesmaeker@syngenta.com

^b Bogazici University, Department of Chemistry, Bebek, 34342 Istanbul, Turkey

Herein, we describe a high yielding approach towards the synthesis of 3-amino-indoles and -benzofurans through 6π -electrocyclization. This was made possible by taking advantage of the high reactivity of keteniminium salts, formed *in-situ* by treating with triflic anhydride and 2-fluoropyridine amides bearing at the α -position either an aniline or a phenoxy moiety. These mild conditions, on top of furnishing rapidly the 3-aminobenzoheteroles, allow the tolerance of various functional groups. Control experiments were carried out to highlight that the keteniminium is, indeed, in most cases, the reactive intermediate and conformational preferences of such species were investigated through a DFT study.

Keywords: aminoindole, aminobenzofuran, keteniminium, electrocyclic reactions.

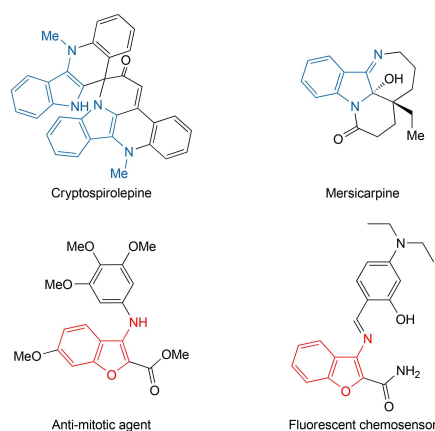


Figure 1. Examples of natural and synthetic 3-aminobenzoheteroles.

Supporting information for this article is available on the WWW under <https://doi.org/10.1002/hlca.201900217>

Introduction

3-Aminoindoles is a rare motif present in nature^[1–4] and none of its benzofuran analogues were isolated to the best of our knowledge (Figure 1). However, both scaffolds are found in synthetic compounds showing attractive properties in various areas. For example, 3-aminoindole is the core of antiviral compounds against hepatitis B virus^[5] and of anti-proliferative agents^[6,7] and such anti-mitotic properties were also observed with 3-aminobenzofuran-based molecules.^[8] Those benzofurans are reported to be involved in potent ischemic cell death inhibitors^[9] and anti-microbials^[10,11] as well as in selective fluorescent chemosensors of Zn²⁺ and CN⁻ ions.^[12,13]

In the literature, the synthesis of 3-amino-indoles and -benzofurans is achieved following three main strategies. The first one is the functionalization of the naked benzoheterole through either direct amination^[14–16] or a nitr(ox)ation/reduction sequence.^[5,17] The second is the generation of the heterocyclic core followed by *in-situ* amination of the latter^[18,19] and the third is the one-step formation of the 3-aminobenzoheterole moiety. In this last approach, the main reaction reported is a *Thorpe–Ziegler*

B.4. Straightforward Synthesis of 3-Aminothiophenes Using Activated Amides (Article 4)



DOI: 10.1002/hlca.201900031

FULL PAPER

HELVETICA

Straightforward Synthesis of 3-Aminothiophenes Using Activated Amides

Dylan Dagoneau,^{a,1} Amandine Kolleth,^{a,1} Alexandre Lumbroso,^a Gamze Tanriver,^b Saron Catak,^b Sarah Sulzer-Mossé,^a and Alain De Mesmaeker^{*a}

^a Syngenta Crop Protection AG, Crop Protection Research, Research Chemistry, Schaffhauserstrasse 101, CH-4332 Stein, Switzerland, e-mail: alain.de_mesmaeker@syngenta.com

^b Bogazici University, Department of Chemistry, Bebek, TR-34342 Istanbul, Turkey

Dedicated to Professor *François Diederich* in recognition of his outstanding achievements in organic chemistry

Herein, we describe a facile approach towards the synthesis of diversely substituted 3-aminothiophenes. A wide range of functional groups can be incorporated at the C(2), C(4), and C(5) positions of the thiophenes, and this route is also suitable for the synthesis of fused bicyclic heterocycles such as 3-aminotetrahydrobenzothiophenes. This methodology relies on a 6π -electrocyclization involving a vinyl sulfide linked to a keteniminium salt, the latter being formed *in-situ* through activation of the corresponding amide with triflic anhydride.

Keywords: aminothiophenes, keteniminium salts, electrocyclic reactions, amide activation.

Introduction

3-Aminothiophenes are rather underrepresented moieties in nature^[1] but nevertheless, they are part of numerous synthetic bioactive products. This core is, indeed, a well-known biosostere of anilines used in drug design and can be found in agrochemicals such as in dimethenamid^[2] and penthiopyrad,^[3] showing herbicidal and fungicidal activity respectively, and also in pharmaceuticals like the local anesthetic articaine^[4] or telenzepine^[5,6] which is used for the treatment of peptic ulcer (Figure 1). Moreover, according to recent studies, this scaffold is present in potent inhibitors of hepatitis C virus^[7,8] and tumor growth,^[9,10] as well as in anti-inflammatory^[11] and anti-microbial^[12] compounds.

The synthesis of 3-aminothiophenes was for the first time reported by *Steinkopf* in 1926 by reduction of 3-nitrothiophenes.^[13] Few decades later, this motif was accessed through either a *Hoffmann*^[14] or a *Curtius* rearrangement^[15,16] of the corresponding 3-thiophene-

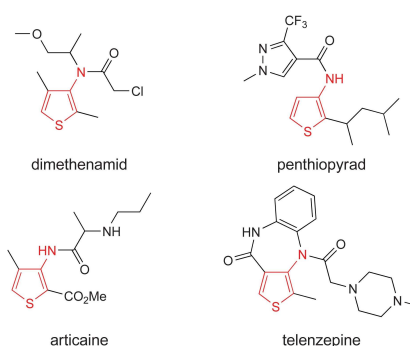


Figure 1. Examples of bioactive compounds containing a 3-aminothiophene core.

carboxamide or -carbonyl chloride, and more recently, palladium-catalyzed amination of 3-halothiophenes was reported by *Watanabe*.^[17] However, the number of direct methods for the synthesis of the 3-aminothiophene nucleus, as an alternative of thiophene

¹ These authors contributed equally to this work.

Supporting information for this article is available on the WWW under <https://doi.org/10.1002/hlca.201900031>

B.5. Access to 3-Aminobenzothiophenes and 3-Aminothiophenes Fused to 5-membered Heteroaromatic Rings through 6π -electrocyclization Reaction of Keteniminium Salts (Article 5)

Tetrahedron Letters 59 (2018) 3242–3248



Contents lists available at ScienceDirect

Tetrahedron Letters

journal homepage: www.elsevier.com/locate/tetlet

Access to 3-aminobenzothiophenes and 3-aminothiophenes fused to 5-membered heteroaromatic rings through 6π -electrocyclization reaction of keteniminium salts



Amandine Kolleth^a, Simona Müller^a, Alexandre Lumbroso^a, Gamze Tanriver^b, Saron Catak^b, Sarah Sulzer-Mossé^a, Alain De Mesmaeker^{a,*}

^aSyngenta Crop Protection AG, Crop Protection Research, Research Chemistry, Schaffhauserstrasse 101, CH-4332, Switzerland

^bBogazici University, Department of Chemistry, Bebek, 34342 Istanbul, Turkey

ARTICLE INFO

Article history:

Received 8 May 2018

Revised 18 June 2018

Accepted 19 June 2018

Available online 21 June 2018

Keywords:

Keteniminium salts

Electrocyclization

Amino-benzothiophenes

DFT calculations

ABSTRACT

We described a general approach to 3-aminobenzothiophenes and 3-aminothiophenes fused to 5-membered heteroaromatic rings as thiophenes, furans and pyrroles through a 6π -electrocyclization reaction of keteniminium salts. We investigated various substituents not only on the aromatic rings, but also at C-2 and on the nitrogen atom of the keteniminium salt. In particular, we have determined the electronic requirements of the nitrogen substitution to secure the efficient formation of the corresponding keteniminium salt. A clear relation between the pK_a of the amine leading to the formation of the keteniminium salt and the yield obtained for benzothiophene is established and should find broad application to other reactions involving these intermediates. Additional insight on the ease of this 6π -electrocyclization reaction was gained through competition reactions and DFT calculations.

© 2018 Elsevier Ltd. All rights reserved.

The conversion of amides into keteniminium intermediates has been described for the first time in 1972 by Ghosez et al. [1]. The [2 + 2] cycloadditions involving alkenes (or alkynes) as partners are, by far, the most explored reactions of keteniminium salts [2–4]. However, the very high electrophilicity of these cumulenes enable them to undergo a much broader variety of reactions [5]. Among them, Pictet-Spengler cyclizations [6], nucleophilic additions followed by a Claisen-like rearrangement [7], cyclization of silylenolethers [8] or hydride shifts [9] have been applied to keteniminium intermediates. More recently access to heteroaromatic scaffolds [10] involving the reactivity of keteniminium salts have been disclosed and could find interesting uses for the synthesis of biologically active substances for medicinal and agronomical applications. In this context, we reported an unprecedented $6\pi/10\pi$ -electrocyclization involving a keteniminium intermediate leading to functionalized amino-naphthalenes [11] and 3-aminobenzothiophenes [12] **C** (generated from amide **A** via keteniminium **B**, Scheme 1). Mechanistic studies and DFT calculations have highlighted that the most favored pathway involves a keteniminium intermediate in the concerted $6\pi/10\pi$ -electrocyclization. Due to the relevance of this approach towards the synthesis of various

5-aminothiophenes and 3-aminothiophenes fused to 5-membered heteroaromatic rings as part of current research projects in our laboratories, we investigated the generality of this process, in particular the role of substituents at C-2, on the aromatic nucleus and on the nitrogen atom of the keteniminium. We describe here a general approach to 3-aminobenzothiophenes and their corresponding analogues having a 5-membered heteroaromatic ring fused to the thiophene **C** (Scheme 1).

We started our study by addressing a crucial parameter relevant to the whole chemistry involving keteniminium intermediates, namely the electronic requirements on the nitrogen atom of the amide precursor, leading first to the amide triflic salt and its conversion into the corresponding keteniminium salt [12]. Preliminary results revealed that for some amides **1** bearing strong electron-withdrawing substituents in the R_1/R_2 residues (entries 10–12 and 14, Table 1), no benzothiophene could be formed and the starting material remained unchanged under the reaction conditions (1.1eq of Tf_2O , 1.2eq of 2F-pyridine) [13]. In order to gain some insight on the electron density of the amide nitrogen atom, ultimately required for the formation of the corresponding keteniminium salt, we have modified the structure of the amine varying its pK_a value. We observed a clear relation between the calculated pK_a of the amines and the yield of the aminobenzothiophenes **3** (Table 1). The value of the pK_a reflects the availability

* Corresponding author.

E-mail address: alain.de_mesmaeker@syngenta.com (A. De Mesmaeker).

<https://doi.org/10.1016/j.tetlet.2018.06.049>

0040-4039/© 2018 Elsevier Ltd. All rights reserved.

B.6. Synthesis of 4-membered Ring Alkaloid Analogues via Intramolecular [2+2] Cycloaddition Involving Keteniminium Salt Intermediates (Article 6)

Tetrahedron Letters 58 (2017) 2904–2909



Contents lists available at ScienceDirect

Tetrahedron Letters

journal homepage: www.elsevier.com/locate/tetlet

Synthesis of 4-membered ring alkaloid analogues *via* intramolecular [2+2] cycloaddition involving keteniminium salt intermediates



Amandine Kolleth^a, Alexandre Lumbruso^a, Gamze Tanriver^b, Saron Catak^b, Sarah Sulzer-Mossé^a, Alain De Mesmaeker^{a,*}

^aSyngenta Crop Protection AG, Crop Protection Research, Research Chemistry, Schaffhauserstrasse 101, CH-4332, Switzerland

^bBogazici University, Department of Chemistry, Bebek, 34342 Istanbul, Turkey

ARTICLE INFO

Article history:

Received 12 April 2017

Revised 6 June 2017

Accepted 12 June 2017

Available online 13 June 2017

Keywords:

Keteniminium salts
Cyclobutane iminiums
[2+2]Cycloaddition
Aminocyclobutane
DFT calculations

ABSTRACT

We have developed a very straightforward method for the synthesis of 4-membered ring alkaloid analogues *via* intramolecular [2+2] cycloadditions. This involves the cyclization of a keteniminium salt in which an alkene is linked by the nitrogen atom, and where, the resulting cyclobutane iminium is reduced in a diastereoselective manner. Competition reactions have been performed to fully understand the features of this sequence. Moreover, DFT calculations have verified that the [2+2] cycloaddition step is driven by kinetic and not thermodynamic factors confirming all the experimental observations.

© 2017 Elsevier Ltd. All rights reserved.

Keteniminium salts (KI) represent valuable intermediates, which have been intensively studied in [2+2] cycloadditions with olefins, alkynes and imines.¹ In particular, they are known to react in an intramolecular fashion and through different pathways. Indeed, the low LUMO of the cumulene confers a powerful electrophilicity² to the central carbon allowing a plethora of transformations, such as Pictet-Spengler cyclizations,³ nucleophilic additions followed by a Claisen-like rearrangement,⁴ cyclization of silylenolethers⁵ or hydride shifts.⁶ Furthermore, keteniminiums can also undergo 6π or $6\pi/10\pi$ electrocyclizations to provide amino-benzothiophenes⁷ or amino-naphthalenes.⁸ However among all intramolecular methods employing keteniminiums, [2+2] cycloadditions involving an amide (A) bearing a terminal alkene tail, have been indisputably the most studied (Scheme 1). The first example was reported by Ghose et al.⁹ who described the formation of polycyclic cyclobutanones in a regio- and diastereo-selective manner. The field of application turned out to be broad, as heteroatoms¹⁰ can be incorporated in the tail containing the alkene, and chiral auxiliaries allowed the development of enantioselective methods. It is worth mentioning that in these [2+2] cycloadditions, the regioselectivity is ruled by the orbital coefficients of intermediate B (Scheme 1): the carbon C1 of the KI plays

the role of electrophile (larger coefficient in the LUMO) and reacts with carbon C4 of the olefin (larger coefficient in the HOMO) to form the cyclobutanone D after hydrolysis of C. Since we recently reported an efficient access to amino-cyclobutanones H *via* an intermolecular [2+2] cycloaddition of *N*-allyl keteniminiums followed by a reduction of the resulting cyclobutane iminium G, we assumed that an intramolecular version employing intermediates J and leading to L could be feasible.

However, in contrast to what was previously described, the interaction between the largest coefficients in the HOMO and the LUMO of J would not dictate the regioselectivity as carbon C1 would react with C3. Instead, the formation of [2+2] cycloadduct K would be the result of geometrical constraints (Scheme 1). Herein, we describe the first intramolecular [2+2] cycloaddition involving a KI in which the alkene partner is linked to the nitrogen atom, followed by a reduction in order to access to 4-membered ring alkaloids.

This work consisted in treating amides 1 bearing an alkene group linked to the nitrogen atom, by triflic anhydride and a non-nucleophilic base such as 2-fluoro-pyridine¹¹ in order to generate keteniminium salts 2. Then a thermal intramolecular [2+2] cycloaddition occurred¹² to give cyclobutane iminiums 3 as intermediates and these were directly reduced¹³ by LiAl(O*t*Bu)₃H providing amines 4.¹⁴ We started our investigations with different amides bearing an allyl substituent as protecting group. Indeed,

* Corresponding author.

E-mail address: alain.de_mesmaeker@syngenta.com (A. De Mesmaeker).<http://dx.doi.org/10.1016/j.tetlet.2017.06.033>

0040-4039/© 2017 Elsevier Ltd. All rights reserved.

B.7. Synthesis of Amino-cyclobutanes via [2+2] Cycloadditions Involving Keteniminium Intermediates (Article 7)

Tetrahedron Letters 57 (2016) 2697–2702



Contents lists available at ScienceDirect

Tetrahedron Letters

journal homepage: www.elsevier.com/locate/tetlet

Synthesis of amino-cyclobutanes via [2 + 2] cycloadditions involving keteniminium intermediates



Amandine Kolleth^a, Alexandre Lumbroso^a, Gamze Tanriver^b, Saron Catak^b, Sarah Sulzer-Mossé^a, Alain De Mesmaeker^{a,*}

^aSyngenta Crop Protection AG, Crop Protection Research, Research Chemistry, Schaffhauserstrasse 101, CH-4332, Switzerland

^bBogazici University, Department of Chemistry, Bebek, 34342, Istanbul, Turkey

ARTICLE INFO

Article history:
Received 18 March 2016
Revised 18 April 2016
Accepted 25 April 2016
Available online 26 April 2016

Keywords:
Keteniminium salts
Cyclobutaniminiums
[2 + 2] cycloaddition
Aminocyclobutane
DFT calculations

ABSTRACT

We describe an efficient method for the synthesis of aminocyclobutanes via a [2 + 2] cycloaddition between a keteniminium salt and an alkene, followed by a reduction step. The use of easily removable *N*-allyl moieties as protecting groups increases the potential of this method to access, in a few steps, highly functionalized cyclobutaneamine-containing building blocks. Moreover, DFT calculations verify the compatibility of *N*-allyl and *N*-propargyl keteniminiums in [2 + 2] cycloaddition reactions.

© 2016 Elsevier Ltd. All rights reserved.

Keteniminium chemistry has been studied for the synthesis of various scaffolds such as α -aryl-amides,¹ indenotetrahydroisoquinolines,² quinoline derivatives³ and more recently, aminonaphthalenes⁴ and 3-amino-benzothiophenes.⁵ But among all the reactions involving keteniminium salts,^{6,7} [2 + 2] cycloadditions⁸ with alkenes have been by far the most studied and intermolecular⁹ as well as intramolecular¹⁰ reactions have been reported. [2 + 2] cycloaddition between keteniminium salts and alkynes have also been described by Ghosez and our group^{11,12} affording cyclobutaniminium salt adducts which were further elaborated by [4 + 2] cycloaddition¹¹ or Michael addition reactions¹² using various dienes or nucleophiles, respectively. However, the scope of the [2 + 2] methodology involving keteniminium salts is rather limited by the fact that the iminium formed is always hydrolyzed to the corresponding ketone. Urch et al. described in 1988 the reduction of cyclobutaniminium salt intermediates obtained by [2 + 2] cycloaddition yielding aminocyclobutanes but this methodology suffers from a very limited scope, covering only morpholine derivatives.¹³ A straightforward general access to substituted aminocyclobutanes from corresponding iminium salts would be therefore a significant advancement, since very few general methods¹⁴ are available to attain this class of compounds.

Herein, we report a one-pot sequence to obtain aminocyclobutanes, relying on a [2 + 2] cycloaddition between a keteniminium

salt and an alkene followed by a diastereoselective reduction step and the mild deprotection of the corresponding *N*-(di)allyl cyclobutylamines (Scheme 1).

N-allyl groups are known to be easily cleaved under mild conditions to provide free amines.¹⁵ Although the allylic double bond in keteniminium salt **C** is expected to be deactivated by the electron withdrawing effect of the iminium cation (Scheme 1), the compatibility of *N*-allylic groups in the [2 + 2] cycloadditions of keteniminium salts was initially assessed to rule out the possibility of an intermolecular competitive reaction. Preliminary results based on a competition reaction highlighted the lower reactivity of the allylammonium salt **3**, which is used to mimic the keteniminium *N*-allyl group. When keteniminium salt **1** (generated by treatment of the amide **A1** with *sym*-collidine and Tf₂O) was added to a 1:1 mixture of alkene **2** and **3**, cyclobutaniminium **4** resulting from the [2 + 2] cycloaddition of **1** and **2**, was exclusively observed and no trace of **5** was detected confirming our hypothesis that the positively charged nitrogen atom in the keteniminium salts would considerably decrease the reactivity of the adjacent *N*-allyl groups toward electrophiles (Scheme 2).

We started our investigation with various amides bearing an *N*-diallyl moiety and ethylene.¹⁶ The generation of the keteniminium salts was initiated by triflic anhydride and required the use of the non-nucleophilic base, 2-fluoropyridine.¹⁷ To our delight, [2 + 2] cycloadditions proceeded very cleanly and the formation of the corresponding cyclobutaniminiums was confirmed by ¹H NMR spectroscopy analysis of aliquots directly taken from

* Corresponding author. Tel.: +41 628 660 268.

E-mail address: alain.de_mesmaeker@syngenta.com (A. De Mesmaeker).

APPENDIX C: COPY-RIGHT LIST

C.1. The License for Article 1 in Chapter 4

3.01.2022 02:39 Rightslink® by Copyright Clearance Center



Home
Help ▾
Email Support
Sign in
Create Account

Impact of Deamidation on the Structure and Function of Antiapoptotic Bcl-xL

 **ACS Publications**
Most Trusted. Most Cited. Most Read.

Author: Gamze Tanriver, Gerald Monard, Saron Catak
Publication: Journal of Chemical Information and Modeling
Publisher: American Chemical Society
Date: Dec 1, 2021
Copyright © 2021, American Chemical Society

PERMISSION/LICENSE IS GRANTED FOR YOUR ORDER AT NO CHARGE

This type of permission/license, instead of the standard Terms and Conditions, is sent to you because no fee is being charged for your order. Please note the following:

- Permission is granted for your request in both print and electronic formats, and translations.
- If figures and/or tables were requested, they may be adapted or used in part.
- Please print this page for your records and send a copy of it to your publisher/graduate school.
- Appropriate credit for the requested material should be given as follows: "Reprinted (adapted) with permission from {COMPLETE REFERENCE CITATION}. Copyright {YEAR} American Chemical Society." Insert appropriate information in place of the capitalized words.
- One-time permission is granted only for the use specified in your RightsLink request. No additional uses are granted (such as derivative works or other editions). For any uses, please submit a new request.

If credit is given to another source for the material you requested from RightsLink, permission must be obtained from that source.

BACK
CLOSE WINDOW

© 2022 Copyright - All Rights Reserved | [Copyright Clearance Center, Inc.](#) | [Privacy statement](#) | [Terms and Conditions](#)
 Comments? We would like to hear from you. E-mail us at customer-care@copyright.com

https://s100.copyright.com/AppDispatchServlet 1/1

C.2. The License for Article 2 in Chapter 8

15.11.2021 20:09

Rightslink® by Copyright Clearance Center



[Home](#)
[Help](#)
[Live Chat](#)
[Sign in](#)
[Create Account](#)

Keteniminium Salts; Reactivity and Propensity toward Electrocyclization Reactions



Author: Gamze Tanriver, Dylan Dagonneau, Ulfet Karadeniz, et al

Publication: The Journal of Organic Chemistry

Publisher: American Chemical Society

Date: Jan 1, 2020

Copyright © 2020, American Chemical Society

PERMISSION/LICENSE IS GRANTED FOR YOUR ORDER AT NO CHARGE

This type of permission/license, instead of the standard Terms and Conditions, is sent to you because no fee is being charged for your order. Please note the following:

- Permission is granted for your request in both print and electronic formats, and translations.
- If figures and/or tables were requested, they may be adapted or used in part.
- Please print this page for your records and send a copy of it to your publisher/graduate school.
- Appropriate credit for the requested material should be given as follows: "Reprinted (adapted) with permission from (COMPLETE REFERENCE CITATION), Copyright (YEAR) American Chemical Society." Insert appropriate information in place of the capitalized words.
- One-time permission is granted only for the use specified in your RightsLink request. No additional uses are granted (such as derivative works or other editions). For any uses, please submit a new request.

If credit is given to another source for the material you requested from RightsLink, permission must be obtained from that source.

[BACK](#)

[CLOSE WINDOW](#)

© 2021 Copyright - All Rights Reserved | [Copyright Clearance Center, Inc.](#) | [Privacy statement](#) | [Terms and Conditions](#)
 Comments? We would like to hear from you. E-mail us at customer@copyright.com

C.3. The License for Article 3 in Chapter 7

15.11.2021 20:16

RightsLink Printable License

JOHN WILEY AND SONS LICENSE
TERMS AND CONDITIONS

Nov 15, 2021

This Agreement between Bogazici University -- Gamze TANRIVER ("You") and John Wiley and Sons ("John Wiley and Sons") consists of your license details and the terms and conditions provided by John Wiley and Sons and Copyright Clearance Center.

License Number 5190281434148

License date Nov 15, 2021

Licensed Content
Publisher John Wiley and Sons

Licensed Content
Publication Helvetica Chimica Acta

Licensed Content
Title Keteniminium Salts as Key Intermediates for the Efficient Synthesis of 3-Amino-Indoles and -Benzofurans

Licensed Content
Author Alain De Mesmaeker, Sarah Sulzer-Mossé, Alexandre Lumbroso, et al

Licensed Content
Date Nov 28, 2019

Licensed Content
Volume 103

Licensed Content
Issue 1

Licensed Content
Pages 12

Type of use Dissertation/Thesis

Requestor type Author of this Wiley article

Format Print and electronic

Portion Full article

Will you be
translating? No

<https://s100.copyright.com/CustomAdmin/PLF.jsp?ref=4e38f727-d3f5-4b59-9c56-8874f8a0bc32>

1/5

15.11.2021 20:16

RightsLink Printable License

Title Molecular modeling of Bel-xL post-translational modifications and of Keteniminium salts

Institution name Bogazici University

Expected presentation date Dec 2021

Requestor Location Bogazici University
BOĞAZIÇI ÜNİVERSİTESİ KUZEY KAMPUS KARE
KİMYA BÖLÜM SEKRETERLİĞİ KAT 3 BEBEK
İstanbul, 34342
Turkey
Attn: Bogazici University

Publisher Tax ID EU826007151

Total 0.00 USD

Terms and Conditions

TERMS AND CONDITIONS

This copyrighted material is owned by or exclusively licensed to John Wiley & Sons, Inc. or one of its group companies (each a "Wiley Company") or handled on behalf of a society with which a Wiley Company has exclusive publishing rights in relation to a particular work (collectively "WILEY"). By clicking "accept" in connection with completing this licensing transaction, you agree that the following terms and conditions apply to this transaction (along with the billing and payment terms and conditions established by the Copyright Clearance Center Inc., ("CCC's Billing and Payment terms and conditions"), at the time that you opened your RightsLink account (these are available at any time at <http://myaccount.copyright.com>).

Terms and Conditions

- The materials you have requested permission to reproduce or reuse (the "Wiley Materials") are protected by copyright.
- You are hereby granted a personal, non-exclusive, non-sub licensable (on a stand-alone basis), non-transferable, worldwide, limited license to reproduce the Wiley Materials for the purpose specified in the licensing process. This license, **and any CONTENT (PDF or image file) purchased as part of your order**, is for a one-time use only and limited to any maximum distribution number specified in the license. The first instance of republication or reuse granted by this license must be completed within two years of the date of the grant of this license (although copies prepared before the end date may be distributed thereafter). The Wiley Materials shall not be used in any other manner or for any other purpose, beyond what is granted in the license. Permission is granted subject to an appropriate acknowledgement given to the author, title of the material/book/journal and the publisher. You shall also duplicate the copyright notice that appears in the Wiley publication in your use of the Wiley Material. Permission is also granted on the understanding that nowhere in the text is a previously published source acknowledged for all or part of this Wiley Material. Any third party content is expressly excluded from this permission.
- With respect to the Wiley Materials, all rights are reserved. Except as expressly granted by the terms of the license, no part of the Wiley Materials may be copied, modified, adapted (except for minor reformatting required by the new Publication),

<https://s100.copyright.com/CustomAdmin/PLF.jsp?ref=4e38f727-d3f5-4b59-9c56-8874f8a0bc32>

2/5

15.11.2021 20:16

RightsLink Printable License

translated, reproduced, transferred or distributed, in any form or by any means, and no derivative works may be made based on the Wiley Materials without the prior permission of the respective copyright owner. **For STM Signatory Publishers clearing permission under the terms of the [STM Permissions Guidelines](#) only, the terms of the license are extended to include subsequent editions and for editions in other languages, provided such editions are for the work as a whole in situ and does not involve the separate exploitation of the permitted figures or extracts.** You may not alter, remove or suppress in any manner any copyright, trademark or other notices displayed by the Wiley Materials. You may not license, rent, sell, loan, lease, pledge, offer as security, transfer or assign the Wiley Materials on a stand-alone basis, or any of the rights granted to you hereunder to any other person.

- The Wiley Materials and all of the intellectual property rights therein shall at all times remain the exclusive property of John Wiley & Sons Inc, the Wiley Companies, or their respective licensors, and your interest therein is only that of having possession of and the right to reproduce the Wiley Materials pursuant to Section 2 herein during the continuance of this Agreement. You agree that you own no right, title or interest in or to the Wiley Materials or any of the intellectual property rights therein. You shall have no rights hereunder other than the license as provided for above in Section 2. No right, license or interest to any trademark, trade name, service mark or other branding ("Marks") of WILEY or its licensors is granted hereunder, and you agree that you shall not assert any such right, license or interest with respect thereto
- NEITHER WILEY NOR ITS LICENSORS MAKES ANY WARRANTY OR REPRESENTATION OF ANY KIND TO YOU OR ANY THIRD PARTY, EXPRESS, IMPLIED OR STATUTORY, WITH RESPECT TO THE MATERIALS OR THE ACCURACY OF ANY INFORMATION CONTAINED IN THE MATERIALS, INCLUDING, WITHOUT LIMITATION, ANY IMPLIED WARRANTY OF MERCHANTABILITY, ACCURACY, SATISFACTORY QUALITY, FITNESS FOR A PARTICULAR PURPOSE, USABILITY, INTEGRATION OR NON-INFRINGEMENT AND ALL SUCH WARRANTIES ARE HEREBY EXCLUDED BY WILEY AND ITS LICENSORS AND WAIVED BY YOU.
- WILEY shall have the right to terminate this Agreement immediately upon breach of this Agreement by you.
- You shall indemnify, defend and hold harmless WILEY, its Licensors and their respective directors, officers, agents and employees, from and against any actual or threatened claims, demands, causes of action or proceedings arising from any breach of this Agreement by you.
- IN NO EVENT SHALL WILEY OR ITS LICENSORS BE LIABLE TO YOU OR ANY OTHER PARTY OR ANY OTHER PERSON OR ENTITY FOR ANY SPECIAL, CONSEQUENTIAL, INCIDENTAL, INDIRECT, EXEMPLARY OR PUNITIVE DAMAGES, HOWEVER CAUSED, ARISING OUT OF OR IN CONNECTION WITH THE DOWNLOADING, PROVISIONING, VIEWING OR USE OF THE MATERIALS REGARDLESS OF THE FORM OF ACTION, WHETHER FOR BREACH OF CONTRACT, BREACH OF WARRANTY, TORT, NEGLIGENCE, INFRINGEMENT OR OTHERWISE (INCLUDING, WITHOUT LIMITATION, DAMAGES BASED ON LOSS OF PROFITS, DATA, FILES, USE, BUSINESS OPPORTUNITY OR CLAIMS OF THIRD PARTIES), AND WHETHER OR NOT THE PARTY HAS BEEN ADVISED OF THE POSSIBILITY OF SUCH DAMAGES. THIS LIMITATION SHALL APPLY NOTWITHSTANDING ANY FAILURE OF ESSENTIAL PURPOSE OF ANY LIMITED REMEDY PROVIDED HEREIN.
- Should any provision of this Agreement be held by a court of competent jurisdiction to be illegal, invalid, or unenforceable, that provision shall be deemed amended to achieve as nearly as possible the same economic effect as the original provision, and the legality, validity and enforceability of the remaining provisions of this Agreement shall not be affected or impaired thereby.
- The failure of either party to enforce any term or condition of this Agreement shall not constitute a waiver of either party's right to enforce each and every term and condition of this Agreement. No breach under this agreement shall be deemed waived or excused by either party unless such waiver or consent is in writing signed by the party granting such waiver or consent. The waiver by or consent of a party to a breach of

<https://s100.copyright.com/CustomerAdmin/PLF.jsp?ref=4e38f727-d3f5-4b59-9c56-8874f8a0bc32>

3/5

15.11.2021 20:16

RightsLink Printable License

any provision of this Agreement shall not operate or be construed as a waiver of or consent to any other or subsequent breach by such other party.

- This Agreement may not be assigned (including by operation of law or otherwise) by you without WILEY's prior written consent.
- Any fee required for this permission shall be non-refundable after thirty (30) days from receipt by the CCC.
- These terms and conditions together with CCC's Billing and Payment terms and conditions (which are incorporated herein) form the entire agreement between you and WILEY concerning this licensing transaction and (in the absence of fraud) supersedes all prior agreements and representations of the parties, oral or written. This Agreement may not be amended except in writing signed by both parties. This Agreement shall be binding upon and inure to the benefit of the parties' successors, legal representatives, and authorized assigns.
- In the event of any conflict between your obligations established by these terms and conditions and those established by CCC's Billing and Payment terms and conditions, these terms and conditions shall prevail.
- WILEY expressly reserves all rights not specifically granted in the combination of (i) the license details provided by you and accepted in the course of this licensing transaction, (ii) these terms and conditions and (iii) CCC's Billing and Payment terms and conditions.
- This Agreement will be void if the Type of Use, Format, Circulation, or Requestor Type was misrepresented during the licensing process.
- This Agreement shall be governed by and construed in accordance with the laws of the State of New York, USA, without regards to such state's conflict of law rules. Any legal action, suit or proceeding arising out of or relating to these Terms and Conditions or the breach thereof shall be instituted in a court of competent jurisdiction in New York County in the State of New York in the United States of America and each party hereby consents and submits to the personal jurisdiction of such court, waives any objection to venue in such court and consents to service of process by registered or certified mail, return receipt requested, at the last known address of such party.

WILEY OPEN ACCESS TERMS AND CONDITIONS

Wiley Publishes Open Access Articles in fully Open Access Journals and in Subscription journals offering Online Open. Although most of the fully Open Access journals publish open access articles under the terms of the Creative Commons Attribution (CC BY) License only, the subscription journals and a few of the Open Access Journals offer a choice of Creative Commons Licenses. The license type is clearly identified on the article.

The Creative Commons Attribution License

The [Creative Commons Attribution License \(CC-BY\)](#) allows users to copy, distribute and transmit an article, adapt the article and make commercial use of the article. The CC-BY license permits commercial and non-

Creative Commons Attribution Non-Commercial License

The [Creative Commons Attribution Non-Commercial \(CC-BY-NC\) License](#) permits use, distribution and reproduction in any medium, provided the original work is properly cited and is not used for commercial purposes.(see below)

Creative Commons Attribution-Non-Commercial-NoDerivs License

The [Creative Commons Attribution Non-Commercial-NoDerivs License \(CC-BY-NC-ND\)](#) permits use, distribution and reproduction in any medium, provided the original work is properly cited, is not used for commercial purposes and no modifications or adaptations are made. (see below)

Use by commercial "for-profit" organizations

<https://s100.copyright.com/CustomerAdmin/PLF.jsp?ref=4e38f727-d3f5-4b59-9c56-8874f8a0bc32>

4/5

15.11.2021 20:16

RightsLink Printable License

Use of Wiley Open Access articles for commercial, promotional, or marketing purposes requires further explicit permission from Wiley and will be subject to a fee.

Further details can be found on Wiley Online Library
<http://olabout.wiley.com/WileyCDA/Section/id-410895.html>

Other Terms and Conditions:

v1.10 Last updated September 2015

Questions? customercare@copyright.com or +1-855-239-3415 (toll free in the US) or +1-978-646-2777.

C.4. The License for Article 4 in Chapter 7

15.11.2021 20:19

RightsLink Printable License

JOHN WILEY AND SONS LICENSE
TERMS AND CONDITIONS

Nov 15, 2021

This Agreement between Bogazici University -- Gamze TANRIVER ("You") and John Wiley and Sons ("John Wiley and Sons") consists of your license details and the terms and conditions provided by John Wiley and Sons and Copyright Clearance Center.

License Number	5190290158095
License date	Nov 15, 2021
Licensed Content Publisher	John Wiley and Sons
Licensed Content Publication	Helvetica Chimica Acta
Licensed Content Title	Straightforward Synthesis of 3-Aminothiophenes Using Activated Amides
Licensed Content Author	Alain De Mesmaeker, Sarah Sulzer-Mossé, Saron Catak, et al
Licensed Content Date	Mar 28, 2019
Licensed Content Volume	102
Licensed Content Issue	4
Licensed Content Pages	10
Type of use	Dissertation/Thesis
Requestor type	Author of this Wiley article
Format	Print and electronic
Portion	Full article
Will you be translating?	No

<https://s100.copyright.com/AppDispatchServlet>

1/5

15.11.2021 20:19

RightsLink Printable License

Title	Molecular modeling of Bcl-xL post-translational modifications and of Keteniminium salts
Institution name	Bogazici University
Expected presentation date	Dec 2021
Requestor Location	Bogazici University BOĞAZIÇI ÜNİVERSİTESİ KUZEY KAMPUS KARE KİMYA BÖLÜM SEKRETERLİĞİ KAT 3 BEBEK İstanbul, 34342 Turkey Attn: Bogazici University
Publisher Tax ID	EU826007151
Total	0.00 USD

Terms and Conditions

TERMS AND CONDITIONS

This copyrighted material is owned by or exclusively licensed to John Wiley & Sons, Inc. or one of its group companies (each a "Wiley Company") or handled on behalf of a society with which a Wiley Company has exclusive publishing rights in relation to a particular work (collectively "WILEY"). By clicking "accept" in connection with completing this licensing transaction, you agree that the following terms and conditions apply to this transaction (along with the billing and payment terms and conditions established by the Copyright Clearance Center Inc., ("CCC's Billing and Payment terms and conditions"), at the time that you opened your RightsLink account (these are available at any time at <http://myaccount.copyright.com>).

Terms and Conditions

- The materials you have requested permission to reproduce or reuse (the "Wiley Materials") are protected by copyright.
- You are hereby granted a personal, non-exclusive, non-sub licensable (on a stand-alone basis), non-transferable, worldwide, limited license to reproduce the Wiley Materials for the purpose specified in the licensing process. This license, **and any CONTENT (PDF or image file) purchased as part of your order**, is for a one-time use only and limited to any maximum distribution number specified in the license. The first instance of republication or reuse granted by this license must be completed within two years of the date of the grant of this license (although copies prepared before the end date may be distributed thereafter). The Wiley Materials shall not be used in any other manner or for any other purpose, beyond what is granted in the license. Permission is granted subject to an appropriate acknowledgement given to the author, title of the material/book/journal and the publisher. You shall also duplicate the copyright notice that appears in the Wiley publication in your use of the Wiley Material. Permission is also granted on the understanding that nowhere in the text is a previously published source acknowledged for all or part of this Wiley Material. Any third party content is expressly excluded from this permission.
- With respect to the Wiley Materials, all rights are reserved. Except as expressly granted by the terms of the license, no part of the Wiley Materials may be copied, modified, adapted (except for minor reformatting required by the new Publication),

<https://s100.copyright.com/AppDispatchServlet>

2/5

15.11.2021 20:19

RightsLink Printable License

translated, reproduced, transferred or distributed, in any form or by any means, and no derivative works may be made based on the Wiley Materials without the prior permission of the respective copyright owner. **For STM Signatory Publishers clearing permission under the terms of the [STM Permissions Guidelines](#) only, the terms of the license are extended to include subsequent editions and for editions in other languages, provided such editions are for the work as a whole in situ and does not involve the separate exploitation of the permitted figures or extracts.** You may not alter, remove or suppress in any manner any copyright, trademark or other notices displayed by the Wiley Materials. You may not license, rent, sell, loan, lease, pledge, offer as security, transfer or assign the Wiley Materials on a stand-alone basis, or any of the rights granted to you hereunder to any other person.

- The Wiley Materials and all of the intellectual property rights therein shall at all times remain the exclusive property of John Wiley & Sons Inc, the Wiley Companies, or their respective licensors, and your interest therein is only that of having possession of and the right to reproduce the Wiley Materials pursuant to Section 2 herein during the continuance of this Agreement. You agree that you own no right, title or interest in or to the Wiley Materials or any of the intellectual property rights therein. You shall have no rights hereunder other than the license as provided for above in Section 2. No right, license or interest to any trademark, trade name, service mark or other branding ("Marks") of WILEY or its licensors is granted hereunder, and you agree that you shall not assert any such right, license or interest with respect thereto
- NEITHER WILEY NOR ITS LICENSORS MAKES ANY WARRANTY OR REPRESENTATION OF ANY KIND TO YOU OR ANY THIRD PARTY, EXPRESS, IMPLIED OR STATUTORY, WITH RESPECT TO THE MATERIALS OR THE ACCURACY OF ANY INFORMATION CONTAINED IN THE MATERIALS, INCLUDING, WITHOUT LIMITATION, ANY IMPLIED WARRANTY OF MERCHANTABILITY, ACCURACY, SATISFACTORY QUALITY, FITNESS FOR A PARTICULAR PURPOSE, USABILITY, INTEGRATION OR NON-INFRINGEMENT AND ALL SUCH WARRANTIES ARE HEREBY EXCLUDED BY WILEY AND ITS LICENSORS AND WAIVED BY YOU.
- WILEY shall have the right to terminate this Agreement immediately upon breach of this Agreement by you.
- You shall indemnify, defend and hold harmless WILEY, its Licensors and their respective directors, officers, agents and employees, from and against any actual or threatened claims, demands, causes of action or proceedings arising from any breach of this Agreement by you.
- IN NO EVENT SHALL WILEY OR ITS LICENSORS BE LIABLE TO YOU OR ANY OTHER PARTY OR ANY OTHER PERSON OR ENTITY FOR ANY SPECIAL, CONSEQUENTIAL, INCIDENTAL, INDIRECT, EXEMPLARY OR PUNITIVE DAMAGES, HOWEVER CAUSED, ARISING OUT OF OR IN CONNECTION WITH THE DOWNLOADING, PROVISIONING, VIEWING OR USE OF THE MATERIALS REGARDLESS OF THE FORM OF ACTION, WHETHER FOR BREACH OF CONTRACT, BREACH OF WARRANTY, TORT, NEGLIGENCE, INFRINGEMENT OR OTHERWISE (INCLUDING, WITHOUT LIMITATION, DAMAGES BASED ON LOSS OF PROFITS, DATA, FILES, USE, BUSINESS OPPORTUNITY OR CLAIMS OF THIRD PARTIES), AND WHETHER OR NOT THE PARTY HAS BEEN ADVISED OF THE POSSIBILITY OF SUCH DAMAGES. THIS LIMITATION SHALL APPLY NOTWITHSTANDING ANY FAILURE OF ESSENTIAL PURPOSE OF ANY LIMITED REMEDY PROVIDED HEREIN.
- Should any provision of this Agreement be held by a court of competent jurisdiction to be illegal, invalid, or unenforceable, that provision shall be deemed amended to achieve as nearly as possible the same economic effect as the original provision, and the legality, validity and enforceability of the remaining provisions of this Agreement shall not be affected or impaired thereby.
- The failure of either party to enforce any term or condition of this Agreement shall not constitute a waiver of either party's right to enforce each and every term and condition of this Agreement. No breach under this agreement shall be deemed waived or excused by either party unless such waiver or consent is in writing signed by the party granting such waiver or consent. The waiver by or consent of a party to a breach of

<https://s100.copyright.com/AppDispatchServ/let>

3/5

15.11.2021 20:19

RightsLink Printable License

any provision of this Agreement shall not operate or be construed as a waiver of or consent to any other or subsequent breach by such other party.

- This Agreement may not be assigned (including by operation of law or otherwise) by you without WILEY's prior written consent.
- Any fee required for this permission shall be non-refundable after thirty (30) days from receipt by the CCC.
- These terms and conditions together with CCC's Billing and Payment terms and conditions (which are incorporated herein) form the entire agreement between you and WILEY concerning this licensing transaction and (in the absence of fraud) supersedes all prior agreements and representations of the parties, oral or written. This Agreement may not be amended except in writing signed by both parties. This Agreement shall be binding upon and inure to the benefit of the parties' successors, legal representatives, and authorized assigns.
- In the event of any conflict between your obligations established by these terms and conditions and those established by CCC's Billing and Payment terms and conditions, these terms and conditions shall prevail.
- WILEY expressly reserves all rights not specifically granted in the combination of (i) the license details provided by you and accepted in the course of this licensing transaction, (ii) these terms and conditions and (iii) CCC's Billing and Payment terms and conditions.
- This Agreement will be void if the Type of Use, Format, Circulation, or Requestor Type was misrepresented during the licensing process.
- This Agreement shall be governed by and construed in accordance with the laws of the State of New York, USA, without regards to such state's conflict of law rules. Any legal action, suit or proceeding arising out of or relating to these Terms and Conditions or the breach thereof shall be instituted in a court of competent jurisdiction in New York County in the State of New York in the United States of America and each party hereby consents and submits to the personal jurisdiction of such court, waives any objection to venue in such court and consents to service of process by registered or certified mail, return receipt requested, at the last known address of such party.

WILEY OPEN ACCESS TERMS AND CONDITIONS

Wiley Publishes Open Access Articles in fully Open Access Journals and in Subscription journals offering Online Open. Although most of the fully Open Access journals publish open access articles under the terms of the Creative Commons Attribution (CC BY) License only, the subscription journals and a few of the Open Access Journals offer a choice of Creative Commons Licenses. The license type is clearly identified on the article.

The Creative Commons Attribution License

The [Creative Commons Attribution License \(CC-BY\)](#) allows users to copy, distribute and transmit an article, adapt the article and make commercial use of the article. The CC-BY license permits commercial and non-

Creative Commons Attribution Non-Commercial License

The [Creative Commons Attribution Non-Commercial \(CC-BY-NC\) License](#) permits use, distribution and reproduction in any medium, provided the original work is properly cited and is not used for commercial purposes.(see below)

Creative Commons Attribution-Non-Commercial-NoDerivs License

The [Creative Commons Attribution Non-Commercial-NoDerivs License \(CC-BY-NC-ND\)](#) permits use, distribution and reproduction in any medium, provided the original work is properly cited, is not used for commercial purposes and no modifications or adaptations are made. (see below)

Use by commercial "for-profit" organizations

<https://s100.copyright.com/AppDispatchServlet>

4/5

15.11.2021 20:19

RightsLink Printable License

Use of Wiley Open Access articles for commercial, promotional, or marketing purposes requires further explicit permission from Wiley and will be subject to a fee.

Further details can be found on Wiley Online Library
<http://olabout.wiley.com/WileyCDA/Section/id-410895.html>

Other Terms and Conditions:

v1.10 Last updated September 2015

Questions? customer@copyright.com or +1-855-239-3415 (toll free in the US) or +1-978-646-2777.

C.5. The Licenses for Articles 5-7 in Chapter 7



[Home](#)
[Help](#)
[Email Support](#)
[Sign in](#)
[Create Account](#)



Access to 3-aminobenzothiophenes and 3-aminothiophenes fused to 5-membered heteroaromatic rings through 6π-electrocyclization reaction of keteniminium salts
Author: Amandine Kolleth, Simona Müller, Alexandre Lumbruso, Gamze Tanriver, Saron Catak, Sarah Sulzer-Mossé, Alain De Mesmaeker
Publication: Tetrahedron Letters
Publisher: Elsevier
Date: 22 August 2018
© 2018 Elsevier Ltd. All rights reserved.

Journal Author Rights

Please note that, as the author of this Elsevier article, you retain the right to include it in a thesis or dissertation, provided it is not published commercially. Permission is not required, but please ensure that you reference the journal as the original source. For more information on this and on your other retained rights, please visit: <https://www.elsevier.com/about/our-business/policies/copyright#Author-rights>

BACK

CLOSE WINDOW



[Home](#)
[Help](#)
[Email Support](#)
[Sign in](#)
[Create Account](#)



Synthesis of 4-membered ring alkaloid analogues via intramolecular [2+2] cycloaddition involving keteniminium salt intermediates
Author: Amandine Kolleth, Alexandre Lumbruso, Gamze Tanriver, Saron Catak, Sarah Sulzer-Mossé, Alain De Mesmaeker
Publication: Tetrahedron Letters
Publisher: Elsevier
Date: 26 July 2017
© 2017 Elsevier Ltd. All rights reserved.

Journal Author Rights

Please note that, as the author of this Elsevier article, you retain the right to include it in a thesis or dissertation, provided it is not published commercially. Permission is not required, but please ensure that you reference the journal as the original source. For more information on this and on your other retained rights, please visit: <https://www.elsevier.com/about/our-business/policies/copyright#Author-rights>

BACK

CLOSE WINDOW



[Home](#)
[Help](#)
[Email Support](#)
[Sign in](#)
[Create Account](#)



Synthesis of amino-cyclobutanes via [2+2] cycloadditions involving keteniminium intermediates
Author: Amandine Kolleth, Alexandre Lumbruso, Gamze Tanriver, Saron Catak, Sarah Sulzer-Mossé, Alain De Mesmaeker
Publication: Tetrahedron Letters
Publisher: Elsevier
Date: 22 June 2016
© 2016 Elsevier Ltd. All rights reserved.

Journal Author Rights

Please note that, as the author of this Elsevier article, you retain the right to include it in a thesis or dissertation, provided it is not published commercially. Permission is not required, but please ensure that you reference the journal as the original source. For more information on this and on your other retained rights, please visit: <https://www.elsevier.com/about/our-business/policies/copyright#Author-rights>

BACK

CLOSE WINDOW